frontiers | Research Topics

Multiphase flow behavior in complex and critical environments

Edited by
Zhiyuan Wang, Huazhou Li and Weiqi Fu

Published in
Frontiers in Earth Science

ISSN 1664-8714
ISBN 978-2-83251-017-9
DOI 10.3389/978-2-83251-017-9

About Frontiers

Frontiers is more than just an open access publisher of scholarly articles: it is a pioneering approach to the world of academia, radically improving the way scholarly research is managed. The grand vision of Frontiers is a world where all people have an equal opportunity to seek, share and generate knowledge. Frontiers provides immediate and permanent online open access to all its publications, but this alone is not enough to realize our grand goals.

Frontiers journal series

The Frontiers journal series is a multi-tier and interdisciplinary set of open-access, online journals, promising a paradigm shift from the current review, selection and dissemination processes in academic publishing. All Frontiers journals are driven by researchers for researchers; therefore, they constitute a service to the scholarly community. At the same time, the *Frontiers journal series* operates on a revolutionary invention, the tiered publishing system, initially addressing specific communities of scholars, and gradually climbing up to broader public understanding, thus serving the interests of the lay society, too.

Dedication to quality

Each Frontiers article is a landmark of the highest quality, thanks to genuinely collaborative interactions between authors and review editors, who include some of the world's best academicians. Research must be certified by peers before entering a stream of knowledge that may eventually reach the public - and shape society; therefore, Frontiers only applies the most rigorous and unbiased reviews. Frontiers revolutionizes research publishing by freely delivering the most outstanding research, evaluated with no bias from both the academic and social point of view. By applying the most advanced information technologies, Frontiers is catapulting scholarly publishing into a new generation.

What are Frontiers Research Topics?

Frontiers Research Topics are very popular trademarks of the *Frontiers journals series*: they are collections of at least ten articles, all centered on a particular subject. With their unique mix of varied contributions from Original Research to Review Articles, Frontiers Research Topics unify the most influential researchers, the latest key findings and historical advances in a hot research area.

Find out more on how to host your own Frontiers Research Topic or contribute to one as an author by contacting the Frontiers editorial office: frontiersin.org/about/contact

Multiphase flow behavior in complex and critical environments

Topic editors
Zhiyuan Wang — China University of Petroleum, Huadong, China
Huazhou Li — University of Alberta, Canada
Weiqi Fu — China University of Mining and Technology, China

Citation
Wang, Z., Li, H., Fu, W., eds. (2022). *Multiphase flow behavior in complex and critical environments*. Lausanne: Frontiers Media SA. doi: 10.3389/978-2-83251-017-9

Table of contents

frontiers | Frontiers in Earth Science

TYPE Editorial
PUBLISHED 28 November 2022
DOI 10.3389/feart.2022.1028442

Editorial: Multiphase flow behavior in complex and critical environments

Weiqi Fu[1]*, Huazhou Li[2] and Zhiyuan Wang[3]

[1]State Key Laboratory of Coal Resources and Safe Mining (CUMT), China University of Mining and Technology, Xuzhou, China, [2]School of Mining and Petroleum Engineering, University of Alberta, Edmonton, AB, Canada, [3]School of Petroleum Engineering, China University of Petroleum (East China), Qingdao, China

KEYWORDS

flow in wellbore, flow assurance, drilling and completion, well stimulations, multiphase flow in reservoir

OPEN ACCESS

EDITED AND REVIEWED BY
David R. Lentz,
University of New Brunswick
Fredericton, Canada

*CORRESPONDENCE
Weiqi Fu,
weiqi_fu@126.com

SPECIALTY SECTION
This article was submitted to Economic Geology,
a section of the journal
Frontiers in Earth Science

RECEIVED 26 August 2022
ACCEPTED 26 October 2022
PUBLISHED 28 November 2022

CITATION
Fu W, Li H and Wang Z (2022), Editorial: Multiphase flow behavior in complex and critical environments.
Front. Earth Sci. 10:1028442.
doi: 10.3389/feart.2022.1028442

Editorial on the Research Topic
Multiphase flow behavior in complex and critical environment

Due to an increasing demand for oil and gas resources in both developed and developing countries, producing crude oil and natural gas from offshore deep-water reservoirs and inland deep tight reservoirs becomes ever more important. However, it is a challenging job to produce hydrocarbons from such reservoirs since the working environments are normally quite tough. The wellbore temperature in deep-water wells can range from 4 to 200°C, while the wellbore pressure can range from 10 to 200 MPa. As a result, multiphase flow under such challenging environments tends to be more complex than that under normal environments. Since multiphase flow can pose a significant effect on well productivity, it is of utmost importance to study the multiphase flow behavior in such complex and critical environments.

This Research Topic aims to report recent developments related to the multiphase flow behavior in complex and critical environments and focuses on the following two aspects: 1) Gas adsorption, single-phase flow, and multiphase flow in porous media, 2) multiphase flow in wellbores and pipelines.

First, we summarize the studies related to the first aspect. Guodai et al. experimentally investigate the adsorption characteristics of CH_4 on different coal samples with different coal structures and find that the D-A adsorption potential model has the highest adaptability to describe the adsorption characteristics of CH_4 on coal. Wang et al. propose a modified desorption model for low-rank coal and couple it to a numerical simulator to study the flow dynamics of gas-water mixtures in coal seam reservoirs. Using the numerical simulation model, they are able to find out the optimal well patterns for developing high-dip-angle coal seam reservoirs. Huang et al. investigate the effects of the magnetic force on ferrofluid flow in complex porous media by the finite element method and reveal the essential mechanisms of ferrofluid flow in fractured porous media. Jia et al. further point out that the ferrofluid is a potential tracer that can locate the displacement front and can also work as a displacing fluid to enhance oil recovery. Jia et al. numerically present an improved two-scale continuum model and study the effects of the physical parameters of an isolated fracture on the outcomes of acidification. They find that the properties of an isolated fracture (including length, aperture, and position) have an obvious influence on the acidification. Cheng et al. use the Eulerian-Eulerian method to study the migration and distribution of proppants in a fracture network. Based on the simulated migration characteristics of proppants, the authors are able to define three distinct regions: corner anomaly area, buffer area and stability area. They point out that the turning angle has a large effect on proppant migration.

Second, we summarize the studies related to the second aspect. Jiang et al. numerically study the flow behavior of high-pressure gas through the orifice of a subsea throttling valve, and point out that a 7–8 MPa prefilling pressure of the pipeline downstream to the throttling valve can help maintain a downstream temperature above 0°C, thereby reducing the risk of hydrate formation and blockage. Guimin et al. propose a new model to predict the hydrate formation region in the drainage line of a gas hydrate production well. The simulation results show that the hydrate formation region is enlarged with an increase in electric submersible pump (ESP) pressure and a decrease in water production rate. Zhang et al. develop a spatio-temporal evolution model to study the hydraulic transport characteristics of particulate solids. The conclusions reached in their study provide useful insights into the optimization of the hydraulic-transport efficiency of particulate solids in pressurized pipelines and open flow channels. Wei et al. study the effect of flute tube on the liquid maldistribution and the gas maldistribution experimentally. Their experimental results indicate that a horizontal manifold without flute tube is more conducive to the suppression of the average liquid maldistribution degree under slug flow patterns and the suppression of the average gas maldistribution degree under annular flow patterns.

Author contributions

WF was a guest associate editor of the Research Topic and drafted the editorial. ZW and HL were guest associate editors of the Research Topic and edited the editorial.

Funding

WF is supported by the National Key Research and Development Program of China (2021YFC2902102), the National Natural Science Foundation of China (NSFC) Youth Fund (52104047), the Natural Science Foundation of Jiangsu Province Youth Fund (BK20210507), CNPC Innovation Found (2021DQ02—1005), and Independent Research Project of State Key Laboratory of Coal Resources and Safe Mining, China University of Mining and Technology (SKLCRSM22X002).

Acknowledgments

We thank the authors for contributing their papers to this Research Topic and the reviewers for providing timely reviews. We also thank the editorial board of Economic Geology, Hydrosphere, Earth and Planetary Materials, and Geochemistry in Frontiers in Earth Science (especially the Frontiers specialist, Fang Chen) for their editorial support.

Conflict of interest

The authors declare that the research was conducted in the absence of any commercial or financial relationships that could be construed as a potential conflict of interest.

Publisher's note

frontiers
in Earth Science

ORIGINAL RESEARCH
published: 07 June 2021
doi: 10.3389/feart.2021.692619

Numerical Simulation Research on Well Pattern Optimization in High–Dip Angle Coal Seams: A Case of Baiyanghe Block

Hongli Wang[1], *Xiao Zhang*[2]*, *Suian Zhang*[1]*, *Hongxing Huang*[3,4] *and Jun Wang*[5]

[1]College of Petroleum Engineering, China University of Petroleum, Beijing, China, [2]College of Science, China University of Petroleum, Beijing, China, [3]China United Coalbed Methane National Engineering Research Center Co. Ltd, Beijing, China, [4]National Engineering Research Center for Coalbed Methane Development and Utilization, Beijing, China, [5]Shanxi Lanyan Coalbed Methane Group Co., Ltd, Jincheng, China

OPEN ACCESS

Edited by:
Huazhou Li,
University of Alberta, Canada

Reviewed by:
Sarada Prasad Pradhan,
Indian Institute of Technology
Roorkee, India
Kai Sheng,
University of Texas at Austin,
United States

***Correspondence:**
Xiao Zhang
zhangxiao@cup.edu.cn
Suian Zhang
sazhang@cup.edu.cn

Specialty section:
This article was submitted to
Economic Geology,
a section of the journal
Frontiers in Earth Science

Received: *08 April 2021*
Accepted: *12 May 2021*
Published: *07 June 2021*

Citation:
Wang H, Zhang X, Zhang S, Huang H
and Wang J (2021) Numerical
Simulation Research on Well Pattern
Optimization in High–Dip Angle Coal
Seams: A Case of Baiyanghe Block.
Front. Earth Sci. 9:692619.
doi: 10.3389/feart.2021.692619

The Baiyanghe block in Fukang, Xinjiang, China, is rich in coalbed methane (CBM) resources, and several pilot experimental wells have yielded high production. Due to the high dip angle (35–55°) of the coal seam in this area, the lack of understanding of the geological characteristics, the physical properties of coal, and gas–water migration law lead to immature development techniques and poor overall development benefits. We first conducted desorption and adsorption tests on low-rank coal of this area and found residual gas in the coal. We established a coalbed methane desorption model suitable for this area by modifying the isotherm adsorption model. Next, by analyzing the influence of the gas–water gravity differentiation in the high–dip angle coal seam and the shallow fired coalbed methane characteristics in this area, we discovered the leakage of CBM from the shallow exposed area of the coal seam. Given the particular physical property of coal and gas–water migration characteristics in this area, we optimized the well pattern: (i) the U-shaped along-dip horizontal well group in coal seams is the main production well for gas production with a spacing distance of 312 m; (ii) a multistage fracturing well drilled in the floor of coal is for water production; and (iii) vertical wells with a spacing distance of 156 m in the shallow area is to capture CBM leakage. Using numerical simulation and net present value (NPV) economics models, we optimized the well pattern details. Applying our CBM desorption model, the numerical simulator can improve the accuracy of the low-rank coalbed methane productivity forecast. The optimization results demonstrated the following: 1) the cumulative gas production of single U-shaped well increased by 89% with the optimal well spacing, 2) the cumulative gas production of the well group increased by 87.54% after adding the floor staged horizontal well, and 3) the amount of CBM leakage decrease by 67.59%.

Keywords: coalbed methane, high–dip angle coal seam, desorption model, reservoir numerical simulation, well pattern optimization, Baiyanghe mining area

INTRODUCTION

Background

Coalbed methane (CBM), also called coal seam gas (CSG), is an unconventional resource. The development of CBM has three practical applications: first, it alleviates energy shortages as a clean energy. Second, it sequesters carbon dioxide to alleviate the greenhouse effect. Most importantly, it reduces the risk of underground coal mine operations by improving the safety of the miners (Zhang et al., 2016). The Baiyanghe block in Fukang, Xinjiang, China, is rich in coal and CBM resources. The CBM development in the Baiyanghe mining area was the first CBM development case in Xinjiang (Mu et al., 2015), which played a positive role in promoting China's low-rank CBM development and made full use of the abundant resources in China's northwest area. During the block's early pilot tests, traditional vertical wells and horizontal wells were drilled. Few wells achieved good production, while most wells did not get a satisfactory development benefit. In this study area, the coal seam is thick with a high dip angle. Optimizing the CBM development method and improving the CBM production and economic benefits are the top priorities.

The accurate CBM reservoir numerical simulation is the most commonly used development optimization method. Using numerical simulation, engineers can provide effective development plans before drilling expensive production wells. They can also update and redescribe the reservoir by history matching during the development process to track and optimize the development plan. Optimizing the well pattern is a crucial task for CBM development. By optimizing the CBM well pattern, we can improve drainage efficiency, accelerate pressure reduction speed, and obtain higher economic benefits. However, the work is arduous and complicated, especially when multiparameter optimization is required. Zulkarnain (2006) conducted a multiparameter simulation to optimize well spacing for CBM production. He found that narrow well spacing can accelerate the drainage process and increase the recovery of CBM. Clarkson and McGovern (2005) developed a new CBM exploration tool to optimize well spacing. Chen et al. (2010) found that the best wellbore direction of four-sided CBM wells should be parallel to the butt cleat direction. The central well angle of a pinnate horizontal well is affected by the anisotropy ratio of permeability. The reservoir simulation conversion method performed by Keim et al. (2011) can optimize the well pattern to maintain high productivity in low-permeability (less than 1.0 MD) coal seam. There are many cases of CBM well spacing optimization, but they mainly focused on horizontal coal seams.

There are also some learning optimization algorithms involved. The main idea is to build many simulation cases and set objective functions for a simulator to run until achieving an optimal value. Beckner and Song (1995) first applied a repetition simulation algorithm and an objective function of the net present value (NPV) to optimize a horizontal well's position with a fixed direction. Genetic algorithm (GA) is one of the most popular optimization algorithms, and Güyagüler et al. (2002) used it to optimize well positions. Bouzarkouna et al. (2013) applied an optimization method based on the covariance matrix adaptation evolution strategy to optimize the well location trajectory. The particle swarm optimization algorithm application can significantly reduce the optimization time (Onwunalu and Durlofsky, 2010). Feng et al. (2012) used it to optimize the layout of a single well and multiple wells by maximizing the NPV in the synthetic reservoirs. However, these methods did not consider the stability and feasibility of wellbore drilling in high-dip coal seams, meaning currently unable to learn particular reservoir characteristics.

There have been some studies on the optimization of well patterns for high–dip angle coal seams. Mu et al. (2014) considered that wells should not be drilled in the structure's shallow area, but rather at the structural wing. Ni et al. (2007) proposed different well layout methods for different structural positions: the inverted trapezoid method was for the anticline and syncline, and the triangular method or rhombus method was for the structural wings. Wang et al. (2019) proposed that horizontal wells should be drilled at the shallow area of the coal seam, along the coal seam at the structural wings, and the end of the horizontal well is at the bottom of the coal seam. Vertical wells or T-shaped wells can be drilled at the deep area. Other well layout ideas for high–dip angle coal seams include fan-shaped well layout methods and small well pattern methods. The above methods focus on drilling particular wells in particular areas, while ignoring the cooperation of different types of wells. Besides, they did not consider the desorption and adsorption characteristics of low-rank coalbed methane and the special gas–water migration characteristics caused by the coal seam's large inclination angle.

The main factors affecting CBM production include the field pressure–volume–temperature (PVT) data, gas content, hydrological data, coal seam structure, and permeability (Tao et al., 2019). Our study focuses on the desorption and adsorption characteristics of low-rank coal, gas–water migration characteristics, and the comprehensive influence of different well types on gas production. Palmer (2008) proposed three specific solutions to utilize CBM reservoirs effectively: 1) locating a high-yield area in the mining area through structural geological maps and coal thickness maps; 2) drilling horizontal wells to produce gas; and 3) developing advanced production stimulation technologies to expand the natural fractures in the coal seam. We started the research with the second and third aspects.

First, we performed adsorption and desorption experiments on low-rank coal samples and found that the coal samples still had a considerable residual gas after negative pressure desorption. Second, we modified the Langmuir isotherm adsorption line to improve the accuracy of absorption data and productivity prediction. Then we analyzed the main negative effects of the high–dip angle coal seam's gas–water gravity phenomenon through numerical simulation methods. Finally, given the above characteristics of high–dip angle coal seams, we optimized the well type, well spacing, and drilling location to combine an optimal well pattern.

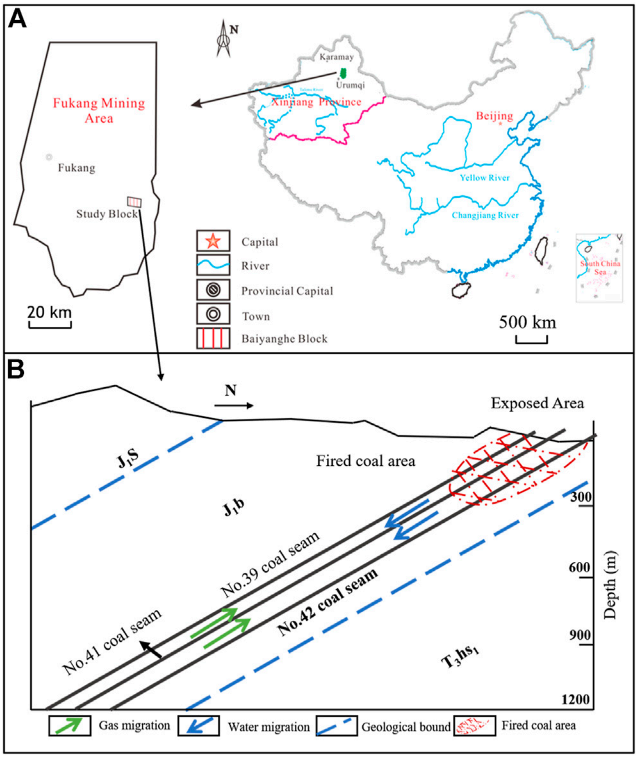

FIGURE 1 | Location and reservoir accumulation diagram of the Baiyanghe mining area: **(A)** the location, **(B)** the reservoir accumulation diagram.

Geological Background of the Research Area

Much of CBM in Xinjiang is low-rank CBM. The estimated CBM resources are 9.5 trillion m^3, accounting for 26% of the national CBM resources. The Baiyanghe block in Fukang is a typical low-rank coal area. CBM exploration and production tests of small well groups have achieved breakthroughs in production, demonstrating that the area has good development prospects. The geographical location is shown in **Figure 1A**. The ridge formed by sandstone of the Sangonghe Formation is located in the southern part of the mining area, while the flat beam formed by flaming rock is located in the northern part of the mining area. The directions of the ridge and the flat beam are consistent with the stratigraphic direction.

The Baiyanghe mining area's overall structure is a south-dipping monoclinic structure, with a strike of nearly east–west direction and a high dip angle. The coal-bearing strata change little in strike and tendency. The structural complexity is a simple structural type. There is a Honggou fault on the west side of the mining area, which is a normal fault, inclined to the west. The main coal seams are the Middle Jurassic Xishanyao Formation and the Lower Badaowan Formation. There are 17 layers of coal seams in the Xishanyao Formation, of which Nos. 39, 41, 42, and 43 coal seams are the main mineable coal seams. The coal seam's thickness is large, with the maximum thickness of a single layer being 22 m. There are 45 seams in the Badaowan Formation. Among them, there are seven mineable and thick coal seams. The maximum thickness of a single layer is 28.15 m. The total thickness of the Badaowan Formation stratum is 940.5 m. The average thickness of the coal seam is 68.5 m, with the coal content coefficient of 7.28%.

We considered No. 42 coal seam as the main research object. The total thickness of the No. 42 coal seam is between 8.67 and 25.01 m, with the average thickness of 19.36 m, the total thickness variation coefficient of 22.38%, and the secondary difference variation index of 42.66%. Its minable thickness is between 8.67 and 22.85 m, with an average thickness of 18.59 m, the recoverable thickness variation coefficient of 21.19%, and the second-order difference variation index of 41.53%. The estimated resource thickness is between 8.67 and 22.39 m, with an average of 18.32 m and the stratum dip of 45–53°. There are 0–3 layers of gangue with a simple structure and lithology of siltstone and carbonaceous mudstone. It is the largest, minable, and stable thick coal seam in the whole area. The roof is a dark gray powder with fine sandstone, with the floor of siltstone and medium sandstone. The distance from the No. 41 coal seam is between 24.91 and 35.66 m. The diagram of the reservoir accumulation is shown in **Figure 1B**.

MODIFIED DESORPTION ISOTHERM FOR LOW-RANK COAL

Coal Samples

The coal samples were from the Baode block, where the coal is also of low rank. The original samples were irregular lumps of different size with a total amount of about 100 kg. We smashed large coal samples into small ones with a diameter of less than 5 cm. Then we crushed them into powder to them pass through sieves. Only the coal samples between the sieves of 60 and 80 mesh were used for the experiment. We prepared three kinds of samples: dry coal samples, moisture equilibrium samples, and moisture saturated samples.

Experimental Method

The device used in the experiment is the Large Sample Adsorption and Desorption Simulation Device version 2.0 developed by Xi'an University of Science and Technology and China University of Petroleum. **Figure 2** shows experimental equipment and the device.

We performed the adsorption experiment following the national standard (GB/T 19560-2004). The temperature of the isothermal adsorption and desorption experiment was 25°C. The maximum experimental pressure point was 8 MPa. There were no less than seven and six pressure points in the adsorption and the desorption process, respectively. We used a computer to record the temperature of the negative pressure desorption experiment and manually read the precision vacuum gauge (-0.1–0 MPa).

In the first step, we weighed the crushed coal sample and added it to the sample cylinder. After sealing, the samples were put in the thermostat. We opened the valve at the inlet of the

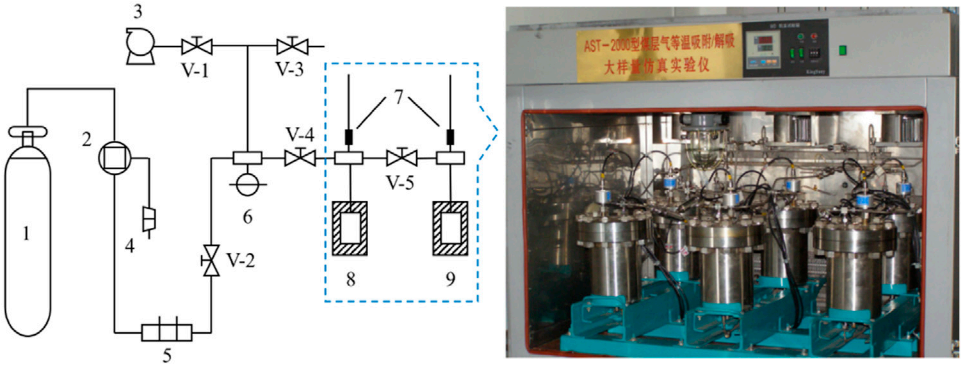

FIGURE 2 | Schematic diagram of CBM negative pressure desorption experiment and desorption device. 1: high-pressure CH_4 cylinder; 2: booster pump; 3: vacuum pump; 4: compressor; 5: gas filter; 6: pressure gauge; 7: pressure sensor; 8: reference cylinder; 9: sample cylinder; V-1 – V-5: valve.

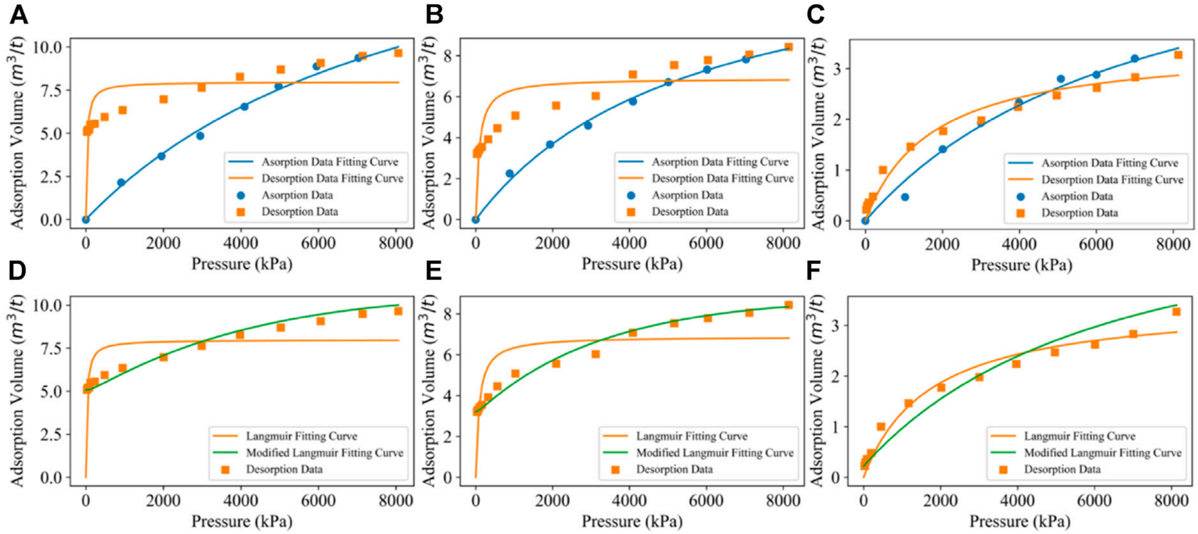

FIGURE 3 | Experiment data fitting: fitting by the Langmuir isotherm: **(A)** dry coal sample, **(B)** moisture-equilibrated coal sample, and **(C)** moisture-saturated coal. Fitting desorption data by modified Langmuir isotherm: **(D)** dry coal sample, **(E)** moisture-equilibrated coal sample, and **(F)** moisture-saturated coal.

intake pipe and filled the reference cylinder and the sample cylinder with methane. After the pressure of the two cylinders reached a certain value, we closed the intake valve. After keeping it for 6 h, we observed whether the pressure in each cylinder changed obviously: if there is, checking whether the equipment is leaking; if not, repeating the steps. We continued to fill each cylinder with gas to increase the pressure until the value reached the highest pressure required for the experiment. Then we evacuated the test system for 12 h and then carried out the negative pressure desorption experiment. We pumped the reference cylinder pressure to negative pressure (about 20 kPa) and opened the balance valve to make the sample cylinder and the reference cylinder pressure balance. Finally, we recorded the pressure after balance and calculated the desorption volume.

Experimental Results and Modified Desorption Model

Figures 3A–C show the experimental results of three kinds of samples. We found that all three kinds of samples had residual gas in the negative pressure desorption experiment. We used the Langmuir isotherm to fit the experimental results. The adsorption data fitted well, while the desorption curve did not fit accurately.

According to Weishauptová and Medek (1998); Weishauptová et al. (2004), they divided the methane adsorption in the coal matrix mainly into five types. The first type is a monolayer of CH_4 molecules adsorbed on the surface of medium and large pores. The second type is the methane molecules controlled by molecular forces near the matrix, which can move freely. They were also included in the calculation of the total gas content of coal. The third type is the dissolved methane molecules in moisture. The fourth type is the methane molecules filled in micropores. The fifth type is the molecules bound to the macromolecular coal matrix structure.

As pressure decreases, the bottleneck-shaped coal matrix gradually swells and the channels shrink, which leads to the generation of residual gas. Therefore, we supposed residual gas is also a function of pressure. To accurately characterize the desorption process of the low-rank coal in the study area, we modified the Langmuir isotherm. When pressure equals 0 kPa, the Langmuir curve returns to zero. Therefore, a residual gas content item *n* needs to be added, as shown in **Eq. 1**. At this time, the curve only moves up as a whole, and the residual gas term needs to be corrected as follows:

$$V = \frac{V_L P}{P_L + P} + n, \tag{1}$$

where V is the gas content at pressure P; V_L is the Langmuir volume, m^3/ton; P_L is the Langmuir pressure, kPa; and n is the residual gas content term, m^3/ton.

From the negative pressure desorption experiment, we can record two data points accurately: the residual gas content and the pressure point at the beginning of the desorption experiment (the maximum test pressure). The minimum pressure of the negative pressure desorption experiment is 20 kPa, approximated as 0 kPa. We used a linear equation of pressure to make the residual gas term as follows:

$$n = V_r - \frac{V_r}{P_{\max}} P, \tag{2}$$

where V_r is the residual gas content, m^3/ton, and $P_{\max}$ is maximum experimental pressure, kPa.

We used the desorption model with a linear residual gas term to fit the data and found that the determination coefficient (R^2) is low. Therefore, we modified the residual gas term to be nonlinear, as shown in **Eq. 3**:

$$n = V_r - \frac{V_r}{P_{\max}^{\alpha}} P^{\alpha}, \tag{3}$$

where α is the residual gas term relevant factor.

In order to retain the adsorption characteristics, we did not fit the Langmuir volume and pressure of the desorption data. Instead, we used the Langmuir volume and pressure of the adsorption data. The modified desorption model is shown as **Eq. 4**:

$$V = \frac{V_L P}{P_L + P} + V_r - \frac{V_r}{P_{\max}^{\alpha}} P^{\alpha}. \tag{4}$$

Now, only the residual gas term relevant factor in **Eq. 4** needs to be fitted. When $P = P_{\max}$, in **Eq. 3**, then $n = 0$. Therefore, **Eq. 4** is equivalent to the Langmuir isotherm. With the decrease in pressure, the bottleneck-shaped coal matrix gradually swells, the hysteresis effect of coalbed methane takes place, and residual gas is gradually generated. Therefore, we can use alpha to fit the generation process of residual gas. When $p = 0$ kPa, then $n = V_r$, which reflects the final residual coalbed methane in the sample.

Table 1 and **Figures 3D–F** show the comparison of fitting the desorption data using the modified and original Langmuir isotherm. Taking dry coal in **Figure 3A**,(a) as an example, R^2 of the Langmuir isotherm fitting the adsorption curve is 0.993 9. The Langmuir volume and pressure are 21.18 m^3/ton and 9,000.91 kPa, respectively. However, R^2 of the Langmuir fitting desorption data is only 0.594 3. The Langmuir volume and pressure obtained are 7.98 m^3/ton and 29.19 kPa, respectively. Then we used the modified Langmuir model to fit the desorption data. First, the Langmuir volume and Langmuir pressure of the Langmuir adsorption curve were retained. Second, we calibrated the starting point of the desorption experiment at 8,000 kPa and the residual gas content under the vacuum state of the negative pressure experiment to 5.08 m^3/ton. Finally, we only fitted the residual gas term relevant factor, which resulted in a value of 0.722 1 with an R^2 of 0.972 3, which is much better than the Langmuir isotherm result.

The coal seams' maximal gas content in the study area is about 10.47 m^3/ton, while the average gas content is only 8.35 m^3/ton. For 8.35 m^3/ton, the critical desorption pressure is about 900 kPa calculated by the Langmuir isotherm adsorption curve. Critical desorption pressure from the new two-point calibrated desorption–adsorption curve is about 600 kPa.

The negative pressure desorption experiment shows that coalbed methane desorption no longer follows the Langmuir isotherm in the low-pressure stage. Therefore, we used the two-point calibration to modify the isotherm. Due to the low-pressure stage, the decompression space is limited, the gas desorption power is insufficient, and the CBM desorption volume relatively shrinks, which is extremely unfavorable to the development of CBM resources. It is necessary to increase the drainage intensity.

NUMERICAL SIMULATION METHOD

Numerical Model

We used the CMG-GEM simulator to build the numerical model and generated the optimization scenarios of development. The GEM is a three-dimensional compositional simulator capable of simulating the sorption, diffusion, dual-porosity, and single-permeability flowing of CBM in coal, which is widely used in CBM development engineering studies (Karacan and Olea, 2015; Zhang et al., 2020).

We built the geological model using Cartesian grids with grid numbers of 100, 80, and 10 in the x, y, and z directions, respectively, and set the grid size to 15 m × 15 m × 2.57 m. The boundary is closed. We used the formula editor to edit the grid top burial depth to set the dip angle to 45 degrees along the y direction. Layers 1–7 and 8–10 are coal seams and sandstone floor layers, respectively, as shown in **Figure 5**. The initial physical property parameters of the model are from the actual geological data of a well in the No. 42 coal seam, as shown in **Table 2**.

Figures 4A,B show the gas content contour and buried depth contour of the pilot test. It can be found that the gas content distribution in the range of 200–1,150 m buried depth is 2-12 m^3/ton. By fitting the gas content with buried depth data, we found that the relationship between the depth and gas content is

TABLE 1 | Fitting results of adsorption and desorption data.

Coal sample	Adsorption data			Desorption data							
	Langmuir isotherm			Langmuir isotherm			Modified isotherm				
	V_L(m^3/ton)	P_L(kPa)	R^2	V_L(m^3/ton)	P_L(kPa)	R^2	V_L(m^3/ton)	P_L(kPa)	α	R^2
Dry	21.18	9000.91	0.9939	7.98	29.19	0.5943	21.18	9000.91	0.7221	0.9723
Moisture-equilibrated	14.15	5655.18	0.9965	6.89	87.24	0.6849	14.15	5655.18	0.7140	0.9834
Moisture-saturated	6.52	7443.01	0.9862	3.48	1722.89	0.9436	6.52	7443.01	1.01	0.9722

TABLE 2 | Original geological parameters and parameters after history matching.

Parameter	Original value	History matching value
Reference reservoir depth (m)	700	700
Formation thickness (m)	18	18
Formation dip (degree)	45	45
Reference cleat permeability (mD)	7	12
Fracture porosity (%)	3.5	0.05
Matrix porosity (%)	10.3	15.3
Reference gas content (m^3)	8.35	8.35
Gas content gradient (m^3/ton·m)	0.009	0.009
Reference fracture pressure (kPa)	6,000	6,000
Pressure gradient (kPa/m)	9.42	9.42
Rock compressibility (kPa^{-1})	1.8×10^{-5}	1.8×10^{-5}

approximately linear. Therefore, we used the gas content gradient of 0.009 m^3/ton m to set up the model. The permeability in this area is strongly anisotropic. Zhang et al. (2021) studied the relationship between permeability and dip angle through experiments and modeled coal seam permeability. We set the permeability of the model in three directions from his theory. Simultaneously, the permeability of the fired coal area, where the buried depth is less than 300 m, is increased tenfold.

Simulation of Gas–Water Gravity Differentiation Phenomenon

During the drainage process, water in the coal seam migrates to the well bottom under the influence of the production pressure difference. Simultaneously, gas is always affected by the vertical downward gravity and the free gas is affected by vertical upward buoyancy. Due to the influence of gravity and buoyancy on gas–water migration, gravity differentiation occurs in the flow process when the production pressure difference is small. Water flows to the deeper part of the reservoir, while gas accumulates on top of the reservoir. Zhou et al. (2015) and Cui et al. (2007) studied the CBM accumulation model of the study area. They revealed exposed areas and fired areas in the study area, which causes particular geological phenomena such as changes in hydrodynamic conditions. Wang et al. (2020) studied the dynamic characteristics of the gas content in the Baiyanghe block. He conducted a simulation and found that when the shallow part of the reservoir is in a closed state, a CBM accumulation area is formed in the shallow part of the coal seam at the later stage of drainage. Therefore, if the shallow area is not closed and the fired coal area has high permeability, CBM will leak from the exposed areas. To simulate CBM leakage, we inserted a row of virtual wells (wells 1, 3, and 5 in **Figure 5**), where the burial depth is 0 m. The study area is a monoclinic structure, while the exposed areas in the north of the Yilinhegel Mountain receive surface water replenishment. Groundwater migrates from shallow to deep areas along the steep slope. Since the water depth is difficult to be obtained, the bottom-hole pressure is assumed as 151 kPa (1.5 atm). To simulate surface water replenishment, we inserted a row of water injection virtual wells (wells 2 and 4 in **Figure 5**) between production wells with a buried depth of 0 m. Bottom-hole

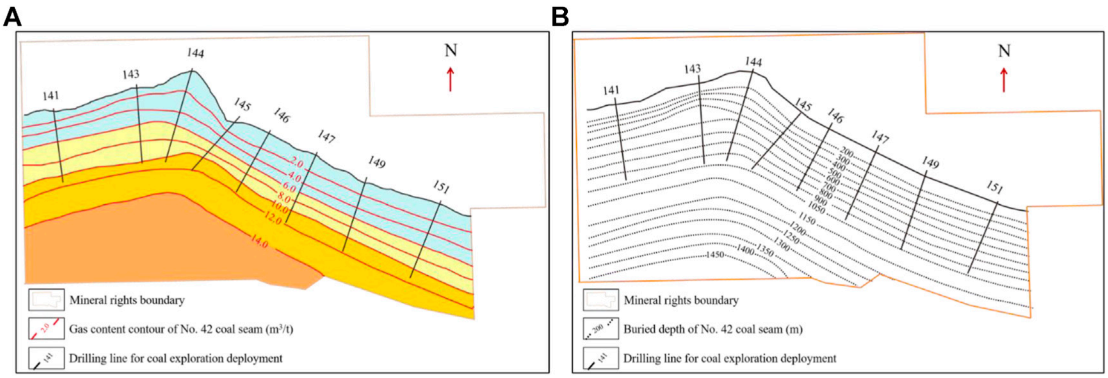

FIGURE 4 | (A) Gas content contour and **(B)** buried depth contour of No. 42 coal seam in the Baiyanghe mining area.

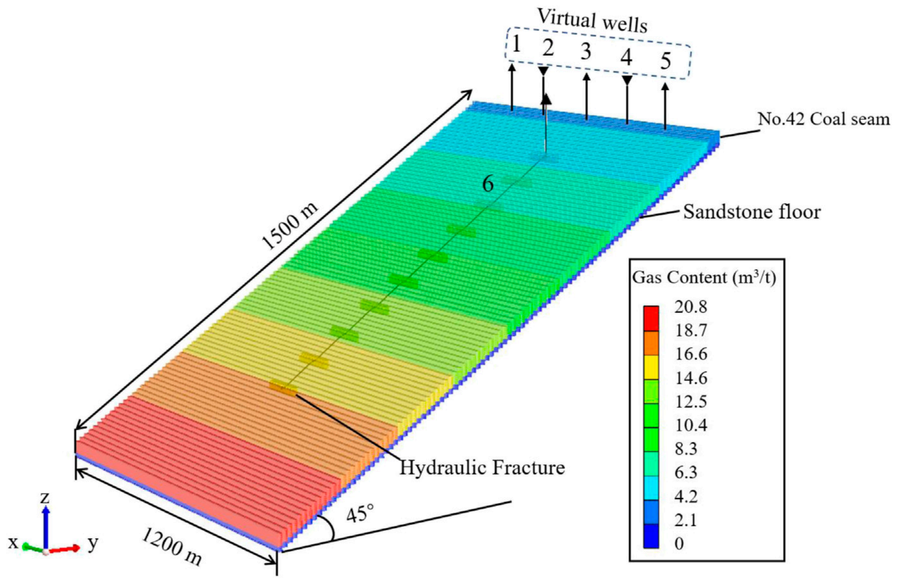

FIGURE 5 | Numerical simulation method of migration of gas and water in the exposed area: wells 1, 3, and 5: the virtual wells for simulating gas leakage; wells 2 and 4: the virtual wells for simulating water replenishment; and well 6, an along-dip horizontal well for production.

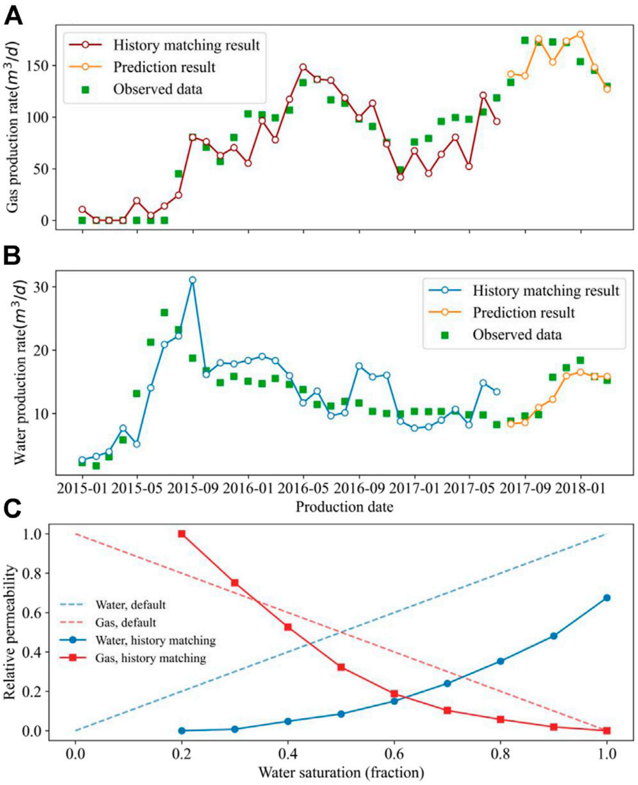

FIGURE 6 | Results of history matching for **(A)** gas production rate, **(B)** water production rate, and **(C)** adjusted relative permeability.

pressure is set to 151 kPa. By observing the simulation results of wells 1, 3, and 5, we discovered CBM leakage from the shallow part.

History Matching

Affected by the uncertainty of the exploration and the limitations of the test method, the parameters obtained during the test may not reflect the actual field conditions. If these parameters are used for simulation, the accuracy of the simulation results cannot be guaranteed. To evaluate the accuracy of the geological model and modify the parameters, we first performed historical matching on the pilot test well data. We used the modified desorption model derived in *Experimental Results and Modified Desorption Model* section.

We selected the vertical well X1 field production data and used the fixed bottom-hole pressure method to fit the water and gas production rate. 80% of the field data are for history matching parameter correction and 20% for production prediction to test the accuracy of the model. **Figures 6A,B** show the history matching results of gas and water production rates. The cumulative gas production and cumulative water production errors in the prediction stage are 4.29 and 1.67%, respectively. The numerical model after history matching restores the actual coal seam characteristics from the perspective of productivity simulation. **Table 2** shows the data after fitting. Relative permeability is an important characteristic for studying gas–water migration. However, the field data of the relative permeability were unavailable. Therefore, we adjusted the curve from the default curve of GEM. **Figure 6C** shows the adjusted relative permeability used in the research.

WELL PATTERN OPTIMIZATION AND RESULTS

Development Optimization Objective Functions and Economic Parameters

We used the productivity and NPV simultaneously as the objective function to perform pattern optimization (Hazlett and Babu, 2005; Zhang, 2010). The NPV model is based on the following:

- The wells produce 330 days a year, and the evaluation time is 15 years.
- The cost of a horizontal well includes the cost of a vertical well and horizontal part.
- The cost of a U-shaped well includes the cost of two vertical wells and horizontal part.
- The cost of a horizontal well contains the cost of staged fracturing operation.
- The cost of a vertical well is constant, neglecting the effect of location.

Eq. 5 shows the NPV prediction model we used to optimize the well pattern:

$$NPV = \sum_{n=1}^{t} \sum_{j=330\times(n-1)+1}^{330\times n} \left[Q_g f \left(P_{gas} - C_M \right) \frac{1}{(1+i)^n} - Q_w C_W \frac{1}{(1+i)^n} \right] - \left(n_f C_F + n_h C_H L \right), \tag{5}$$

where NPV is the economic net present value of the well pattern, Chinese Yuan (CNY); Q_g is the gas production rate, m^3/d; Q_w is the water production rate, m^3/d; f is the commodity rate of CBM; P_{gas} is the sale price of CBM, CNY/m^3; C_M is the operation and management cost of CBM, CNY/m^3; C_W is the processing cost of water, CNY/m^3; i is the benchmark rate of return; t is the production date, year; C_F is the cost of drilling a vertical well, CNY; C_H is the cost of drilling a horizontal well, CNY/m; n_f is the number of vertical wells in a well pattern; and n_h is the number of horizontal wells in a well pattern.

The economic evaluation data were taken from Zhang (2010): the horizontal well drilling cost is 0.35×10^6 CNY/m; the vertical well drilling cost is 7×10^5 CNY per well; the CBM sales price is 1.2 CNY/m^3; the commodity rate is 95%; the operation and management cost of CBM is 0.36 CNY/m^3; the processing cost of water is 6.5 CNY/m^3; and the benchmark rate of return is 15%.

Development and Optimization Cases

We performed the optimization from three aspects: well type, drilling method, and well pattern spacing. First, we investigated the primary gas well type with its drilling direction, and well spacing distance. Second, we focused on water production in the deep area of high–dip angle coal seam. Finally, we studied how to capture gas, which can move to the fired coal area and leak into the air.

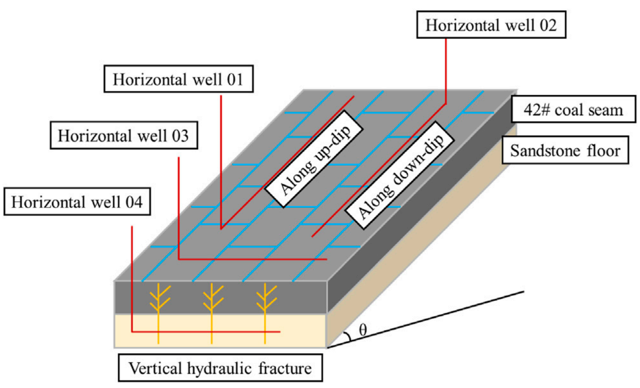

FIGURE 7 | Different well-drilling styles: well 01 was drilled along the up-dip direction; well 02 was drilled along the down-dip; well 03 was drilled along the direction of the coal seam trend; and well 04 was a horizontal well drilled in the coal seam floor with vertical fractures through a specific staged fracturing process.

Wang et al. (2014) analyzed the influence of gas–water gravity difference, solid-phase blockage, and pressure drop propagation characteristics in the process of CBM extraction. He also analyzed the gas production of CBM wells. He found that there is an apparent negative gas–water gravity differentiation impact in vertical wells. The coal powders are easy to concentrate and block the migration channel, resulting in the slow transfer of pressure and difficulty to form effective well interference. The stable inclined section of an along-dip horizontal well can effectively reduce the negative impact of gas–water gravity differentiation. Therefore, we chose horizontal wells as the main development wells and studied the optimal drilling method.

There are some different types of horizontal wells in high-dip coal seams, which are easy to confuse. **Figure 7** shows four different horizontal wells in high-dip coal seams. A horizontal well in high–dip angle coal seam refers to well drilling along the horizontal direction, shown as wells 03 and 04 in **Figure 7**. An along-dip horizontal well indicates that after the drill bit enters the coal seam, the wellbore trajectory maintains the same angle as the coal seam and has a particular extension, shown as wells 01 and 02 in **Figure 7**.

Optimization of Primary Production Well Pattern

Dong et al. (2018) studied the drilling stability of inclined coal seams. He proposed the action zone, the transition zone, and the reversal zone based on drilling stability at different angles. In the Baiyanghe block, drilling horizontal wells along inclination is the safest, while drilling along the coal extension is dangerous. The greater the anisotropy of ground stress, the higher the collapse pressure is and the smaller the range of safe drilling azimuths is. Therefore, we chose the horizontal well drilling along the dip as the primary gas production well.

The buried depth of the No. 42 coal seam under development is around 300–1,100 m with an angle of 45 degrees and the length along the dip angle of about 900 m. Therefore, we designed the length of the drilling the along-dip well as 900 m. The production duration was set to 15 years, which covers the general life span of

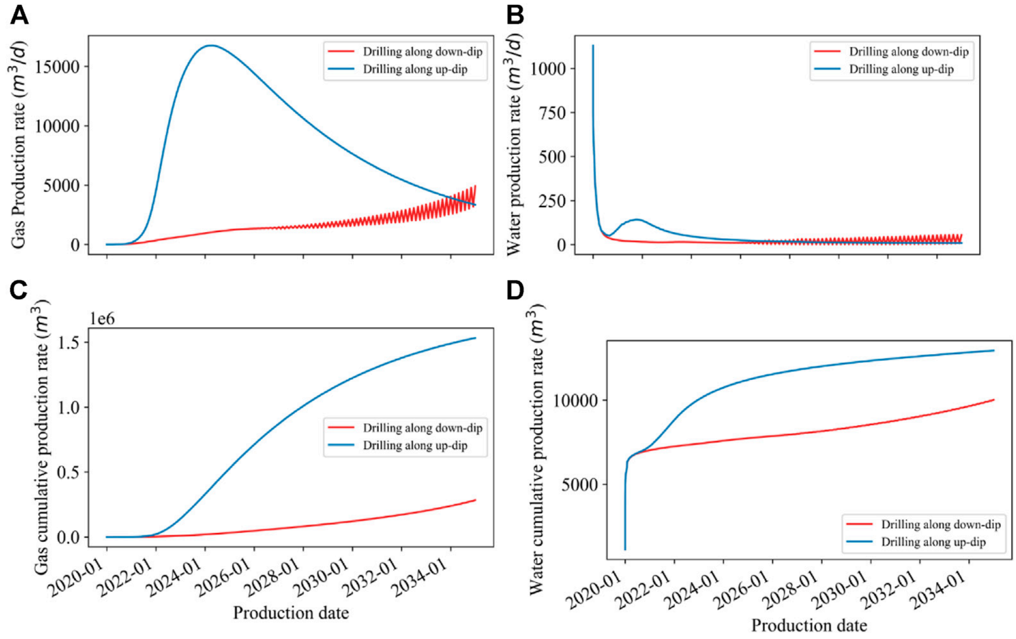

FIGURE 8 | Production comparison between different drilling directions: **(A)** gas production, **(B)** water production, **(C)** cumulative gas production, and **(D)** cumulative water production.

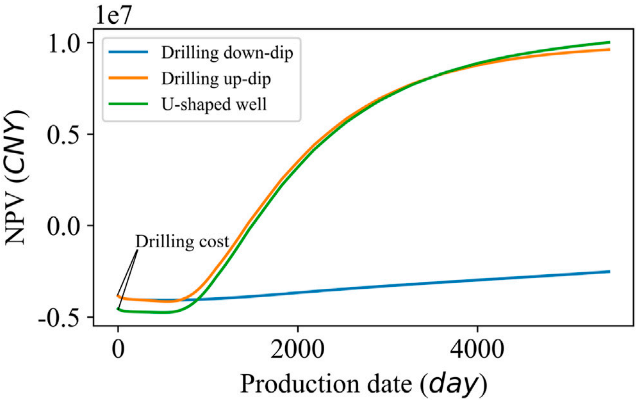

FIGURE 9 | Comparison of NPVs of different well drilling types.

CBM wells (Feng et al., 2012; Salmachi et al., 2013; Feng et al., 2014).

Figure 8 shows the results of the drilling direction optimization. The daily gas production curve of up-dip drilling shows the characteristics of a typical CBM production curve. It reaches a peak of 16,755 m^3/d at 1,858 d. When drilling along the down-dip direction, the gas production showed an increasing trend. Meanwhile, the production fluctuated sharply in the later period. The highest value only reached 4,912 m^3/d after 15 years. The cumulative gas production of the up-dip and down-dip horizontal wells is 4.66×10^7 m^3 and 0.861×10^7 m^3, respectively. The results of the up-dip drilling method are 5.18 times more than those of the down-dip drilling method.

A problem in drilling along the up-dip direction is the turning corner of the drill bit. Therefore, we modified the plan to use down-dip drilling. Besides, we finally added a vertical well at the end of the horizontal well to form a U-shaped well. **Figure 9** shows the NPV of the three wells. Although the U-shaped well case increases the cost of a vertical well, the ultimate NPV is the highest.

Furthermore, we optimized the well spacing distance of the U-shaped wells. According to the microseismic data, the hydraulic fracture length of the pilot test well is 60–80 m. Therefore, we built cases with well spacing distances of 100, 200, 300, 400, and 500 m to prevent fracture interference and ensure economic benefits. For the well spacing distance optimization schemes, we used a production group of all three wells. In order to ensure the correct single well control range, we will set the grids close to the boundary to null grids to meet the distance between the well and the boundary of half the well spacing distance, when the model boundary is too large. Since the boundary is closed, the pressure interference characteristics and the control area of a single well can be guaranteed according to the mirror principle.

Figure 10 shows the results of well spacing optimization. We took the influence of the number of wells in the NPV model into consideration. The R^2 of cumulative production and NPV parabola fitting is 0.9221 and 0.9783, respectively. From the perspective of productivity, productivity is optimal when well spacing reaches 299 m. From the perspective of NPV, the NPV reaches its peak when well spacing is 312 m. We determined

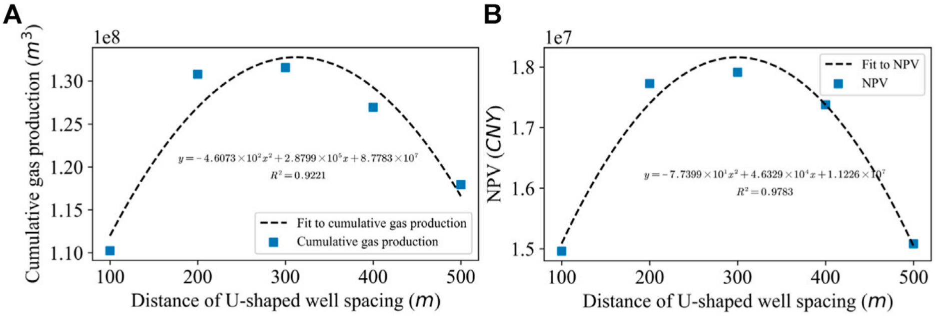

FIGURE 10 | Simulation results of different well spacing distances: **(A)** Cumulative gas production rate and **(B)** NPV.

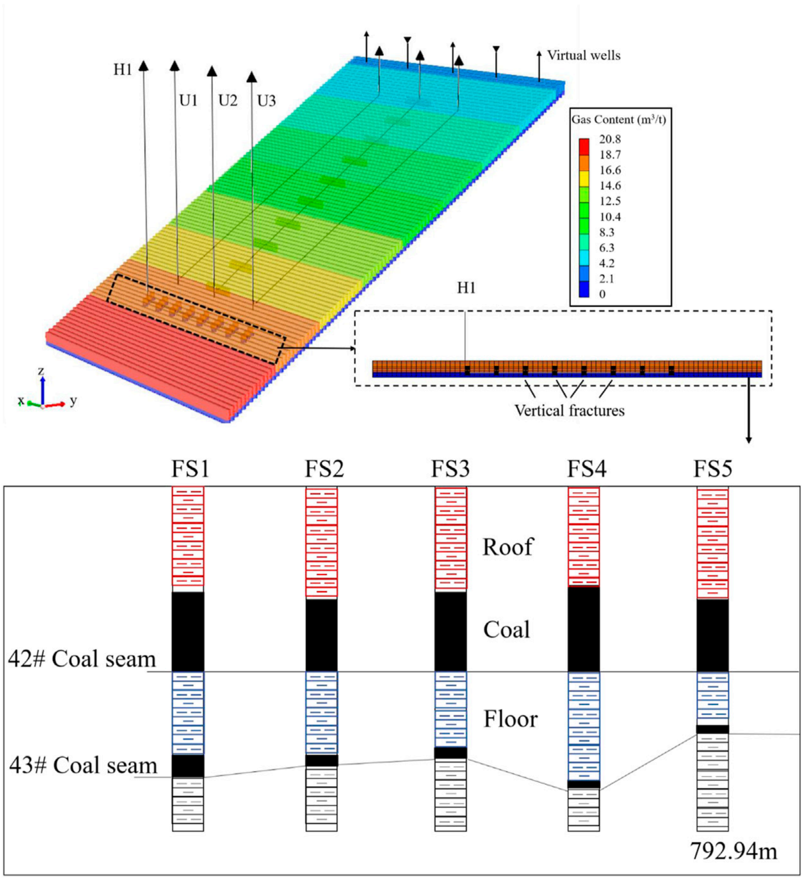

FIGURE 11 | Schematic diagram of numerical simulation of the floor fracturing horizontal well and coal pillar connection among a pilot test well group: U1-3 is the U-shaped along-dip horizontal well group; H1 is the horizontal well drilled in the floor; and FS1-5 is the pilot test well group.

optimal well spacing based on the NPV, which can ensure the well-controlling area, the effect of well interference, and economic benefit.

When a single U-shaped well produces, the cumulative production of 15 years is 4.66 × 10^7 m^3. When the three wells with the optimal spacing produce, the cumulative production of the group is 2.66 × 10^8 m^3. The cumulative production of each well is 8.85 × 10^7 m^3, with an increase of 89%.

Optimization of Drainage Well

The negative impact of gas–water gravity differentiation during development is that a large amount of water migrates to the deep part of the coal seam, resulting in difficult production. We proposed a plan to drill a staged fracturing horizontal well in the sandstone floor of the coal seam for drainage. According to the formation stress analysis, it is more challenging to drill horizontal wells directly in the coal seam. Therefore, we chose

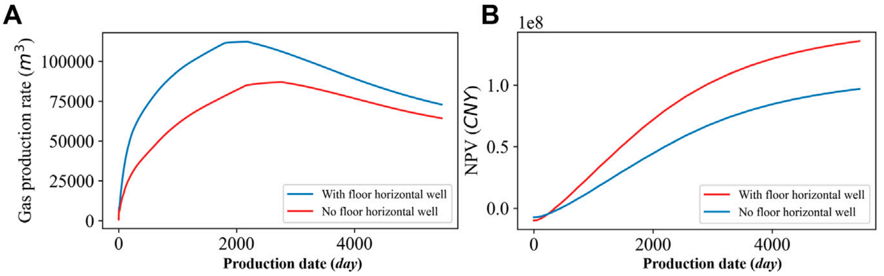

FIGURE 12 | Comparison of the simulation cases: **(A)** Gas production rate, **(B)** NPV.

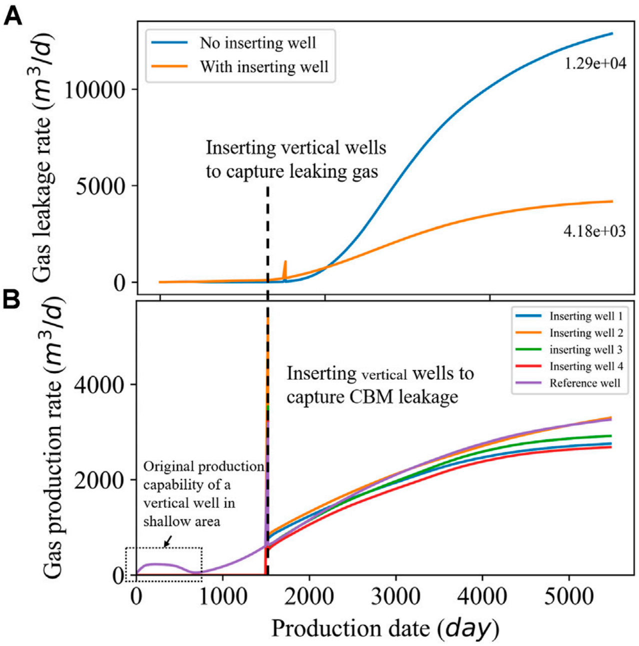

FIGURE 13 | Results of inserting well simulation: **(A)** gas leakage rate and **(B)** gas production rate.

a relatively stable sandstone layer for horizontal wells and fracturing vertical fractures. The gravity plays a significant role in drainage. Cao et al. (2017) gave the feasibility study of CBM floor fracturing. He proposed that water gravity can assist coal seam drainage and pressure drop. This feature is more prominent in the high–dip angle coal seam, so floor horizontal well fracturing has advantages over horizontal wells in the coal seam in the study area.

Figure 11 shows the coal pillar connection among a pilot test well group. We found a stable sandstone layer under the No. 42 coal seam. A horizontal well can be drilled into this layer and fractured to generate vertical fractures into coal. We used the production well pattern optimized in *Optimization of Drainage Well* section as the base case, including three U-shaped along-dip horizontal wells. The well H1 in **Figure 11** shows the numerical simulation method of the floor fracturing horizontal well. **Figure 12** shows the simulation results after the floor fracturing horizontal well added. The gas production of the horizontal well is 0 m^3, while the water production remained at about 900 m^3. After 15 years, the NPV reaches 1.36×10^8 CNY with an increase of 40% compared to the original well pattern of 9.69×10^7 CNY. The cost of the horizontal well becomes negligible.

Optimization of Inserting Wells

Another negative impact of gas–water gravity differentiation is the leakage of CBM. We used the well pattern optimized above to simulate the CBM leakage phenomenon. **Figure 13A** shows the amount of CBM leakage. The phenomenon starts on day 1,423 with the amount of CBM leakage gradually increasing with production. After 15 years, the daily leakage rate reaches 12,882 m^3/d, leading to a total waste of 2.9×10^7 m^3 of resources and production capacity affection. In order to capture leaked gas, we inserted wells in the beginning of the CBM leakage. We inserted five vertical wells at a depth of 300 m. To control a larger area, we set the spacing of inserting wells to half of the optimal bedding well spacing, 156 m. Simultaneously, we chose a well as a reference well and set it to start production together with the U-shaped wells.

Operators also considered the characteristics of gas–water gravity differentiation and upward migration of gas in the early pilot test and drilled a vertical well in the shallow part. However, the test result was not good. From **Figure 13B**, we can observe that if the reference well starts producing from the initial production date, the productivity of the reference well is indeed not ideal. On the one hand, the gas content of the shallow part is low. On the other hand, the CBM from the deep coal seam has not migrated up to the well. After 1,423 days, the productivity of the vertical well has increased significantly. The leakage of CBM has been effectively limited at the same time.

Discussion

Figure 14 shows the specific process of well pattern optimization, the statistical values of the cost, productivity, and NPV of each case. We first optimized the well spacing and found that 312 m is the optimal well spacing, of which the productivity and the NPV reach 2.66×10^7 m^3, and 5.44×10^7 CNY, respectively. In order to solve the problem of the difficulty in producing deep water caused by the gas–water gravity differentiation, we proposed a plan to drill a staged and fractured horizontal well in the floor. Although

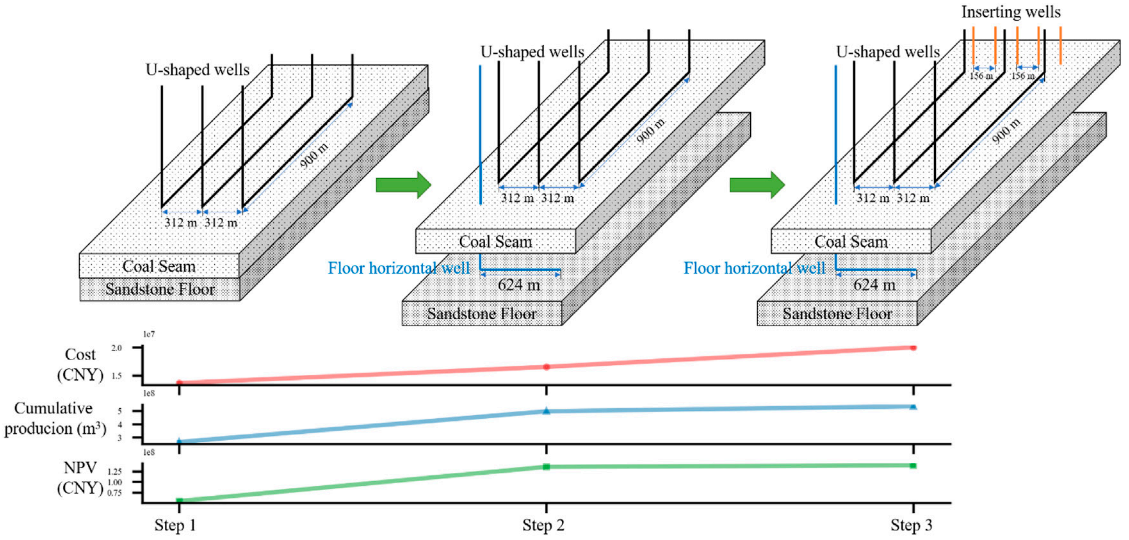

FIGURE 14 | Optimization process and result statistics of well pattern in the high-dip coal seam.

the well did not produce gas, the overall productivity reaches 4.97 × 10^8 m^3 with an increase of 87.54%. The NPV reached 1.16 × 10^8 CNY with an increase of 123.23%. Finally, in order to solve the impact of CBM leakage, we inserted a vertical well in the shallow part to capture the upwardly moving gas. The production capacity reaches 5.34 × 10^8 m^3 with an increase of 6.93%. The NPV reaches 1.21 × 10^8 CNY with an increase of 4.3%.

From the above data, we found that the most effective measure to increase productivity is to drill a horizontal well in the floor to increase drainage capacity. In the research, the cost of a staged fractured horizontal well is 2.88 × 10^6 CNY. However, the NPV increases by 6.16 × 10^7 CNY for the well pattern. Although the five vertical wells inserting at the shallow area did not make a significant contribution to the increase in productivity and NPV, they effectively reduced the leakage of CBM.

CONCLUSION

We proposed a modified desorption model for low-rank coal and an optimal well pattern for the high–dip angle coal seam. The desorption model can record the information adsorption process and mark the residual gas of low-rank coal. Besides, the desorption model was applied to improve the accuracy of the numerical simulation. We optimized the well pattern, by determining the primary production well, optimizing the wells for producing water, and inserting the wells for capturing CBM leakage.

The U-shaped wells were chosen as the primary production wells, with the optimal well spacing of 312 m. A staged fracturing horizontal well drilled in the floor of the coal seam was chosen for producing water. To capture the leaking CBM from the shallow area, we inserted some vertical wells when leakage starts. The optimal well pattern can improve the NPV significantly and reduce the waste of resources effectively.

The modified desorption model, along-dip horizontal well spacing optimization method, and horizontal wells drilled in the floor proposed in this study can be applied to other inclined low-rank coal reservoirs. Because there are an exposed area and shallow fire coal areas with high permeability in the Baiyanghe mining area, inserting wells that capture CBM leakage are specifically proposed. At the same time, in order to improve the accuracy of the simulation of CBM leakage, field tests should be carried out in the future.

DATA AVAILABILITY STATEMENT

The original contributions presented in the study are included in the article/Supplementary Material, further inquiries can be directed to the corresponding authors.

AUTHOR CONTRIBUTIONS

HW: conceptualization, methodology, formal analysis, visualization, and writing an original draft. XZ: investigation, review and editing, and funding acquisition. SZ: project administration, supervision, review and editing. HH: validation and data curation. JW: resources.

FUNDING

This research was conducted under the financial support of the Major Science and Technology Project of Shanxi Province (Grant Nos. 20181101013 and 20201102002).

REFERENCES

Beckner, B. L., and Song, X., (1995). Field Development Planning Using Simulated Annealing-Optimal Economic Well Scheduling and Placement: SPE annual technical conference and exhibition, Dallas, TX, October 1995. doi:10.2118/30650-ms

Bouzarkouna, Z., Ding, D. Y. Y., and Auger, A. (2013). Partially Separated Metamodels with Evolution Strategies for Well-Placement Optimization. *SPE J.* 18, 1003–1011. doi:10.2118/143292-pa

Cao, L., Yang, X., Zhang, S., Wang, H., Wang, K., Liu, J., and Zhao, J., (2017). Research of Floor Horizontal Well Staged Fracturing Technology: SPE/IATMI Asia Pacific Oil & Gas Conference and Exhibition, Jakarta, Indonesia, October 2017. doi:10.2118/186370-ms

Chen, D., Liu, J., Pan, Z., and Connell, L., (2010). Coalbed Methane Production: Why Coal Permeability Matters: SPE Asia Pacific Oil and Gas Conference and Exhibition, Queensland, Australia, October 2010. doi:10.2118/133328-ms

Clarkson, C. R., and McGovern, J. M. (2005). Optimization of CBM Reservoir Exploration and Development Strategies through Integration of Simulation and Economics. *SPE. Reservoir. Evaluation. Engineering.* 8 (6), 502–519. SPE-88843-PA. doi:10.2118/88843-pa

Cui, S., Liu, H., Wang, B., Yang, Y., Ning, N., and Sang, S. (2007). Trapping Characteristics of Coalbed Methane in Low-rank Coal Zhungaer Basin. *Geoscience* 21, 719–724. doi:10.3969/j.issn.1000-8527.2007.04.019

Dong, Z., Bao, Q., Zhang, J., Sun, Q., Chen, S., Dong, H., et al. (2018). Research on Drilling along Steep Coal Seam:A Case Study of Changji Area in Southern Margin of the Junggar Basin. *J. China Coal Soc.* 43, 1041–1051. doi:10.13225/j.cnki.jccs.2017.0990

Feng, Q., Zhang, J., Zhang, X., and Hu, A. (2012). Optimizing Well Placement in a Coalbed Methane Reservoir Using the Particle Swarm Optimization Algorithm. *Int. J. Coal Geology* 104, 34–45. doi:10.1016/j.coal.2012.09.004

Feng, Q., Zhang, X., Zhang, J., and Chen, D. (2014). Numerical Simulation of Commingling Production for Coalbed Methane and Adjoining sandstone Gas Reservoirs. *J. China. Coal. Soc.* 39, 169–173. doi:10.13225/j.cnki.jccs.2013.0141

Güyagüler, B., Horne, R. N., Rogers, L., and Rosenzweig, J. J. (2002). Optimization of Well Placement in a Gulf of Mexico Waterflooding Project. *SPE Reservoir Eval. Eng.* 5, 229–236. doi:10.2118/78266-pa

Hazlett, R. D., and Babu, D. K. (2005). Optimal Well Placement in Heterogeneous Reservoirs via Semi-analytic Modeling. *SPE J.* 10 (3), 286–296. doi:10.2118/84281-pa

Karacan, C. Ö., and Olea, R. A. (2015). Stochastic Reservoir Simulation for the Modeling of Uncertainty in Coal Seam Degasification. *Fuel* 148, 87–97. doi:10.1016/j.fuel.2015.01.046

Keim, S. A., Luxbacher, K. D., and Karmis, M. (2011). A Numerical Study on Optimization of Multilateral Horizontal Wellbore Patterns for Coalbed Methane Production in Southern Shanxi Province, China. *Int. J. Coal Geology.* 86, 306–317. doi:10.1016/j.coal.2011.03.004

Mu, F., Jia, C., Mu, L., and Yang, J. (2014). Coal-bed Methane Development Modes in China. *Unconventional Oil and Gas* 1, 41–46.

Mu, F., Zhong, W., Zhao, X., Che, C., Chen, Y., Zhu, J., et al. (2015). Strategies for the Development of CBM Gas Industry in China. *Nat. Gas Industry B* 2, 383–389. doi:10.1016/j.ngib.2015.09.013

Ni, X., Wang, Y., Jie, M., and Wu, J. (2007). The Relations between Geological Structure in the Western Jincheng Diggings and Coal-Bed Methane wells Arrangement. *J. China Coal Soc.* 2, 146–149. doi:10.3321/j.issn:0253-9993.2007.02.008

Onwunalu, J. E., and Durlofsky, L. J. (2010). Application of a Particle Swarm Optimization Algorithm for Determining Optimum Well Location and Type. *Comput. Geosci.* 14, 183–198. doi:10.1007/s10596-009-9142-1

Palmer, I. (2008). Coalbed Methane wells Are Cheap, but Permeability Can Be Expensive. *Energy Tribune* 3, 10–13.

Salmachi, A., Sayyafzadeh, M., and Haghighi, M. (2013). Infill Well Placement Optimization in Coal Bed Methane Reservoirs Using Genetic Algorithm. *Fuel* 111, 248–258. doi:10.1016/j.fuel.2013.04.022

Tao, S., Pan, Z., Tang, S., and Chen, S. (2019). Current Status and Geological Conditions for the Applicability of CBM Drilling Technologies in China: A Review. *Int. J. Coal Geology* 202, 95–108. doi:10.1016/j.coal.2018.11.020

Wang, C., Peng, X., Zhu, S., Sun, H., Zhang, J., and Lin, L. (2019). Coalbed Methane Well-type Optimization and Well Pattern Arrangement for Thick Coal Seam with a Large Dip Angle. *Chin. J. Rock Mech. Eng.* 38, 313–320. doi:10.13722/j.cnki.jrme.2018.0911

Wang, S., Wang, F., Houg, G., Wu, X., Zhang, C., Zhang, Y., and Hu, Q. (2014). CBM development well type for steep seam in Fukang Baiyanghe mining area: Xiangjiang Pet. *Geology.* 39 (9), 1914–1918. doi:10.13225/j.cnki.jccs.2014.8018

Wang, H., Zhang, S., Chen, D., Huang, H., and Zhao, Z. (2020). Dynamic Distribution of Remaining Gas Content in Steep and Thick Coal Seams in Baiyanghe Mining Area of Fukang. *Xinjiang Pet. Geology.* 41, 587. doi:10.7657/XJPG20200512

Weishauptová, Z., and Medek, J. (1998). Bound Forms of Methane in the Porous System of Coal. *Fuel* 77, 71–76. doi:10.1016/s0016-2361(97)00178-6

Weishauptová, Z., Medek, J., and Kovář, L. (2004). Bond Forms of Methane in Porous System of Coal II. *Fuel* 83, 1759–1764. doi:10.1016/j.fuel.2004.03.001

Zhang, J., Feng, Q., Zhang, X., Hu, Q., Wen, S., Chen, D., et al. (2020). Multi-fractured Horizontal Well for Improved Coalbed Methane Production in Eastern Ordos basin, China: Field Observations and Numerical Simulations. *J. Pet. Sci. Eng.* 194, 107488. doi:10.1016/j.petrol.2020.107488

Zhang, S., Yuan, Y., and Meng, F. (2016). Progress on Coalbed Methane Development Technology in China. *Coal Sci. Tech.* 44, 1–5. doi:10.13199/j.cnki.cst.2016.05.001

Zhang, T., Tao, S., Tang, D., Tang, S., Xu, H., Zhang, A., et al. (2021). Permeability Anisotropy in High Dip Angle Coal Seam: A Case Study of Southern Junggar Basin. *Nat. Resour. Res.* 30 (3), 2273–2286. doi:10.1007/s11053-021-09831-7

Zhang, X. (2010). *Migration Models of Fluids in Complicated Coalbed Methane Reservoirs and Their Numerical Simulations:* Qingdao: China University of Petroleum East China. PhD thesis.

Zhou, S., Liu, D., Sun, S., and Cai, Y. (2015). Factors Affecting Coalbed Methane Enrichment and CBM Favorable Area of Liuhuanggou Area in the Southern Jungger Basin. *Geoscience* 29, 179–189. doi:10.3969/j.issn.1000-8527.2015.01.022

Zulkarnain, I. (2006). *Simulation Study of the Effect of Well Spacing, Effect of Permeability Anisotropy, and Effect of Palmer and Mansoori Model on Coalbed Methane Production.* Texas: Texas AM University.

Conflict of Interest: Author HH was employed by the company China United Coalbed Methane National Engineering Research Center Co. Ltd. and National Engineering Research Center for Coalbed Methane Development and Utilization. Author JW was employed by the company Shanxi Lanyan Coalbed Methane Group Co., Ltd.

The remaining authors declare that the research was conducted in the absence of any commercial or financial relationships that could be construed as a potential conflict of interest.

frontiers
in Earth Science

ORIGINAL RESEARCH
published: 24 June 2021
doi: 10.3389/feart.2021.693531

Numerical Simulation of Ferrofluid Flow in Heterogeneous and Fractured Porous Media Based on Finite Element Method

Tao Huang[1]*, **Xin Liao**[1], **Zhaoqin Huang**[2] **and Renyi Wang**[1]

[1]School of Petrochemical Engineering and Environment, Zhejiang Ocean University, Zhoushan, China, [2]School of Petroleum Engineering, China University of Petroleum (East China), Qingdao, China

Ferrofluid is a kind of magnetic fluid, the flow of which is controlled by an external magnetic field. Owing to this property, ferrofluid, as a new function material, has raised extensive concern in the oil industry. In this paper, the issue of ferrofluid flow in complex porous media has been studied by numerical simulation, and the validity and accuracy of the numerical algorithm are demonstrated through a 1-D horizontal tube example. Later, the effects of the magnetic force on ferrofluid flow in complex porous media, such as heterogeneous and fractured porous media, are investigated. The results show that there is basically no flow in low permeability or secondary fracture without a magnetic field, due to the characteristics of porous media and displacement pressure distribution. However, the ferrofluid flow velocity and domain can be changed by applying an external magnetic field. This novel phenomenon may provide a new idea to enhance oil recovery based on controllable flooding technology or meet other industrial needs by using ferrofluid.

Keywords: ferrofluid flow, porous media, numerical simulation, multi-field coupled, finite element method

Edited by:
Weiqi Fu,
China University of Mining and Technology, China

Reviewed by:
Jianlin Zhao,
ETH Zürich, Switzerland
Xiaoyu Gu,
Xi'an Shiyou University, China

****Correspondence:***
Tao Huang
huangtao@zjou.edu.cn

Specialty section:
This article was submitted to Economic Geology, a section of the journal Frontiers in Earth Science

Received: *11 April 2021*
Accepted: *10 May 2021*
Published: *24 June 2021*

Citation:
Huang T, Liao X, Huang Z and Wang R (2021) Numerical Simulation of Ferrofluid Flow in Heterogeneous and Fractured Porous Media Based on Finite Element Method. Front. Earth Sci. 9:693531. doi: 10.3389/feart.2021.693531

INTRODUCTION

Water flooding, as is well recognized, is an effective approach to maintain reservoir pressure and improve oil recovery. However, heterogeneities or fractures present in reservoirs can significantly decrease the sweep efficiency, leading to poor utilization ratios, and low oil recovery (Qitai, 2000; Han, 2007; Li, 2009). Therefore, how to change the direction of the displacement fluid to increase the flooding area plays a vital role in enhancing oil recovery. At present, there are many methods to achieve that. First, the subsurface fluid flow can be regulated by optimizing the well production and injection. Second, increasing rock permeability in low-sweep zones, such as by fracturing and acidizing methods (Zeng et al., 2018; Lei et al., 2019; Lu et al., 2020; Zeng et al., 2020; Jia et al., 2021), can significantly improve the flow capacity of the zones. In addition, it is also an alternative to apply polymer flooding or surfactant flooding to change the properties of the displacement fluid and reduce its flow ability in high-sweep zones or increase its flow ability in low-sweep zones (Zhu et al., 2019a; Zhu et al., 2019b; Sidiq et al., 2019). However, all of the above methods are time-consuming and labor-intensive work.

Ferrofluid is a stable colloid composed of nanoscale magnetic particles (usually magnetite, Fe_3O_4) which are coated with a molecular layer of a dispersant (amphiphilic molecules, like oleic acid) and suspended in a liquid carrier (Popplewell and Charles, 1981), as is shown in **Figure 1**. Ferrofluid

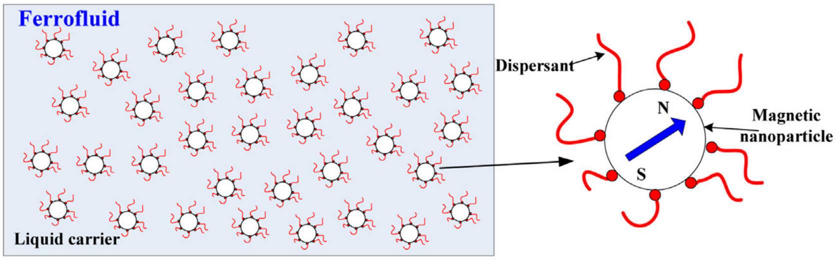

FIGURE 1 | Sketch of ferrofluid composition.

exhibits the characteristics of a general fluid in that its motion follows the hydrodynamic law. However, it is a magnetic substance that receives the magnetic body force in the presence of an external magnetic field, so that its behavior and property can be controlled by the magnetic field (Odenbach, 2008). The idea of creating a colloidal fluid with ferromagnetic properties was put forward independently and almost simultaneously by several investigators. One of the first and most easily prepared colloidal systems was developed by NASA in the early 1960's (Rosensweig, 1982). At present, ferrofluid has many industrial applications, such as dynamic sealing, inertial and viscous damper, magnetic drug targeting, liquid microrobots, and so on (Raj and Moskowitz, 1990; Hou et al., 1999; Scherer and FigueiredoNeto, 2005; Fan et al., 2020). Recently, researchers have been studying the potential of using ferrofluid to detect fractures and heterogeneity in reservoirs (Sengupta, 2012; Rahmani et al., 2015).

In this paper, we focus on the ferrofluid flow in porous media using the numerical simulation method based on the finite element method. First, the validity and accuracy of the model and the numerical algorithm are demonstrated. Then, several problems of the heterogeneous and fractured porous media flow are studied. The results show that the ferrofluid flow in complex porous media can be manipulated by applying an external magnetic field. For example, the flow velocity and the flow region can be changed under the action of magnetic force. This phenomenon may provide a new idea for enhancing oil recovery, such as using ferrofluid as controllable displacement fluid in complex or unconventional reservoirs.

COMPUTATIONAL METHODOLOGY

Magnetic Body Force

When applying an external magnetic field, the secondary magnetic field produced by the magnetic particles in the ferrofluid and the interaction between the two magnetic fields produce a magnetic body force on the ferrofluid (Neuringer and Rosensweig, 1964):

$$\boldsymbol{F}_m = \mu_0 M \nabla H \tag{1}$$

where $\mu_0 = 4\pi \times 10^{-7}$ Tm/A is the magnetic permeability of vacuum, M (A/m) is magnetization, and H (A/m) is magnetic field strength.

We considered a water-based ferrofluid whose properties are provided by a nanomaterial company in China. Its viscosity and density respectively equal 5.8 mPa·s and 1,187 kg/m^3. Although the composition of the fluid was not offered, the magnetization curve of the fluid was provided to us as is shown in **Figure 2**. The ferrofluid magnetization curve can be generally approximated by simple two-parameter arctan functions of the form (Oldenburg et al., 2000):

$$M = \alpha \times \arctan(\beta \times H) \tag{2}$$

where $\alpha = 1 \times 10^4$, $\beta = 3.5 \times 10^{-5}$.

Calculation of Magnetic Field

In this paper, the external magnetic field provided by the NdFeB magnets and the three-dimensional magnetic field could be calculated by analytic equations (Maccaig, 1987) :

$$H_d = G_d(x,y,z) - G_d(x+L,y,z), d = x,y,z \tag{3}$$

where,

$$G_x(x,y,z) = \frac{B_r}{4\pi\mu_0}\left\{ arctan\left[\frac{(y+a)(z+b)}{x\left[(y+a)^2+(z+b)^2+x^2\right]^{\frac{1}{2}}}\right] + arctan\left[\frac{(y-a)(z-b)}{x\left[(y-a)^2+(z-b)^2+x^2\right]^{\frac{1}{2}}}\right] - arctan\left[\frac{(y+a)(z-b)}{x\left[(y+a)^2+(z-b)^2+x^2\right]^{\frac{1}{2}}}\right] - arctan\left[\frac{(y-a)(z+b)}{x\left[(y-a)^2+(z+b)^2+x^2\right]^{\frac{1}{2}}}\right]\right\} \tag{4}$$

$$G_y(x,y,z) = \frac{B_r}{4\pi\mu_0}\ln\left\{\frac{(z+b)+\left[(z+b)^2+(y-a)^2+x^2\right]^{\frac{1}{2}}}{(z-b)+\left[(z-b)^2+(y-a)^2+x^2\right]^{\frac{1}{2}}} \times \frac{(z-b)+\left[(z-b)^2+(y+a)^2+x^2\right]^{\frac{1}{2}}}{(z+b)+\left[(z+b)^2+(y+a)^2+x^2\right]^{\frac{1}{2}}}\right\} \tag{5}$$

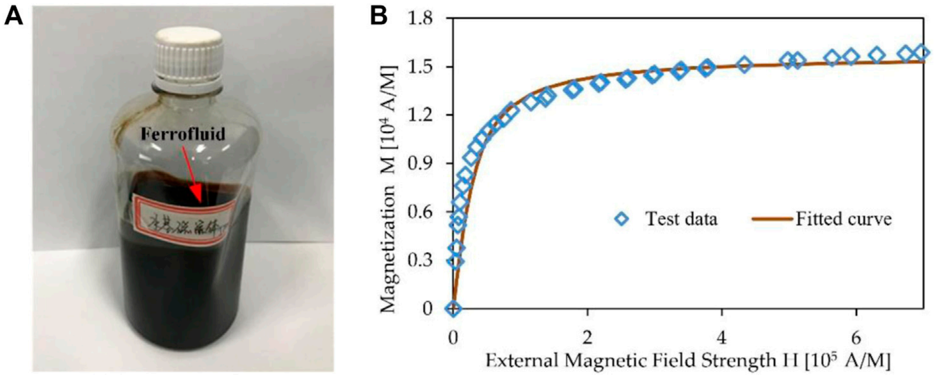

FIGURE 2 | Schematic diagram of ferrofluid: **(A)** A bottle of water-based ferrofluid; **(B)** Magnetization vs. magnetic field strength curve of the ferrofluid.

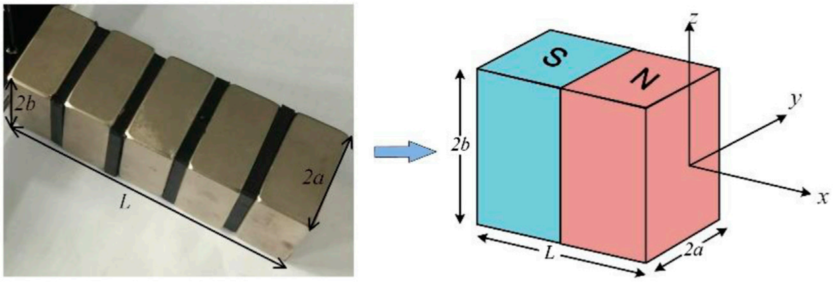

FIGURE 3 | A sample of NdFeB magnet and its local coordinate system.

$$G_z(x,y,z) = \frac{B_r}{4\pi\mu_0}\ln\left\{\frac{(y+a)+\left[(z-b)^2+(y+a)^2+x^2\right]^{\frac{1}{2}}}{(y-a)+\left[(z-b)^2+(y-a)^2+x^2\right]^{\frac{1}{2}}} \times \frac{(y-a)+\left[(z+b)^2+(y-a)^2+x^2\right]^{\frac{1}{2}}}{(y+a)+\left[(z+b)^2+(y+a)^2+x^2\right]^{\frac{1}{2}}}\right\} \tag{6}$$

B_r is residual flux density of the magnet and is measured in Tesla (T) in SI units. $2a$, $2b$, and L are the length of the magnet in three directions as is shown in **Figure 3**.

Single-phase Ferrofluid Flow Equations

For a ferrofluid affected by an external magnetic field, a body force Fm is produced, as is shown in **Eq. 1**. Thus, an additional magnetic force term appears in Darcy's equation：

$$\mathbf{v} = -\frac{\mathbf{k}\rho}{\mu}\left[\nabla p - \rho\left(g\nabla z + \frac{\mu_0 M}{\rho}\nabla H\right)\right] \tag{7}$$

where **v** is the mass flow velocity, **k** is permeability tensor which changes into scalar k in isotropic porous media, ρ is the density of ferrofluid, μ is the viscosity of ferrofluid, and g is the acceleration of gravity. And the conservation of mass equation is shown as：

$$\nabla\cdot\mathbf{v} + Q = \frac{\partial(\rho\phi)}{\partial t} \tag{8}$$

where Q is the source term and ϕ is the porosity of porous media.

Finite Element Discretization

In this paper, we only take the isothermal flow of impressible single-phase ferrofluid into consideration whereas we neglect the impact of gravity for simplicity, which is similar to the analysis of other flow problems. **Eqs.7**, **8** can be simplified as:

$$\begin{cases} -\nabla\cdot\boldsymbol{v} = Q \\ \boldsymbol{v} = -\dfrac{\mathbf{k}\rho}{\mu}(\nabla p - \mu_0 M\nabla H) \end{cases} \tag{9}$$

Define mobility as $\boldsymbol{\lambda} = \mathbf{k}/\mu$, then:

$$-\nabla\cdot\boldsymbol{\lambda}(\nabla p - \mu_0 M\nabla H) = \frac{Q}{\rho} \tag{10}$$

The Galerkin weighted residual method is used to derive the formulation of the finite element in the above equation：

$$-\int_\Omega \Phi\nabla\cdot[\boldsymbol{\lambda}(\nabla p - \mu_0 M\nabla H)]d\Omega = \int_\Omega \Phi q d\Omega \tag{11}$$

where q equals Q/ρ. By applying the Integration by Parts method and considering the impermeable boundary, **Eq. 11** turns into:

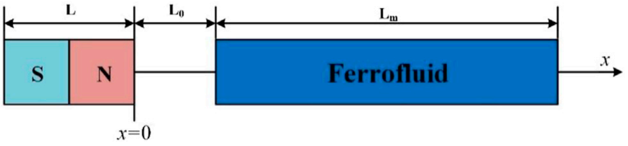

FIGURE 4 | Configuration of the 1-D horizontal tube model.

$$\int_\Omega \nabla\Phi\boldsymbol{\lambda}\nabla p d\Omega - \int_\Omega \nabla\Phi\boldsymbol{\lambda}\mu_0 M\nabla H d\Omega = \int_\Omega \Phi q d\Omega \tag{12}$$

The finite element approximation of the pressure p, magnetic field strength H, and potential function Φ on the grid unit are:

$$\mathbf{P}_e \approx \sum_{i=1}^{m} N_i P_i = \mathbf{NP},\quad H_e \approx \sum_{i=1}^{m} N_i H_i = \mathbf{NH},\quad \Phi_e \approx \sum_{i=1}^{m} N_i \Phi_i = \mathbf{N\Phi} \tag{13}$$

where m is the number of grid points, $\boldsymbol{N} = [N_1, \ldots, N_m]$ is the shape function at grid point, $\boldsymbol{P} = [P_1, \ldots, P_m]^T$ is the pressure at grid point, $\boldsymbol{H} = [H_1, \ldots, H_m]^T$ is the magnetic field strength at grid point, and $\boldsymbol{\Phi} = [\Phi_1, \ldots, \Phi_m]^T$ is the potential function at grid point. Taking **Eq. 13** into **Eq.12**, we can obtain a set of pressure equations:

$$\mathbf{AP} = \mathbf{BH} + \mathbf{R} \Rightarrow \mathbf{P} = (\mathbf{BH} + \mathbf{R})/\mathbf{A} \tag{14}$$

where $\mathbf{A} = \int_\Omega \nabla^T \mathbf{N}\boldsymbol{\lambda}\nabla\mathbf{N} d\Omega$, $\mathbf{B} = \int_\Omega \nabla^T \mathbf{N}(\boldsymbol{\lambda}\mu_0 M)\nabla\mathbf{N} d\Omega$, $\mathbf{R} = \int_\Omega \mathbf{N}^T q d\Omega$. The ferrofluid pressure can be obtained by solving the above equations, and then be combined with **Eq.7** to obtain the velocity.

VERIFICATION OF ALGORITHM

Morris et al. set up a one-dimensional experimental system to verify the validity of the magnetic force expression by comparing the experimental and theoretical results (Moridis et al., 1998). Here we used this method to verify the correctness of the algorithm.

Consider a one-dimensional closed horizontal tube model with a radius that is small enough to approximate the porous media. The tube is filled with ferrofluid and a magnet is placed on the left side, as is shown in **Figure 4**. The length L of the magnet is 0.127 m, the width $2a$ and height $2b$ of the magnet are both 0.0508 m, and the residual magnetization B_r of the magnet is 1.19 T. The distance L_0 between the magnet and the tube is 0.01 m while the length of the tube is 0.19 m.

For the 1-D model, combined **Eqs 3**, **4**, the calculation of magnetic field strength can be simplified as:

$$H_x = \frac{B_r}{4\pi\mu_0}\left\{\arctan\left[\frac{ab}{x(a^2+b^2+x^2)^{\frac{1}{2}}}\right] - \arctan\left[\frac{ab}{(x+L)(a^2+b^2+(x+L)^2)^{\frac{1}{2}}}\right]\right\} \tag{15}$$

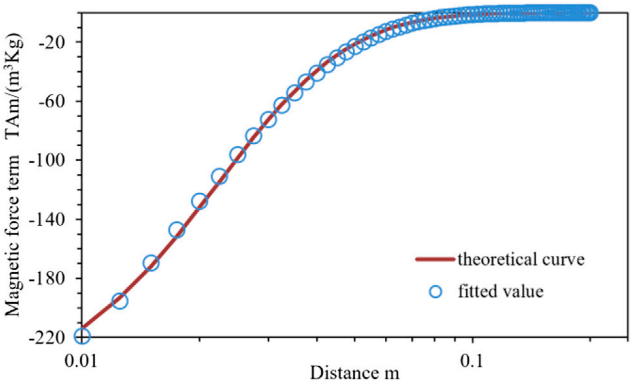

FIGURE 5 | Comparison of theoretical value and fitting value of magnetic force term.

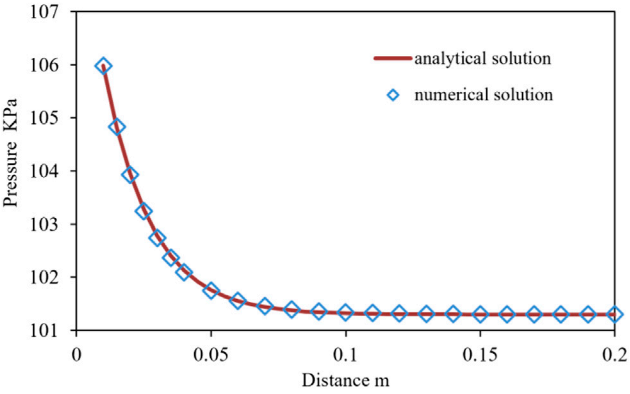

FIGURE 6 | Analytical and computational ferrofluid pressure vs. distance from a magnet.

Based on the **Eq.15**, the magnetic field strength gradient can be obtained:

$$\frac{\mathrm{d}H_x}{\mathrm{d}x} = -\frac{B_r}{\pi\mu_0}\left\{\frac{ab(a^2+b^2+2x^2)}{x^2(a^2+b^2+x^2)^{\frac{1}{2}} + a^2b^2(a^2+b^2+x^2)^{\frac{1}{2}}} - \frac{ab\left[a^2+b^2+2(x+L)^2\right]}{(x+L)^2\left[a^2+b^2+(x+L)^2\right]^{\frac{1}{2}} + a^2b^2\left[a^2+b^2+(x+L)^2\right]^{\frac{1}{2}}}\right\} \tag{16}$$

Combining **Eqs 1**, **2**, **16**, the magnetic force term $\frac{\mu_0 M}{\rho}\nabla H$ can be obtained. Moridis et al. used a single exponential function to fit the magnetic force term (Moridis et al., 1998). Based on this form, here the magnetic force term is fitted by a double exponential function to obtain higher precise fitting:

$$\frac{\mu_0 M}{\rho}\nabla H = \frac{\mu_0 M}{\rho}\frac{\mathrm{d}H_x}{\mathrm{d}x} \approx u_1 e^{-\mu_2 x} + u_3 e^{-\mu_4 x} \tag{17}$$

where these coefficients $u_1 = -1860$ TAm/(m^{3}Kg), $u_2 = 51.55$, $u_3 = 1465$ TAm/(m^{3}Kg), and $u_4 = 50.3$. The fitting results of magnetic force term are shown in **Figure 5**:

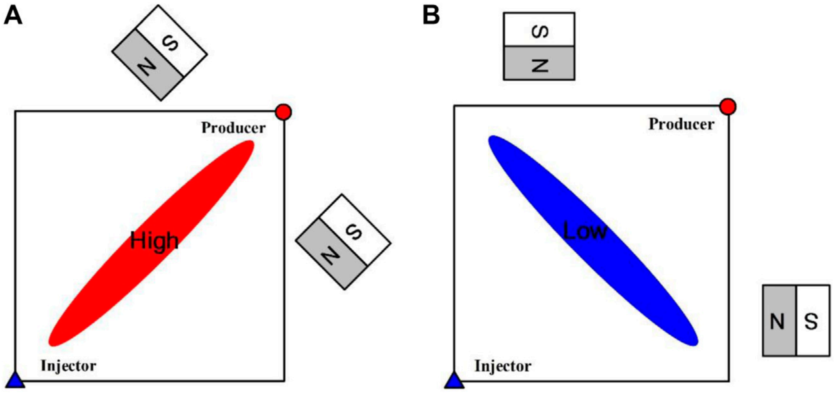

FIGURE 7 | Two different kinds of heterogeneous porous media models and the location of permanent magnets: **(A)** Porous media with a high-permeability zone; **(B)** Porous media with a low-permeability zone.

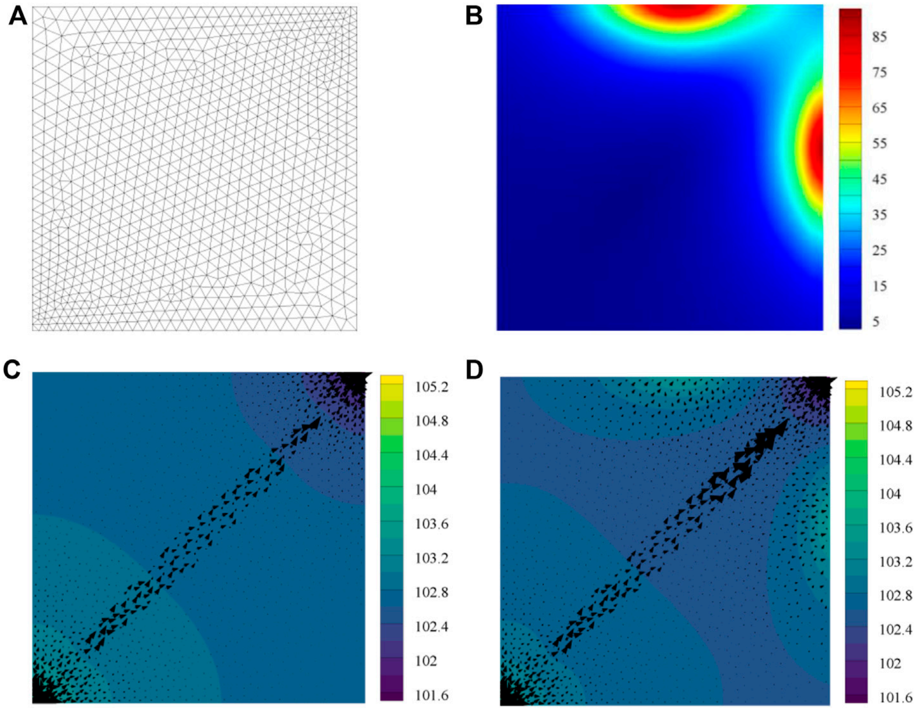

FIGURE 8 | Distribution of ferrofluid pressure and external magnetic field strength, the black arrow stands for flow velocity: **(A)** Mesh grid; **(B)** External magnetic field strength, 10^3A/m; **(C)** Pressure map without external magnetic field influence, KPa; **(D)** Pressure map with external magnetic field influence, KPa.

Because the tube is closed and horizontal, **v** and ∇z equals zero. Combining **Eqs 7**, **17**, one can obtain:

$$-\frac{\mathbf{k}\rho}{\mu}\left[\frac{dp}{dx}-\rho\left(u_1 e^{-\mu_2 x}+u_3 e^{-\mu_4 x}\right)\right]=0 \tag{18}$$

Solving the above equation, the analytic solution of pressure can be obtained:

$$p=p_0-\rho\frac{u_1}{u_2}e^{-\mu_2 x}-\rho\frac{u_3}{u_4}e^{-\mu_4 x} \tag{19}$$

where P_0 is the initial pressure and is assumed to equal the atmospheric pressure, which is 101.3 × 10^3 Pa, the distance $x \in [0.01,\ 0.2]$. The analytic solutions obtained by **Eq.19** and the numerical solutions obtained by the finite element method are basically the same, as is shown in **Figure 6**. Therefore, the

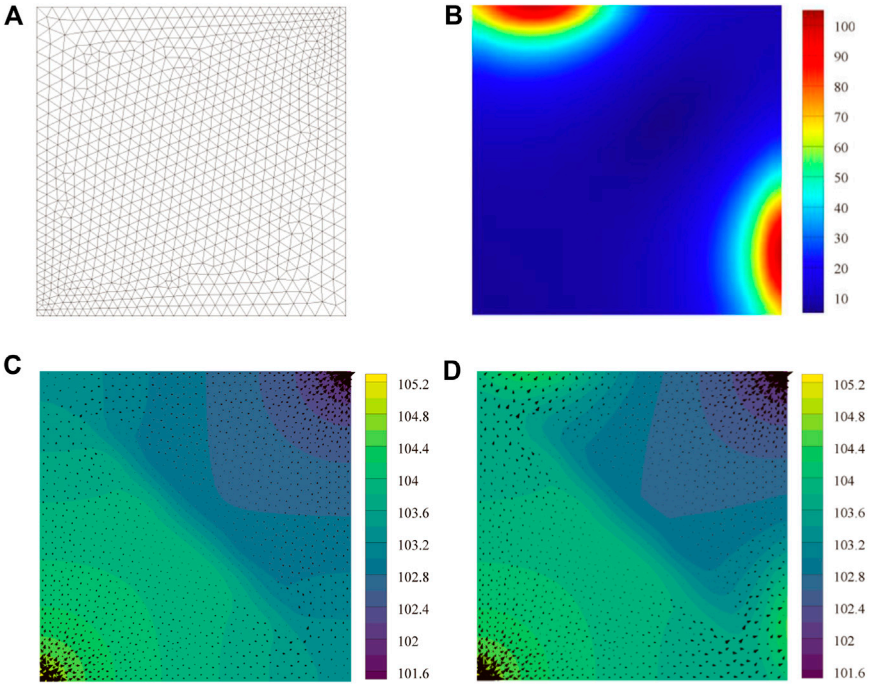

FIGURE 9 | Distribution of ferrofluid pressure and external magnetic field strength, the black arrow stands for flow velocity: **(A)** Mesh grid; **(B)** External magnetic field strength, 10^3A/m; **(C)** Pressure map without external magnetic field influence, KPa; **(D)** Pressure map with external magnetic field influence, KPa.

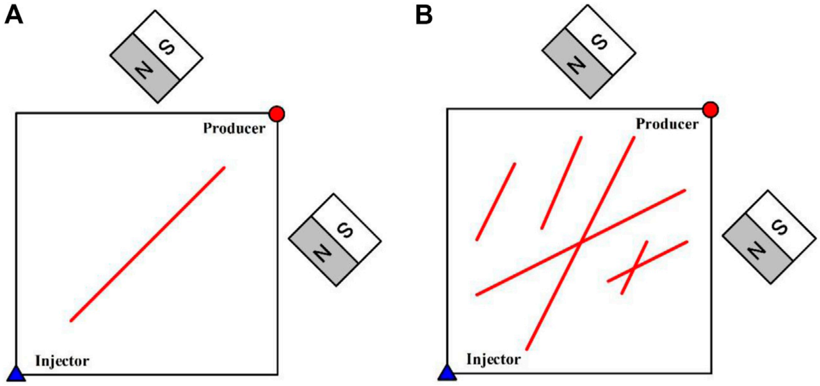

FIGURE 10 | Two different kinds of fractured porous media models and the location of permanent magnets: **(A)** Porous media with a single-fracture; **(B)** Porous media with multiple-fracture.

validity and effectiveness of the presented algorithm, which is mentioned in *Finite Element Discretization*, have been illustrated.

EXAMPLES AND DISCUSSIONS

Porous Media With Horizontal Heterogeneities

Consider two 1/4 five-spot horizontal heterogeneous porous media models, as **Figure** 7 shows, both with a size of 0.2 m × 0.2 m. The first model contains elliptical high-permeability zones while the second model contains elliptical low-permeability zones. The former permeability is $1.0 \times 10^{-13}\,\mathrm{m}^2$ and the latter permeability is $1.0 \times 10^{-16}\,\mathrm{m}^2$. Assuming both models have a porosity of 0.2 it are outside of the elliptical zones, then the permeability will be $1.0 \times 10^{-14}\,\mathrm{m}^2$. The injection and production rates of both models were set to 1.0 PV/min, where PV is the total pore volume. The initial pressure is 101.3×10^3 Pa. Two magnets were placed on both porous media models, as is shown in **Figure** 7, and the magnet properties have been mentioned in *Verification of Algorithm*.

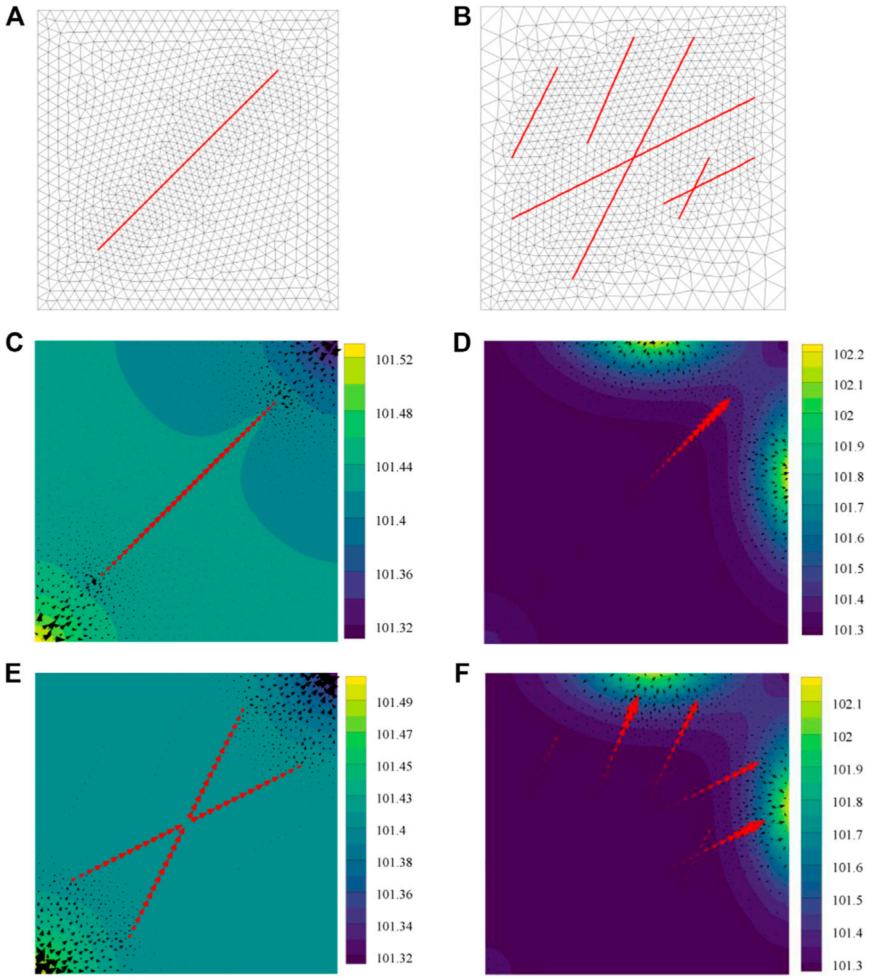

FIGURE 11 | Distribution of ferrofluid pressure, the red and black arrows stand for flow velocity in fractures and matrix respectively: **(A)** Mesh grid of single-fracture model; **(B)** Mesh grid of multiple-fracture model; **(C)** Pressure map of single-fracture model without external magnetic field influence, KPa; **(D)** Pressure map of single-fracture model with external magnetic field influence, KPa; **(E)** Pressure map of multiple-fracture model without external magnetic field influence, KPa; **(F)** Pressure map of multiple-fracture model with external magnetic field influence, KPa.

For the former heterogeneous model, the injected ferrofluid mainly flows through the high permeability zone when there is no external magnetic field (the size and direction of black arrows represent the flow velocity). While in the lower permeability area, ferrofluid is barely flowing because the pressure gradient is too low, as is shown in **Figure 8C**

However, when applied to an external magnetic field (**Figure 8B**), ferrofluid begins to flow towards the magnets and the pressure increases under the effect of the magnetic force. The magnetic force acts as a “shunt effect,” as is shown in **Figure 8D**.

For the latter heterogeneous porous media, the flow velocity in the low permeability zone is nearly zero. Ferrofluid flows bypassing the low permeability zone and the velocity is low when there is no external magnetic field, as is shown in **Figure 9C**.

When an external magnetic field is applied (**Figure 9B**), the magnetic force speeds up the flow of ferrofluid around the low permeability zone which leads to a “drainage effect.” The magnetic force leads to the flow velocity and the fluid pressure increases, as is shown in **Figure 9D**.

Porous Media With Fractures

The fractures’ geometric configuration was simplified by using the discrete-fracture method (Huang et al., 2011). Assuming the representative element volumes of both matrix and fracture system exist, and the flow equations (FEQ) are applied to the entire research area, then for the discrete-fracture model, the integral form of the flow equation can be expressed as:

$$\int_{\Omega} FEQ d\Omega = \int_{\Omega_m} FEQ d\Omega_m + \alpha \times \int_{\Omega_f} FEQ d\Omega_f \tag{20}$$

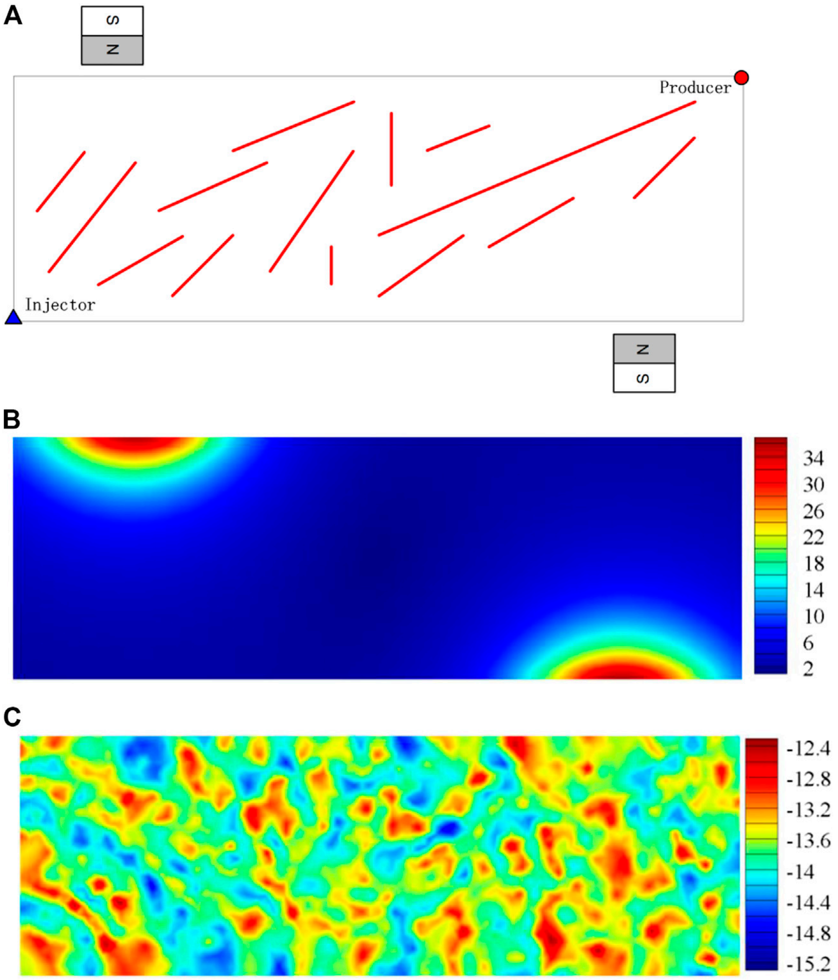

FIGURE 12 | A heterogeneous and fractured porous media model and the location of permanent magnets: **(A)** Model diagram; **(B)** External magnetic field strength, 10^3A/m; **(C)** Permeability map, $\log_{10}$(K).

where m represents the matrix, f represents the fracture, and α is the aperture of fracture.

Consider two horizontal fractured porous media models as are shown in **Figure 10**, and the model size is 0.2 m× 0.2 m. The aperture of fracture equals 1 mm, and the permeability of fracture is $8.33 \times 10^{-10}\,\mathrm{m}^2$. The other parameters are the same as mentioned above. Both two models have the same magnetic field as is shown in **Figure 8B**.

Because fracture is regarded as a kind of preferential pathway, the injected ferrofluid mainly flows along with the primary fractures (between the injector and producer), but the ferrofluid in the matrix or secondary fractures hardly flow, as is shown in **Figure 11C,E** (the red and black arrows stand for flow velocity in fractures and matrix respectively). When an external magnetic field is applied, the ferrofluid is forced to flow towards the magnet. As a result, the flow velocity in the primary fracture decreases and the ferrofluid in the matrix and secondary fractures begins to flow, as is shown in **Figure 11D,F**.

Heterogeneous and Fractured Porous Media

Consider a heterogeneous and fractured porous media model as is shown in **Figure 12A**, and the model size is 0.6 m × 0.2 m. The magnetic field and heterogeneous permeability map are shown in **Figure 12B,C**.

When there is no external magnetic field, the ferrofluid mainly flows in the fractures and the matrix with high permeability between injector and producer, as is shown in **Figure 13B**. However, the fluid flows slowly in the upper left and lower right corners of the reservoir due to the small pressure gradient.

Instead, if an external magnetic field (shown in **Figure 12B**) was applied, the flow state of the ferrofluid was changed, as is shown in **Figure 13C**. First, the flow velocity of the fluid in the matrix and fractures near the magnet increased due to magnetic force. Second, the flow velocity in the area far away from the magnetic source became relatively small. Third, the direction of fluid flow in some fractures is even reversed because the magnetic field force overcomes the displacement pressure gradient. The above results show that the flow of ferrofluid

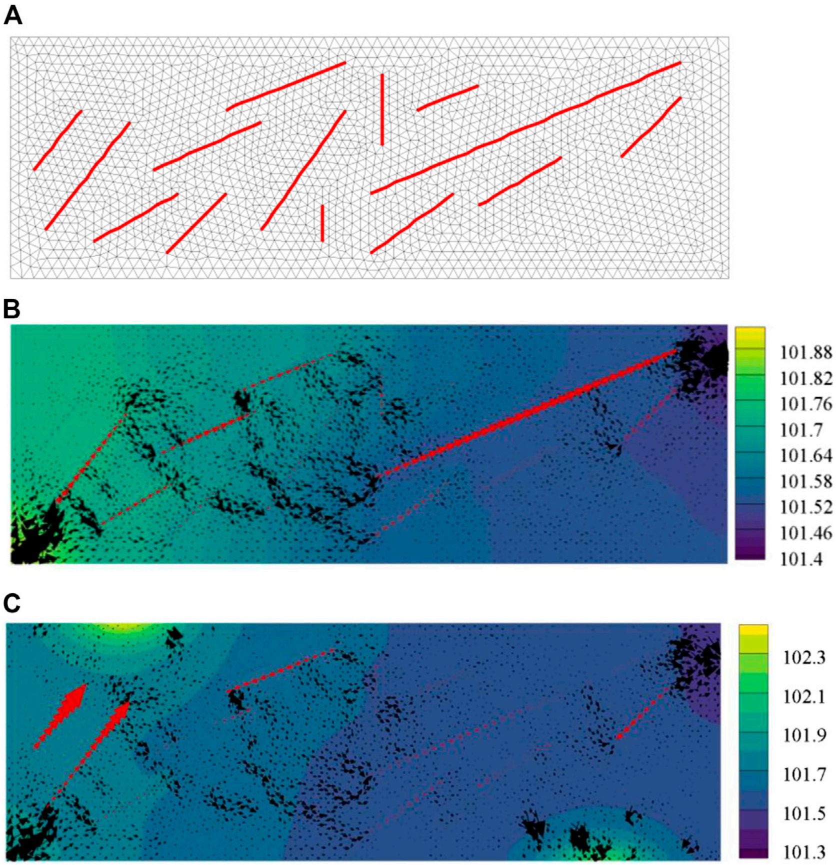

FIGURE 13 | Distribution of ferrofluid pressure, the red and black arrows stand for flow velocity in fractures and matrix respectively: **(A)** Mesh grid; **(B)** Pressure map without external magnetic field influence, KPa; **(C)** Pressure map with external magnetic field influence, KPa.

can be significantly affected by the external magnetic field, and therefore, its flow can be changed and the flow region can be expanded.

CONCLUSION

In this paper, the ferrofluid flow in complex porous media is investigated. The magnetic force is introduced into the Darcy equation and the Galerkin finite element method is used for discrete equations. From the simulation results, it is found that the ferrofluid flow in complex porous media can be manipulated by applying an external magnetic field. Moreover, some interesting phenomenon during ferrofluid flow in heterogeneous and fractured porous media have been found: 1) there is basically no flow in low permeability areas or secondary fractures without a magnetic field due to small displacement pressure; and 2) the ferrofluid flow direction and velocity can be changed, so that the magnetic force allows this magnetic fluid to be manipulated to flow in the desired direction through control of the external magnetic field, and makes the flow area larger.

DATA AVAILABILITY STATEMENT

The original contributions presented in the study are included in the article/supplementary material, further inquiries can be directed to the corresponding author.

AUTHOR CONTRIBUTIONS

TH conceived the idea and wrote the manuscript. XL, ZH, and RW contributed to the study and gave final approval for the manuscript.

FUNDING

This work was supported by the Fundamental Research Funds for Zhejiang Provincial Universities and Research Institutes (Grant No. 2020J00009), the National Natural Science Foundation of China (Grant No. 52004246); the Natural Science Foundation of Zhejiang Province (Grant No. LQ20E040003, Grant No. LY20D020002); the Science and Technology Project of Zhoushan Bureau (Grant No. 2021C21016).

REFERENCES

Fan, X., Sun, M., Sun, L., and Xie, H. (2020). Ferrofluid Droplets as Liquid Microrobots with Multiple Deformabilities. *Adv. Funct. Mater.* 30, 2000138. doi:10.1002/adfm.202000138

Han, D. (2007). Precisely Predicting Abundant Remaining Oil and Improving the Secondary Recovery of Mature Oilfields. *Acta Petrolei Sinica* 28, 73–38. doi:10.3321/j.issn:0253-2697.2007.02.013

Hou, H., Zhang, S., and Yang, N. (1999). Development on the Hydro-Magnetic Technology and its Application. *Vacuum Technology Mater.* 5, 8–12. doi:10.13385/j.cnki.vacuum.1999.05.003

Huang, Z., Yao, J., and Wang, Y. (2011). Numerical Simulation on Water Flooding Development of Fractured Reservoirs in a Discrete-Fracture Model. *Chin. J. Comput. Phys.* 1, 41–49. doi:10.19596/j.cnki.1001-246x.2011.01.006

Jia, C., Sepehrnoori, K., Huang, Z., and Jun, Y. (2021). Modeling and Analysis of Carbonate Matrix Acidizing Using a New Two-Scale Continuum Model. *SPE J.*, 1–30. doi:10.2118/205012-PA

Lei, Q., Guan, B., Cai, B., Wang, X., Xu, Y., Tong, Z., et al. (2019). Technological Progress and Prospects of Reservoir Stimulation. *Pet. Exploration Development* 46, 605–613. doi:10.1016/s1876-3804(19)60040-6

Li, Y. (2009). Study on Enhancing Oil Recovery of continental Reservoir by Water Drive Technology. *Acta Petrolei Sinica* 30, 396–399. doi:10.3321/j.issn:0253-2697.2009.03.013

Lu, M., Su, Y., Zhan, S., and Almrabat, A. (2020). Modeling for Reorientation and Potential of Enhanced Oil Recovery in Refracturing. *Adv. Geo-energ. Res.* 4, 20–28. doi:10.26804/ager.2020.01.03

Maccaig, M. (1987). *Permanent Magnets in Theory and Practice*. London: Pentech Press.

Moridis, G. J., Borglin, S. E., and Oldenburg, C. M. (1998). *Theoretical and Experimental Investigations of Ferrofluids for Guiding and Detecting Liquids in the Subsurface*. Office of Scientific & Technical Information Technical Reports. Berkeley. doi:10.2172/296663

Neuringer, J. L., and Rosensweig, R. E. (1964). Ferrohydrodynamics. *Phys. Fluids* 7, 1927. doi:10.1063/1.1711103

Odenbach, S. (2008). *Magnetoviscous Effects in Ferrofluids*. Berlin, Heidelberg: Springer.

Oldenburg, C. M., Borglin, S. E., and Moridis, G. J. (2000). Numerical Simulation of Ferrofluid Flow for Subsurface Environmental Engineering Applications. *Transport in Porous Media* 38, 319–344. doi:10.1023/a:1006611702281

Popplewell, J., and Charles, S. (1981). Ferromagnetic Liquids - Their Magnetic Properties and Applications. *IEEE Trans. Magn.* 17 (6), 2923–2928. doi:10.1109/tmag.1981.1061670

Qitai, Y. (2000). Three Major Rich Areas of “Large Scale” Unswept Remaining Oil in Water Flooded Bedded Sandstone Reservoirs. *Acta Petrolei Sinica* 21, 45–50. doi:10.7623/syxb200002009

Rahmani, A. R., Bryant, S. L., and Huh, C. (2015). “Characterizing Reservoir Heterogeneities Using Magnetic Nanoparticles,” in Proceedings of the SPE Reservoir Simulation Symposium, Houston, USA, February 23–25, 2015 (Houston: SPE).

Raj, K., and Moskowitz, R. (1990). Commercial Applications of Ferrofluids. *J. Magnetism Magn. Mater.* 85, 233–245. doi:10.1016/0304-8853(90)90058-x

Rosensweig, R. E. (1982). Magnetic Fluids. *Sci. Am.* 247, 136–145. doi:10.1038/scientificamerican1082-136

Scherer, C., and Figueiredo Neto, A. M. (2005). Ferrofluids: Properties and Applications. *Braz. J. Phys.* 35, 718–727. doi:10.1590/s0103-97332005000400018

Sengupta, S. (2012). “An Innovative Approach to Image Fracture Dimensions by Injecting Ferrofluids,” in Proceedings of the Abu Dhabi International Petroleum Exhibition and Conference, Abu Dhabi, UAE, November 11–14, 2012 (Abu Dhabi: SPE).

Sidiq, H., Abdulsalam, V., and Nabaz, Z. (2019). Reservoir Simulation Study of Enhanced Oil Recovery by Sequential Polymer Flooding Method. *Adv. Geo-energy Res.* 3, 115–121. doi:10.26804/ager.2019.02.01

Zeng, Q.-D., Yao, J., and Shao, J. (2018). Numerical Study of Hydraulic Fracture Propagation Accounting for Rock Anisotropy. *J. Pet. Sci. Eng.* 160, 422–432. doi:10.1016/j.petrol.2017.10.037

Zeng, Q., Yao, J., and Shao, J. (2020). An Extended Finite Element Solution for Hydraulic Fracturing with Thermo-Hydro-Elastic-Plastic Coupling. *Computer Methods Appl. Mech. Eng.* 364, 112967. doi:10.1016/j.cma.2020.112967

Zhu, G., Kou, J., Yao, B., Wu, Y.-s., Yao, J., and Sun, S. (2019a). Thermodynamically Consistent Modelling of Two-phase Flows with Moving Contact Line and Soluble Surfactants. *J. Fluid Mech.* 879, 327–359. doi:10.1017/jfm.2019.664

Zhu, G., Kou, J., Yao, J., Li, A., and Sun, S. (2019b). A Phase-Field Moving Contact Line Model with Soluble Surfactants. *J. Comput. Phys.* 405, 109170. doi:10.1017/jfm.2019.664

Conflict of Interest: The authors declare that the research was conducted in the absence of any commercial or financial relationships that could be construed as a potential conflict of interest.

frontiers in Earth Science

ORIGINAL RESEARCH
published: 08 July 2021
doi: 10.3389/feart.2021.698086

Effect of Isolated Fracture on the Carbonate Acidizing Process

Cunqi Jia[1]*, Tao Huang*[2]**, Jun Yao*[1]*, Hongchuan Xing*[1] *and Haiyang Zhang*[3]

[1]School of Petroleum Engineering, China University of Petroleum (East China), Qingdao, China, [2]School of Petrochemical Engineering and Environment, Zhejiang Ocean University, Zhoushan, China, [3]Petroleum Department, Khalifa University, Abu Dhabi, United Arab Emirates

Carbonate reservoirs are one of the most important fossil fuel sources, and the acidizing stimulation is a practical technique for improving the recovery of carbonate reservoirs. In this study, the improved two-scale continuum model, including the representative elementary volume (REV) scale model and the upscaling model, is used to study the acidizing process with an isolated fracture. Based on this model, a comprehensive discussion is presented to study the effect of the physical parameters of the isolated fracture on the acidizing results and dissolution images, including the isolated fracture geometry, location, and morphology. Results show that the isolated fracture system is still the target system for the acidizing stimulation. The isolated fracture provides a limited contribution to the core porosity. The permeability of the core sample with fracture can be obviously increased only when the fracture penetrates through the whole sample. The existence of the isolated fracture reduces the consumption of acid solution to achieve a breakthrough. The acidizing curve is sensitive to the change of the length, aperture, and position of the isolated fracture. The acidizing curve difference corresponding to different rotation angles has not changed significantly for clockwise rotation and anticlockwise rotation groups.

Keywords: fracture acidizing, two-scale continuum model, carbonate reservoirs, reactive flow, carbonate acidizing

Edited by:
Weiqi Fu,
China University of Mining and Technology, China

Reviewed by:
Jiazheng Qin,
Southwest Petroleum University, China
Bo Ren,
University of Texas at Austin, United States

****Correspondence:***
Tao Huang
huangtaozjou@126.com

Specialty section:
This article was submitted to Economic Geology, a section of the journal Frontiers in Earth Science

Received: *20 April 2021*
Accepted: *14 June 2021*
Published: *08 July 2021*

Citation:
Jia C, Huang T, Yao J, Xing H and Zhang H (2021) Effect of Isolated Fracture on the Carbonate Acidizing Process.
Front. Earth Sci. 9:698086.
doi: 10.3389/feart.2021.698086

INTRODUCTION

Carbonate reservoirs are one of the significant parts of fossil fuel sources (Zhao et al., 2018; Liu et al., 2020). Compared with sandstone sedimentary rocks, carbonate reservoirs have strong heterogeneity due to complex geological processes, which result in more formation energy consumption in some carbonate reservoirs with low permeability (Zhao et al., 2020; Liu et al., 2021). Carbonate acidizing is a widely used stimulation technology to effectively improve the oil recovery of carbonate reservoirs using the acid solution to dissolve the low permeability matrix (Wei et al., 2019).

Large numbers of articles have been published to study the carbonate matrix acidizing process. Experimental studies are mainly conducted through core flooding experiments, in which constant concentration acid solution is pumped at the inlet boundary of the core sample (Fredd and Fogler, 1999; Dong, 2012). During the experimental process, the pressure at the inlet boundary of the core sample is always recorded as an indirect indicator variable for monitoring the acidizing implementation. As the pore structure inside the core sample is constantly dissolved by the acid solution, the migration resistance of the acid fluid inside the core sample also constantly changes, causing the pressure at the core entrance to vary from time to time. Usually, the core displacement test is stopped when the inlet boundary pressure of the core sample is observed to decrease significantly (Zakaria and Nasr-El-Din, 2016). The obvious decrease of pressure means that the fluid migration resistance inside the core sample has dropped significantly, which is usually defined as the breakthrough moment during the acidizing process. The amount of acid consumed at the breakthrough time has been widely determined as a quantitative indicator to study the effectiveness of the acidizing process and evaluate the impact of different influencing factors on the acidizing process, including the acid solution types, concentration, injection rate, and core sample geometry (Dong, 2012; Furui et al., 2012; Wadekar and Pandya, 2014; Sarmah et al., 2020). One of the most important findings of these experimental studies is that there exists an optimum value for the acid breakthrough consumption curve, at which the injected acid solution consumes the minimum amount of the acid solution to achieve a breakthrough (Fredd and Fogler, 1999; Furui et al., 2012). Another important finding is that when acid solution is injected into the core sample at different rates, the final dissolution structure inside the core sample is also different when achieving the breakthrough (Sarmah et al., 2020). The high acid injection rate makes the acid solution to be transported to most of the core sample, causing the solid matrix to be uniformly dissolved. When the acid injection rate is reduced at the optimum value, the migration of the acid solution is controlled by the convection, diffusion, and core heterogeneity together. Finally, a major dissolution channel is formed inside the core sample named as the wormhole. When the acid solution injection rate further decreases, the width of the main wormhole is enlarged because the acid solution obtains sufficient time to dissolve the solid matrix.

Several mathematical models have also been developed to capture and reproduce the important results observed in the experimental studies, including the pore network model, empirical model, and continuum model (Maheshwari et al., 2013). The pore network model is the most realistic model, in which the initial calculation domain uses the pore network obtained through the true target stimulated core sample. The acidizing process is simulated inside each pore and throat of the real core sample (Tansey, 2014). However, huge calculation expense decides that the pore network model can only be conducted within the limited domain (Tansey and Balhoff, 2016). The empirical model has the smallest calculation expense, but the model accuracy depends on the assumptions for deriving the empirical model and the benchmark data obtained through the experimental studies (Maheshwari et al., 2016; Palharini Schwalbert et al., 2019). Finally, the continuum model has been extensively developed recently due to the high model accuracy compared to the empirical model and less computational consumption compared to the pore network model. The continuum model was first proposed by Panga et al. (2005) including the Darcy-scale model and pore-scale model. Hence, the continuum model is also referred to as the two-scale continuum model (Panga et al., 2005; Maheshwari et al., 2013; Liu et al., 2017). Recently, the two-scale continuum model was further improved by Jia et al. (2021a) to more accurately simulate the stimulation process, in which the additional mass term is added in the fluid phase continuity equation to consider mass exchange term between the solid matrix and acid solution. Also, the Stoke–Darcy equation is used instead of the Darcy equation to describe acid solution flow (Jia et al., 2021b).

Apart from the solid matrix, fractures are also very common in carbonate reservoirs. And, the carbonate rocks with isolated fractures are also the target reservoirs for the acidizing stimulation (Li and Voskov, 2021). However, few studies are conducted to study the acidizing process in carbonate rocks with isolated fractures. One of the reasons is that the efficient and accurate characterization of fractures is still a challenge in numerical simulation. Usually, the fracture models can be divided into the discrete fracture model and the duel-medium model according to the fractures' descriptions. The discrete fracture model explicitly distinguishes the location of each fracture, and the fluid flow in each single fracture can be simulated (Neuzil and Tracy, 1981; Tsang and Witherspoon, 1981). The simplest discrete fracture model uses two parallel, infinite planes to represent single fracture (Snow, 1969). The cubic law is used to determine the fracture permeability used in the Darcy equation (Muralidhar, 1990). In actual application, the fracture aperture is generated through a random function to consider the effect of the roughness of the fracture surface (Zimmerman et al., 1991; Zimmerman et al., 1992). Different from the discrete fracture model, the duel-medium model assumes that the simulated domain contains both the solid matrix and the fracture (Moreno et al., 1988; Tsang and Tsang, 1989). The governing equations are developed both for the solid matrix region and the fracture region (Meyer and Bazan, 2011). The flow exchange between the solid matrix region and the fracture region is a function of the fluid pressure difference in the solid matrix region and the fracture region (Wu, 2015). It is worth noting that the fluid flow in the above fracture models is all described by the Darcy equation. However, the matrix acidizing results have proven that the applicability of the Darcy equation is only validated when the acid injection rate is relatively high, and the solid matrix is uniformly dissolved. When wormholes appear, the Darcy equation is not able to accurately describe the fluid flow because it only considers the effect of the structure of porous media (Jia et al., 2021b). However, in the wormhole region, the complex porous structure is dissolved into free-flow region. And, for the fracture region, it can also be seen as a special wormhole region, in which the applicability of the Darcy equation is still challenged and needs to be further validated. Hence, a more general mathematical model is still needed to simulate the acidizing process with fractures.

In this study, the improved two-scale continuum model is used to study the acidizing process with an isolated fracture. The detailed model descriptions are given in the next section. In the discussions and results section, both the classical and the improved two-scale models are used to simulate the acidizing process with an isolated fracture. Several cases are designed to investigate the effect of the fracture physical parameters on the stimulation results and compare the differences between the classical and the improved two-scale models. The main conclusions are summarized in the last section.

Model Descriptions

The mathematical models used in the acidizing process simulation with an isolated fracture is referred as the improved two-scale continuum model (Panga et al., 2005), which contains the representative elementary volume scale model and the upscaling model.

Representative Elementary Volume Scale Model

The representative elementary volume scale model is developed based on the mass and momentum conservation principles. The chemical reaction between the solid matrix and the acid solution proceeds according to the following equation:

$$CaCO_3 + 2HCl \rightarrow CaCl_2 + H_2CO_3. \tag{1}$$

The specific reaction rate is expressed by the concentration of hydrochloric acid in the acid solution system:

$$R_{HCl} = k_s c_{HCl,s}, \tag{2}$$

where k_s is the acid surface reaction rate and $c_{HCl,s}$ is the acid surface concentration. Then, the mass conservation equations of the fluid phase, acid solution, and solid matrix are given in turn as follows:

$$\frac{\partial(\phi\rho_f)}{\partial t} = -\nabla\cdot(\mathrm{u}\rho_f) + \frac{M_{CaCO_3}}{2}R_{HCl}s, \tag{3}$$

$$\frac{\partial(\phi c_{HCl})}{\partial t} = -\nabla\cdot(\mathrm{D}_{HCl}\cdot\nabla c_{HCl} + \mathrm{u}c_{HCl}) - R_{HCl}s, \tag{4}$$

$$\frac{\partial((1-\phi)\rho_s)}{\partial t} = -\frac{M_{CaCO_3}}{2}R_{HCl}s, \tag{5}$$

where ϕ is the porosity, ρ_f is the fluid phase density, u is the fluid phase velocity, M_{CaCO_3} is the molar mass of calcite, s is the specific surface area, c_{HCl} is the acid bulk concentration, D_{HCl} is the acid diffusion coefficient, and ρ_s is the solid phase density. As for the determination of fluid phase velocity, the Darcy equation is most commonly used in both matrix and fracture regions (Wu, 2015):

$$0 = -\nabla p - \frac{\mu}{k}\mathrm{u}, \tag{6}$$

where μ is the fluid viscosity, k is the permeability, and p is the fluid phase pressure. Because it is usually accepted that fluid flow inside the porous media is mainly influenced by the porous media structure, however, our recent study results (Jia et al., 2021b) have proved that acid solution migration in porous media is affected by the porous structure for acidizing processes. The influence of viscous dissipation between acid solutions becomes more significant in the wormhole region and should also be considered. Instead, the Stokes–Darcy equation is adopted in the improved two-scale continuum model to determine acid solution convection velocity (Jia et al., 2021b):

$$0 = \nabla\cdot\left(\mu\left(\nabla\frac{\mathrm{u}}{\phi} + \left(\nabla\frac{\mathrm{u}}{\phi}\right)^T\right)\right) - \nabla p - \frac{\mu}{k}\mathrm{u}. \tag{7}$$

In this work, both the Darcy equation and the Stokes–Darcy equation are used to simulate the acidizing process with an isolated fracture to further compare the effect of differences between the classical and the improved two-scale models on the acidizing results.

Upscaling Model

The upscaling model is developed to link the actual acidizing process with the REV scale model. In the actual stimulation process, the chemical reaction between the acid solution and the solid matrix occurs on the pore surface inside the solid matrix. However, the reaction terms involved in the model established on the REV scale are based on the control volume. The connection between the actual chemical reaction rate at the pore scale and the equivalent, chemical reaction term on the REV scale is achieved through the mass transfer equation:

$$k_s c_{HCl,s} = k_c(c_{HCl} - c_{HCl,s}), \tag{8}$$

where k_c is the acid mass transfer rate, which is determined by an analytical expression (Balakotaiah and West, 2002):

$$k_c = \frac{ShD_m}{2r}, Sh = Sh_\infty + 0.7\mathrm{Re}_p^{\frac{1}{2}}Sc^{\frac{1}{3}}, \tag{9}$$

where Sh, Sh_∞, Re_p, and Sc are the dimensionless numbers, the asymptotic Sherwood number, Sh_∞, is usually valued as 3.66 for circular pore structure, pore Reynold number, Re_p, and Schmidt number, and Sc is defined as $Re_p = 2r|\mathrm{u}|/\nu$ and $Sc = \nu/D_m$, ν is the dynamic viscosity. During the acidizing process, the continuous dissolution of the solid matrix by the acid solution causes the porous structure to change from time to time. The modified Carman–Kozeny equations update the change of the physical parameters of the solid matrix (Panga et al., 2005; Maheshwari et al., 2013):

$$\frac{k}{k_0} = \left(\frac{\phi}{\phi_0}\right)^{\gamma}\left(\frac{\phi(1-\phi_0)}{\phi_0(1-\phi)}\right)^{\beta}, \tag{10}$$

$$\frac{r}{r_0} = \left(\frac{\phi(1-\phi_0)}{\phi_0(1-\phi)}\right)^{\beta}, \tag{11}$$

$$\frac{s}{s_0} = \left(\frac{\phi}{\phi_0}\right)\left(\frac{\phi(1-\phi_0)}{\phi_0(1-\phi)}\right)^{-\beta}, \tag{12}$$

where k_0, r_0, and s_0 are the initial rock parameters of permeability, pore radius, and specific surface area, respectively, and γ and β are the parameters related to pore connection and cementation. At the same time, the porous

TABLE 1 | Values of physical parameters used in numerical models.

Parameter	Value	Parameter	Value
Fluid density	1 g/cm^3	Solid density	2.71 g/cm^3
Fluid viscosity	1 mPa s	Calcite molar mass	100.1 g/mol
Pore radius	0.5 μm	Specific surface area	50 cm^{-1}

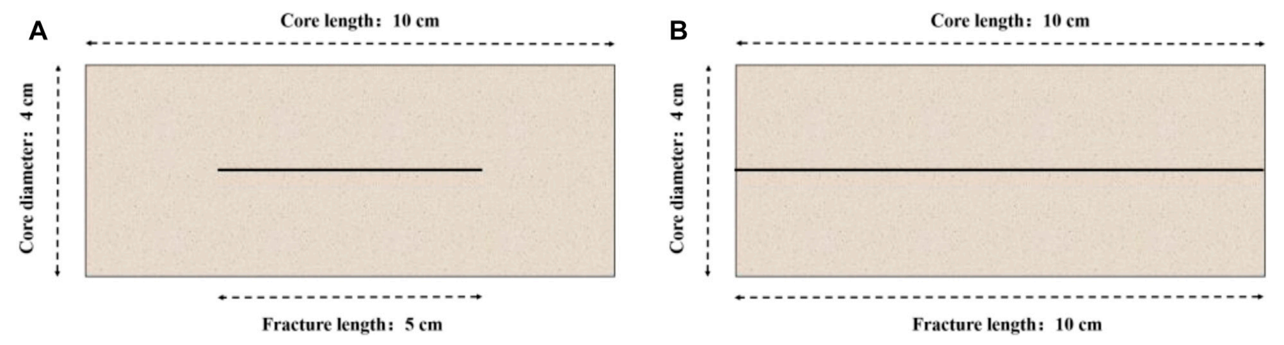

FIGURE 1 | Typical fracture patterns inside the core sample: **(A)** isolated fracture; **(B)** connected fracture.

structure of the solid matrix also affects the diffusion process of the acid solution:

$$D_{HCl} = D_m \mathrm{I} + \frac{2r}{\phi|\mathrm{u}|}\left[\, u^2 \quad v^2 \,\right], \tag{13}$$

where D_m is the molecular diffusion coefficient, I is the unit vector, r is the pore radius, |u| is the fluid velocity norm, and u and v are the components of fluid phase velocity.

Initial and Boundary Conditions

The application of the initial and boundary conditions is consistent with the core displacement experiment (Fredd and Fogler, 1999; Dong, 2012). The core sample is saturated with water at the beginning. When the acidizing stimulation begins, the acid solution is continuously injected from the core inlet boundary at a constant injection rate and concentration, and the right boundary of the core sample maintains a constant pressure. The surrounding of the core sample is kept closed (Dong et al., 2014).

RESULTS AND DISCUSSION

The study domain is selected as a common core sample size adopted in the experimental study with a dimension of 4 cm width and 10 cm length. The initial porosity and permeability of the core sample are measured as 0.15 and 5 m D (Dong et al., 2014). The isolated fracture is located in the center of the core sample with a length of 5 cm and an aperture of 0.15 mm. The acid system is selected as a hydrochloric acid solution with an injection concentration of 15% (4.42 mol/L). The molecular diffusion coefficient of the acid solution is determined as 3.5×10^{-5} cm^2/s and surface reaction rate is determined as 1.1×10^{-3} cm/s (Panga et al., 2005; Jia et al., 2021b). The values of other physical parameters used in numerical models are summarized in **Table 1**. The governing equations are discrete and solved based on the finite element method. During the calculation process, the core inlet boundary pressure is detected to monitor the acidizing process. The calculation stops when the core apparent permeability increases 100 times (Dong et al., 2014). The apparent permeability is determined based on the Darcy equation using the pressure difference between the inlet and the outlet boundaries. The volume of acid consumed at the calculation stops is normalized by the core initial pore volume to obtain the evaluation variable for the acidizing result, pore volume to breakthrough (PVBT) (Panga et al., 2005).

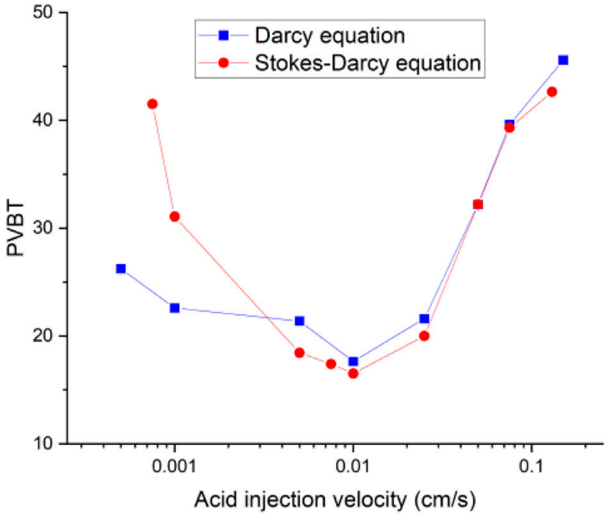

FIGURE 2 | Matrix acidizing curves of pore volume to breakthrough.

Model Comparison with the Existence of an Isolated Fracture

This section mainly investigates the influence of the isolated fracture on the acidizing process. We first study the influence of the single fracture on the core porosity and permeability. **Figure 1** shows two typical single fracture patterns inside the core sample, separately named as the connected fracture and the isolated fracture. The porosity values are determined as 0.1815 and 0.1657, respectively, for the connected fracture and isolated fracture core samples. The permeability of the isolated fracture core sample is numerically measured at 7.94 mD, while the

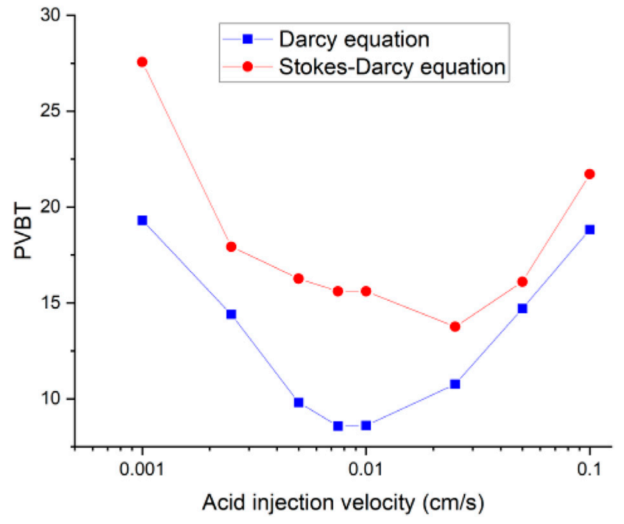

FIGURE 3 | Isolated fracture acidizing curves of pore volume to breakthrough.

permeability of the connected fracture core sample is at 50 mD. The matrix porosity and permeability is 0.15 and 5 mD. It can be observed that both the isolated fracture and the connected fracture have a limited influence on porosity. The isolated fracture also has limited contribution for the core permeability. Only the connected fracture obviously increases the core permeability. Hence, the core sample with an isolated fracture is still the target core sample for the acidizing stimulation.

In the classical two-scale continuum model (Panga et al., 2005), the Darcy equation is used to describe the fluid flow during the acidizing process. In our recent work (Jia et al., 2021b), the Stokes–Darcy equation is suggested to determine the fluid phase velocity instead of the Darcy equation. Because the applicability of the Darcy equation is questioned within the wormhole regions, in the wormhole regions, the porosity value is very high, even up to 1. The effect of the porous structure on the fluid flow becomes less and less obvious. The viscous dispersion between the fluid phase becomes more important and should be considered. **Figure 2** shows the carbonate matrix acidizing curves separately determined by the Darcy equation and the Stokes–Darcy equation. The results support the application of the Stokes–Darcy equation. When the acid solution is injected at high rates, the difference between the two acidizing curves is not very obvious. Because most of the solid matrix is not totally dissolved into wormholes with high acid injection rates. The effect of porous structure on the fluid flow is still dominated in this case compared to fluid phase viscous dispersion. The acidizing curve difference becomes apparent with low acid injection rates. When the acid injection rate is very low, the acid solution has sufficient time to react with the solid matrix, causing most of the solid matrix to completely dissolve into wormholes. Because the Darcy equation cannot consider the effect of fluid viscosity dissipation, the acid breakthrough volume calculated by the Darcy equation is obviously less than that determined by the Stokes–Darcy equation. The acidizing efficiency of the acid solution is artificially enhanced by using the Darcy equation. **Figure 3** further compares the acidizing curves separately determined by the Darcy equation and the Stokes–Darcy equation with an isolated fracture. With contrast to **Figure 2**, the difference between the acidizing curves with an isolated fracture becomes obvious within the whole injection rate interval, even though the acid injection rate is at high values. The results show that the existence of an isolated fracture also challenges the applicability of the Darcy equation at high injection rates.

Figure 4 continues to compare the acidizing curves with an isolated fracture and without an isolated fracture. The results show that the acid breakthrough volume with an isolated fracture is smaller than that of the matrix acidizing result within in both acidizing curves determined by the Darcy equation and the Stokes–Darcy equation. The acid breakthrough volume difference between the acidizing curves with and without an isolated fracture is quite obvious when the acid injection rate is at a high value for both the Darcy equation and the Stokes equation. The acid breakthrough volume difference between the acidizing curves with and without an isolated fracture starts to differ at lower injection rates. The acid breakthrough volume difference determined by the Stokes–Darcy equation gradually becomes less apparent at low injection rates. The acid breakthrough volume difference determined by the Darcy equation is still significant when the injection rate is low. **Figure 5** compares the dissolution images of the core sample with and without an isolated fracture. The isolated fracture greatly influences the final dissolution patterns especially when the acid solution is injected into the core sample with high and intermediate rates. The isolated fracture provides an advantageous passage for acid migration in porous media, in which isolated fracture prevents more acid from being ineffectively consumed to dissolve the solid matrix. **Table 2** further studies the effect of mass exchange term between solid matrix and acid fluid solution on the stimulation results with an isolated fractured, which is neglected by most previous numerical studies (Panga et al., 2005). The results show that ignoring the mass exchange term still leads to an overestimated acid breakthrough volume, which is consistent with the conclusions obtained from the matrix acidification process (Jia et al., 2021a).

Effect of Isolated Fracture Geometry

This section mainly studies the influence of fracture geometry on the stimulation process, including fracture length and fracture aperture. The fracture length is selected to vary from 3 to 8 cm, in which the fracture remains in the middle of the core sample with an aperture of 1.5 mm. The results show that the porosity of the core increases from 0.16 for a 3 cm fracture length to 0.18 for an 8 cm fracture length. The core permeability increases from 6.1 mD for a 3 cm fracture length to 15.1 mD for an 8 cm fracture length. The permeability and porosity of the matrix core sample correspond to 0.15 and 5 mD, separately. As for the influence of the aperture, the porosity increases from the matrix porosity of 0.15–0.18, corresponding to the fracture aperture of 3 cm. The permeability increases from the matrix

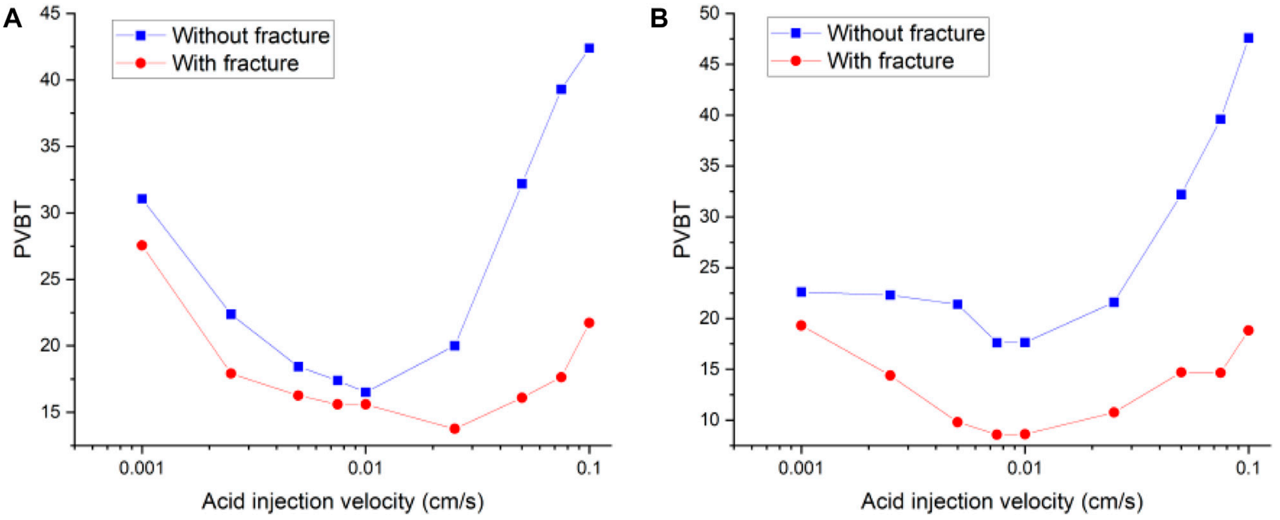

FIGURE 4 | Comparison of acidizing curves of pore volume to breakthrough between matrix and isolated fracture: **(A)** Stokes–Darcy equation; **(B)** Darcy equation.

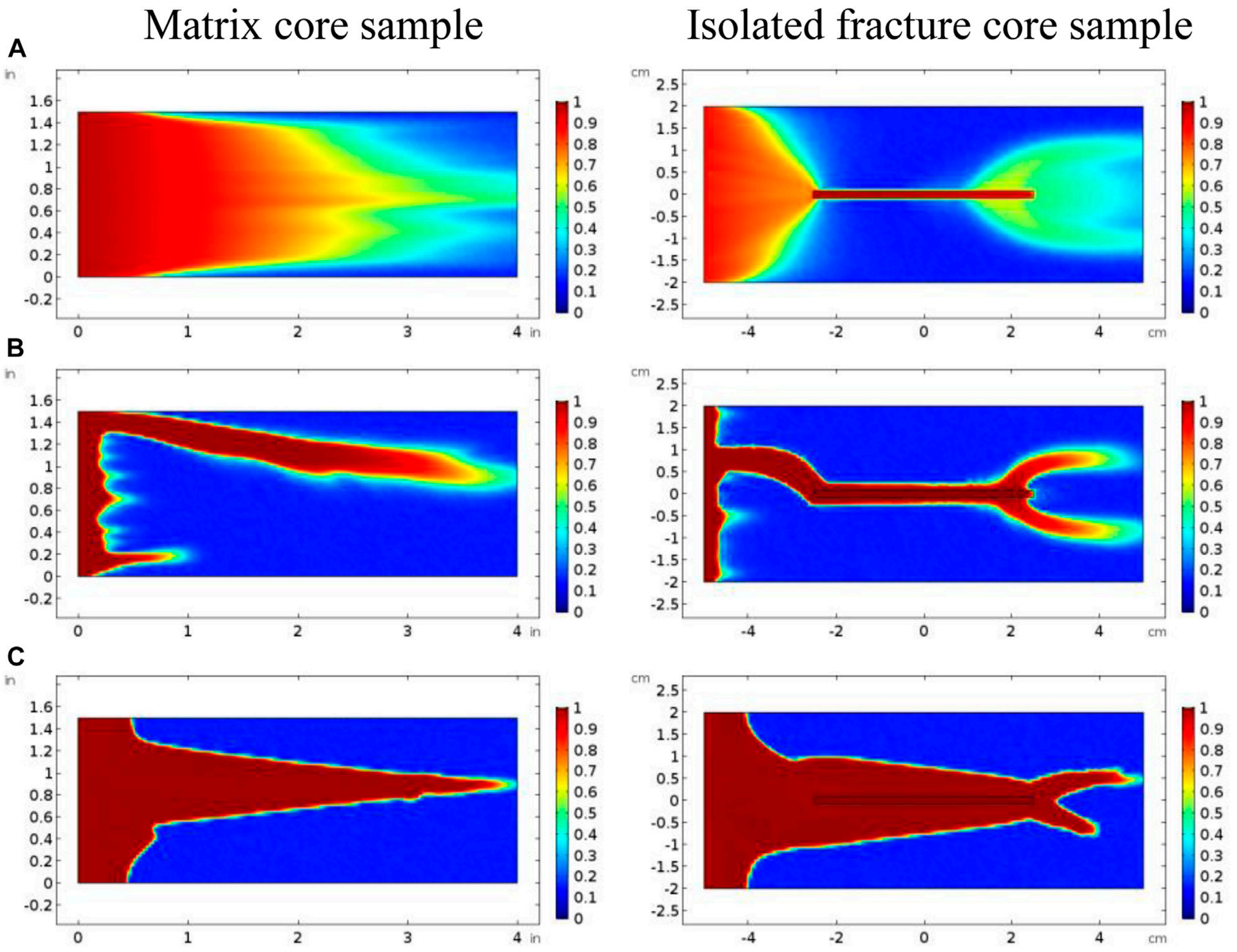

FIGURE 5 | Comparison of dissolution images of matrix and isolated fracture core samples: **(A)** 0.1 cm/s; **(B)** 0.01 cm/s; **(C)** 0.001 cm/s.

TABLE 2 | Effect of mass transfer term on acidizing results of isolated fracture core sample.

Acid injection velocity	Pore volume to breakthrough		Relative error
cm/s	Without mass exchange	With mass exchange	%
1.00E-01	22.08	21.72	1.64
7.50E-02	19.28	17.65	8.45
5.00E-02	18.28	16.11	11.88
2.50E-02	18.55	13.76	25.85
1.00E-02	18.64	15.60	16.31
7.50E-03	19.87	15.61	21.45
5.00E-03	18.57	16.27	12.38
2.50E-03	21.27	17.93	15.70

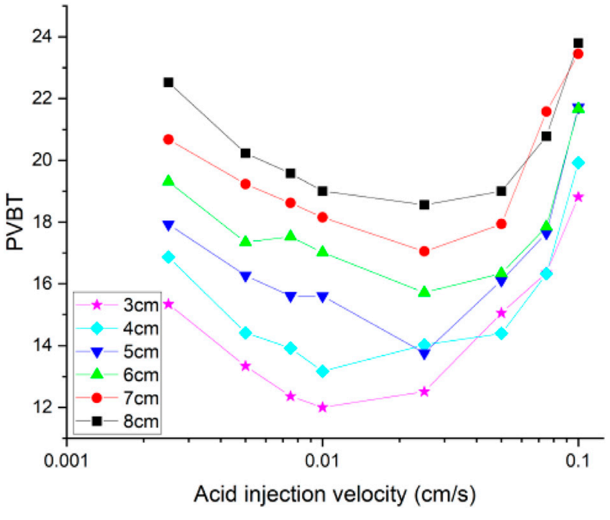

FIGURE 6 | Isolated fracture acidizing curves of pore volume to breakthrough with different lengths.

permeability of 5 to 8.2 mD. Hence, different fracture lengths and apertures have a very limited effect on the growth of core porosity and permeability.

Figure 6 shows the acidizing curves corresponding to different fracture lengths. The results show that the acid breakthrough volume increases with the increase of the isolated fracture length. And, the existence of isolated fracture can obviously affect the distribution of pressure and velocity inside the core sample, as shown in **Figure 7**. Inside the matrix core sample, the acid fluid injection rate is parallel to the length direction of the core sample, and the pressure gradient also decreases uniformly along the core length. When an isolated fracture exists, the uniformly changing pressure gradient inside the matrix core sample is intuitively broken. The pressure within an isolated fracture is generally lower than the pressure of the matrix core sample. A pressure convergence zone and a pressure divergence zone separately forms at the inlet and the outlet boundaries of the isolated fracture. Hence, the fluid tends to flow into the convergence zone and the divergence zone and also leads to the formation of wormhole branches at the outlet boundary of the isolated fracture. **Figure 8** continues to study the influence of fracture aperture on the acidizing results. The results show that the increase of the fracture opening can reduce the amount of acid consumed at breakthrough. High fracture apertures increase the affected domain generated by the isolated fracture and causes the acid solution migration within the core sample affected more obviously. More acid solution is induced by the high fracture aperture, resulting in less acid solution consumed.

Effect of Isolated Fracture Location

In this section, several cases are designed to study the isolated fracture locations on the acidizing results. The isolated fracture developed in the center of the core sample is selected as the reference comparison case. Here, nine different isolated

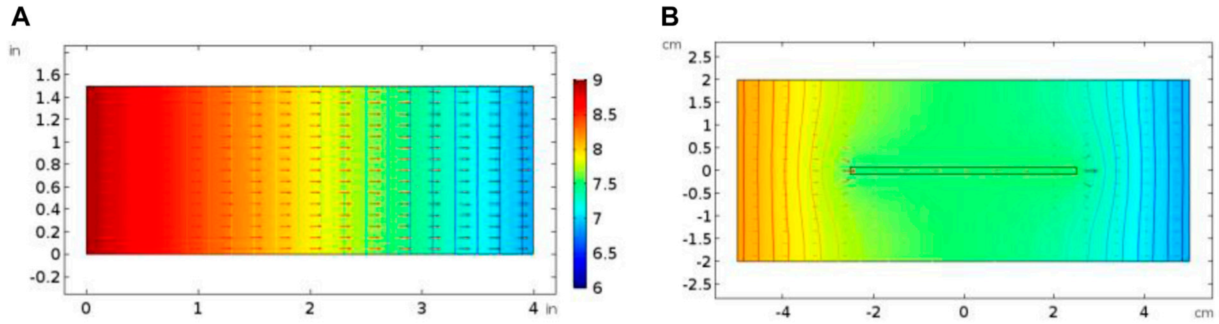

FIGURE 7 | Comparison of velocity and pressure profiles with acid injection rate at 0.01 cm/s: **(A)** matrix core sample; **(B)** isolated fracture core sample.

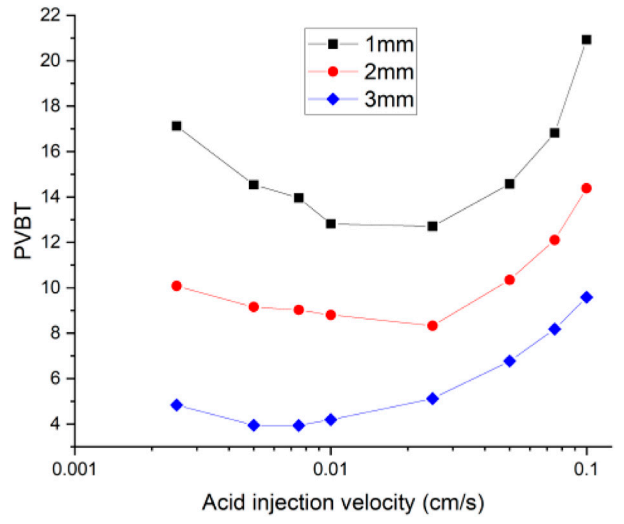

FIGURE 8 | Isolated fracture acidizing curves of pore volume to breakthrough with different apertures.

fracture locations are assumed, covering the top, middle, bottom, left, and right positions. For the simplicity, these nine positions can be divided into three categories: left group (left-up, left-center, and left-down), center group (center-up, center-center, and center-down), and right group (right-up, right-center, and right-down). These nine types of core samples at different isolated fracture locations have the same porosity of 0.17.

Figure 9 compares the acidizing curves corresponding to different groups of fracture positions. It can be found that there is no obvious difference between the acidizing curves with the same group of isolated fractures in the up, center, and down positions. The difference in the acidizing curves becomes obvious between the different groups of left, center, and right positions. The acid consumption volume with the fracture position at the left boundary of the core sample is larger than the breakthrough volume of the acid corresponding to the fracture position at the right boundary of the core sample. When the fracture is located at the entrance boundary, the existence of fracture provides an advantageous channel for the migration of acid solution. During the acidizing process, the acid solution tends to migrate along the main direction of the fracture. Until the acid moves to the right end of the fracture, the acid begins to come into contact with the core sample with low permeability, which causes the acid solution not to be transported as efficiently as it moves in the fracture. The acid solution is forced to accumulate in the fracture and ineffectively consumed. More acid solution is used to increase the width of the fracture, as shown in **Figure 10**. When the fracture is at the outlet boundary, the acid tends to contact the fracture. Moreover, once the wormhole formed inside the matrix begins to contact the fracture, the core breakthrough can be easily realized. Because the fracture directly communicates with the right boundary, the negative acid accumulation no longer exists. Less acid is needed to break through the core.

Effect of Isolated Fracture Morphology

This section studies the influence of fracture morphology on acidizing process by rotating the isolated fracture at a certain angle. Two rotation directions, clockwise and anticlockwise rotation, are adopted. Each type is rotated by 10, 20, and 30°, respectively. Finally, six different fracture morphologies are obtained. The isolated fracture results with 0° rotation is selected for reference comparison. Although the isolated fracture has different rotation angles inside the core sample, the change of permeability is not obvious. The permeability values are estimated around 7 mD, and the permeability of the matrix core corresponds to 5 mD. **Figure 11** studies the acidizing curves corresponding to different rotation angles. The acidizing curves corresponding to different rotation angles are divided into the clockwise rotation and anticlockwise rotation groups. The results show that the change of the acidizing curve corresponding to different rotation angles of the same rotation sequence is very similar. The difference between them has not changed significantly both for clockwise rotation and anticlockwise rotation groups.

Then, we continue to consider an extreme case, in which the rotation angle of the isolated fracture reaches 90°, and the fracture is vertically distributed inside the core sample. Both the vertically distributed and the horizontally distributed isolated fractured cores have a porosity of 0.16. The permeability of vertical and horizontal isolated fracture cores is measured as 5.2 mD and 6.1 mD, respectively. The increase in porosity and permeability is still not obvious. However, the difference between the acidizing curves corresponding to the horizontally and the vertically distributed fracture begins to become obvious, as shown in **Figure 12**. Compared with the horizontal distribution of fracture, the vertical distribution of fracture simultaneously reduces the breakthrough volume of acid solution and the optimal injection rate. When the fracture is distributed horizontally, the horizontal tips of the fracture form a convergence zone and a divergence zone to attract the acid solution. The acid solution tends to penetrate the fracture through the inlet boundary and form a branch structure at the outlet boundary of the fracture, as shown in **Figure 13**. When the fracture becomes vertically distributed inside the core sample, the convergence zone and divergence zone are also formed around the fracture. Nevertheless, unlike the divergence zone formed by horizontal fracture, the divergence direction of the velocity corresponding to the vertical fracture divergence zone is consistent with the direction of core breakthrough flow. In contrast, the divergence zone formed by horizontal fracture maintains a certain angle with the direction of core breakthrough. Hence, the formation of the horizontal fracture divergence zone shows an impediment to the breakthrough of acid solution in contrast to vertically developed fracture.

CONCLUSION

Apart from the low-permeability matrix, carbonate rocks with isolated fractures are also the target reservoirs for the acidizing stimulation. In this study, the improved two-scale continuum model is used to study the acidizing process with an isolated

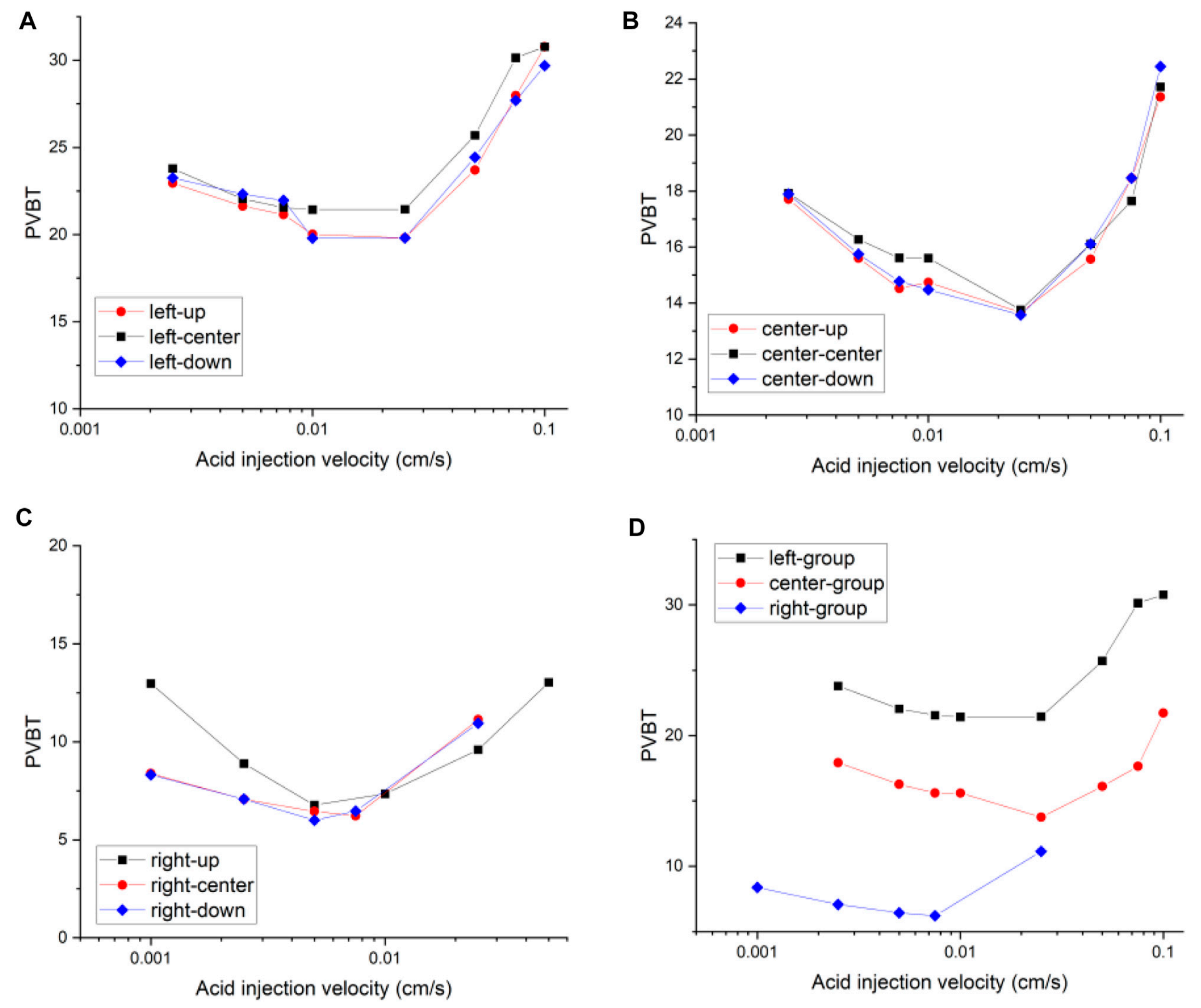

FIGURE 9 | Isolated fracture acidizing curves of pore volume to breakthrough with different locations: **(A)** left group; **(B)** center group; **(C)** right group; **(D)** group comparison.

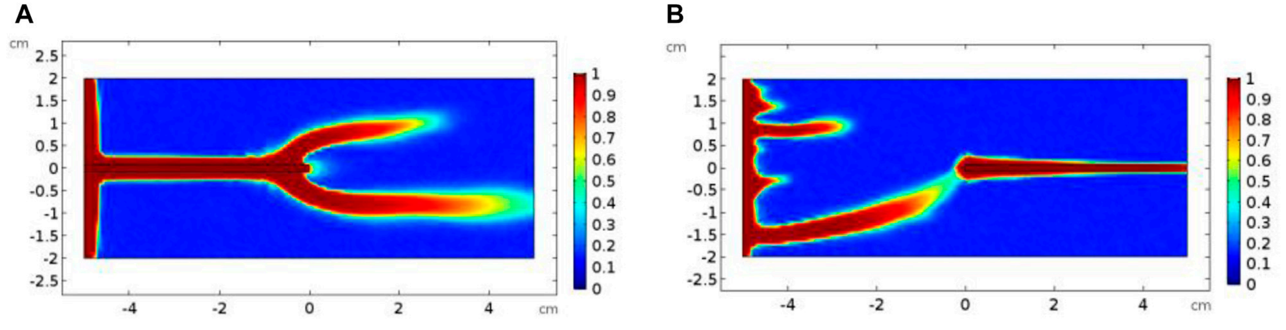

FIGURE 10 | Comparison of dissolution images of isolated fracture core samples with different positions: **(A)** left-center; **(B)** right-center.

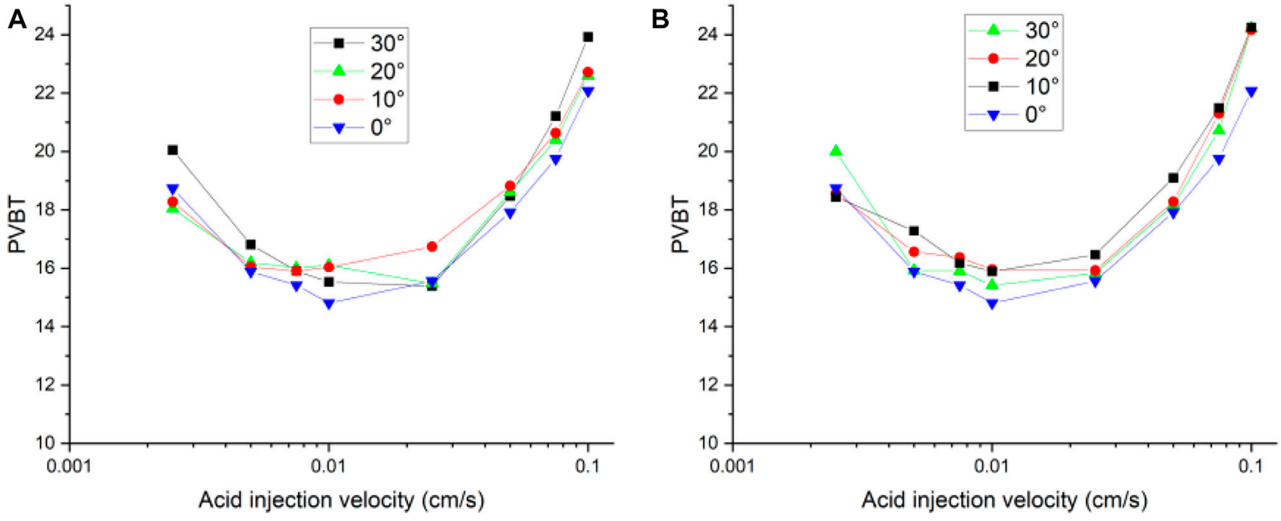

FIGURE 11 | Isolated fracture acidizing curves of pore volume to breakthrough with different angles: **(A)** clockwise; **(B)** anticlockwise.

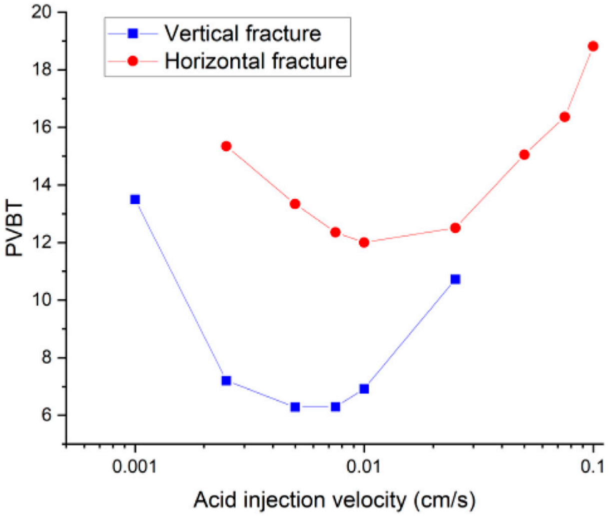

FIGURE 12 | Isolated fracture acidizing curves of pore volume to breakthrough.

fracture. Several cases are designed to present a comprehensive discussion on the isolated fracture parameters, including the isolated fracture geometry, location, and morphology. The main conclusions are summarized below:

1) Both the isolated fracture and the connected fracture have a limited influence on the core sample porosity. Only the connected fracture obviously increases the core permeability. The core sample with an isolated fracture is still the target core sample for the acidizing stimulation.
2) The isolated fracture provides an advantageous passage for the acid migration, in which the isolated fracture prevents more acid from being ineffectively consumed to dissolve the solid matrix reducing the amount of acid breakthrough.
3) Ignoring the mass exchange term still leads to an overestimated acid breakthrough volume, which is consistent with the conclusions obtained from the matrix acidizing process.
4) The existence of an isolated fracture also challenges the applicability of the Darcy equation at high injection rates.

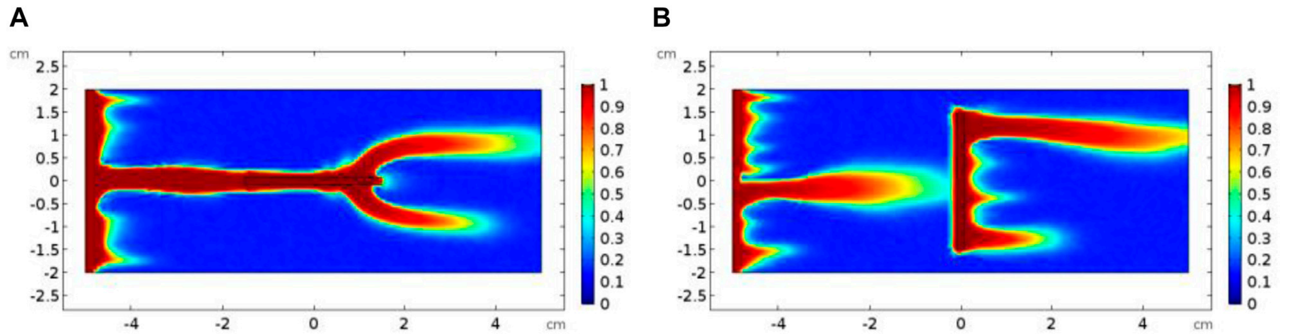

FIGURE 13 | Comparison of dissolution images of isolated fracture core samples: **(A)** horizontal fracture; **(B)** vertical fracture.

5) The isolated fracture length, aperture, and position have an obvious influence on the acidizing process. The difference of the acidizing curve corresponding to different rotation angles has not changed significantly both for clockwise rotation and anticlockwise rotation groups.

DATA AVAILABILITY STATEMENT

The original contributions presented in the study are included in the article/Supplementary Material; further inquiries can be directed to the corresponding author.

AUTHOR CONTRIBUTIONS

CJ conceptualized the study, developed the methodology, and wrote the original draft; JY supervised and reviewed and edited the study; HX and HZ helped with software support; TH: supervised the study and carried out funding acquisition.

FUNDING

The authors are grateful for the financial support from the following sources: Zhejiang Provincial Universities and Research Institutes (Grant no. 2020J00009), National Major Science and Technology Projects of China (Grant no. 52034010), National Natural Science Foundation of China (Grant no. 52004246), Natural Science Foundation of Zhejiang Province (Grant no. LQ20E040003), and Science and Technology Project of Zhoushan Bureau (Grant No. 2021C21016), China scholarship council (201906450038).

REFERENCES

Balakotaiah, V., and West, D. H. (2002). Shape Normalization and Analysis of the Mass Transfer Controlled Regime in Catalytic Monoliths. *Chem. Eng. Sci.* 57, 1269–1286. doi:10.1016/s0009-2509(02)00059-3

Dong, K. (2012). *Experimental Investigation for the Effect of the Core Length on the Optimum Acid Flux in Carbonate Acidizing*. College Station: Texas A & M University.

Dong, K., Jin, X., Zhu, D., and Hill, A. D. (2014). *The Effect of Core Dimensions on the Optimal Acid Flux in Carbonate AcidizingSPE International Symposium and Exhibition on Formation Damage Control*. Lafayette, Louisiana, USA: Society of Petroleum Engineers, 10.

Fredd, C. N., and Fogler, H. S. (1999). Optimum Conditions for Wormhole Formation in Carbonate Porous Media: Influence of Transport and Reaction. *SPE-56995-PA*. 4, 196–205. doi:10.2118/56995-pa

Furui, K., Burton, R. C. C., Burkhead, D. W. W., Abdelmalek, N. A. A., Hill, A. D. D., Zhu, D., et al. (2012). A Comprehensive Model of High-Rate Matrix-Acid Stimulation for Long Horizontal Wells in Carbonate Reservoirs: Part I-Scaling up Core-Level Acid Wormholing to Field Treatments. *SPE-56995-PA*. 17, 271–279. doi:10.2118/134265-pa

Jia, C., Huang, Z., Sepehrnoori, K., and Yao, J. (2021). Modification of Two-Scale Continuum Model and Numerical Studies for Carbonate Matrix Acidizing. *J. Pet. Sci. Eng.* 197, 107972. doi:10.1016/j.petrol.2020.107972

Jia, C., Sepehrnoori, K., Huang, Z., and Yao, J. (2021). Modeling and Analysis of Carbonate Matrix Acidizing Using a New Two-Scale Continuum Model. *SPE J.*, 1–30. doi:10.2118/205012-PA

Li, L., and Voskov, D. (2021). A Novel Hybrid Model for Multiphase Flow in Complex Multi-Scale Fractured Systems. *J. Pet. Sci. Eng.* 203, 108657. doi:10.1016/j.petrol.2021.108657

Liu, L., Huang, Z., Yao, J., Di, Y., and Wu, Y.-S. (2020). An Efficient Hybrid Model for 3D Complex Fractured Vuggy Reservoir Simulation. *SPE J.* 25, 907–924. doi:10.2118/199899-pa

Liu, P., Li, J., Sun, S., Yao, J., and Zhang, K. (2021). Numerical Investigation of Carbonate Acidizing with Gelled Acid Using a Coupled thermal-hydrologic-chemical Model. *Int. J. Therm. Sci.* 160, 106700. doi:10.1016/j.ijthermalsci.2020.106700

Liu, P., Yao, J., Couples, G. D., Huang, Z., Sun, H., and Ma, J. (2017). Numerical Modelling and Analysis of Reactive Flow and Wormhole Formation in Fractured Carbonate Rocks. *Chem. Eng. Sci.* 172, 143–157. doi:10.1016/j.ces.2017.06.027

Maheshwari, P., Maxey, J., and Balakotaiah, V. (2016). Reactive-Dissolution Modeling and Experimental Comparison of Wormhole Formation in Carbonates with Gelled and Emulsified Acids. *SPE-191148-PA*. 31, 103–119. doi:10.2118/171731-pa

Maheshwari, P., Ratnakar, R. R., Kalia, N., and Balakotaiah, V. (2013). 3-D Simulation and Analysis of Reactive Dissolution and Wormhole Formation in Carbonate Rocks. *Chem. Eng. Sci.* 90, 258–274. doi:10.1016/j.ces.2012.12.032

Meyer, B. R., and Bazan, L. W. (2011). *A Discrete Fracture Network Model for Hydraulically Induced Fractures—Theory, Parametric and Case Studies. SPE Hydraulic Fracturing Technology Conference*. The Woodlands: The Society of Petroleum Engineers (SPE). doi:10.2118/140514-ms

Moreno, L., Tsang, Y. W., Tsang, C. F., Hale, F. V., and Neretnieks, I. (1988). Flow and Tracer Transport in a Single Fracture: A Stochastic Model and its Relation to Some Field Observations. *Water Resour. Res.* 24, 2033–2048. doi:10.1029/wr024i012p02033

Muralidhar, K. (1990). Flow and Transport in Single Rock Fractures. *J. Fluid Mech.* 215, 481–502. doi:10.1017/s0022112090002725

Neuzil, C. E., and Tracy, J. V. (1981). Flow through Fractures. *Water Resour. Res.* 17, 191–199. doi:10.1029/wr017i001p00191

Palharini Schwalbert, M., Hill, A. D., and Zhu, D. (2019). *A New Up-Scaled Wormhole Model Grounded on Experimental Results and in 2-Scale Continuum SimulationsSPE International Conference on Oilfield Chemistry*. Galveston, Texas, USA: Society of Petroleum Engineers, 30.

Panga, M. K. R., Ziauddin, M., and Balakotaiah, V. (2005). Two-scale Continuum Model for Simulation of Wormholes in Carbonate Acidization. *Aiche J.* 51, 3231–3248. doi:10.1002/aic.10574

Sarmah, A., Farid Ibrahim, A., Nasr-El-Din, H., and Jackson, J. (2020). A New Cationic Polymer System that Improves Acid Diversion in Heterogeneous Carbonate Reservoirs. *PE J.* 25 (05), 2281–2295. doi:10.2118/194647-pa

Snow, D. T. (1969). Anisotropie Permeability of Fractured media. *Water Resour. Res.* 5, 1273–1289. doi:10.1029/wr005i006p01273

Tansey, J., and Balhoff, M. T. (2016). Pore Network Modeling of Reactive Transport and Dissolution in Porous media. *Transp Porous Med.* 113, 303–327. doi:10.1007/s11242-016-0695-x

Tansey, J. (2014). *Pore-Network Modeling of Carbonate Acidization, SPE Annual Technical Conference and Exhibition*. Amsterdam, Netherlands: Society of Petroleum Engineers, 10.

Tsang, Y. W., and Tsang, C. F. (1989). Flow Channeling in a Single Fracture as a Two-Dimensional Strongly Heterogeneous Permeable Medium. *Water Resour. Res.* 25, 2076–2080. doi:10.1029/wr025i009p02076

Tsang, Y. W., and Witherspoon, P. A. (1981). Hydromechanical Behavior of a Deformable Rock Fracture Subject to normal Stress. *J. Geophys. Res.* 86, 9287–9298. doi:10.1029/jb086ib10p09287

Wadekar, S., and Pandya, N. (2014). *Use of Emulsified Acid System with Corrosion Protection up to 350°F, SPE Saudi Arabia Section Technical Symposium and Exhibition*. Al-KhobarSaudi Arabia: Society of Petroleum Engineers, 6.

Wei, W., Varavei, A., Sanaei, A., and Sepehrnoori, K. (2019). Geochemical Modeling of Wormhole Propagation in Carbonate Acidizing Considering Mineralogy Heterogeneity. *SPE-65400-PA*. 24, 2163–2181. doi:10.2118/195593-pa

Wu, Y.-S. (2015). *Multiphase Fluid Flow in Porous and Fractured Reservoirs*. Houston: Gulf Professional Publishing.

Zakaria, A. S., and Nasr-El-Din, H. A. (2016). A Novel Polymer-Assisted Emulsified-Acid System Improves the Efficiency of Carbonate Matrix Acidizing. *SPE-56995-PA* 21, 1061–1074. doi:10.2118/173711-pa

Zhao, J., Kang, Q., Yao, J., Viswanathan, H., Pawar, R., Zhang, L., et al. (2018). The Effect of Wettability Heterogeneity on Relative Permeability of Two-Phase Flow in Porous Media: A Lattice Boltzmann Study. *Water Resour. Res.* 54, 1295–1311. doi:10.1002/2017wr021443

Zhao, J., Qin, F., Derome, D., and Carmeliet, J. (2020). Simulation of Quasi-Static Drainage Displacement in Porous media on Pore-Scale: Coupling Lattice Boltzmann Method and Pore Network Model. *J. Hydrol.* 588, 125080. doi:10.1016/j.jhydrol.2020.125080

Zimmerman, R. W., Chen, D.-W., and Cook, N. G. W. (1992). The Effect of Contact Area on the Permeability of Fractures. *J. Hydrol.* 139, 79–96. doi:10.1016/0022-1694(92)90196-3

Zimmerman, R. W., Kumar, S., and Bodvarsson, G. S. (1991). Lubrication Theory Analysis of the Permeability of Rough-Walled Fractures, International Journal of Rock Mechanics and Mining Sciences & Geomechanics Abstracts. *Elsevier*. 28, 325–331. doi:10.1016/0148-9062(91)90597-f

Conflict of Interest: The authors declare that the research was conducted in the absence of any commercial or financial relationships that could be construed as a potential conflict of interest.

frontiers
in Earth Science

ORIGINAL RESEARCH
published: 30 July 2021
doi: 10.3389/feart.2021.712566

Numerical Studies and Analyses on the Acidizing Process in Vug Carbonate Rocks

*Cunqi Jia[1,2], Kamy Sepehrnoori[2], Haiyang Zhang[3] and Jun Yao[1]**

[1]School of Petroleum Engineering, China University of Petroleum (East China), Qingdao, China, [2]Hildebrand Department of Petroleum and Geosystems Engineering, The University of Texas at Austin, Austin, TX, United States, [3]Petroleum Department, Khalifa University, Abu Dhabi, United Arab Emirates

A vug porosity system, in addition to a matrix, is also the target rocks for the acidizing. In this work, the acidizing process in two typical core-scale separate-vug porosity systems is studied in detail. Numerous cases are conducted to discuss a parametric study on the acidizing process and hydraulic behavior. Results indicate that the presence of vug reduces the pore volume of acid solution consumed to achieve a breakthrough, which is consistent with experimental observations. Increasing the vug diameter and porosity decreases pore volume to breakthrough both for a vugular carbonate rock and isolated vug carbonate rock. In comparison, the acid mass does not change a lot. Typical dissolution patterns can also be observed in the acidizing process when a vug exists. Compared to matrix dissolution patterns, the presence of vug induces wormhole to pass through the vug region.

Keywords: two-scale continuum model, carbonate acidizing, vug carbonate reservoir, reactive flow in porous media, carbonate reservoirs

Edited by:
Zhiyuan Wang,
China University of Petroleum
(Huadong), China

Reviewed by:
Mingzheng Yang,
Louisiana State University,
United States
Youwei He,
Southwest Petroleum University,
China

Correspondence:
Jun Yao
upc_cmfpm@126.com

Specialty section:
This article was submitted to
Earth and Planetary Materials,
a section of the journal
Frontiers in Earth Science

Received: *26 May 2021*
Accepted: *29 June 2021*
Published: *30 July 2021*

Citation:
Jia C, Sepehrnoori K, Zhang H and Yao J (2021) Numerical Studies and Analyses on the Acidizing Process in Vug Carbonate Rocks.
Front. Earth Sci. 9:712566.
doi: 10.3389/feart.2021.712566

INTRODUCTION

Reactive flow in porous media plays an essential role in various physical, chemical, and biological processes in nature and has many applications (Fredd and Scott Fogler, 1998; Acharya et al., 2007; Li et al., 2008; Bijeljic et al., 2013; Nick et al., 2013; Menke et al., 2015; Li et al., 2018). This work is conducted to study the carbonate acidizing process in vug carbonate rocks.

Before, lots of studies have been conducted to study the carbonate matrix acidizing process. Both experimental (Bernadiner et al., 1992; Wang et al., 1993; Frick et al., 1994; Fredd and Fogler, 1999; Izgec et al., 2008; Furui et al., 2012a; Furui et al., 2012b; Dong, 2012; Aidagulov et al., 2018; Qiu et al., 2018) and numerical (Kanaka and Panga, 2003; Panga et al., 2005; Kalia and Balakotaiah, 2007; Kalia and Balakotaiah, 2009; Maheshwari et al., 2013; Maheshwari et al., 2016b; Liu et al., 2019) results show that an optimum acid injection rate widely exists, at which the minimum amount of acid solution is consumed to achieve a breakthrough (Jia et al., 2021). Meanwhile, different dissolution patterns (Hoefner and Fogler, 1989; Fredd and Fogler, 1998; Fredd and Fogler, 1999; Huang et al., 2000; Izgec et al., 2008; Aidagulov et al., 2018) can also be observed through visualization techniques at different acid injection velocities. Apart from the matrix, vug is also a widespread presence in carbonate rocks, which is a void space in the reservoir rock and provides the main storage space for reserves (Kossack and Gurpinar, 2001; Wang et al., 2016; Yue et al., 2018). According to the vug interconnection, a vuggy pore space can be divided into the separate-vug porosity system and toughing-vug porosity system (Nair et al., 2008). Because of complex porosity systems, a flow behavior is more complicated in vug carbonate rocks (Sadeghnejad and Gostick, 2020). In the toughing-vug porosity system, a vug is usually associated with fabric dissolution and karst process (Lucia, 2007), in which an interconnected pore system forms and has a much larger permeability (Zhang et al., 2005) of average 10^3–10^6 times more than that of the disconnected vug system (Kossack and Gurpinar, 2001). For a separate-vug porosity system, the addition of vug only increases the total porosity but has no significant contribution for the core permeability (Zhang et al., 2005). Such rocks are also the target reservoirs for the acidizing stimulation. However, a few studies have been performed to study the acidizing process in the separate-vug porosity system. For an experimental study, Izgec et al. (2008) have shown that the presence of vug does affect the acidizing process for calcite rocks. The pore volumes to breakthrough decreases with the increase of the vuggy fraction. Furthermore, Izgec et al. (2009) also developed a two-scale continuum model to simulate the acidizing process in the separate-vug porosity system, in which vuggy carbonates are divided into two distinct regions of the matrix region and the vuggy region. The Darcy equation is used in the matrix region, and the Stokes equation is used to account for the fluid flow in the vug (free flow) region. However, it is worth noting that when most of the matrix is dissolved, compared to the damping effect of porous media, the fluid phase viscous dissipation becomes dominant and cannot be ignored anymore. In such cases, the Darcy equation is not applicable any longer. Also, Izgec's model neglects mass exchange between solid and liquid phases. Hence, a more accurate mathematical model is still needed to study the acidizing process in the separate-vug porosity system.

In this work, the Stokes–Darcy equation is used to describe the fluid flow instead of the Darcy equation, and a source term is added to the fluid mass conservation equation for considering the dissolution mass term from the solid phase to the fluid phase. A detailed explanation of the two-scale continuum model is given in the next section. In the third section, numerous cases are conducted to discuss a comprehensive parametric study on the acidizing process, including acid injection velocity, acid injection concentration, vug filling degrees, vug diameter, and matrix porosity heterogeneity.

MODEL DEVELOPMENT

Reaction and Kinetics

In this study, a solid mineral is supposed to only containing calcite ($CaCO_3$) (Alkhaldi et al., 2010; Maheshwari et al., 2016a; Mahrous et al., 2017). For simplicity, an overall chemical reaction equation is adapted to represent the acid consumption and calcite dissolution, which is given below:

$$2HCl + CaCO_3 \rightarrow CaCl_2 + H_2CO_3. \tag{1}$$

Calcite ($CaCO_3$) and hydrochloric acid (HCl) react to form calcium chloride ($CaCl_2$) and carbonic acid (H_2CO_3). The surface reaction rate is dependent on the concentration by the power law expression:

$$R_{HCl} = k_s c_{HCl,s}^n, \tag{2}$$

where R_{HCl} is the acid reaction rate, k_s is the acid reaction rate at the solid surface, n is the reaction order, and $c_{HCl,s}$ is the surface acid concentration. The reaction rate of other components can be further determined according to **Eq. 1**.

Governing Equations

Modeling and numerical simulation of vuggy carbonate reservoirs is still challenging because of vug's presence (Popov et al., 2009). The modeling of vuggy media is traditionally done based on the multiple-continuum concept model. In this model, the matrix and vug are assumed to have uniform and homogeneous properties, and the intercommunication flow between the matrix region and the vug region is at a pseudo-steady state (Kang et al., 2006; Wu et al., 2007). The continuum approaches behave pretty well in vug well-developed reservoirs, but the challenging part of this mode is that it is hard to determine accurate rock properties such as porosity and permeability (Yao et al., 2010). Another popular approach is based on the coupled Stokes and Darcy equations, in which the Darcy equation is only used in the porous region, and the Stokes equation is used in the free-flow region. Moreover, at the interface between the porous and free-flow regions, the additional boundary condition is employed to guarantee continuity of mass and momentum across the interface (Izgec et al., 2009; Yao et al., 2010). However, it is still very complicated and less practical to apply the coupled Darcy–Stokes approach to vuggy reservoirs. Because, on the one hand, the interface condition also introduces additional parameters such as material property, α_{BJ}, in Beavers–Joseph–Saffman (BJS) condition (Beavers and Joseph, 1967; Saffman, 1971), which needs to be further determined numerically or experimentally. On the other hand, the Stokes equation used in the free-flow region can only handle the vug region free of any obstacles (Popov et al., 2009). The limitation of the coupled Darcy and Stokes approach can be overcome by using the Stokes–Brinkman equation, which uses a single equation rather than coupled equations to describe the fluid flow in entire vuggy reservoirs and avoids explicit modeling of the interface (Popov et al., 2009; De Oliveira et al., 2012; Fadlelmula F et al., 2016). In this work, a new two-scale continuum model is inspired by the Stokes–Brinkman equation. The Stokes–Darcy equation is employed to predict the momentum transport behavior of the fluid phase. The equation is given below:

$$0 = -\nabla p + \nabla \cdot \left(\mu \left(\nabla \frac{\mathbf{u}}{\phi} + \left(\nabla \frac{\mathbf{u}}{\phi} \right)^T \right) \right) - \frac{\mu}{k} \mathbf{u}, \tag{3}$$

where ϕ is the porosity, ρ_{fluid} is the density of fluid phase, $\mathbf{u} = \begin{bmatrix} u & v \end{bmatrix}^T$ is the superficial velocity, k is the permeability, μ is the viscosity, and p is the fluid pressure. The equation can represent all regions during the acidizing process. For example, in an undissolved matrix region with a low permeability, the damping effect of the solid structure is relatively significant, which is represented by the last term in **Eq. 3**. Moreover, in wormhole and vug regions, the influence of solid skeleton is gradually diminishing with a large permeability, and the viscous dissipation of fluid behaves dominantly, which can be considered by the viscous term in **Eq. 3**.

Then we continue to develop the mass conservation equations. According to **Equation 1**, the fluid phase consists of water (H_2O), acid (HCl), calcium chloride ($CaCl_2$), and carbonic acid (H_2CO_3). And the acid component (HCl) is chosen as the main component. The matrix only contains calcite ($CaCO_3$). Therefore, the governing equations for the fluid phase, acid solution, and calcite are independently developed by (Jia et al., 2021), which is as follows:

$$\frac{\partial}{\partial t}\left(\phi\rho_{fluid}\right) = -\nabla\cdot\left(\rho_{fluid}\mathbf{u}\right) + s\left(\frac{M_{CaCl_2}}{2}+\frac{M_{H_2CO_3}}{2}-M_{HCL}\right)R_{HCl}, \tag{4}$$

$$\frac{\partial}{\partial t}\left(\phi c_{HCl}\right) = -\nabla\cdot\left(\mathbf{D}_{HCL}\cdot\nabla c_{HCl} + c_{HCl}\mathbf{u}\right) - sR_{HCl}, \tag{5}$$

$$\frac{\partial}{\partial t}\left(\left(1-\phi\right)\rho_{CaCO_3}\right) = -s\frac{M_{CaCO_3}}{2}R_{HCl}\left(c_{HCl,s}\right), \tag{6}$$

where s stands for the specific surface area; M_{HCL}, M_{CaCl_2}, $M_{H_2CO_3}$, and M_{CaCO_3} are the component for HCl, $CaCl_2$, H_2CO_3, and $CaCO_3$, respectively; c_{HCl} is the acid concentration in the bulk phase; $\mathbf{D}_{HCL}$ is the acid diffusion coefficient, determined as $\mathbf{D}_{HCL} = \phi D_m\mathbf{I}$; $\mathbf{I}$ is the unit tensor; D_m is the molecular diffusion rate; and ρ_{CaCO_3} is the matrix density. The main difference between the conventional two-scale continuum model (Panga et al., 2005; Kalia, 2008) and the model used in this study is reflected in the last term in **Eq. 4**, which represents a source term to the fluid mass conservation equation for considering the dissolution mass term from the solid phase to the fluid phase. Almost all of the previous numerical studies neglect it. The acid reaction rate (R_{HCl}) is further determined as follows:

$$R_{HCl} = k_s c_{HCl,s}^{n} = k_c\left(c_{HCl} - c_{HCl,s}\right), \tag{7}$$

where k_c is the mass transfer rate, and it is quantified by a model derived by Balakotaiah (Balakotaiah and West, 2002)

$$Sh = \frac{2k_c r}{D_m} = Sh_\infty + 0.7\mathrm{Re}_p^{\frac{1}{2}}Sc^{\frac{1}{3}}, \tag{8}$$

where Sh is the Sherwood number, Sh_∞ is the asymptotic Sherwood number, the value used in this work is 3.66 for a circular pore structure, Re_p is defined as $\mathrm{Re}_p = 2|\mathbf{u}|r/\nu$, ν is defined by $\nu = \mu/\rho_{liquid}$, and Sc is the Schmidt number defined by $Sc = \nu/D_m$. The modified Carman–Kozeny equations are used to determine the changes of core parameters (Edery et al., 2011; Jia et al., 2021) which is given as follows:

$$\frac{k}{k_0} = \left(\frac{\phi}{\phi_0}\right)^{\gamma}\left(\frac{\phi\left(1-\phi_0\right)}{\phi_0\left(1-\phi\right)}\right)^{2\beta}, \tag{9}$$

$$\frac{r}{r_0} = \left(\frac{\phi\left(1-\phi_0\right)}{\phi_0\left(1-\phi\right)}\right)^{\alpha}, \tag{10}$$

$$\frac{s}{s_0} = \left(\frac{\phi}{\phi_0}\right)\left(\frac{\phi\left(1-\phi_0\right)}{\phi_0\left(1-\phi\right)}\right)^{-\alpha}, \tag{11}$$

where γ, α, and β are the parameters describing pore connectivity and broadening structure, and ϕ_0, k_0, r_0, and s_0 are the initial porosity, permeability, pore diameter, and specific surface area, respectively.

Boundary and Initial Conditions

The calculation domain is selected as a 2D cross section of a cylindrical core with 4 cm diameter and 10 cm height. The boundary and initial conditions refer to the core flooding experiments (Izgec et al., 2008). Acid is injected at a constant velocity and concentration from one side of the core sample. The acid injection concentration is identical to the value, 15%, used in the experimental study. Constant pressure is held on the other core sample side. Because in the experiment process, the core sample is always surrounded by a high confining pressure to avoid the acid solution going through the gap between the core sample and the core holder plug. Initially, the core sample is saturated with water, and matrix porosity has a value of 0.15. Matrix permeability is assumed isotropic and has a value of 5 mD. Furthermore, a uniform distribution random function creates a heterogeneous distribution of porosity (Maheshwari et al., 2016a; Wei et al., 2017). Boundary and initial conditions are summarized below:

$$-\mathbf{n}\cdot\mathbf{u} = u_0 \ \text{ at } \ x = 0, \tag{12}$$

$$-\mathbf{n}\cdot\left(\mathbf{u}c_{HCl} + D_{HCl}\nabla c_{HCl}\right) = u_0 c_0 \ \text{ at } \ x = 0, \tag{13}$$

$$p = p_e \ \text{ at } \ x = L, \tag{14}$$

$$\mathbf{n}\cdot D_{HCl}\nabla c_{HCl} = 0 \ \text{ at } \ x = L, \tag{15}$$

$$\mathbf{n}\cdot\overline{\mathbf{v}} = 0, \mathbf{n}\cdot\left(\mathbf{u}c_{HCl} + D_{HCl}\nabla c_{HCl}\right) = 0 \ \text{ on transverse boundaries}, \tag{16}$$

$$c_{HCl} = 0, \phi = \phi_0 + \Delta\phi_0 \text{ at } t = 0, \tag{17}$$

where $\mathbf{n}$ is the boundary unit direction vector, u_0 is the injection velocity, c_0 is the injection concentration, p_e is the pressure at the core outside, and $\Delta\phi_0$ is the initial heterogeneity magnitude of porosity.

RESULTS AND DISCUSSIONS

The separate-vug porosity system covers a wide range of structures from millimeters to meters in the diameter (Arns et al., 2005; Sok et al., 2010; Mousavi et al., 2012; Sadeghnejad and Gostick, 2020). This study is concerned with two typical core-scale separate-vug porosity systems: the vugular carbonate rock and the isolated vug carbonate rock, as shown in **Figure 1**. For numerical studies, vug in vugular carbonate rock is supposed uniformly embedded in the matrix region, and each vug initially has a diameter of 3 mm (Casar-Gonzalez and Suro-Perez, 2000; Izgec et al., 2010). Moreover, for the isolated vug carbonate rock, vug has a centimeter diameter, 1.5 cm (Zhang et al., 2004; Casar-Gonzalez and Suro-Perez, 2000). For a separate-vug porosity system, the addition of vug only contributes to the increasing storage space. The acid breakthrough condition is still consistent with matrix acidizing, determined by a 100 times increase of the core average permeability (De Oliveira et al., 2012). The pore

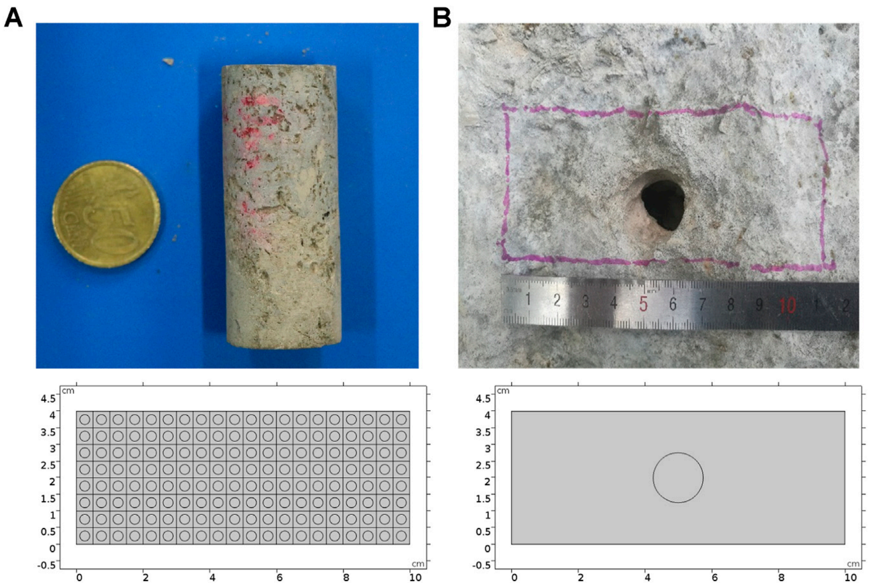

FIGURE 1 | Two typical core-scale separate-vug porosity systems: **(A)** vugular carbonate rock and **(B)** isolated vug carbonate rock.

TABLE 1 | Comparison of PVBT values of different two-scale continuum models.

Acid injection velocity (cm/s)	PVBT of the current model	PVBT of the previous model
1.00E+00	88.00	88.00
5.00E-01	54.00	54.00
1.00E-02	16.36	17.76

volume at a breakthrough condition is counted and normalized with the sample initial pore volume as an evaluation parameter cited as pore volume to breakthrough (PVBT) (Jia et al., 2021). Besides, acid breakthrough injection mass (AMBT) is also collected in this work because PVBT is simultaneously a function of porosity.

Model Comparison and Validation

The two-scale continuum model is widely accepted and used to describe the core scale stimulation process (Kalia and Balakotaiah, 2007; Liu et al., 2017; Maheshwari et al., 2013). The Darcy equation is usually employed to determine the superficial velocity of the fluid phase. In this study, the Stokes–Darcy equation, as shown in **Eq. 3**, is employed to predict the fluid phase momentum transport behavior. When the acid solution acquires a very high injection rate, the core sample is uniformly dissolved by acid and still keeps the characteristic of porous media because of no existence of a wormhole. At this time, the Darcy equation can still be applicable. The acid breakthrough consumption volume calculated based on the Darcy equation has little difference from the value of PVBT calculated based on the Stokes–Darcy equation (Jia et al., 2021). Thus, the model can be validated by comparing PVBT values with the previous two-scale continuum model with high acid injection velocities. **Table 1** shows the values of PVBT separately calculated by the current and previous two-scale continuum models with high acid injection velocities. The results show that the difference of PVBT values between the current and previous two-scale continuum model is not noticeable when acid acquires a very high injection rate. **Figure 2** further compares dissolution images of current and previous two-scale continuum models with very high acid injection velocities. The current two-scale continuum model is well validated.

Effect of Acid Injection Velocity

This section studies the effect of the acid injection rate on the acidizing process of the vugular carbonate rock and the isolated vug carbonate rock. The porosity of the vug region is initially set as a high value of 0.99. The whole sample porosity is calculated as 0.3875 for vugular carbonate rock and 0.1871 for isolated vug carbonate rock. The whole sample mean permeability of the vugular carbonate rock and the isolated vug carbonate rock is measured as 10 and 6.6 mD, respectively. In comparison, the permeability of the matrix zone is 5 mD. The results show that the existence of vug in the vugular carbonate rock and the isolated vug carbonate rock does provide more storage space but has a little contribution to hydraulic conductivity for the matrix core sample.

Figure 3 shows the acidizing results of vugular carbonate rock. It can be observed from **Figure 3A** that the pore volume to breakthrough (PVBT) of vugular carbonate rock is less than the PVBT of matrix carbonate rock. The same change trend of the PVBT is also observed in the experimental study (Izgec et al., 2008). The acid mass to breakthrough (AMBT) change of the vugular carbonate rock and the matrix carbonate rock is not apparent compared to the change of the PVBT. The AMBT value

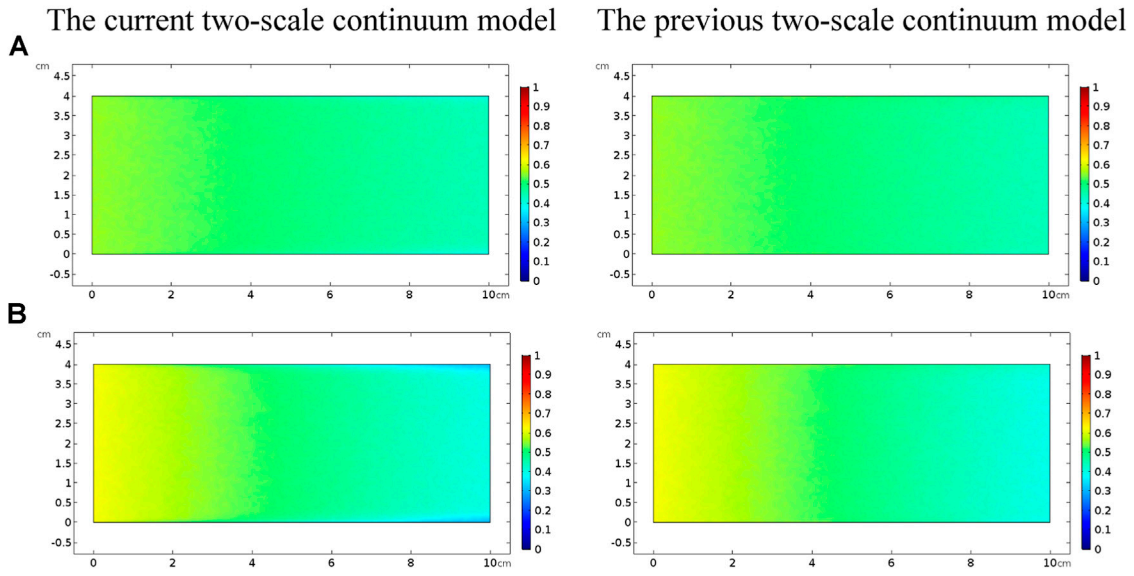

FIGURE 2 | Comparison of dissolution images between the current and previous two-scale continuum model with high injection rates: **(A)** 1 cm/s and **(B)** 0.5 cm/s.

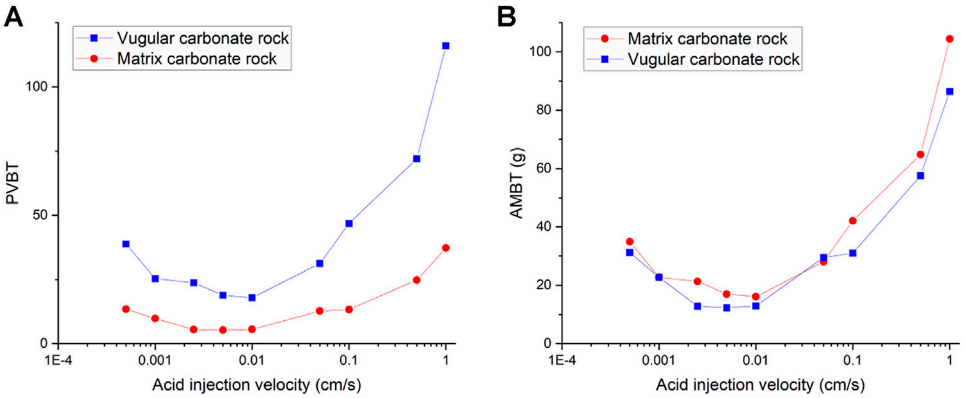

FIGURE 3 | Effect of the acid injection rate on acidizing curves of the vugular carbonate rock: **(A)** PVBT and **(B)** AMBT.

of vugular carbonate rock is slightly lower than the AMBT value of matrix carbonate rock. However, in general, the AMBT values of the vugular carbonate rock and matrix carbonate rock are very close, as shown in **Figure 3B**. **Figure 4** compares the dissolution patterns of the vugular carbonate rock and the matrix carbonate rock with different acid injection velocities. Typical dissolution patterns, including uniform, ramified wormhole, wormhole, and conical wormhole dissolution patterns (Jia et al., 2021), are also observed in the acidizing process of vugular carbonate rock. Compared to dissolution patterns of matrix carbonate rock, vug presence induces wormhole to pass through the vug region. Besides, more wormholes can be stimulated due to vug existence with a high acid injection rate, as shown in **Figure 4B**. Also, because of the existence of vug, less acid is used to dissolve the solid matrix. The apparent difference in pore volume to breakthrough is mainly caused by the vug increasing initial pore volume. Furthermore, according to the definition of PVBT, a higher initial pore volume leads to lower PVBT.

Figure 5 and **Figure 6** compare acidizing curves and dissolution patterns of the isolated vug carbonate rock and matrix carbonate rock, respectively. Similar conclusions can also be observed with the vugular carbonate rock. Because the presence of isolated vug is increasing the initial pore volume, the PVBT of isolated vug carbonate rock is higher than the PVBT of matrix carbonate rock, which is also consistent with the experimental observation (Izgec et al., 2008). Four typical dissolution patterns can also be observed in the acidizing process of the isolated vug carbonate rock, as shown in **Figure 6**. The induction effect of isolated vug on wormhole growth is more intuitive for the isolated vug

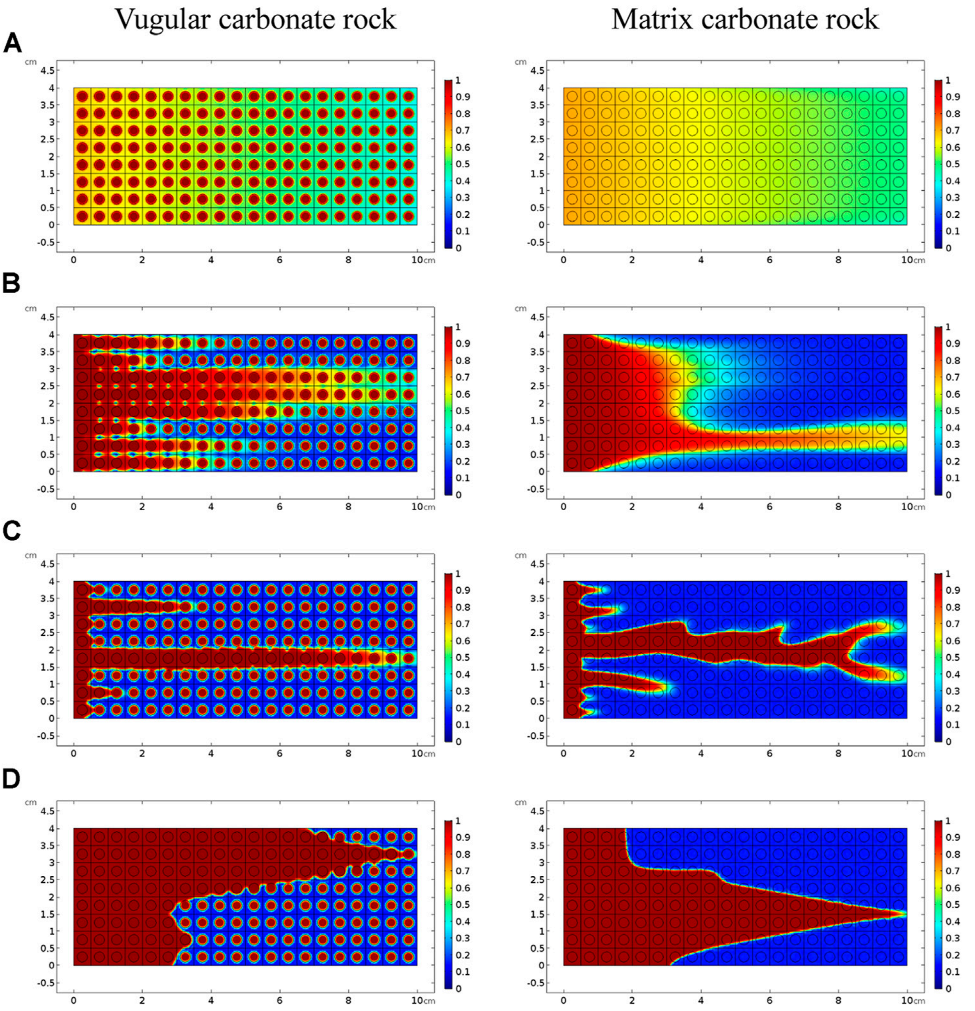

FIGURE 4 | Comparison of dissolution patterns with different acid injection velocities: **(A)** 0.5 cm/s, **(B)** 0.05 cm/s, **(C)** 0.005 cm/s, and **(D)** 0.0005 cm/s.

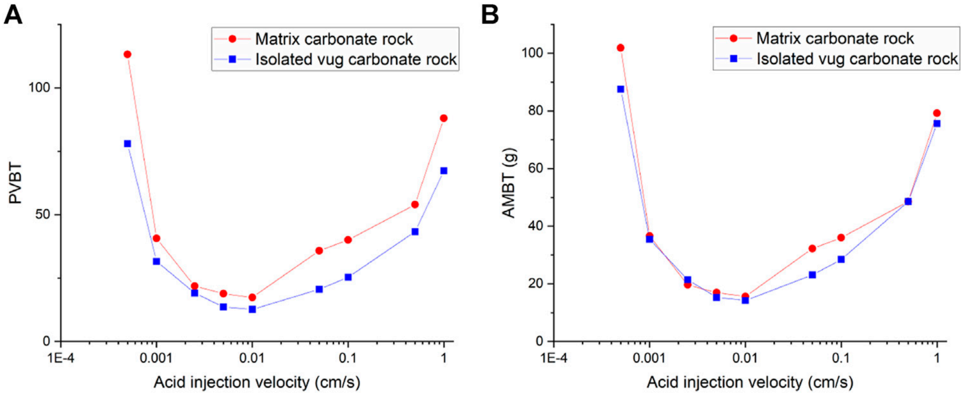

FIGURE 5 | Effect of the acid injection rate on acidizing curves of the isolated vug carbonate rock: **(A)** PVBT and **(B)** AMBT.

carbonate rock. The main wormhole has a trend to close to and go through isolated vug. The main wormhole grows in a single direction for the matrix carbonate rock without any turning trend. The difference of the AMBT between the isolated vug carbonate rock and matrix carbonate rock is still not noticeable.

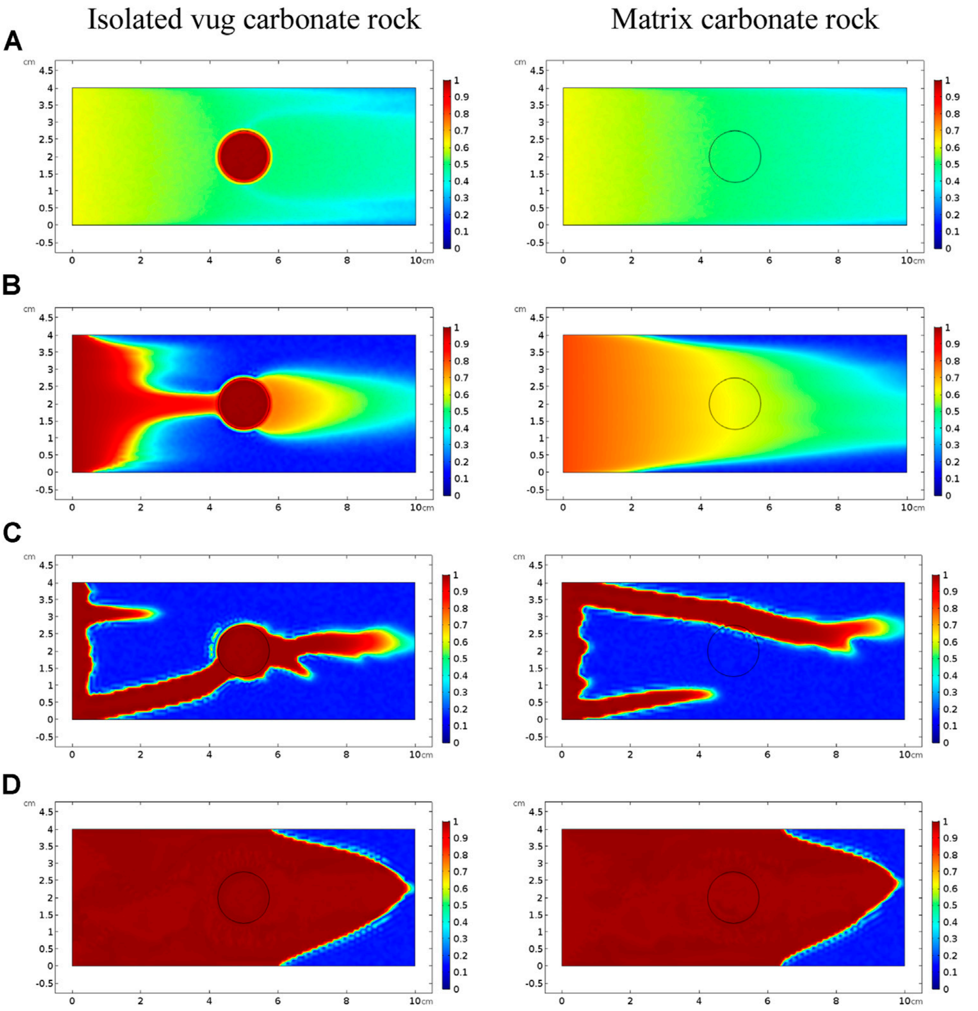

FIGURE 6 | Comparison of dissolution patterns with different acid injection velocities: **(A)** 0.5 cm/s, **(B)** 0.05 cm/s, **(C)** 0.005 cm/s, and **(D)** 0.0005 cm/s.

Effect of Acid Injection Concentration

Acid injection concentration is also significant for the practical acidizing application. Initially, Fredd and Fogler (1999) adopted the concentration of 2% in core-flooding experiments. The concentration of 15% is widely used in the subsequent experimental studies (Furui et al., 2012a; Dong et al., 2014; Aidagulov et al., 2018; Kumar et al., 2020). Wang et al. (1993) ever used different concentrations such as 0.5, 3.4, and 15% to experimentally study the influence of acid injection concentration on the acidizing results. The results indicate that increasing acid injection concentration decreases the PVBT, while the optimum injection rate change is not apparent.

Figure 7 numerically calculates the acidizing curves with acid injection concentration changing from 5 to 25%. It can be found that when the acid injection concentration increases from 5 to 25%, PVBT values shows a pronounced decrease both for the vugular carbonate rock and isolated vug carbonate rock, which is consistent with experimental studies conducted by Wang et al. (1993) and numerical studies of matrix acidizing presented by Jia et al. (2020a). Besides, acid mass to breakthrough (AMBT) is also compared with different acid injection concentrations. Because it is very important to note that when we are studying the influence of acid injection concentration on acidizing results, the amount of acid solute and acid solvent are both changing. The change of PVTB reflects more information on the amount of acid solute (Fredd and Fogler, 1999; Panga et al., 2005). Few studies before noticed and discussed the change of acid solvent mass. **Figure 7** shows that compared to the apparent change of PVBT, the amount of acid mass required to breakthrough does not change apparently with increasing acid injection concentration. Hence, the amount of solute in the acid system has an apparent relationship with the acid injection concentration, but the solvent required to achieve a breakthrough has a less obvious influence.

Effect of Vug Porosity

The filling phenomenon is widespread in vug carbonate rocks. It is affected by multiple factors, such as mechanical deposition, collapsed deposition, chemical deposition, and so on, which eventually leads to the vug with different porosities (Li, 2017).

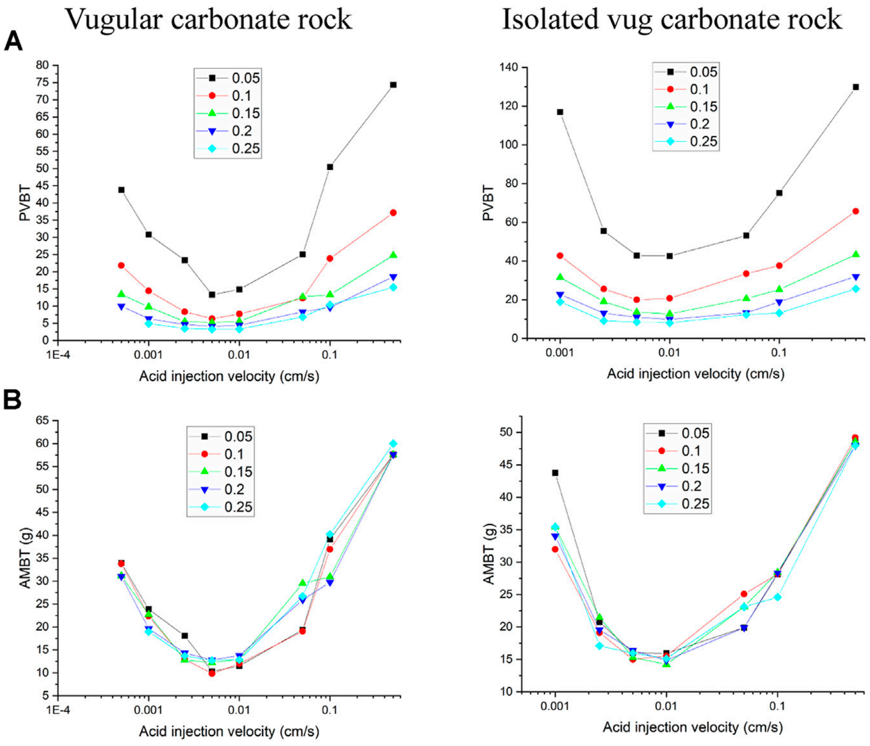

FIGURE 7 | Effect of acid injection concentration on the acidizing results: **(A)** pore volume to breakthrough (PVBT) and **(B)** acid mass to breakthrough (AMBT).

This section studies the influence of vug porosity on the acidizing process of vugular carbonate rock and isolated vug carbonate rock. **Figure 8** summarizes the change of core porosity and permeability, with the vug porosity varying from 15 to 99% considering different degrees of filling. The results show that both core porosity and permeability increase as the vug porosity increases. For the vugular carbonate rock, compared to the change of core porosity increasing from 15 to 40%, the change of core permeability is limited, increasing from 5 to 10 mD. The increase of core porosity and permeability in isolated vug carbonate rock is not apparent. Core porosity increases from 15 to 19%, and core permeability increases from 5 to 5.6 mD. **Figure 9** further compares the acidizing results with different vug porosities from the low filling degree with vug porosity of 15% to the high filling degree with vug porosity of 99%. The results show that vug porosity mainly has a noticeable influence on the pore volume to breakthrough. Higher vug porosity results in a lower value of the PVBT. However, the difference of acid injection mass consumed to achieve breakthrough between different vug porosities is still not apparent.

Effect of Vug Diameter

This section studies the influence of vug diameter on the acidizing performance of vugular carbonate rock and isolated vug carbonate rock. Here, we suppose that for the vugular carbonate rock, the diameter of vug has the magnitude of a millimeter (Casar-Gonzalez and Suro-Perez, 2000; Ramakrishnan et al., 2001; Sok et al., 2010; Mousavi et al., 2012). **Figure 10** shows core porosity and permeability with a vug diameter varying from 0.5 to 3.5 mm. It can be observed that when the vug diameter reaches 3.5 mm, core permeability is different from core permeability of other core samples with a vug diameter less than 3.5 mm. Besides, core porosity with a vug diameter of 3.5 mm reaches 47.33%. Hence, the final vug diameter below 3.5 mm is determined as the threshold diameter for the acidizing stimulation for the vugular carbonate rock. Then, we study the effect of isolated vug diameter on the acidizing process. The diameter of isolated vug on the core scale is supposed to have a centimeter magnitude (Casar-Gonzalez and Suro-Perez, 2000; Zhang et al., 2004; Arns et al., 2005). Unlike the vugular carbonate rock, the core porosity and permeability slowly increase with an increase of the isolated vug diameter. With the isolated vug diameter varying from 0.5 to 3 cm, the core porosity increases from 15.41 to 29.84% and core permeability increases from 5.1 to 6.9 mD.

Finally, two varying vug diameters from 0.5 to 3 mm and 0.5 to 2.5 cm are separately chosen to study the influence of vug diameter on acidizing curves, as shown in **Figure 11**. The results indicate that the PVBT decreases as the vug diameter increases. The difference of the AMBT between different vug diameters is also not noticeable. For the isolated vug carbonate rock, the results indicate that the PVBT decreases as the isolated vug diameter increases. Acid mass does not change a lot with different isolated vug diameters. The noticeable difference of

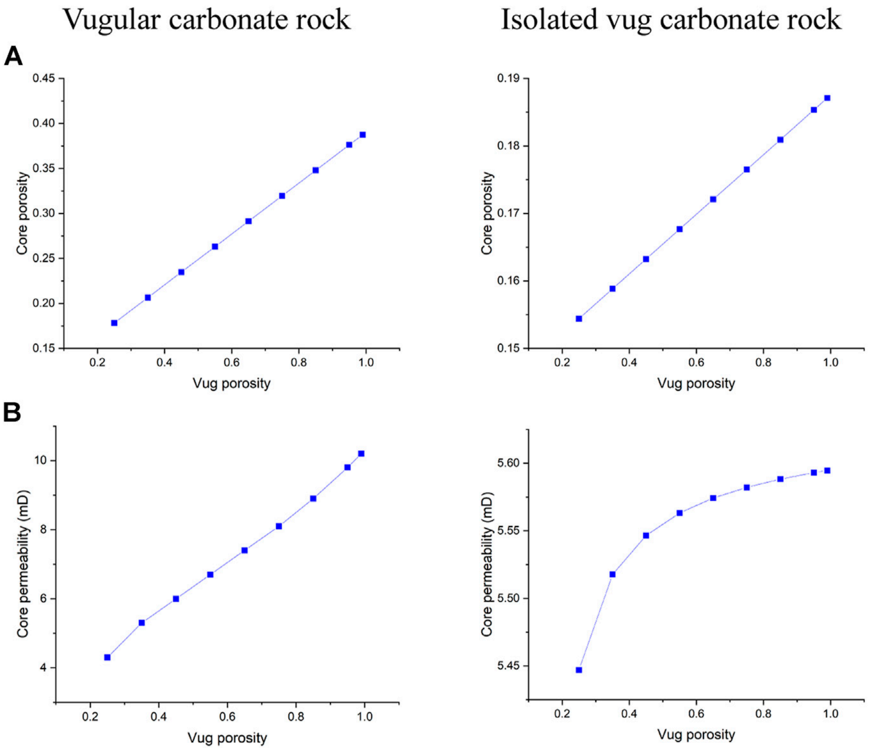

FIGURE 8 | Effect of vug porosity on core physical parameters: **(A)** core porosity and **(B)** core permeability.

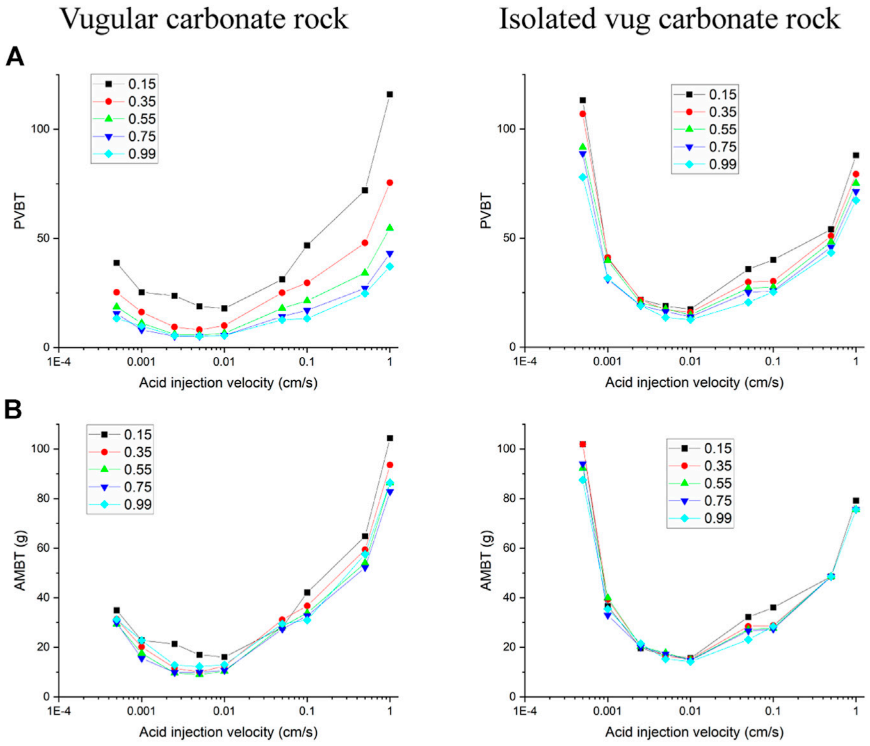

FIGURE 9 | Effect of vug porosity on acidizing curves: **(A)** pore volume to breakthrough (PVBT) and **(B)** acid mass to breakthrough (AMBT).

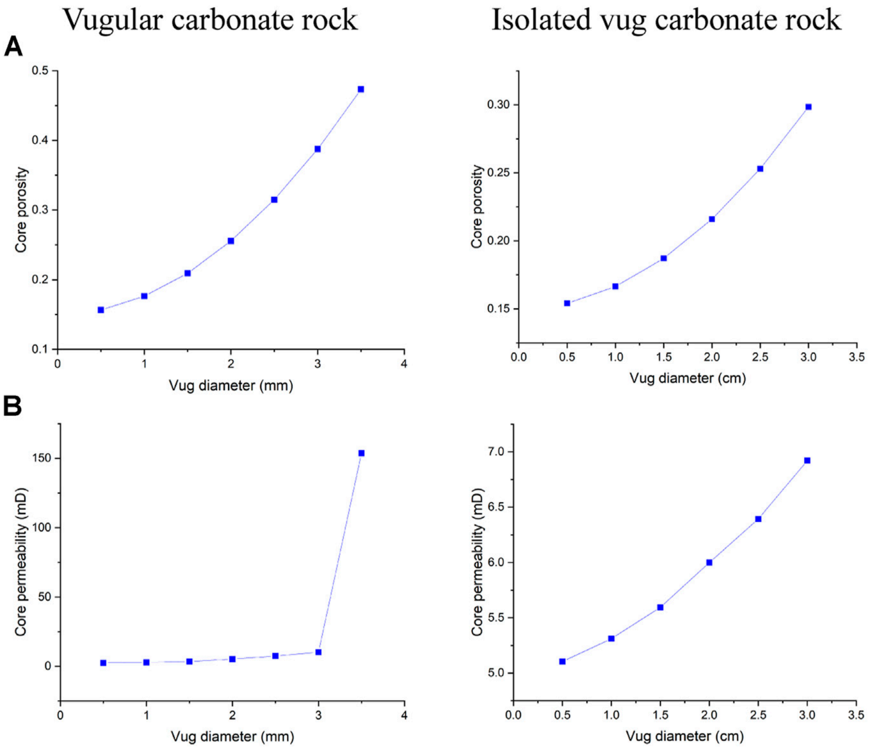

FIGURE 10 | Effect of vug diameter on core physical parameters: **(A)** core porosity and **(B)** core permeability.

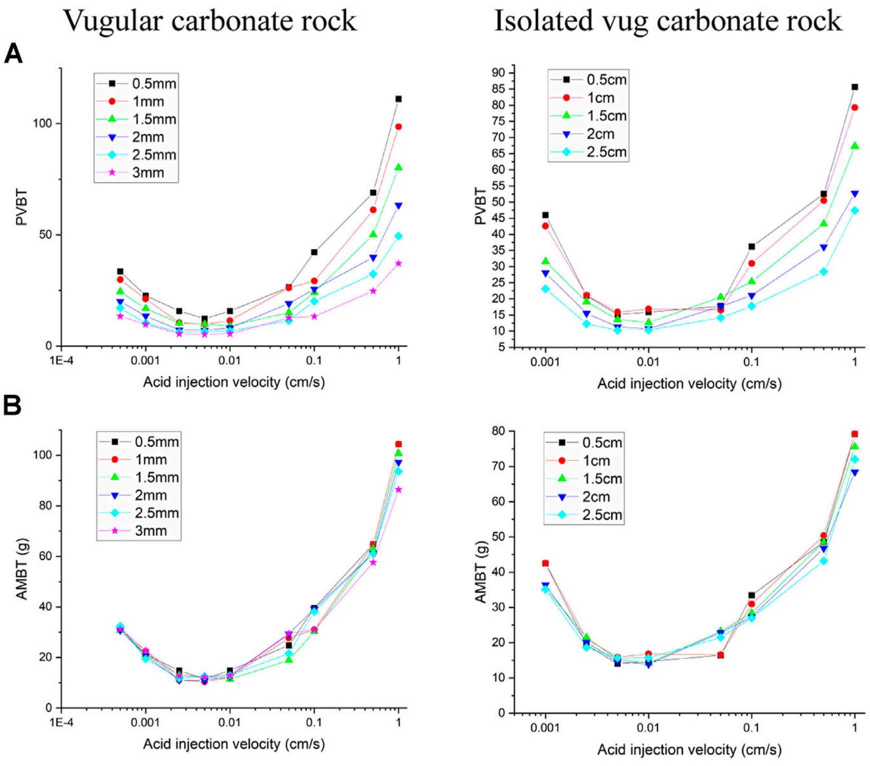

FIGURE 11 | Effect of vug diameter on acidizing curves: **(A)** pore volume to breakthrough (PVBT) and **(B)** acid mass to breakthrough (AMBT).

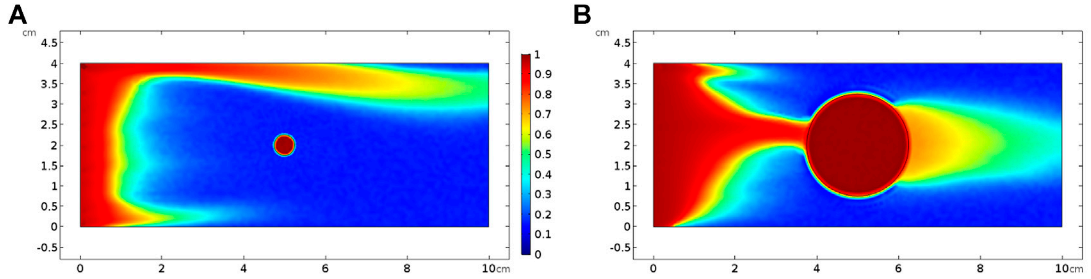

FIGURE 12 | Effect of isolated vug porosity on dissolution pattern with an acid injection velocity of 0.05 cm/s: **(A)** isolated vug diameter of 0.5 cm and **(B)** isolated vug diameter of 2.5 cm.

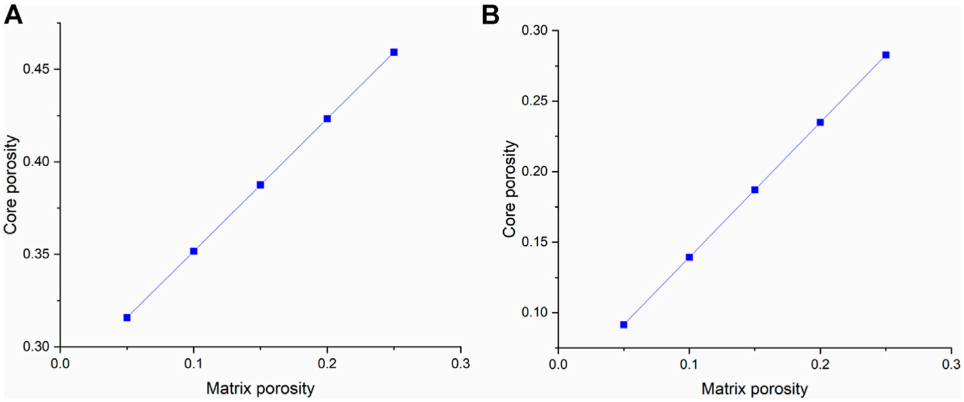

FIGURE 13 | Effect of matrix porosity on core porosity: **(A)** vugular carbonate rock and **(B)** isolated vug carbonate rock.

the AMBT in different isolated vug diameters is only shown when acid solution is pumped at an intermediate injection velocity of 0.05 cm/s. Compared to a core sample with a big isolated vug diameter, less acid is needed to achieve the breakthrough with a low isolated vug diameter. In acid solution with intermediated rates, a wormhole-shaped dissolution image is formed, as shown in **Figure 12**. The isolated vug with a higher diameter induces a wormhole to pass through the isolated vug, which leads to more acid consumption. Lower isolated vug diameter has little effect on the development of wormhole.

Effect of Matrix Porosity

Unlike sandstones, the pore structure of carbonate rock is more complex due to complicated geology processes, which makes the carbonate rock with obvious porosity heterogeneity (Sok et al., 2010; Kim et al., 2011; Milad et al., 2020). This section studies the effect of matrix porosity on the acidizing process of vugular carbonate rock and isolated vug carbonate rock. In a recent work by Jia et al. (2020b), lots of rock sample porosity values measured by experiments are collected and compared. The results show that matrix acidizing target carbonate rock samples usually have rock porosity varying between 0.05 and 0.3.

Figure 13 first studies the effect of matrix porosity on carbonate core porosity. It can be founded that the matrix porosity has a more evident effect on the vugular carbonate rock porosity. The core porosity of vugular carbonate rock increases from 0.31 to 0.46, with an increase of the matrix porosity from 0.05 to 0.25. While for isolated vug carbonate rock, the core porosity only increases from 0.09 to 0.28. **Figure 14** further compares the effect of matrix porosity on acidizing results. It can be observed from **Figure 14** that matrix porosity mainly has an apparent influence on the stimulation process when acid is injected into the vugular carbonate rock and isolated vug carbonate rock core sample with high rates. Acid consumption mass increases as matrix porosity increases. Compared to the high acid injection rates, the acidizing curve difference becomes less obvious. It is because when the acid injection rate is high, the acid transportation process is more governed by the convection process, and acid is preferred to being uniformly transported into the core sample. Core samples with higher matrix porosity can provide more storage space, which results in more acid being stored in the solid matrix. When acid injection velocity is low, the PVBT slightly decreases as the matrix porosity increases.

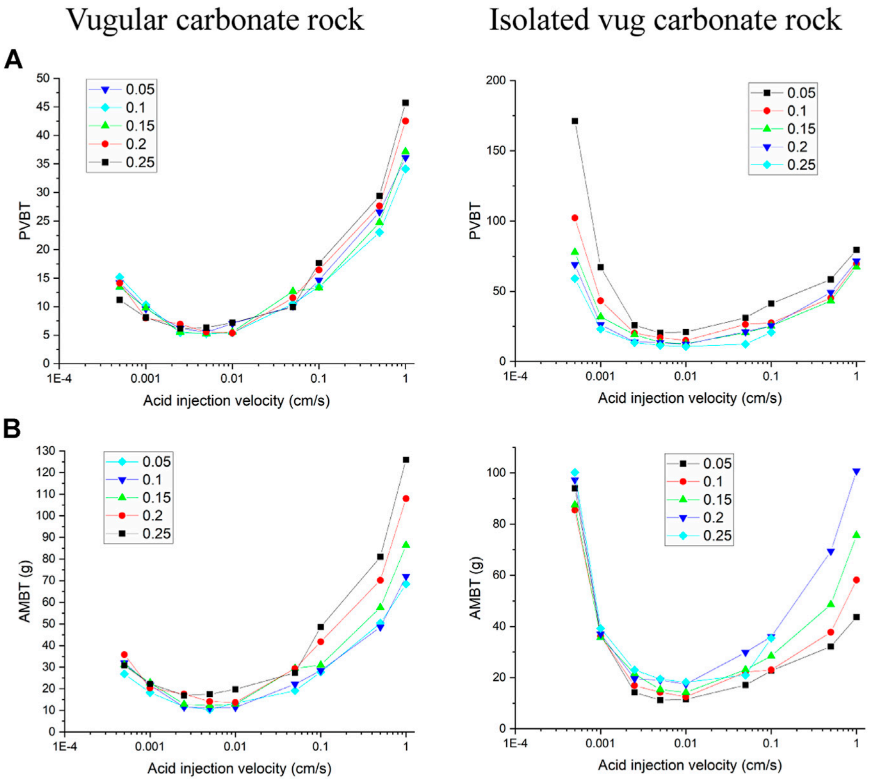

FIGURE 14 | Effect of matrix porosity on the acidizing results: **(A)** pore volume to breakthrough (PVBT) and **(B)** acid mass to breakthrough (AMBT).

CONCLUSION

Apart from the matrix region, the presence of vug is very common in the carbonate rock, which provides the main storage space for reserves. In this work, the acidizing process in two typical core-scale separate-vug porosity systems, the vugular carbonate rock and the isolated vug carbonate rock, is studied in detail. The Stokes–Darcy equation is used to describe the fluid flow to avoid using different equations in the free-flow region and porous media region. Parameter sensitivity analysis is preformed to ascertain the effect of acid injection velocity, vug filling degrees, and vug diameter on acidizing results. The main conclusions are presented below:

1) Acid injection velocity and concentration have a noticeable influence on pore volume to breakthrough (PVBT) both for the vugular carbonate rock and isolated vug carbonate rock. The existence of vug reduces the PVBT values of both vugular carbonate rock and isolated vug carbonate rock, which is consistent with the experimental observations. In contrast, acid injection velocity has little influence on acid mass to breakthrough (AMBT).
2) Typical dissolution patterns, including uniform, ramified wormhole, wormhole, and conical wormhole dissolutions, can also be observed in the acidizing process when vug exists. Compared to dissolution patterns of matrix carbonate rock, the wormhole is induced to pass through the vug region.
3) The presence of vug in a separate-vug porosity system contributes to more storage space but has little contribution to hydraulic conductivity. Core porosity and permeability both increase as filling degrees of vug and vug diameter increase. However, the increasing core permeability is limited.
4) Increasing the vug diameter and vug porosity decreases the pore volume to breakthrough both for the vugular carbonate rock and isolated vug carbonate rock.

To sum up, this study provides a powerful two-scale continuum model for the 2D vug acidizing simulation. The improved two-scale continuum model can avoid to use different governing equations in the vug region and the matrix region. The fluid phase continuity equation is also modified to consider the solid matrix dissolution mass term into the fluid phase. Further, the 3D vug simulation will be performed in our following studies.

DATA AVAILABILITY STATEMENT

The original contributions presented in the study are included in the article/Supplementary Material; further inquiries can be directed to the corresponding author.

AUTHOR CONTRIBUTIONS

CJ: conceptualization, methodology, and writing—original draft; KS: supervision, writing—review, and editing; HZ: software support; JY: supervision and funding acquisition.

ACKNOWLEDGMENTS

We are here grateful for the financial support from the National Major Science and Technology Projects of China (No. 52034010), and China Scholarship Council (201906450038).

REFERENCES

Acharya, R. C., Valocchi, A. J., Werth, C. J., and Willingham, T. W. (2007). Pore-scale Simulation of Dispersion and Reaction along a Transverse Mixing Zone in Two-Dimensional Porous media. *Water Resour. Res.* 43. doi:10.1029/2007wr005969

Aidagulov, G., Qiu, X., Brady, D., Abbad, M., Onel, Y., and Ewert, U. (2018). New Insights into Carbonate Matrix Stimulation from High-Resolution 3D Images of Wormholes Obtained in Radial Acidizing Experiments in SPE Kingdom of Saudi Arabia Annual Technical Symposium and Exhibition, Dammam, Saudi Arabia (Richardson: Society of Petroleum Engineers), 19.

Alkhaldi, M. H., Nasr-El-Din, H. A., and Sarma, H. K. (2010). Kinetics of the Reaction of Citric Acid with Calcite. *SPE J.* 15, 704–713. doi:10.2118/118724-pa

Arns, C. H., Bauget, F., Limaye, A., Sakellariou, A., Senden, T., Sheppard, A., et al. (2005). Pore Scale Characterization of Carbonates Using X-Ray Microtomography. *SPE J.* 10, 475–484. doi:10.2118/90368-pa

Balakotaiah, V., and West, D. H. (2002). Shape Normalization and Analysis of the Mass Transfer Controlled Regime in Catalytic Monoliths. *Chem. Eng. Sci.* 57, 1269–1286. doi:10.1016/s0009-2509(02)00059-3

Beavers, G. S., and Joseph, D. D. (1967). Boundary Conditions at a Naturally Permeable wall. *J. Fluid Mech.* 30, 197–207. doi:10.1017/s0022112067001375

Bernadiner, M. G., Thompson, K. E., and Fogler, H. S. (1992). Effect of Foams Used during Carbonate Acidizing. *SPE Prod. Eng.* 7, 350–356. doi:10.2118/21035-pa

Bijeljic, B., Mostaghimi, P., and Blunt, M. J. (2013). Insights into Non-fickian Solute Transport in Carbonates. *Water Resour. Res.* 49, 2714–2728. doi:10.1002/wrcr.20238

Casar-Gonzalez, R., and Suro-Perez, V. (2000). "Stochastic Imaging of Vuggy Formations," in SPE International Petroleum Conference and Exhibition in Mexico, Villahermosa, Mexico (Richardson: Society of Petroleum Engineers), 11.

De Oliveira, T. J. L., De Melo, A. R., Oliveira, J. A. A., and Pereira, A. Z. I. (2012). Numerical Simulation of the Acidizing Process and PVBT Extraction Methodology Including Porosity/Permeability and Mineralogy Heterogeneity in SPE International Symposium and Exhibition on Formation Damage Control, Lafayette, Louisiana, USA (Richardson: Society of Petroleum Engineers), 9.

Dong, K. (2012). *Experimental Investigation for the Effect of the Core Length on the Optimum Acid Flux in Carbonate Acidizing*. College Station: Texas A & M University.

Dong, K., Jin, X., Zhu, D., and Hill, A. D. (2014). The Effect of Core Dimensions on the Optimal Acid Flux in Carbonate Acidizing in SPE International Symposium and Exhibition on Formation Damage Control, Lafayette, Louisiana, USA (Richardson: Society of Petroleum Engineers), 10.

Edery, Y., Scher, H., and Berkowitz, B. (2011). Dissolution and Precipitation Dynamics during Dedolomitization. *Water Resour. Res.* 47. doi:10.1029/2011wr010551

Fadlelmula F, M. M., Qian, S., Wang, Y., Fraim, M., He, J., Gao, S., and Killough, J. E. (2016). Separable Multiple-Point Geostatistical Modeling of Three-Dimensional Discrete Fracture-Vug Networks in Abu Dhabi International Petroleum Exhibition & Conference, Abu Dhabi, UAE (Richardson: Society of Petroleum Engineers), 11.

Fredd, C. N., and Fogler, H. S. (1998). Alternative Stimulation Fluids and Their Impact on Carbonate Acidizing. *SPE J. - SPE J* 3, 34–41. doi:10.2118/31074-pa

Fredd, C. N., and Fogler, H. S. (1999). Optimum Conditions for Wormhole Formation in Carbonate Porous Media: Influence of Transport and Reaction. *SPE J.* 4, 196–205. doi:10.2118/56995-pa

Fredd, C. N., and Scott Fogler, H. (1998). The Kinetics of Calcite Dissolution in Acetic Acid Solutions. *Chem. Eng. Sci.* 53, 3863–3874. doi:10.1016/s0009-2509(98)00192-4

Frick, T. P., Mostofizadeh, B., and Economides, M. J. (1994). Analysis of Radial Core Experiments for Hydrochloric Acid Interaction with Limestones in SPE Formation Damage Control Symposium, Lafayette, Louisiana (Richardson: Society of Petroleum Engineers), 16.

Furui, K., Burton, R. C. C., Burkhead, D. W. W., Abdelmalek, N. A. A., Hill, A. D. D., Zhu, D., et al. (2012a). A Comprehensive Model of High-Rate Matrix-Acid Stimulation for Long Horizontal Wells in Carbonate Reservoirs: Part I-Scaling up Core-Level Acid Wormholing to Field Treatments. *SPE J.* 17, 271–279. doi:10.2118/134265-pa

Furui, K., Burton, R. C. C., Burkhead, D. W. W., Abdelmalek, N. A. A., Hill, A. D. D., Zhu, D., et al. (2012b). A Comprehensive Model of High-Rate Matrix-Acid Stimulation for Long Horizontal Wells in Carbonate Reservoirs: Part II-Wellbore/Reservoir Coupled-Flow Modeling and Field Application. *SPE J.* 17, 280–291. doi:10.2118/155497-pa

Hoefner, M. L., and Fogler, H. S. (1989). Fluid-Velocity and Reaction-Rate Effects during Carbonate Acidizing: Application of Network Model. *SPE Prod. Eng.* 4, 56–62. doi:10.2118/15573-pa

Huang, T., Ostensen, L., and Hill, A. D. (2000). Carbonate Matrix Acidizing with Acetic Acid in SPE International Symposium on Formation Damage Control, Lafayette, Louisiana (Richardson: Society of Petroleum Engineers), 6.

Izgec, O., Keys, R. S., Zhu, D., and Hill, A. D. (2008). An Integrated Theoretical and Experimental Study on the Effects of Multiscale Heterogeneities in Matrix Acidizing of Carbonates in SPE Annual Technical Conference and Exhibition, Denver, Colorado, USA (Richardson: Society of Petroleum Engineers), 14.

Izgec, O., Zhu, D., and Hill, A. D. (2009). Models and Methods for Understanding of Early Acid Breakthrough Observed in Acid Core-Floods of Vuggy Carbonates in 8th European Formation Damage Conference, Scheveningen, The Netherlands (Richardson: Society of Petroleum Engineers), 15.

Izgec, O., Zhu, D., and Hill, A. D. (2010). Numerical and Experimental Investigation of Acid Wormholing during Acidization of Vuggy Carbonate Rocks. *J. Pet. Sci. Eng.* 74, 51–66. doi:10.1016/j.petrol.2010.08.006

Jia, C., Huang, Z., Sepehrnoori, K., and Yao, J. (2020b). A New Mathematical Model and Numerical Studies for Carbonate Matrix Acidizing. *SPE J.* 197.

Jia, C., Huang, Z., Sepehrnoori, K., and Yao, J. (2020a). Modification of Two-Scale Continuum Model and Numerical Studies for Carbonate Matrix Acidizing. *J. Pet. Sci. Eng.* 197, 107972.

Jia, C., Huang, Z., Sepehrnoori, K., and Yao, J. (2021). Modification of Two-Scale Continuum Model and Numerical Studies for Carbonate Matrix Acidizing. *J. Pet. Sci. Eng.* 197, 107972. doi:10.1016/j.petrol.2020.107972

Kalia, N., and Balakotaiah, V. (2009). Effect of Medium Heterogeneities on Reactive Dissolution of Carbonates. *Chem. Eng. Sci.* 64, 376–390. doi:10.1016/j.ces.2008.10.026

Kalia, N., and Balakotaiah, V. (2007). Modeling and Analysis of Wormhole Formation in Reactive Dissolution of Carbonate Rocks. *Chem. Eng. Sci.* 62, 919–928. doi:10.1016/j.ces.2006.10.021

Kalia, N. (2008). *Modeling and Analysis of Reactive Dissolution of Carbonate Rocks*. Houston: University of Houston.

Kanaka, M., and Panga, R. (2003). *Multiscale Transport and Reaction: Two Case Studies*. Richardson: University of Houston.

Kang, Z., Wu, Y.-S., Li, J., Wu, Y., Zhang, J., and Wang, G. (2006). Modeling Multiphase Flow in Naturally Fractured Vuggy Petroleum Reservoirs. SPE Annual Technical Conference and Exhibition. San Antonio, Texas, USA (Richardson: Society of Petroleum Engineers), 10.

Kim, D., Peters, C. A., and Lindquist, W. B. (2011). Upscaling Geochemical Reaction Rates Accompanying Acidic CO2-Saturated Brine Flow in Sandstone Aquifers. *Water Resour. Res.* 47 (1).

Kossack, C. A., and Gurpinar, O. (2001). A Methodology for Simulation of Vuggy and Fractured Reservoirs in SPE Reservoir Simulation Symposium, Houston, Texas (Richardson: Society of Petroleum Engineers), 12.

Kumar, H. T., Muhemmed, S., and Nasr-El-Din, H. A. (2020). Impact of Oil Saturation, CO2 Evolution, and Rock Wettability on Acid Efficiencies during Carbonate Acidizing: A Three-phase Perspective in SPE International Conference and Exhibition on Formation Damage Control, Lafayette, Louisiana, USA (Richardson: Society of Petroleum Engineers), 20.

Li, J., Ma, Y., Huang, K., Zhang, Y., Wang, W., Liu, J., et al. (2018). Quantitative Characterization of Organic Acid Generation, Decarboxylation, and Dissolution in a Shale Reservoir and the Corresponding Applications-A Case Study of the Bohai Bay Basin. *Fuel* 214, 538–545. doi:10.1016/j.fuel.2017.11.034

Li, L., Steefel, C. I., and Yang, L. (2008). Scale Dependence of mineral Dissolution Rates within Single Pores and Fractures. *Geochimica et Cosmochimica Acta* 72, 360–377. doi:10.1016/j.gca.2007.10.027

Li, Y. (2017). *Development Theories and Methods of Fracture-Vug Carbonate Reservoirs*. Academic Press.

Liu, P., Yan, X., Yao, J., and Sun, S. (2019). Modeling and Analysis of the Acidizing Process in Carbonate Rocks Using a Two-phase thermal-hydrologic-chemical Coupled Model. *Chem. Eng. Sci.* 207, 215–234. doi:10.1016/j.ces.2019.06.017

Liu, P., Yao, J., Couples, G. D., Huang, Z., Sun, H., and Ma, J. (2017). Numerical Modelling and Analysis of Reactive Flow and Wormhole Formation in Fractured Carbonate Rocks. *Chem. Eng. Sci.* 172, 143–157. doi:10.1016/j.ces.2017.06.027

Lucia, F. (2007). *Carbonate Reservoir Characterization: An Integrated Approach*. Springer-Verlag Berlin Heidelberg.

Maheshwari, P., Gharbi, O., Thirion, A., Ali, N. S. E. C., Peyrony, V., Aubry, E., Poitrenaud, H. M., and Benquet, J. C. (2016a). "Development of a Reactive Transport Simulator for Carbonates Acid Stimulation," in SPE Annual Technical Conference and Exhibition, Dubai, UAE (Richardson: Society of Petroleum Engineers), 11.

Maheshwari, P., Maxey, J., and Balakotaiah, V. (2016b). Reactive-Dissolution Modeling and Experimental Comparison of Wormhole Formation in Carbonates with Gelled and Emulsified Acids. *SPE Prod. Operations* 31, 103–119. doi:10.2118/171731-pa

Maheshwari, P., Ratnakar, R. R., Kalia, N., and Balakotaiah, V. (2013). 3-D Simulation and Analysis of Reactive Dissolution and Wormhole Formation in Carbonate Rocks. *Chem. Eng. Sci.* 90, 258–274. doi:10.1016/j.ces.2012.12.032

Mahrous, M., Sultan, A., and Sonnenthal, E. (2017). Towards Geochemically Accurate Modeling of Carbonate Acidizing with HCl Acid in SPE Annual Technical Conference and Exhibition, San Antonio, Texas, USA (Richardson: Society of Petroleum Engineers), 22.

Menke, H. P., Bijeljic, B., Andrew, M. G., and Blunt, M. J. (2015). Dynamic Three-Dimensional Pore-Scale Imaging of Reaction in a Carbonate at Reservoir Conditions. *Environ. Sci. Technol.* 49, 4407–4414. doi:10.1021/es505789f

Milad, M., Shadizadeh, S. R., Manshad, A. K., and Mohammadi, A. H. (2020). Experimental Study of the Relationship between Porosity and Surface Area of Carbonate Reservoir Rocks. *J. Pet. Explor. Prod. Technol.* 1–18.

Mousavi, M., Prodanovic, M., and Jacobi, D. (2012). New Classification of Carbonate Rocks for Process-Based Pore-Scale Modeling. *SPE J.* 18, 243–263. doi:10.2118/163073-pa

Nair, N. G., Bryant, S. L., and Jennings, J. W. (2008). Finding the Continuum Scale in Highly Heterogeneous Rocks: Example of a Large Touching Vug Carbonate in SPE Annual Technical Conference and Exhibition, Denver, Colorado, USA (Richardson: Society of Petroleum Engineers), 13.

Nick, H. M., Raoof, A., Centler, F., Thullner, M., and Regnier, P. (2013). Reactive Dispersive Contaminant Transport in Coastal Aquifers: Numerical Simulation of a Reactive Henry Problem. *J. Contaminant Hydrol.* 145, 90–104. doi:10.1016/j.jconhyd.2012.12.005

Panga, M. K. R., Ziauddin, M., and Balakotaiah, V. (2005). Two-scale Continuum Model for Simulation of Wormholes in Carbonate Acidization. *Aiche J.* 51, 3231–3248. doi:10.1002/aic.10574

Popov, P., Qin, G., Bi, L., Efendiev, Y., Ewing, R. E., and Li, J. (2009). Multiphysics and Multiscale Methods for Modeling Fluid Flow through Naturally Fractured Carbonate Karst Reservoirs. *SPE Reservoir Eval. Eng.* 12, 218–231. doi:10.2118/105378-pa

Qiu, X., Edelman, E., Aidagulov, G., Ghommem, M., Brady, D., and Abbad, M. (2018). Experimental Investigation of Radial and Linear Acid Injection into Carbonates for Well Stimulation Operations in SPE Kingdom of Saudi Arabia Annual Technical Symposium and Exhibition, Dammam, Saudi Arabia (Richardson: Society of Petroleum Engineers), 15.

Ramakrishnan, T. S., Ramamoorthy, R., Fordham, E., Schwartz, L., Herron, M., Saito, N., and Rabaute, A. (2001). A Model-Based Interpretation Methodology for Evaluating Carbonate Reservoirs in SPE Annual Technical Conference and Exhibition, New Orleans, Louisiana (Richardson: Society of Petroleum Engineers), 15.

Sadeghnejad, S., and Gostick, J. (2020). Multiscale Reconstruction of Vuggy Carbonates by Pore-Network Modeling and Image-Based Technique. *SPE J.* 25, 253–267. doi:10.2118/198902-pa

Saffman, P. G. (1971). On the Boundary Condition at the Surface of a Porous Medium. *Stud. Appl. Math.* 50, 93–101. doi:10.1002/sapm197150293

Sok, R. M., Knackstedt, M. A., Varslot, T., Ghous, A., Latham, S., and Sheppard, A. P. (2010). Pore Scale Characterization of Carbonates at Multiple Scales: Integration of Micro-CT, BSEM, and FIBSEM. *Petrophysics* 51, 9.

Wang, D., Li, Y., Hu, Y., Li, B., Deng, X., and Liu, Z. (2016). Integrated Dynamic Evaluation of Depletion-Drive Performance in Naturally Fractured-Vuggy Carbonate Reservoirs Using DPSO-FCM Clustering. *Fuel* 181, 996–1010. doi:10.1016/j.fuel.2016.05.009

Wang, Y., Hill, A. D., and Schechter, R. S. (1993). The Optimum Injection Rate for Matrix Acidizing of Carbonate Formations in SPE Annual Technical Conference and Exhibition, Houston, Texas (Richardson: Society of Petroleum Engineers), 13.

Wei, W., Varavei, A., and Sepehrnoori, K. (2017). Modeling and Analysis on the Effect of Two-phase Flow on Wormhole Propagation in Carbonate Acidizing. *SPE J.* 22, 2067–2083. doi:10.2118/186111-pa

Wu, Y.-S., Ehlig-Economides, C. A., Qin, G., Kang, Z., Zhang, W., Ajayi, B. T., and Tao, Q. (2007). A Triple-Continuum Pressure-Transient Model for a Naturally Fractured Vuggy Reservoir in SPE Annual Technical Conference and Exhibition (Anaheim, California, U.S.A.: Society of Petroleum Engineers), 10.

Yao, J., Huang, Z., Li, Y., Wang, C., and Lv, X. (2010). Discrete Fracture-Vug Network Model for Modeling Fluid Flow in Fractured Vuggy Porous Media in International Oil and Gas Conference and Exhibition in China, Beijing, China (Richardson: Society of Petroleum Engineers), 14.

Yue, P., Xie, Z., Huang, S., Liu, H., Liang, S., and Chen, X. (2018). The Application of N2 Huff and Puff for IOR in Fracture-Vuggy Carbonate Reservoir. *Fuel* 234, 1507–1517. doi:10.1016/j.fuel.2018.07.128

Zhang, L., Bryant, S. L., Jennings, J. W., Jr., Arbogast, T. J., and Paruchuri, R. (2004). Multiscale Flow and Transport in Highly Heterogeneous Carbonates in SPE Annual Technical Conference and Exhibition, Houston, Texas (Richardson: Society of Petroleum Engineers), 9.

Zhang, L., Nair, N. G., Jennings, J. W., and Bryant, S. L. (2005). Models and Methods for Determining Transport Properties of Touching-Vug Carbonates in SPE Annual Technical Conference and Exhibition, Dallas, Texas (Richardson: Society of Petroleum Engineers), 9.

Conflict of Interest: The authors declare that the research was conducted in the absence of any commercial or financial relationships that could be construed as a potential conflict of interest.

frontiers in Earth Science

ORIGINAL RESEARCH
published: 03 August 2021
doi: 10.3389/feart.2021.691311

Adaption of Theoretical Adsorption Model on Coal: Physical Structure

Wu Guodai[1,2,3,4], Pan Linhua[2,3], Huang Bingxiang[1]*, Luan Jinhua[2,3,4], Zhang Ye[2,3], Zhang Ruigang[2,3,4] and Sun Zheng[1]*

[1]State Key Laboratory of Coal Resources and Safe Mining, China University of Mining and Technology, Xuzhou, China, [2]National and Local Joint Engineering Research Center of Shale Gas Exploration and Development, Chongqing Institute of Geology and Mineral Resources, Chongqing, China, [3]Key Laboratory of Shale Gas Exploration, Ministry of Land and Resources, Chongqing Institute of Geology and Mineral Resources, Chongqing, China, [4]Chongqing Key Laboratory of Exogenic Mineralization and Mine Environment, Chongqing Institute of Geology and Mineral Resources, Chongqing, China

OPEN ACCESS

Edited by:
Zhiyuan Wang,
China University of Petroleum (Huadong), China

Reviewed by:
Tao Zhang,
Southwest Petroleum University, China
Yisheng Liu,
Chengdu University of Technology, China

***Correspondence:**
Pan Linhua
panlinhua21915@163.com
Huang Bingxiang
huangbingxiang@cumt.edu.cn

Specialty section:
This article was submitted to Economic Geology, a section of the journal Frontiers in Earth Science

Received: 06 April 2021
Accepted: 07 May 2021
Published: 03 August 2021

Citation:
Guodai W, Linhua P, Bingxiang H, Jinhua L, Ye Z, Ruigang Z and Zheng S (2021) Adaption of Theoretical Adsorption Model on Coal: Physical Structure. Front. Earth Sci. 9:691311. doi: 10.3389/feart.2021.691311

With the motivation to investigate the role of coal physical structure on the adsorption performance of coal reservoir, 18 different types of coal samples with different coal structures were collected from six coal profiles of four production mines located at China. The adsorption characteristics of CH_4 on coal samples with different coal structures were examined, and then experimental results were fitted and analyzed by the Langmuir model and the adsorption potential model (D-R and D-A). The prominent factors in terms of adsorption capacity of coal with different coal structures and its adaptability to the model were discussed. Results indicate the following: a) under the condition of a similar coal rank, the adsorption performance of coal is governed by coal rock composition and adsorption heat, the effect of structural deformation on the adsorption performance of coal is not obvious; b) the Langmuir model has a certain adaptability to coal samples with different coal structures, while the D-R model is evidently not suitable to describe coal samples with scaly coal, part of broken coal with small vitrinite content; c) the D-A model has a high adaptability to coal samples with various coal structure types, and the stronger the coal deformation is, the higher the accuracy is.

Keywords: theoretical adsorption model, coal structure, laboratory experiment, data analysis, coal rank

INTRODUCTION

Adsorption is a kind of surface interaction between coal solid surface and gas or liquid, and coalbed methane mainly exists in the adsorption state in coal reservoirs. All the metamorphic degree of coal, coal rock composition, moisture, temperature, reservoir pressure, and other factors have important impacts on the adsorption performance of coal. Previous studies have made many achievements in this area (Fu, 2001; Zhong et al., 2002; Zhong, 2004; Su et al., 2005; Sang et al., 2005; Zhang et al., 2006; Zhang and Sang, 2008), and the structural coal reservoir is the critical research subject for the development and prevention of coalbed methane (Zhang et al., 2007; Sang et al., 2005; Sun et al., 2019), associated deformation mechanism and structural evolution of tectonic coal have attracted extensive attention (Wang and Zhu, 1998; Jiang et al., 1998; Jiang and Ju, 2004). The coupling characteristics of different structural types of tectonic coal to gas have required due attention as well (Li, 2001; Jiang et al., 1998, Jiang and Ju, 2004; Jiang et al., 2009, Zhao et al., 2019). Moreover, the soft stratification in tectonic coal is the dangerous area of gas enrichment and outburst, which has formed a consensus in both the academy and industry. With the strengthening of structural deformation, the alteration of the occurrence state of gas inside coal takes place. And, it is worth mentioning that the

TABLE 1 | Vitrinite reflectance measurement and industrial analysis of samples.

Index	Coal structure	Ro, max, %	Water content, %	Ash content, %	Volatile matter, %
A-2	Mylonitic coal	0.821	1.72	49.62	43.75
A-4	Broken coal	0.759	1.14	11.95	37.89
A-5	Scaly coal	0.815	1.25	31.74	43.05
B-2	Broken coal	0.84	1.38	14.64	35
B-4	Scaly coal	0.846	1.3	26.96	37.81
B-5	Cataclastic coal	0.849	1.5	14.95	36.24
C-1	Primary structure coal	0.799	0.96	17.73	39.74
C-2	Cataclastic coal	0.761	1.14	7.66	41.61
C-3	Cataclastic coal	0.753	1.07	21.33	41.82
C-4	Broken coal	0.762	1.62	11.15	39.08
D-2	Cataclastic coal	0.725	1.11	10.35	44.17
D-3	Cataclastic coal	0.736	1.6	7.03	38.17
E-1	Primary structure coal	0.739	1.66	8.94	39.06
E-2	Cataclastic coal	0.74	1.86	13.44	36.96
E-3	Broken coal	0.725	1.72	24.43	38.87
E-4	Mylonitic coal	0.745	1.51	44.25	47.1
F-1	Cataclastic coal	0.829	1.93	18.93	32.78
F-2	Primary structure coal	0.821	1.36	22.4	37.6

evolution of coal structure leads to the change of pores and fissures, which inevitably imposes a direct impact on the adsorption behavior of coal. However, there are few reports on the related research, and current research is heavily dependent on the theoretical analysis of the Langmuir model (Ju, 2003; Zhang and Liu, 2009), while the application of the Langmuir model in the adsorption of coal with a complex pore structure remains in debate (Chen et al., 1998; Sun et al., 2020). In contrast, the volume filling model (D-R) and the optimal volume filling model (D-A), which are important models in the field of adsorption theory, both have been widely used in the study of adsorption behavior of coal (Crosdale et al., 1998; Laxminarayana and Crosdale, 1999; Dai et al., 2009). However, both D-R and D-A models have not been used in the study of adsorption behavior of coal samples with different coal structures. Therefore, adaption of different theoretical adsorption models on coal is of great significance for further understanding the influence of coal structure evolution on the adsorption performance of coal reservoir.

SAMPLE SELECTION AND ADSORPTION EXPERIMENT

In this study, 18 samples of primary structure coal, catallactic coal, granulated coal, flake coal, and mylonitic coal were collected from four production mines in China. The evolution of coal structure on the same coal rock section is continuous, which is beneficial to reduce the interference of other factors in the following comparative analysis. Concrete experimental contents include industrial analysis, vitrinite reflectance measurement, equilibrium water test, and isothermal adsorption experiment. The basic physical properties of each sample are shown in **Table 1**.

The high-pressure isothermal adsorption instrument produced by raven ridge company of the United States is used for isothermal adsorption. The sample processing and experimental procedures are introduced in detail in our previous literature (Wu, 2010). This experiment simulates the temperature and reservoir pressure under formation conditions: the experimental temperature is 30°C and the maximum reservoir pressure is 12 MPa. The pressure adsorption capacity at seven equilibrium points is tested.

RESULTS AND DISCUSSION

Basic Physical Characteristics

The maximum reflectance (RO, max) of vitrinite falls in the range of 0.725–0.849%, which belongs to gas coal. The metamorphic degree of the same coal section is similar.

Adsorption Characteristics of Coal Samples With Different Coal Structures

The adsorption characteristics of coal samples with different coal structures are depicted in **Figure 1**. It can be observed that when temperature is 30°C and the maximum pressure is 12 MPa, on the same coal rock section, with the evolution of coal structure, the adsorption characteristics of coal samples behave differently. The isothermal adsorption curves of flake coal and crushed coal are close, which have stronger adsorption capacity than deformed mylonitic coal. The adsorption capacity of three samples on the section of working face B is the largest under the maximum equilibrium pressure; it can be demonstrated that adsorption capacity increases with the increase of coal deformation strength. The adsorption capacity of mylonitic coal on the working face C is the largest. The results suggest that the adsorption capacity of one broken coal is similar to that of the mylonitic coal, while the adsorption capacity of the other broken coal is smaller than that of the primary structure coal. The adsorption curves of the two broken coal on the working face D are similar, but the adsorption capacity is different. The adsorption capacity of the primary structure coal, broken coal, broken coal, and mylonitic coal on the working face E is the largest, in which the adsorption capacity

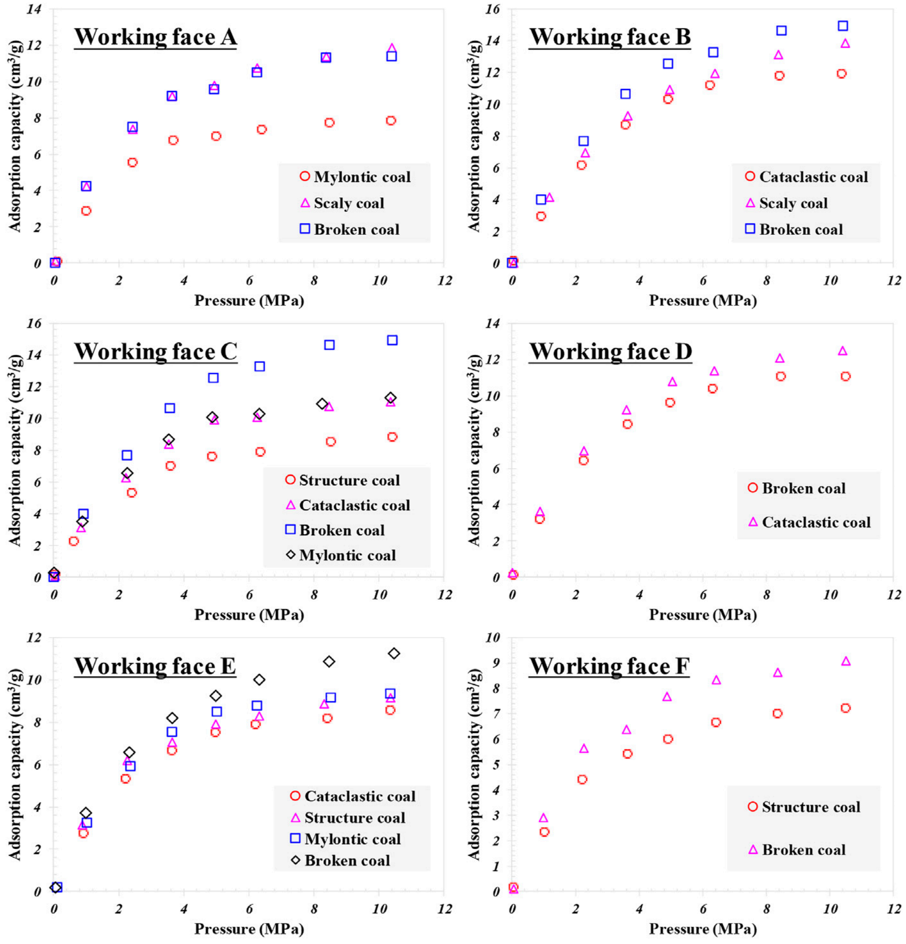

FIGURE 1 | Distribution map of MRE to adsorption model of sheared coal.

of the broken coal is the highest. Notably, the adsorption capacity of fractured coal in working face F is evidently larger than that of primary structure coal.

According to the comparative analysis of adsorption curves (**Figure 2**) and basic physical property characteristics (**Table 1**), it can be concluded that the adsorption characteristics of the studied coal samples is obviously governed by coal structure, ash content, and metamorphic degree. As for the case of the same coal rock section, adsorption capacity of coal increases with the increase of structural deformation but decreases with the increase of ash content due to the weak adsorption capacity of the ash content. Among the rock sections, coal section B shares the highest metamorphic degree and the largest overall adsorption capacity.

Model Fitting and Evaluation

Kinetic models (Langmuir monolayer model, BET multilayer model, etc.) and Polanyi adsorption potential models (D-A model and D-R model) are commonly used to describe the coal adsorption mechanism. Different theoretical adsorption models are supported by a large number of experimental data; also each model has its own application scope. It is generally believed that Langmuir equation is mainly used to describe type-I adsorption isotherm, which is suitable for solid substances with developed pores such as activated carbon or solids with uniform surface without pores. The BET equation is mainly applied to describe porous substances with rich mesopores, while the deviation enlarges when it comes to supercritical fluids; therefore, it can be used to describe type I, II, and III adsorption isotherm and calculate specific surface area of porous substances. The D-R equation is generally suitable for adsorbents with small pore size, in which the multilayer adsorption or capillary condensation is unfavorable (Clarkson, 1997). The parameter *n* in D-A equation varies with the pore structure of adsorbents, which considerably expand its application scope.

Because the premise of the application of the BET model is to determine four or five points in the range of P/Po (the ratio of equilibrium gas pressure and saturated vapor pressure) = 0.05–0.35, and the monolayer adsorption volume (*Vm*) can be calculated, while the P/Po of the seven equilibrium points in isothermal adsorption test is mostly greater than 0.35, the calculation of BET model parameters from the data of seven equilibrium points will be seriously distorted or even have no

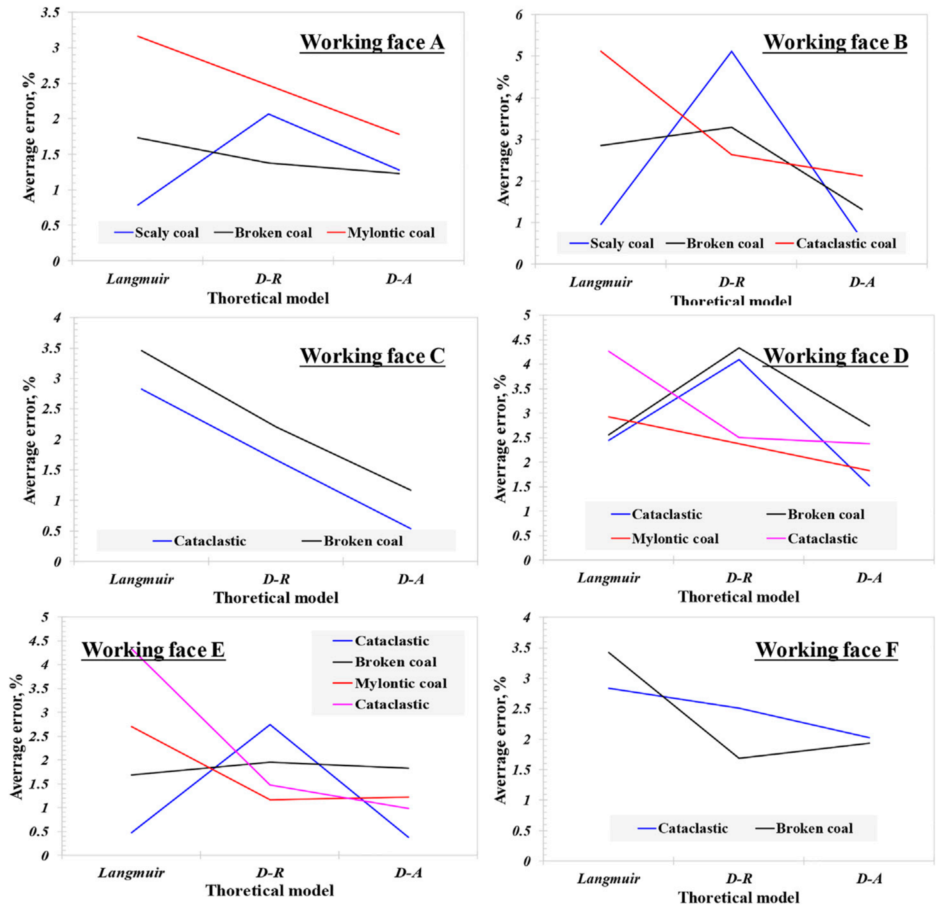

FIGURE 2 | Adsorption Characteristics of coals with different structures on the same coal rock section.

solution. However, the Langmuir, D-R, and D-A models are not limited by the above factor, so this study uses the Langmuir, D-R, and D-A models to analyze coal samples with different coal structures.

The calculation formulas of the three models are as follows. For the Langmuir monolayer localization adsorption model:

$$V = \frac{V_L P}{P_L + P},$$

where V is the adsorption capacity, m^3/g; *VL* is the Langmuir volume, m^3/g, which represents the adsorption capacity when the surface of each gram of coal is covered with monolayer; *PL* is the Langmuir pressure, MPa, which represents the corresponding equilibrium pressure when the adsorption reaches half of the maximum adsorption capacity; and P is the equilibrium gas pressure, MPa.

The theoretical adsorption potential models (D-R model and D-A model) are as follows:

$$V = V_0 \exp\left[-D\left(Ln^2\left(\frac{P_0}{P}\right)\right)\right], \quad \text{(D−R)},$$

$$V = V_0 \exp\left[-D\left(Ln^{\mathrm{n}}\left(\frac{P_0}{P}\right)\right)\right], \quad \text{(D−A)},$$

where V is the adsorption capacity, m^3/g; *V0* is the volume of micropore per gram (regarded as completely filled with adsorbed gas molecules), m^3/g; D is the constant related to net adsorption heat in the equation; n is the parameter related to temperature and pore distribution of coal; and P is the equilibrium gas pressure, MPa.

Under the condition of 30°C, CH_4 belongs to the supercritical state. The virtual saturated vapor pressure of CH_4 can be calculated according to the formula of P0 = PC * (T/TC) 2 (PC denotes the critical pressure and TC denotes the critical temperature). After calculation, the saturated vapor pressure of CH_4 is 11.68 MPa.

Notably, SPSS17.0 software was used to fit the adsorption capacity of seven equilibrium points, and the seven parameters of the Langmuir, D-R, and D-A models, the standard deviation of each parameter, and the correlation degree of curve fitting (**Table 2**) were obtained. It can be observed from the table that the correlation of Langmuir model fitting parameters of 18 samples ranges from 0.980 ~ 1, the correlation of D-R model fitting parameters was between 0.978 ~ 0.999, and the correlation degree of D-A model fitting parameters was between 0.992 and 1. From this perspective, the fitting correlation of each model is

TABLE 2 | Characteristic parameters and fitting characteristics obtained from fitting models.

Index	Langmuir model			D-R model			D-A model			
	VL	*PL*	Correlation	*Vo*	*D*	Correlation	*Vo*	*D*	*n*	Correlation
A-2	9.474	1.736	0.983	7.957	0.147	0.990	7.857	0.123	2.219	0.992
A-4	13.381	1.813	0.995	11.117	0.147	0.994	11.257	0.170	1.830	0.995
A-5	14.220	2.047	0.998	11.542	0.158	0.991	11.834	0.203	1.690	0.997
B-2	20.482	3.465	0.994	14.747	0.222	0.994	15.120	0.270	1.728	0.999
B-4	18.906	3.689	0.999	13.282	0.222	0.978	14.155	0.337	1.430	0.999
B-5	16.473	3.352	0.984	12.015	0.222	0.997	12.101	0.236	1.913	0.997
C-1	10.990	2.334	0.991	8.680	0.170	0.987	8.904	0.216	1.717	0.992
C-2	14.324	2.660	0.984	11.053	0.192	0.994	11.093	0.199	1.952	0.994
C-3	9.931	2.098	0.992	8.003	0.158	0.997	8.380	0.239	1.492	0.995
C-4	14.331	2.466	0.990	11.220	0.181	0.995	11.331	0.199	1.877	0.995
D-2	16.188	2.896	0.991	12.224	0.200	0.997	12.371	0.223	1.856	0.998
D-3	14.553	2.724	0.994	11.149	0.192	0.998	11.297	0.217	1.840	1.000
E-1	10.996	1.985	0.996	8.976	0.155	0.992	9.138	0.188	1.772	0.995
E-2	10.509	2.199	0.993	8.434	0.169	0.999	8.467	0.178	1.952	0.999
E-3	14.115	2.637	1.000	10.867	0.186	0.992	11.220	0.245	1.639	1.000
E-4	11.683	2.254	0.980	9.366	0.176	0.997	9.256	0.152	2.188	0.998
F-1	11.519	2.650	0.993	8.867	0.187	0.990	9.072	0.230	1.733	0.995
F-2	9.381	2.754	0.991	7.172	0.195	0.995	7.238	0.212	1.883	0.996

Note*:* V_L *is Langmuir volume, cm*^{3}*/g;* V_P *is Langmuir pressure, MPa;* V_0 *is micropore volume per gram, cm*^{3}*/g;* D *constant related to net adsorption heat;* n *parameter related to temperature and pore distribution of coal.*

fairly high; in other words, all the three models are favorable to describe the adsorption behavior of the coal reservoir.

The *VL* of the Langmuir model represents the theoretical maximum adsorption, and the *VL* of 18 coal samples ranges from 9.381 to 20.482 m^3/g. The *VL* of the primary structure coal on working face F is the smallest and fragmental coal on working face B is the largest. There is no consistent rule in the variation of *VL* in each coal petrography section. There exist differences in the *VL* of the same type of fragmental coal in the same coal petrography section. However, from primary structure coal to fragmental coal, *VL* of scale coal is larger than that of fragmental coal, while that of mylonitic coal is the smallest on the working face A, the same as the broken coal in working face C, and larger than the broken coal in working face E, showing complex variation characteristics. *PL* represents the equilibrium pressure when the adsorption reaches half of the maximum adsorption capacity. The *VP* of 18 coal samples ranges from 1.736 to 3.689 MPa. In general, VP increases with the increase of VL, but PL of scaly coal on working face B and primary structure coal on working face F with weak deformation are larger than the *VP* with strong deformation, suggesting opposite characteristics.

As for the adsorption potential models (D-R and D-A), *V0* is the volume of micropores per gram (regarded as completely filled with adsorbed gas molecules), *D* is the constant related to net adsorption heat, and n is the parameter related to temperature and pore distribution of coal. The isothermal adsorption tests of 18 coal samples are performed at 30°C; therefore, n is mainly related to the pore size distribution. When $n = 2$, the D-A model becomes the D-R model, and *V0* in the D-R model falls in the range of 7.171–14.747 m^3/g and *V0* in the D-A model is in the range of 7.238–15.120 m^3/g. The results show that the primary structure coal on working surface F is the smallest and the broken coal on working surface B is the largest, which is the same as the *VL* in the Langmuir model. The *V0* in the D-R model is generally smaller than that in the D-A model, but the *V0* in the D-R model of two mylonitic coal on working face A and E is larger than that in the D-A model. *D* in the D-R model ranges from 0.147 and 0.222, and D in the D-A model is between 0.123 and 0.337. The variation range of adsorption heat constant of the D-A model is wide. From the distribution of adsorption heat constant *D* in the same coal profile and coal structure of the two models, the adsorption heat parameters of the D-A model are obviously more accurate. Obviously, this is due to the introduction of pore structure parameters. n ranges from 0.143 to 2.219. The n of mylonitic coal on working face A and E are larger than 2, the smallest is scaly coal, the largest is mylonitic coal on working face A, and the corresponding adsorption heat constant is the opposite, scaly coal on working face B is the largest, the smallest is mylonitic coal on working face A, which is closely related to the pore characteristics of coal reservoir. The complexity of pore structure in turn affects the decrease of adsorption heat constant.

Adaptability of Structural Coal Adsorption Model

Although the Langmuir, D-R, and D-A models fit the adsorption equation with high correlation, they can be used to describe the adsorption behavior of tectonic coal to methane. However, the standard deviation of the ideal value and fitting value of each parameter is different, which indicates that different models describe different coal samples with different accuracy. In order to analyze the reliability of different models describing coal samples with different coal structures, this study introduces the parameter of average relative error (MRE%) to analyze. The calculation formula of MRE% is as follows:

$$MRE\% = \frac{\sum_{i=1}^{N} \left| \left(V^{\exp} - V^{cal} \right) / V^{\exp} \right|}{N} \times 100,$$

where *Vexp* is the adsorption capacity of experimental test, *Vcal* is the fitting value of the model, taking the pressure of each equilibrium point into the equation, cm^3/g. $n = 7$, corresponds to the seven equilibrium points collected from the experimental test. The average relative error curve of each coal and rock profile model fitting is shown in **Figure 1**. It can be observed that the average relative error has two variation characteristics: a) gradually decreasing; b) small at both ends and large in the middle. Actually, the three models are almost consistent in describing the adsorption accuracy of coal samples with different coal structures. The average relative error of the Langmuir model of minced coal is the largest, then the D-R model, and that of the D-A model is the smallest. For the majority of the fractured coal and mylonitic coal, the average relative error of the Langmuir model is higher than that of the D-R and D-A models, while the average relative error of fractured coal sample on working face A is significantly higher than that of the Langmuir and D-A models. The average relative error of scaly coal ranges from the Langmuir model to the D-R to D-A models, and the average relative error manifests an inverted “V” shape. For broken coal on working face A, the average relative error is not different. On the same coal rock section, the average relative error of the Langmuir model and D-R model is complex with the aggravation of coal structure deformation, and there is no obvious rule. However, the D-A model generally shows the trend of decreasing with the aggravation of coal structure deformation.

The average relative error is a comprehensive reflection of the standard deviation of each model parameter, through which the fitting accuracy of each model can be directly reflected. From the above analysis, it can be seen that for the three models, the Langmuir model has a certain adaptability to different deformation types of tectonic coal, but the change is larger with the coal sample, while the D-R model is obviously not suitable for describing the scale coal and the D-A model has high adaptability to all kinds of coal structure types, also the stronger coal deformation will contribute to higher accuracy.

CONCLUSION

Under the condition of 30°C and 12 MPa maximum pressure, CH_4 adsorption isotherm experiments was carried out on 18 primary structure coal, catallactic coal, granulated coal, scaly coal, and mylonitic coal with different coal structures under the condition of equilibrium water. The results show that the isothermal adsorption capacity of coal increases with the increase of pressure and increases with the increase of structural deformation under the same pressure. However, the isothermal adsorption capacity of coal samples with strong deformation degree is not greater than that of coal samples with weak deformation degree. It is obvious that structural deformation has a significant impact on the adsorption of coal, but it is not the only factor. Key insights regarding adaptability of theoretical model on adsorption behavior of coal are summarized.

1) The Langmuir model, D-R model, and D-A model can be used to describe the CH_4 adsorption behavior of 18 coal samples. There is no consistent rule for the alteration of *VL* of Langmuir volume, but from primary structure coal to crushed coal, *VL* increases with the increase of coal structure, and the change of *VL* of mylonitic coal in different coal rock sections is complex. Generally speaking, the pressure *VP* increases with the increase of the volume *VL*. The variation trend of *V0* in D-R and D-A is the same as that in the Langmuir model. *V0* in the D-R model is generally smaller than that in the D-A model, but *V0* in the D-R model is larger than that in the D-A model. The variation range of adsorption heat constant of the D-A model is larger than that of the D-R model, due to the introduction of pore structure parameters.
2) The standard deviation of the Langmuir model is generally larger than that of the D-R and D-A models, and the standard deviation of adsorption heat constant *D* is very small. In theory, the D-A model is more accurate than the D-R model due to the introduction of parameter *n*, but its parameters are less accurate. The standard deviation of *D* is larger than that of the D-R model.
3) According to the analysis of the average relative error of different models for 18 coals with different coal structures, it can be demonstrated that the Langmuir model has certain adaptability for different deformation types of structural coal, while the D-R model is obviously not suitable for describing flake coal and part of broken coal. The D-A model has high adaptability for all kinds of coal structure types, and the stronger coal deformation will contribute to its higher accuracy.

DATA AVAILABILITY STATEMENT

The raw data supporting the conclusions of this article will be made available by the authors, without undue reservation.

AUTHOR CONTRIBUTIONS

GW—investigation; LP—funding acquisition and supervision; BH—investigation and supervision; JL—methodology; YZ—investigation; RZ—data analysis; ZS—manuscript drafting.

FUNDING

The authors would like to acknowledge the funding by Chongqing Science and Technology Bureau project (No. cstc2017jcyjBX0076) and Fundamental Research Funds for the Central Universities (No. 2019XKQYMS25).

REFERENCES

Amankwah, K. A. G., and Schwarz, J. A. (1995). A Modified Approach for Estimating Pseudo-vapor Pressures in the Application of the Dubinin-Astakhov Equation. *Carbon* 33 (9), 1313–1319. doi:10.1016/0008-6223(95)00079-s

Chen, C., Xian, X., Zhang, D., et al. (1998). Study on Adsorption Characteristics of Anthracite and Carbon for Methane by Micropore Filling Theory [J]. *J. Chongqing Univ.* 21 (2), 75–79.

Clarkson, C. R., Bustin, R. M., and Levy, J. H. (1997). Application of the Mono/multilayer and Adsorption Potential Theories to Coal Methane Adsorption Isotherms at Elevated Temperature and Pressure. *Carbon* 35, 1689–1705. doi:10.1016/s0008-6223(97)00124-3

Crosdale, P. J., Beamish, B. B., and Valix, M. (1998). Coalbed Methane Sorption Related to Coal Composition. *Int. J. Coal Geology.* 35, 147–158. doi:10.1016/s0166-5162(97)00015-3

Dai, S., Zhang, B., Peng, S., et al. (2009). Discussion on the Adsorption Model of CO2 and CH4 on Late Paleozoic Coal in Kailuan Mining Area of Hebei Province [J]. *Acta geologica Sinica* 83 (5), 731–737.

Fu, X. (2001). *Physical Simulation and Numerical Simulation of Physical Properties of Coal and Rock Mass in Multiphase media [D]*. Xuzhou, Jiangsu: China University of mining and technology.

Jiang, B., and Ju, Y. (2004). Structural Coal Structure and Reservoir Properties [J]. *Nat. gas industry* 24 (5), 27–29.

Jiang, B., Qin, Y., and Jin, F. (1998). Deformation Characteristics of Coal Ultrastructure under High Temperature and High Pressure [J]. *Geoscience* 33 (1), 17–24.

Jiang, B., Qin, Y., Ju, Y., et al. (2009). Coupling Mechanism between Chemical Structure Evolution and Gas Characteristics of Tectonic Coal [J]. *Frontier of Geosciences* 16 (2), 262–270.

Ju, Y. (2003). *Structural Evolution of Tectonic Coal, Physical Properties of Reservoir and its Working Mechanism [D]*. Xuzhou: China University of mining and technology.

Laxminarayana, C., and Crosdale, P. J. (1999). Role of Coal Type and Rank on Methane Sorption Characteristics of Bowen Basin, Australia Coals. *Int. J. Coal Geology.* 40, 309–325. doi:10.1016/s0166-5162(99)00005-1

Li, H. (2001). Major and Minor Structural Features of a Bedding Shear Zone along a Coal Seam and Related Gas Outburst, Pingdingshan coalfield, Northern China. *Int. J. Coal Geology.* 47 (2), 101–113. doi:10.1016/s0166-5162(01)00031-3

Ozawa, S., Kusumi, S., and Ogino, Y. (1976). Physical Adsorption of Gases at High Pressure. IV. An Improvement of the Dubinin-Astakhov Adsorption Equation. *J. Colloid Interf. Sci.* 56, 83–91. doi:10.1016/0021-9797(76)90149-1

Qingdao Institute of chemical technology (2002b). *Data Manual of Chemical and Physical Properties (Inorganic) [M]*. Beijing: Chemical Industry Press.

Qingdao Institute of chemical technology (2002a). *Data Manual of Chemical and Physical Properties (Organic) [M]*. Beijing: Chemical Industry Press.

Sang, S., Zhu, Y., and Zhang, J. (2005). Experimental Study on the Effect of Liquid Water on Methane Adsorption by Coal: a Case Study of Coal Reservoir in Southern Qinshui Basin [J]. *Sci. Bull.* 50 (Zeng 1), 70–75. doi:10.1007/bf03184087

Shuxun, S., Hongjie, X., Liangcai, F., Guojun, L., and Huazhou, H. (2010). Stress Relief Coalbed Methane Drainage by Surface Vertical Well in China. *international J. coal geology[J]* 82, 196–203.

Su, X., Zhang, L., and Lin, X. (2005). Effect of Coal Rank on Adsorption Capacity of Coal [J]. *Nat. gas industry* 25 (1), 19–21.

Sun, Z., Li, X., Liu, W., Zhang, T., He, M., and Nasrabadi, H. (2020). Molecular Dynamics of Methane Flow Behavior through Realistic Organic Nanopores under Geologic Shale Condition: Pore Size and Kerogen Types. *Chem. Eng. J.* 398, 124341. doi:10.1016/j.cej.2020.124341

Sun, Z., Shi, J., Wu, K., Zhang, T., Feng, D., and Li, X. (2019). Effect of Pressure-Propagation Behavior on Production Performance: Implication for Advancing Low-Permeability Coalbed-Methane Recovery. *SPE J.* 24 (02), 681–697. doi:10.2118/194021-pa

Wang, G., and Zhu, Y. (1998). On Coal Seam Rheology. *J. China Univ. mining Technol.* (3), 16–25.

Wu, G. (2010). *Microstructure and Adsorption Characteristics of Tectonic Coal in Huainan Mining Area [D]*. Xuzhou: Master's thesis of China University of mining and Technology.

Zhang, L., Su, X., and Zeng, R. (2006). Discussion on the Control of Coal Properties on Coal Adsorption Capacity [J]. *Acta geologica Sinica* 80 (6), 910–915.

Zhang, S., and Sang, S. (2008). Effect of Liquid Water on Methane Adsorption of Different Coal Grades and its Mechanism [J]. *Acta geologica Sinica* 82 (10), 1350–1354.

Zhang, X., Liu, H., et al. (2009). Adsorption Response and Control Mechanism of Coal Structure Difference [J]. *Geosci. J. China Univ. Geosciences* 34 (5), 848–854.

Zhang, Y., Zhang, Z., and Cao, Y. (2007). Journal of Structural Coal Structure and Gas Outburst [J]. 3 (23), 281–284.

Zhao, X., Huang, B., and Xu, J. (2019). Experimental Investigation on the Characteristics of Fractures Initiation and Propagation for Gas Fracturing by Using Air as Fracturing Fluid under True Triaxial Stresses. *Fuel* 236, 1496–1504. doi:10.1016/j.fuel.2018.09.135

Zhao, Z., and Tang, X. (2002). Discussion on Langumir Equation of Methane Adsorption by Coal [J]. *J. Jiaozuo Inst. Technol.* 21 (1), 1–4.

Zhong, L. (2004). Adsorption Properties of Coal and its Influencing Factors [J]. *Earth Sci. J. China Univ. Geosciences* 29 (3), 327–332.

Zhong, L., Zhang, H., Yuan, Z., and Lei, C. (2002). Effect of Specific Surface Area and Pore Volume of Coal on Adsorption Capacity of Coal [J]. *Coalfield Geology. Exploration* 30 (3), 26–29.

Zhou, Y., and Zhou, L. (1997). Study on Adsorption Isotherm of Supercritical Hydrogen on Activated Carbon [J]. *Acta physicochemical Sinica* 13 (2), 119–126.

Conflict of Interest: The authors declare that the research was conducted in the absence of any commercial or financial relationships that could be construed as a potential conflict of interest.

frontiers in Earth Science

ORIGINAL RESEARCH
published: 13 September 2021
doi: 10.3389/feart.2021.759862

Numerical Simulation Study of Tracking the Displacement Fronts and Enhancing Oil Recovery Based on Ferrofluid Flooding

Tao Huang, Fuquan Song, Renyi Wang and Xiaohe Huang*

School of Petrochemical Engineering and Environment, Zhejiang Ocean University, Zhoushan, China

Water flooding is crucial means to improve oil recovery after primary production. However, the utilization ratio of injected water is often seriously affected by heterogeneities in the reservoir. Identification of the location of the displacement fronts and the associated reservoir heterogeneity is important for the management and improvement of water flooding. In recent years, ferrofluids have generated much interest from the oil industry owning to its unique properties. First, saturation of ferrofluids alters the magnetic permeability of the porous medium, which means that the presence of ferrofluids should produce magnetic anomalies in an externally imposed magnetic field or the local geomagnetic field. Second, with a strong external magnetic field, ferrofluids can be guided into regions that were bypassed and with high residual oil saturation. In view of these properties, a potential dual-application of ferrofluid as both a tracer to locate the displacement front and a displacing fluid to improve recovery in a heterogeneous reservoir is examined in this paper. Throughout the injection process, the magnetic field generated by electromagnets and altered by the distribution of ferrofluids was calculated dynamically by applying a finite element method, and a finite volume method was used to solve the multiphase flow. Numerical simulation results indicate that the displacement fronts in reservoirs can indeed be detected, through which the major features of reservoir heterogeneity can be inferred. After the locations of the displacement fronts and reservoir heterogeneities are identified, strong magnetic fields were applied to direct ferrofluids into poorly swept regions and the efficiency of the flooding was significantly improved.

Keywords: ferrofluid, tracking displacement front, enhance oil recovery, heterogeneous reservoir, numerical simulation

Edited by:
Zhiyuan Wang,
China University of Petroleum
(Huadong), China

Reviewed by:
Mingzheng Yang,
Louisiana State University,
United States
Ye Tian,
Southwest Petroleum University,
China
Fei Liu,
China University of Petroleum
(Huadong), China

****Correspondence:***
Tao Huang
huangtao@zjou.edu.cn

Specialty section:
This article was submitted to
Economic Geology,
a section of the journal
Frontiers in Earth Science

Received: *17 August 2021*
Accepted: *31 August 2021*
Published: *13 September 2021*

Citation:
Huang T, Song F, Wang R and Huang X (2021) Numerical Simulation Study of Tracking the Displacement Fronts and Enhancing Oil Recovery Based on Ferrofluid Flooding.
Front. Earth Sci. 9:759862.
doi: 10.3389/feart.2021.759862

INTRODUCTION

Ferrofluids are stable colloids composed of small nano-scale solid, magnetic particles coated with a molecular layer of dispersant and suspended in a liquid carrier (Rosensweig, 1997). Thermal agitation keeps the particles suspended, and the coatings prevent the particles from coagulation. Its behavior and property can be controlled and changed by the magnetic field (Odenbach, 2008). Therefore, ferrofluid has many industrial applications, such as dynamic sealing, inertial and viscous damper, magnetic drug targeting, liquid microrobots, and so on (Raj and Moskowitz, 1990; Hou et al., 1999; Scherer and Figueiredo, 2005; Fan et al., 2020).

In the past years, ferrofluid flow in porous media has been the subject of various experimental and numerical studies. Borglin, Moridis, and Oldenburg et al. investigated the flow behavior of ferrofluid in porous media, the results showed that the effect of an external magnetic field on the flow of a ferrofluid in porous media is equivalent to the imposition of a magnetic body force, which means the flow of ferrofluids can be guided (Moridis et al., 1998; Oldenburg and Moridis, 1998; Borglin et al., 2000; Oldenburg et al., 2000). The above works, however, did not consider the impact of the ferrofluid on the magnetic field. The presence of ferrofluids should produce anomalies in the magnetic field because these fluids alter the magnetic permeability. Such anomalies, in principle, can be detected by magnetic anomaly detectors. Based on this feature, Sengupta (Sengupta, 2012) proposed an innovative approach to determining the fracture length and width by injecting ferrofluids into the fracture. When applying an external magnetic field, the ferrofluids in the fracture shall generate a secondary magnetic field which will have a definite phase difference from the original magnetic field. Once the phase difference is detected and processed by software an accurate representation of fractures can be made. Schmidt (Schmidt and Tour, 2012) proposed methods for magnetic imaging of geological structures, the principle is similar to Sengupta. Rahmani et al. used a ferrofluid slug to track the movement of a flooding front and studied reservoir permeability heterogeneity (Rahmani et al., 2014; Rahmani et al., 2015).

Water flooding, as is well recognized, is an effective approach to maintain reservoir pressure and improve oil recovery. However, heterogeneities or fractures present in China's continental reservoirs can significantly decrease the sweep efficiency, leading to poor utilization ratios and low oil recovery. There is still a great potential to enhance the recovery (Han, 1995; Yu, 2000; Han, 2007; Yang, 2009; Han 2010). Therefore, it is urgent to find new oil displacement technology and method to overcome the problem of low oil displacement efficiency caused by reservoir heterogeneity and complex structure. In this paper, we study the potential of using ferrofluid both as a tracer and controllable displacing fluid during the whole flooding process. First, since the superparamagnetic nanoparticles in the ferrofluid can change the magnetic permeability of the flooded region, we study the magnetic anomalies and indicate the locations of displacement fronts, as shown in **Figure 1A**. And then as a displacing fluid that, guided by strong magnetic fields, can overcome reservoir heterogeneities and improve sweep efficiency and oil recovery, as shown in **Figure 1B**.

COMPUTATIONAL METHODOLOGY

Magnetic Field Calculation

In a quasi-static magnetic problem, the relations between the magnetic field strength **H**, the magnetic flux density **B**, the current density **J**, and the magnetization **M** are given by Maxwell equations and the magnetic properties of the material of concern:

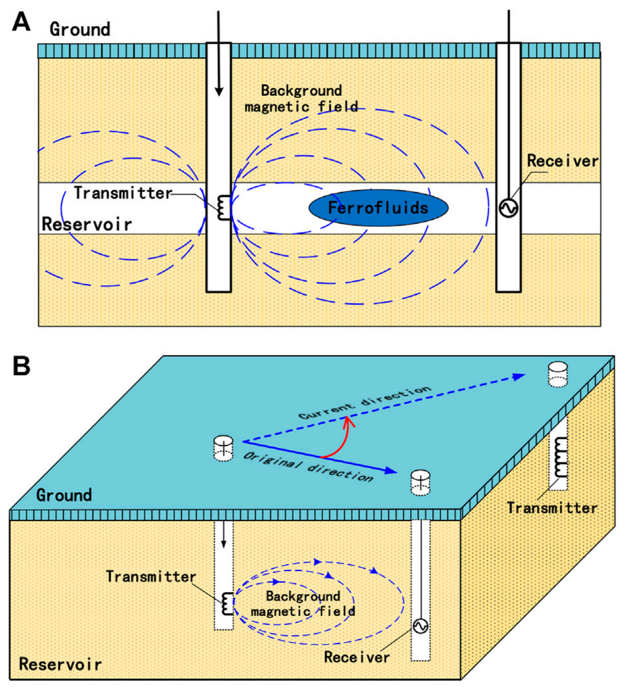

FIGURE 1 | Schematic diagram of ferrofluid flooding technology: **(A)** Displacement front monitoring and tracking; **(B)** Displacement direction guiding and controlling.

$$\nabla \times \mathbf{H} = \mathbf{J} \tag{1}$$

$$\nabla \cdot \mathbf{B} = 0 \tag{2}$$

$$\mathbf{B} = \mu_0 (\mathbf{H} + \mathbf{M}) \tag{3}$$

Where μ_0 is the permeability of vacuum.

Introducing the vector potential **A**, which is defined by:

$$\mathbf{B} = \nabla \times \mathbf{A} \tag{4}$$

with the additional assumption that $\nabla \cdot \mathbf{A} = 0$, considering **Eqs 3–5** can be transformed into

$$\nabla \times \left(\frac{1}{\mu_0} \nabla \times \mathbf{A} - \mathbf{M} \right) = \mathbf{J} \tag{5}$$

In order to solve the differential **Eq. 5**, it is formulated into a boundary value problem by using the energy functional (Silvester and K. Chari, 1970; Kamminga, 1975)

$$I = \int_{\Omega} \left(\frac{1}{\mu_0} \int \mathbf{B} \cdot d\mathbf{B} - \int \mathbf{M} \cdot d\mathbf{B} - \mathbf{J} \cdot \mathbf{A} \right) dV \tag{6}$$

where Ω is the area of the region of study.

The variation δI caused by a small variation of $\delta \mathbf{A}$ is equal to

$$\delta I = \int_{\Omega} \left(1/\mu_0 \mathbf{B} \cdot \delta \mathbf{B} - \mathbf{M} \cdot \delta \mathbf{B} \right) dV - \int_{\Omega} \mathbf{J} \cdot \delta \mathbf{A} dV \tag{7}$$

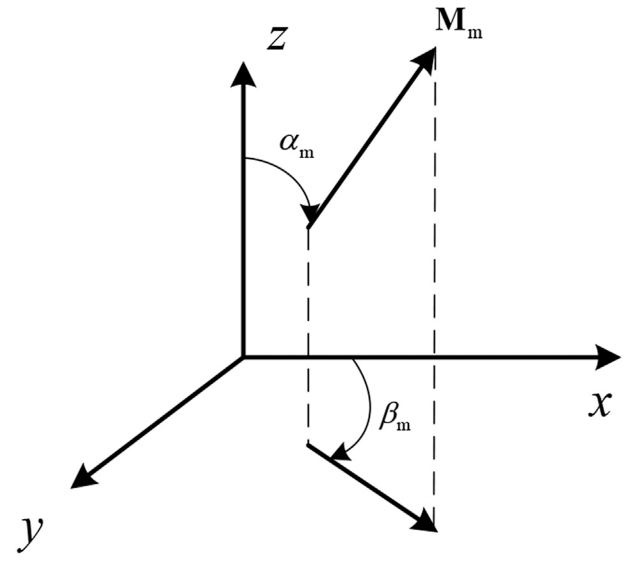

FIGURE 2 | Diagram of the magnetization direction of permanent magnet.

Since the energy functional is stationary to any small variation in $\mathbf{A}$, the variation δI must be zero, which gives

$$\int_\Omega \left(1/\mu_0 \mathbf{B}\cdot\delta\mathbf{B} - \mathbf{M}\cdot\delta\mathbf{B}\right)\, dV - \int_\Omega \mathbf{J}\cdot\delta\mathbf{A} dV = 0 \tag{8}$$

In regions occupied by a ferrofluid, the magnetic solid particles in the ferrofluid become polarized with the imposition of an external magnetic field, and the ferrofluid is said to be "magnetized." In this paper, we considered a water-based ferrofluid Hinano-FFW provided by a nanomaterials company in China. Although the composition of the fluid was not revealed, the magnetization curve of the fluid was provided to us. Ferrofluid magnetization curves are generally approximated by simple two-parameter arctan functions of the form (Oldenburg et al., 2000):

$$M_\mathrm{ff} = \alpha\times\arctan\left(\beta\times H\right) \tag{9}$$

where the subscript ff stands for ferrofluid. For our particular fluid, $\alpha = 1{\times}10^4$, $\beta = 3.5\times10^{-5}$.

Considering a permanent magnet, and the magnetization $\mathbf{M}_\mathrm{m}$ can be defined by:

$$\mathbf{M}_\mathrm{m} = M_\mathrm{m}\sin\alpha_\mathrm{m}\cos\beta_\mathrm{m}\mathbf{i} + M_\mathrm{m}\sin\alpha_\mathrm{m}\sin\beta_\mathrm{m}\mathbf{j} + M_\mathrm{m}\cos\alpha_\mathrm{m}\mathbf{k} \tag{10}$$

Where M_m is the residual magnetization of a permanent magnet, α_m is the angle between the direction of the magnetization of the permanent magnet and the positive direction of the z axis, β_m is the angle between the direction of the magnetization of the permanent magnet and the positive direction of the x axis, as shown in **Figure 2**.

In this paper, we consider the 2-D problem and the quasi-static magnetic problem solved by the finite element method. The magnetization $\mathbf{M}_\mathrm{m}$ of a permanent magnet can be simplified:

$$\mathbf{M}_\mathrm{m} = M_\mathrm{m}\sin\alpha_\mathrm{m}\cos\beta_\mathrm{m}\mathbf{i} + M_\mathrm{m}\sin\alpha_\mathrm{m}\sin\beta_\mathrm{m}\mathbf{j} \tag{11}$$

Thus, the magnetization term $\mathbf{M}$ in the **Eq. 8** consists of two parts:

$$\mathbf{M} = \mathbf{M}_\mathrm{ff} + \mathbf{M}_\mathrm{m} \tag{12}$$

The computational region Ω was discretized by triangular grids. The current density $\mathbf{J}$ and the vector potential $\mathbf{A}$ only have component in z direction:

$$\mathbf{A} = (0,\ 0,\ A),\ \mathbf{J} = (0,\ 0,\ J) \tag{13}$$

From the requirement that the energy functional takes a stationary value, a set of n equations are obtained:

$$\frac{\partial I}{\partial A_i}\left(A_1,\ldots,A_n\right) = 0,\ \ i = 1,\ldots,n \tag{14}$$

where n is the number of grid point.

Substituting **Eqs 8**, **9**, **11**, **12** into **Eq. 14**, we obtain **Eq. 15** as follows:

$$\begin{aligned}&\int_\Omega \frac{1}{\mu_0}\left(B_x\frac{\partial B_x}{\partial A_i} + B_y\frac{\partial B_y}{\partial A_i}\right)\, dV - \int_\Omega\left(M_\mathrm{m}\sin\alpha_\mathrm{m}\cos\beta_\mathrm{m}\frac{\partial B_x}{\partial A_i}\right.\\ &\left.+ M_\mathrm{m}\sin\alpha_\mathrm{m}\sin\beta_\mathrm{m}\frac{\partial B_y}{\partial A_i}\right)dV - \int_\Omega\left[\alpha\arctan\left(\frac{\beta}{\mu_0}B_x\right)\frac{\partial B_x}{\partial A_i}\right.\\ &\left.+ \alpha\arctan\left(\frac{\beta}{\mu_0}B_y\right)\frac{\partial B_y}{\partial A_i}\right]dV - \int_\Omega J\frac{\partial A}{\partial A_i}\, dV = 0\end{aligned} \tag{15}$$

The potential in the k-th triangular element is assumed to be equal to

$$A^k = \frac{1}{2\Delta^k}\sum_i\left(a_i + b_i x + r_i y\right)A_i,\qquad i = 1, 2, 3 \tag{16}$$

where Δ^k is the volume of k-th element, A_i is the potential at the element's vertex, a_i,b_i,r_i are the coefficients associated with the element's vertex positions x_i,y_i:

$$\begin{aligned}a_1 &= x_2y_3 - x_3y_2, & b_1 &= y_2 - y_3, & r_1 &= x_3 - x_2\\ a_2 &= x_3y_1 - x_1y_3, & b_2 &= y_3 - y_1, & r_1 &= x_1 - x_3\\ a_3 &= x_1y_2 - x_2y_1, & b_3 &= y_1 - y_2, & r_1 &= x_2 - x_1\end{aligned} \tag{17}$$

Because the magnetic flux density $\mathbf{B} = \nabla\times\mathbf{A}$, considering **Eq. 16**, the components of magnetic induction can be obtained:

$$B_x^k = \frac{1}{2\Delta^k}\sum_i r_iA_i,\quad B_y^k = -\frac{1}{2\Delta^k}\sum_i b_iA_i \tag{18}$$

Take the **Eqs 16**, **18** into **Eq. 15**, we can obtain a set of nonlinear equations:

$$F_q\left(A_1,\ldots,A_n\right) = 0,\ \ q = 1,\ldots,n \tag{19}$$

and the solution was obtained by using the Newton-Raphson iterative method. Once the vector potential $\mathbf{A}$ was obtained, one can calculate the magnetic flux density by $\mathbf{B} = \nabla\times\mathbf{A}$.

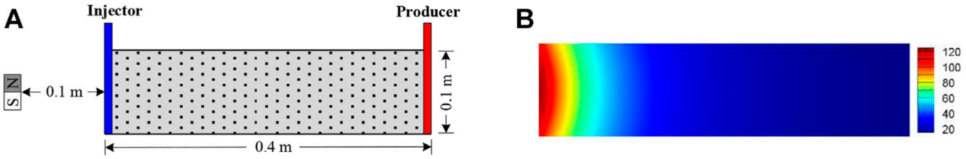

FIGURE 3 | Simple porous media model. **(A)** Model geometry; **(B)** Distribution of background magnetic flux density norm |B| in units of Gs.

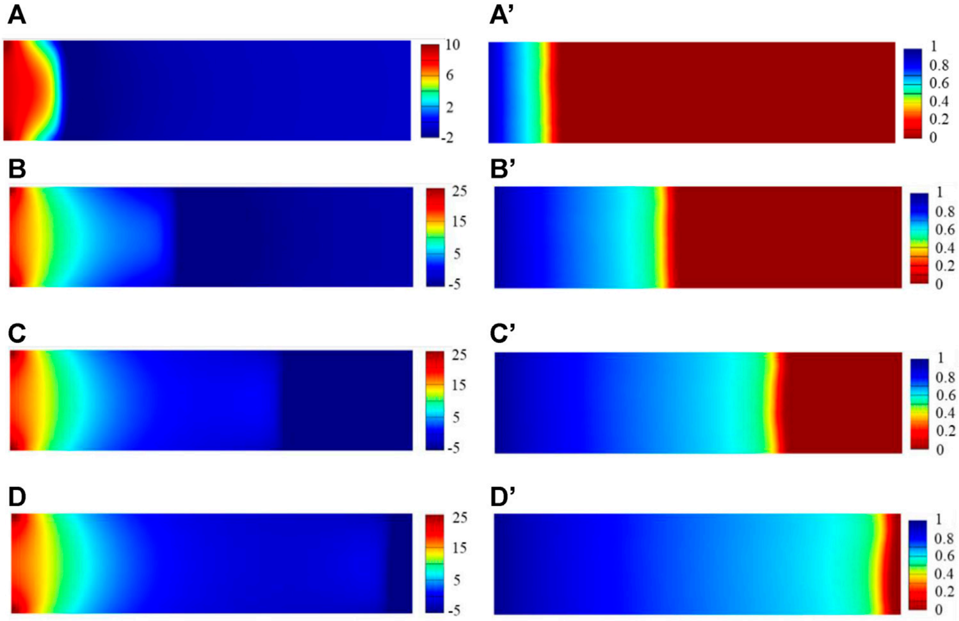

FIGURE 4 | The ferrofluid saturation and magnetic anomaly distribution of numerical simulation at different time. **(A–D)** respectively show the magnetic anomaly at 10, 30, 50, 70 min; **(A′-D′)** respectively show the saturation distribution at 10, 30, 50, 70 min.

Simulation of Ferrofluid Flowing in Porous Media

The magnetization of bulk ferrofluid increases with increasing external magnetic field strength, following **Eq. 9**. In the case of immiscible two-phase flows in porous media, and additional assumption that magnetization increases linearly with ferrofluid's saturation was given by:

$$M(S_{\mathrm{ff}}) = M(S_{\mathrm{ff}} = 1)S_{\mathrm{ff}} \tag{20}$$

When an external magnetic field is applied, the ferrofluid receives a magnetic body force $\mathbf{F}_m = \mu_0 M \nabla H$. This additional magnetic force term is added to the multiphase Darcy's Equation (Oldenburg et al., 2000):

$$\mathbf{v}_{\mathrm{ff}} = -\frac{k_{r\mathrm{ff}}}{\mu_{\mathrm{ff}}}\mathbf{k}\cdot\left(\nabla p_{\mathrm{ff}} - \rho_{\mathrm{ff}} g \nabla D - \mu_0 M \nabla H\right) \tag{21}$$

where $\mathbf{k} = (k_x, k_y, k_z)$ is the permeability tensor, k_r is the relative permeability, μ is fluid viscosity, p is the fluid pressure, ρ is the fluid density, and D denotes the depth which is positive on the upward side, g is the gravitational acceleration.

For simplicity, we considered the flow as isothermal and incompressible. Such simplifications are common in the analysis of water flooding. From the law of mass conservation, we know that a fluid in a control volume should meet:

$$\int_{\partial V} -\left(\rho_\beta \mathbf{v}_\beta\right)\cdot \mathbf{n}\ dA + \int_V q_{\mathrm{m}\beta}\ dV = \int_V \frac{\partial}{\partial t}\left(\rho_\beta \phi S_\beta\right)\ dV \tag{22}$$

where the subscript $\beta = (\mathrm{o}, \mathrm{w}, \mathrm{ff})$ distinguishes the fluid, $\mathbf{n}$ is the outward normal unit vector of region boundary ∂V, $q_{\mathbf{m}\beta}$ is the source term that represents mass change per unit time and unit volume, ϕ is the porosity.

Using a finite volume method to discretize the mass conservation equation, and the discrete nonlinear equation was also solved by using the Newton-Raphson iterative method.

EXAMPLES AND DISCUSSIONS

Tracking the Displacement Fonts of Ferrofluid Flooding

The first example that we considered is a horizontal porous media model as shown in **Figure 3A**, the left and right boundary is

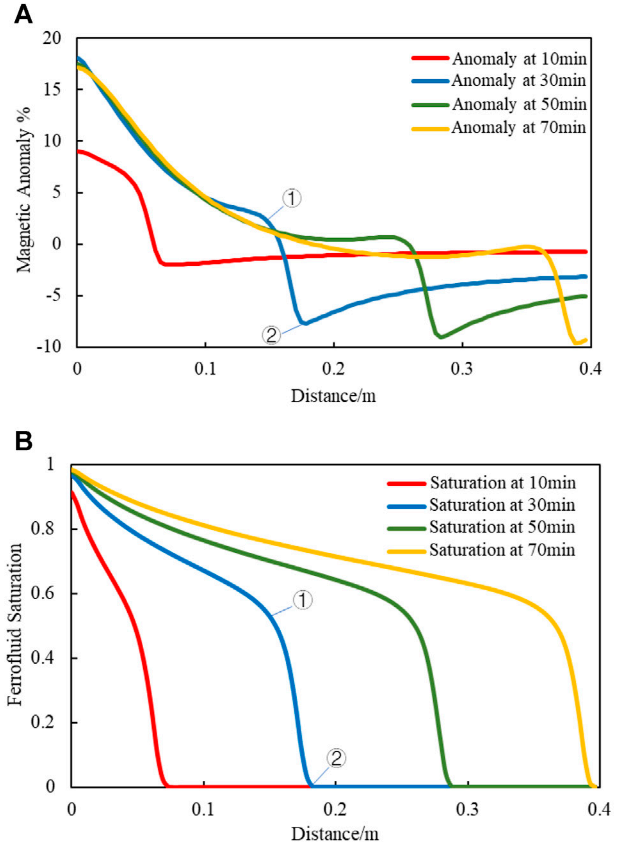

FIGURE 5 | The ferrofluid saturation and magnetic anomaly curves along the porous media at 10, 30, 50,70 min. **(A)** Magnetic anomaly curves; **(B)** Saturation curves.

injector and producer, respectively. We assumed the top and bottom of porous media are closed boundaries. This model can be used to approximate flooding with a line drive pattern. The porosity is 0.2 and the permeability is 100 mD(10^{-3} μm^2). A tiny permanent magnet was placed on the left side of porous media to generate a background magnetic field, the dimension is 2 cm × 4 cm and the residual flux density of the magnet is 1.19T, the background magnetic field is shown in **Figure 3B**.

In the beginning, the model was saturated with oil, and the oil viscosity equals 5 mPa·s and the density equal 850 kg/m^3. Then we used ferrofluid to flooding this porous media, viscosity and density of ferrofluid are 3 mPa·s and 1,187 kg/m^3, respectively. The relative permeability of the ferrofluid phase $k_{rff} = S_{ff}^2$. The relative permeability of the oil phase $k_{ro} = (1 - S_{ff})^2$. Both injection and production rates were set to 0.01 V_p/min, where V_p is the total pore volume. Since a week magnetic field generated by a tiny magnet, we assumed the magnetic force generated on the ferrofluid was neglected in this case.

The magnetic anomaly is defined as:

$$|\mathbf{B}|_{\text{anomaly}} = \frac{|\mathbf{B}|_{\text{current}} - |\mathbf{B}|_{\text{background}}}{|\mathbf{B}|_{\text{background}}} (\%) \tag{23}$$

where $|\mathbf{B}|_{\text{current}}$ is the norm magnetic flux density during ferrofluid flooding, and $|\mathbf{B}|_{\text{background}}$ is the normal of the magnetic flux density provided by the magnet before the ferrofluid flooding starts.

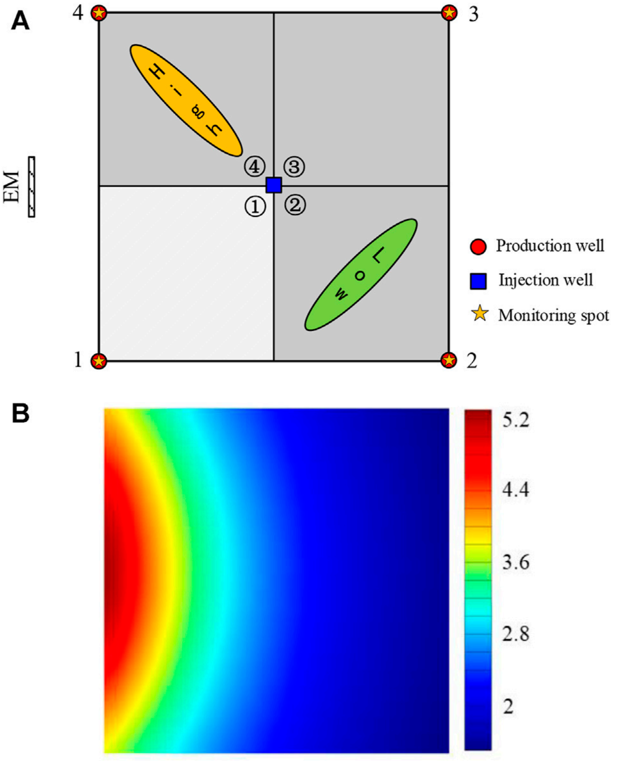

FIGURE 6 | A five-spot heterogeneous reservoir model. **(A)** Model geometry; **(B)** Distribution of background magnetic flux density norm $\log_{10}|B|$ in units of Gs.

As **Figure 4** shown, the distribution of magnetic anomalies is basically consistent with the ferrofluid saturation distribution. Near the injector is a high magnetic anomalous area because of the highest ferrofluid saturation, however, the decrease of ferrofluid saturation from the injector to the displacement font leads to a magnetic anomaly decrease.

Figure 5 shows the ferrofluid saturation and magnetic anomaly curves from the left side to the right side of the porous media at several flooding periods. Note that the inflection point of each anomaly curve basically corresponds to the displacement fonts. For example, point 1 and point 2 of the anomaly curve at 30 min in **Figure 5A**, correspond to point 1 and point 2 of the saturation curve at 30 min in **Figure 5B**. It is worth noting that the area between these two points is exactly the displacement front. Thus, this remarkable fact indicates that one can track the ferrofluid fonts based on the magnetic anomaly information at every displacement stage.

Evaluation of the Major Features of Reservoir Heterogeneity

It can be seen from the above section, that the ferrofluid displacement front can be tracked by capturing magnetic anomalies. Furthermore, the flow path of the ferrofluid can be

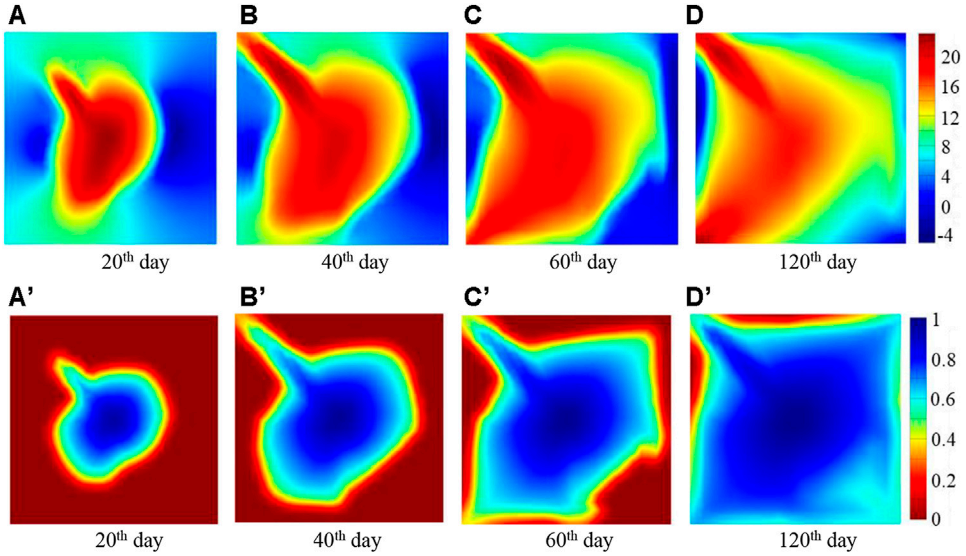

FIGURE 7 | The magnetic anomaly and ferrofluid saturation distribution at different time. **(A–D)** respectively show the magnetic anomaly at 20th, 40th, 60th, 120th day; **(A′–D′)** respectively show the ferrofluid saturation at 20th, 40th, 60th, 120th day.

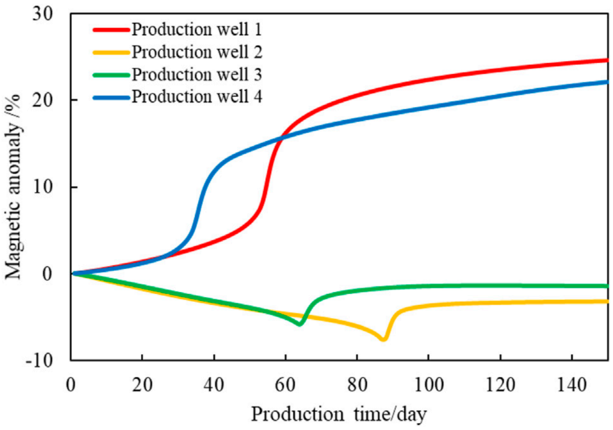

FIGURE 8 | Magnetic anomaly curves of production well in different reservoir regions.

obtained from the displacement front position, thus, the major geological characteristics of the reservoir can be inferred.

Consider a five-spot heterogeneous reservoir as **Figure 6A** shows, the reservoir size is 100 m × 100 m. The heterogeneous reservoir is divided into four regions with an injection well in the center and a production well at each of the four corners. The injection and production rates were set to 0.01 V_p/day. Assuming the reservoir has a porosity of 0.2, the permeability in region 1 is $k_1 = 200$ mD, and the permeability in regions 2, 3 and 4 is $k_2 = k_3 = k_4 = 100$ mD. In particular, the second region contains an elliptical low-permeability zone while the fourth region contains an elliptical high-permeability zone. The permeability of the two elliptical zones is 10 and 500 mD, respectively. In the beginning, the model was saturated with oil, and the fluid properties are the same as mentioned above. In order to provide a background magnetic field, an electromagnet EM was placed. The size of EM is 10 m × 0.4 m and the current intensity of EM is 10^5 A/m^2. The background magnetic field is shown in **Figure 6B**.

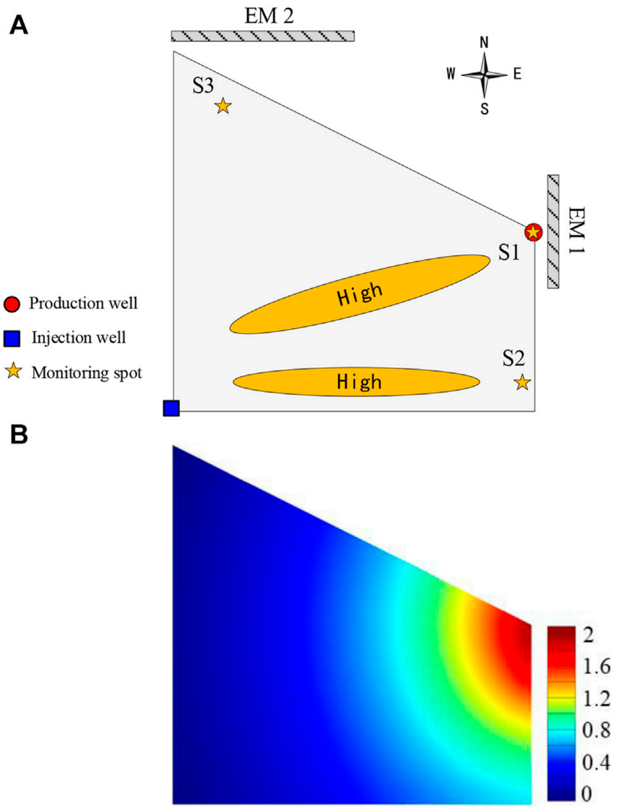

FIGURE 9 | A heterogeneous reservoir model. **(A)** Model geometry; **(B)** Distribution of background magnetic flux density norm $\log_{10}|B|$ in units of Gs.

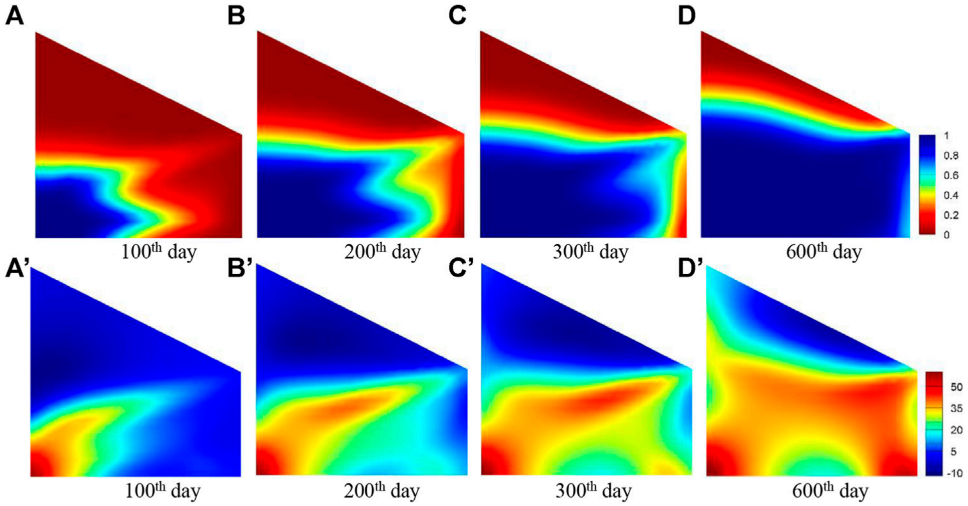

FIGURE 10 | The ferrofluid saturation and magnetic anomaly distribution at different time. **(A–D)** respectively show the ferrofluid saturation at 100th, 200th, 300th, 600th day; **(A′–D′)** respectively show the magnetic anomaly at 100th, 200th, 300th, 600th day.

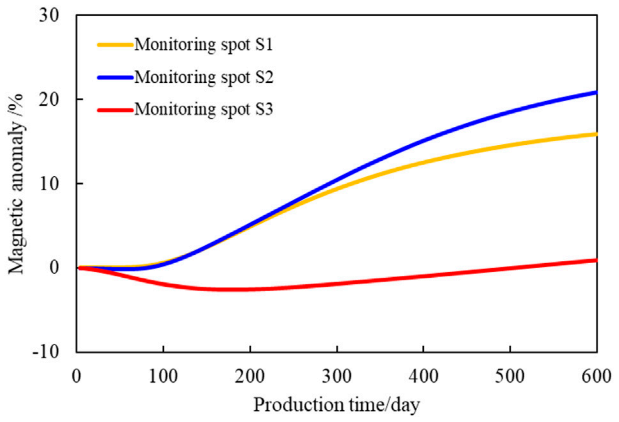

FIGURE 11 | Magnetic anomaly curves of monitoring spots located in different region.

As shown in **Figure 7**, due to the relatively high permeability of region 1 and region 4, the injected ferrofluid propagates faster in these areas, resulting in larger magnetic anomalies. On the contrary, the magnetic anomalies in region 2 and region 3 are relatively small. In particular, the magnetic anomaly in region 4 presents a fingering phenomenon. This is because there is a high permeability elliptical zone in region 4, which makes the injected ferrofluid flow to the production well faster than the other regions. So that the ferrofluid saturation is high at the same time, and resulting in a large magnetic anomaly. However, because the presence of the low permeability elliptical zone in region 2 blocks the flow of ferrofluid to the production well, the ferrofluid in region 2 has a small spread range and low saturation, so the magnetic anomalies are small. In the same way, the lower overall permeability of region 3 is also the reason for the smaller magnetic anomalies.

As shown in **Figure 8**, from the magnetic anomaly curves of production wells in different reservoir regions (star mark in **Figure 6A**), it can be seen that: 1) In the early stage of production, the magnetic anomalies of production well 1, 4 increased and decreased in production well 2, 3. This phenomenon indicates that the injected ferrofluid flows faster in regions 1, 4 than in regions 2, 3, and reflecting indirectly that the permeability of regions 1, 4 is higher than regions 2, 3; 2) Each magnetic anomaly curve has a rapidly rising time point, which corresponds to the moment when the ferrofluid flows into the production well; 3) Because the distribution of magnetic anomalies reflects the distribution of ferrofluid saturation, the magnetic anomaly change information can be used to analyze the flooding process in the reservoir, and so as to recognize the heterogeneous characteristics of the reservoir in general.

Monitoring-Controlling Integrated Ferrofluid Flooding Technology

From the above studies, it can be inferred that the ferrofluid flooding process can be monitored through the magnetic anomaly information, while the major heterogeneity characteristics of the reservoir can be recognized according to the flooding status. In addition, when there is an external magnetic field, the ferrofluid receives a magnetic force, and its flow behavior can be controlled by the magnetic force.

Consider a heterogeneous reservoir as **Figure 9A** shows. Assuming the reservoir has a porosity of 0.25, and the permeability is 500 mD. In particular, the reservoir contains two elliptical high-permeability zones. The permeability of the two elliptical zones is both 1,500 mD. In order to generate magnetic anomalies during the flooding process, an electromagnet EM1 is placed near the eastern part of the reservoir to provide a background magnetic field. The

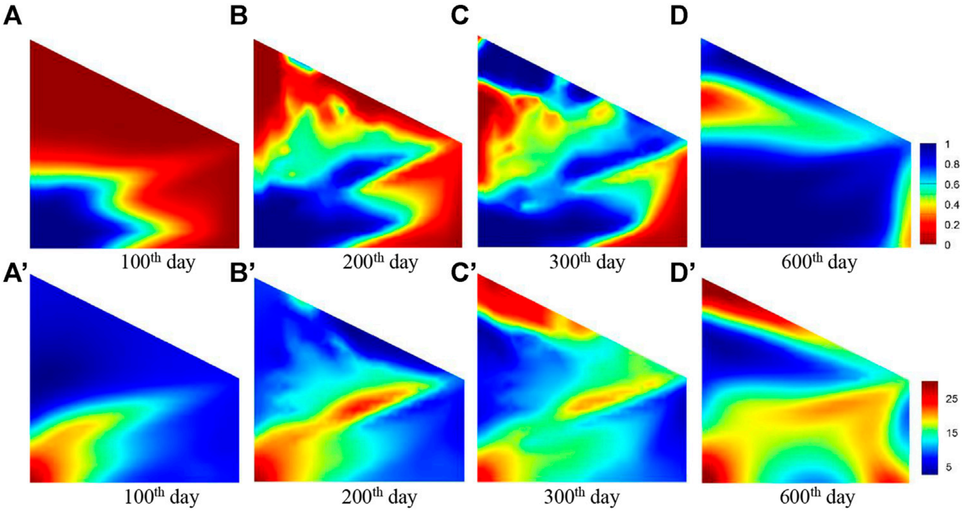

FIGURE 12 | The ferrofluid saturation and magnetic anomaly distribution at different time. **(A–D)** respectively show the ferrofluid saturation at 100th, 200th, 300th, 600th day; **(A′–D′)** respectively show the magnetic anomaly at 100th, 200th, 300th, 600th day.

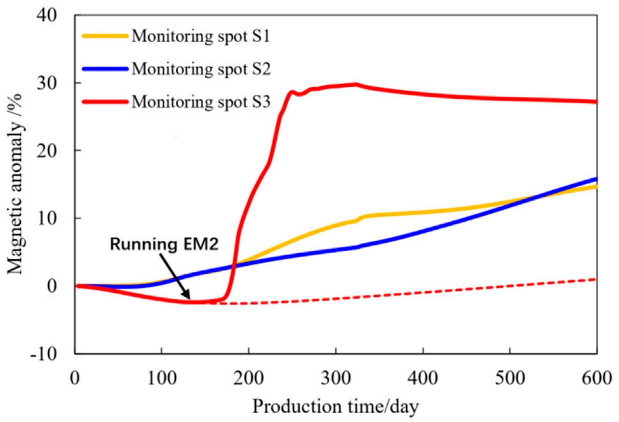

FIGURE 13 | Magnetic anomaly curves of monitoring spots located in different region when apply EM2.

electromagnet EM1 with a size of 5 m × 0.4 m and a current density of 10^5 A/m^2. The background magnetic field is shown in **Figure 9B**. It is worth noting that the background magnetic field is a weak magnetic field, and the generated magnetic force in ferrofluid is very small. So that its influence on the flooding can be ignored. The reservoir is initially saturated with oil, and ferrofluid is used to displace the reservoir. The fluid properties are the same as mentioned above. The injection and production rates were set to 0.025 V_p/day.

As the high-permeability zone is the dominant channel for flow, the injected ferrofluid mainly flows along the high-permeability zone, so the swept areas are mainly concentrated in the central and southern parts of the reservoir. When the $1.5V_p$ ferrofluid was injected, the oil in the central and southern areas of the reservoir was almost completely displaced, but the oil in the northern area of the reservoir was not displaced, as shown in **Figures 10A–D**.

The distribution of magnetic anomalies in **Figures 10A′–D′** shows: 1) At the early stage of flooding, the magnetic anomaly in the central region of the reservoir is relatively large, while the magnetic anomalies in the eastern and northern region of the reservoir are small; 2) At the middle stage of flooding, the magnetic anomaly in the central region of the reservoir is relatively large. These areas gradually increase and spread to the northern region of the reservoir; 3) At the later stage of flooding, the magnetic anomaly in the central and southern regions of the reservoir are generally large, while the magnetic anomaly in the northern region is still low.

From the analysis of the magnetic anomaly changes in the entire flooding process, it can be known that due to the existence of the high permeability zone, the injected ferrofluid is mainly displaced in the central and southern parts of the reservoir, so that the saturation of the ferrofluid is larger, and the magnetic anomaly is larger.

Figure 11 shows the magnetic anomaly curves of different monitoring spots in the reservoir, and the positions of the monitoring spots are shown in **Figure 9A** (star mark). It can be seen from the curves that the ferrofluid mainly flows to the production well and the eastern part of the reservoir because of the existence of the high permeability zone. Therefore, the magnetic anomaly curve of S1 and S2 which is located in the production well and the eastern part of the reservoir gradually increases with the flooding process, while the magnetic anomaly curve of S3 which is located in the northern part of the reservoir basically remains unchanged.

The magnetic anomaly curves of the three monitoring spots show that the injected ferrofluid is more inclined to flood the central and southern areas of the reservoir. Thus, there may be a “dominant flow channel" in this area. The northern part of the

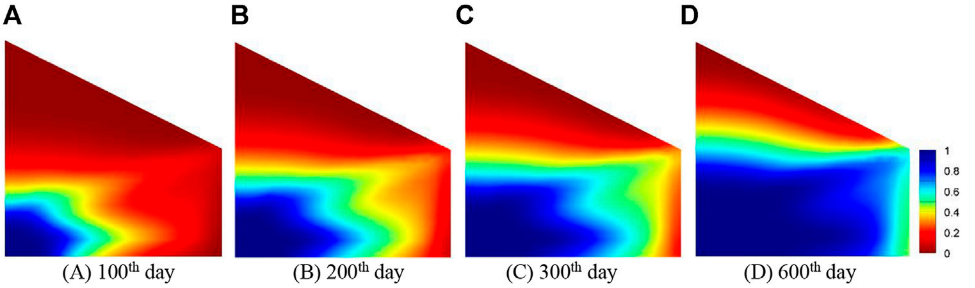

(A) 100th day (B) 200th day (C) 300th day (D) 600th day

FIGURE 14 | The water saturation and magnetic anomaly distribution at different time. **(A–D)** respectively show the water saturation at 100th, 200th, 300th, 600th day.

reservoir has not been affected, and there is still remaining oil in this area, which is the key area for development.

According to the analysis of the above magnetic anomaly curves, it can be seen that the ferrofluid displacement is mainly in the central and eastern parts of the oil reservoir. Therefore, the electromagnet EM2 is deployed near the northern part of the reservoir from the 120th day, and the strong magnetic field generated by EM2 is used to apply a huge magnetic field force on the ferrofluid, leading the ferrofluid to displace to the northern part of the reservoir. The electromagnet EM2 with a size of 10 m × 0.4 m and a current density of 10^8 A/m^2, and has a running time of 200 days.

Figure 12 shows the ferrofluid saturation and magnetic anomaly distribution in the process of ferrofluid flooding after the application of a strong magnetic field. It can be seen that under the control of the external strong magnetic field, the injected ferrofluid can overcome the influence of the reservoir heterogeneity and displace towards the northern part of the reservoir, so that to recover the remaining oil in these areas.

As shown in **Figure 13**, the magnetic anomaly curve of the monitoring spot S3 in the northern part of the reservoir began to rise rapidly (the dotted red line is without a strong magnetic field) after EM2 was applied. This reflects the rapid increase of ferrofluid saturation, meaning that the ferrofluid is guided to displace to the northern part of the reservoir.

In addition, the water flooding is simulated for the same reservoir. Due to the large difference in oil and water viscosity, the injected water is easier to flow along the high permeability zone to the production well. Therefore, the scope of water flooding in the reservoir is smaller, and there is a large amount of remaining oil in the northern area of the reservoir that has not been displaced, as shown in **Figure 14**. After 600 days of production, the oil recovery of water flooding is 63.3%, and the oil recovery of ferrofluid flooding under the control of an external magnetic field is 79.5%.

CONCLUSION

In this paper, a novel ferrofluid flooding method was proposed. The ferrofluid plays the dual role of “tracer” and displacement fluid in the flooding process, that is, the flooding process can be monitored and the flooding path can be controlled.

The simulation results show that: 1) By monitoring the magnetic anomaly change information in different areas of the reservoir, the flow direction of the injected ferrofluid can be reflected, so that the heterogeneous characteristics of the reservoir can be understood; 2) The displacement direction can be changed artificially by applying a strong magnetic field to further improve the sweep range; 3) Compared with the traditional water flooding, the monitoring-controlling integrated ferrofluid flooding technology can greatly improve oil recovery.

However, there are still many problems and challenges in applying ferrofluid flooding technology. For example, how electromagnets are placed in the field and the retention loss of ferrofluid during flooding process. In the future, the authors will develop the ferrofluid flooding numerical simulation method for three-dimensional problems, and carry out ferrofluid flooding experimental research to further verify the feasibility of this technology. Nevertheless, the research in this article can still provide new ideas and theoretical guidance for further enhancing oil recovery.

DATA AVAILABILITY STATEMENT

The original contributions presented in the study are included in the article/Supplementary Material, further inquiries can be directed to the corresponding author.

AUTHOR CONTRIBUTIONS

TH conceived the idea and wrote the manuscript. FS, RW, and XH contributed to the study and gave final approval for the manuscript.

FUNDING

This work was supported by the Fundamental Research Funds for Zhejiang Provincial Universities and Research Institutes (Grant No. 2020J00009), the National Natural Science Foundation of China (Grant No.52004246); the Natural Science Foundation of Zhejiang Province (Grant No. LQ20E040003, Grant No.LY20D020002); the Science and Technology Project of Zhoushan Bureau (Grant No. 2021C21016).

REFERENCES

Borglin, S., Moridis, G., and Oldenburg, C. (2000). Experimental Studies of the Flow of Ferrofluid in Porous Media[J]. *Transport in Porous Media* 41, 61–80. doi:10.1023/a:1006676931721

Fan, X., Sun, M., Sun, L., and Xie, H. (2020). Ferrofluid Droplets as Liquid Microrobots with Multiple Deformabilities. *Adv. Funct. Mater.* 30, 2000138. doi:10.1002/adfm.202000138

Han, D. (1995). Discussion on Deep Development of High Water-Cut Oilfields Enhance Oil Recovery Problem[J]. *Pet. Exploration Develop.* 22 (2), 47–55.

Han, D. (2010). Discussions on Concepts, Countermeasures and Technical Routes for the Redevelopment of High Water-Cut Oilfields[J]. *Pet. Exploration Develop.* 37 (5), 583–591. doi:10.1016/S1872-5813(11)60005-4

Han, D. (2007). Precisely Predicting Abundant Remaining Oil and Improving the Secondary Recovery of Mature Oilfields[J]. *Acta Petrolei Sinica* 28 (2), 73–78. doi:10.3321/j.issn:0253-2697.2007.02.013

Hou, H., Zhang, S., and Yang, N. (1999). Development on the Hydro-Magnetic Technology and its Application[J]. *Vacuum Tech. Mater.* 5, 8–12.

Kamminga, W. (1975). Finite-element Solutions for Devices with Permanent Magnets. *J. Phys. D: Appl. Phys.* 8 (7), 841–855. doi:10.1088/0022-3727/8/7/017

Moridis, G. J., Borglin, S. E., and Oldenburg, C. M. (1998). *Theoretical and Experimental Investigations of Ferrofluids for Guiding and Detecting Liquids in the Subsurface.* Office of Scientific & Technical Information Technical Reports.

Odenbach, S. (2008). *Magnetoviscous Effects in Ferrofluids.* Springer Berlin Heidelberg.

Oldenburg, C. M., Borglin, S. E., and Moridis, G. J. (2000). Numerical Simulation of Ferrofluid Flow for Subsurface Environmental Engineering Applications[J]. *Transport in Porous Media* 38, 319–344. doi:10.1023/a:1006611702281

Oldenburg, C., and Moridis, G. (1998). *Ferrofluid Flow for TOUGH2.* Office of Scientific & Technical Information Technical Reports.

Rahmani, A. R., Bryant, S., and Huh, C. (2014). *Crosswell Magnetic Sensing of Superparamagnetic Nanoparticles for Subsurface Applications[J].* SPE J.

Rahmani, A. R., Bryant, S. L., and Huh, C. (2015). Characterizing Reservoir Heterogeneities Using Magnetic Nanoparticles[A]. *Proceedings of the SPE Reservoir Simulation Symposium[C].* Houston: Society of Petroleum Engineers.

Raj, K., and Moskowitz, R. (1990). Commercial Applications of Ferrofluids[J]. *J. Magnetism Magn. Mater.* 85, 233–245. doi:10.1016/0304-8853(90)90058-x

Rosensweig, R. E. (1997). *Ferrohydrodynamics[M].* New York: Dover Publications Inc.

Scherer, C., and Figueiredo, A. M. (2005). Ferrofluids: Properties and Applications [J]. *Braz. J. Phys.* 35, 718–727. doi:10.1590/s0103-97332005000400018

Schmidt, H. K., and Tour, J. M. (2012). *Methods for Magnetic Imaging of Geological Structures [M].* Google Patents.

Sengupta, S. (2012). "An Innovative Approach to Image Fracture Dimensions by Injecting Ferrofluids[A]," in Proceedings of the Abu Dhabi International Petroleum Conference and Exhibition[C]. Abu Dhabi: Society of Petroleum Engineers.

Silvester, P., and K. Chari, M. (1970). Finite Element Solution of Saturable Magnetic Field Problems. *IEEE Trans. Power Apparatus Syst.* PAS-89 (7), 1642–1651. doi:10.1109/tpas.1970.292812

Yang, L. I. (2009). Study on Enhancing Oil Recovery of continental Reservoir by Water Drive Technology[J]. *Acta Petrolei Sinica* 30 (3), 396–399. doi:10.3321/j.issn:0253-2697.2009.03.013

Yu, Q. (2000). Oil Field Development Three Major Rich Areas of Large Scale Unswept Remaining Oil in Water Flooded Bedded Sanstone Reservoirs[J]. *Acta Petrolei Sinica* 21 (2), 45–50.

Conflict of Interest: The authors declare that the research was conducted in the absence of any commercial or financial relationships that could be construed as a potential conflict of interest.

frontiers in Earth Science

ORIGINAL RESEARCH
published: 28 September 2021
doi: 10.3389/feart.2021.752548

Spatio-Temporal Evolution Model of the Hydraulic Transport Characteristics of Particulate Solids

Zhi Zhang, Baojiang Sun, Zhiyuan Wang*, Shaowei Pan, Wenqiang Lou and Shikun Tong

School of Petroleum Engineering, China University of Petroleum (East China), Qingdao, China

The hydraulic transport of solid materials is widely used in various industrial fields owing to its high efficiency, low cost, and environmental friendliness, and it has received extensive attention. However, the violent interaction between the liquid and solid phases during transportation makes the slurry flow strongly unsteady and heterogeneous, and it is difficult to use the existing mathematical models describing the motion characteristics in the hydraulic transport of slurry because of the limitations of a single theory or experimental data basis. In this study, considering the randomness and uncertainty in the transportation of solids, a spatio-temporal evolution model of the hydraulic transport characteristics of particulate solids was established. This model is suitable for hydraulic transport in pressure pipelines and open channels, and it can be used to analyze the influence of changes in the motion and property parameters of the liquid–solid phase on the characteristics of the temporal-spatial evolution of the slurry velocity and concentration distributions. The rationality of the model was verified through laboratory experiments. Through an interaction analysis of slurry components, this work explores the influence of the transport of solids on the slurry motion and property parameters, fills the gap in the evolution mechanism of the slurry velocity and concentration distributions in existing models, and overcomes the limitation that layer-based models can only be used in pressure pipelines. Therefore, it has important guiding significance for the engineering design of particulate solid hydraulic transport.

Keywords: Solid hydraulic transport, spatio-temporal evolution model, unsteady and heterogeneous flow, liquid-solid two-phase flow, randomness and uncertainty

OPEN ACCESS

Edited by:
Jean-louis Vigneresse,
Université de Lorraine, France

Reviewed by:
Florent Ravelet,
Arts et Metiers Institute of Technology, France
Arvind Kumar,
YMCA University of Science and Technology, India

****Correspondence:***
Zhiyuan Wang
wangzy1209@126.com

Specialty section:
This article was submitted to Geochemistry, a section of the journal Frontiers in Earth Science

Received: *03 August 2021*
Accepted: *15 September 2021*
Published: *28 September 2021*

Citation:
Zhang Z, Sun B, Wang Z, Pan S, Lou W and Tong S (2021) Spatio-Temporal Evolution Model of the Hydraulic Transport Characteristics of Particulate Solids. Front. Earth Sci. 9:752548. doi: 10.3389/feart.2021.752548

INTRODUCTION

The hydraulic transport of solid materials has become the fourth largest transportation method, after road, railway, and water transportation, because of its high efficiency, low cost, and environmental friendliness (Ravelet et al., 2013; Pati et al., 2017). This transportation mode is flexible, and it includes transport of materials in pressure pipelines (Orell, 2007; Ihle et al., 2014) and, under favorable terrain conditions, in open channels (Kempe et al., 2014). The conveyed materials are various, including fuels (natural gas hydrate, coal, etc.) (You and Liu, 2002), raw materials (metal or non-metallic minerals, building materials, etc.) (Stanić et al., 2017), waste (power plant fly ash, metallurgical or chemical mine tailings, etc.) (Patterson and Maloney, 2016; Pullum et al., 2018), and siltation removed from rivers or reservoirs (Cuisinier et al., 2011; Muddle and Briggs, 2019). This mode is widely applied in various industries and has broad prospects for development. During hydraulic transport, solid particles are activated under the action of a lateral flow, and the flow is gradually transformed from a single-phase liquid to multiphase slurry (Kaushal et al., 2002). This process is accompanied by mass, momentum, and energy exchange between the liquid and solid phases, and the slurry velocity and concentration distributions also evolve gradually with transportation. This leads to strong unsteadiness and heterogeneity of the slurry flow, and significantly increases the difficulty of hydraulic transportation engineering design. As for the transportation in a pressure pipeline, under the influence of the non-uniformity of the slurry concentration distribution, the momentum exchange between the solid particles and the pipe wall is concentrated at the bottom of the pipe, where the pipeline will be worn more seriously (Xie et al., 2015). Thus, the pipeline should be rotated regularly to improve its safety and economic performance. For transportation in an open channel, under the influence of the unsteady velocity distribution, the erosion intensity of the slurry on the trough bed evolves gradually, and the slurry concentration and velocity distributions should be closely monitored to ensure the safety and reliability of the construction (Zhang et al., 2013). Therefore, the temporal and spatial evolution of the characteristics of particulate solid transportation affects the stress state of particles (Yu et al., 2015), the ability of the fluid to transport particles, and the variation in the hydraulic gradient (Kaushal and Tomita, 2003). This is of great significance for the optimal design of hydraulic transport systems.

To describe the characteristics of the slurry velocity and concentration distributions in hydraulic transport, scholars have carried out relevant laboratory/field experiments and theoretical research. Mathematical models describing the hydraulic transport characteristics of particulate solids have been established, which can be divided into layer-based theoretical models and empirical models (Hunt, 1954; Karabelas, 1977; Roco and Balakrishnam, 1985; Wilson, 1987; Pope, 2001; Matousek, 2002). The layered theoretical model can be further divided into two- and three-layer models.

(1) Empirical Model

Based on the characterization model of a two-dimensional slurry flow in an open channel of Hunt (1954), Karabelas (1977). proposed a method to determine the slurry velocity and solid concentration distributions in a horizontal pipeline by using the dimensionless particle diffusion coefficient K_j. Empirical expressions of K_j for different pipe diameters and material particle diameters were established in combination with laboratory experiments. Roco and Balakrishnam (1985) established a constitutive equation for slurry motion through laboratory experiments and applied the N–S equation to describe the motion law of a high-concentration slurry during pipeline transportation. The effects of liquid–liquid, solid–solid, and liquid–solid interactions on the velocity and concentration distributions of the slurry were analyzed, and the rationality of the method was verified by laboratory experiments. Based on the Prandtle mixing length theory (Pope, 2001), Wilson (1987) developed a prediction model for the velocity and solid concentration distributions of a slurry flow in an open channel by analyzing the characteristics of the shear stress distribution of a homogeneous slurry flow and modified the model by combining it with laboratory tests to expand its application scope. Matousek (2002) conducted laboratory experiments to study the slurry flow in pipelines under different fluid and material particle characteristics. By combining the experimental data of constant-temperature flows of sand, shimmering, and coarse coal slurry in industrial-scale pipelines, an empirical model of the slurry motion and property parameters was obtained. On this basis, a fixed-bed thickness prediction model for the formation of particle transport in a pipeline was proposed.

(2) Two-Layer Model

Based on the liquid–solid pipe flow theory of Wilson (1987), Levy and Mason (2000) divided the slurry drainage area in a pressure pipeline into two parallel layers: a sedimentary bed with a high solid concentration and a suspension layer with a low solid concentration. By analyzing the conservation of mass between layers and the conservation of momentum in each layer, the distributions of bed thickness, solid concentration, and average velocity along the pipeline under the condition of a uniform particle size distribution were obtained. Kaushal and Tomita (2002) carried out a simulation experiment of hydraulic transportation of zinc tailing slurry in a horizontal pipe and measured the slurry solid concentration distribution under different particle sizes and flow velocities on the vertical plane. Combined with the experimental data, the empirical model of Karabelas (1977). for prediction of the particle concentration distribution was modified, but this model is suitable for relatively low-concentration slurry and can only calculate the velocity distribution when the slurry is homogeneous, which limits its application. Gillies et al. (2004) expanded the application scope of the two-layer model through laboratory experiments and studied the distribution of the motion parameters of high-concentration slurry transport in a horizontal pipeline. Capecelatro, J. (Capecelatro and Desjardins, 2013). considered the effects of particle collision and liquid viscous shear force on the distribution of the motion and property parameters in the suspension layer, and established an Eulerian–Lagrangian model to simulate the unsteady flow characteristics of a slurry in a horizontal pipeline. The simulation results were verified by the laboratory data of Roco and Balakrishnam (1985).

(3) Three-Layer Model

Based on the previous two-layer theoretical model, Doron and Barnea (1993) proposed that the actual slurry flow should include a transition zone, which is placed between the sedimentary bed formed by the continuous deposition of particles at the bottom of the pipeline and the suspension layer formed by the turbulent diffusion of fluid. In the transition zone, the interaction between the phases was intense, and the internal slurry had a large velocity gradient and solid-phase concentration gradient. Nguyen and Rahman (1996) established the mass and momentum conservation equations corresponding to each layer and pointed out that the velocity gradient and solid concentration distribution of the transition layer slurry follow the Wilson (1987) distribution law. The model does not consider the changes in the slurry properties and motion parameters with time and is a steady-state flow model. Assuming that the velocity distribution of the transition layer conforms to the logarithmic distribution law, and the solid phase concentration obeys the basic equation of convection and diffusion, Cho et al. (2002)

considered the influence of slurry rheology, material size/sphericity, pipeline geometry, and other factors and established a three-layer steady-state model of slurry flow in an annular space. The simulation results are in good agreement with the experimental data of Nguyen and Rahman (1996). Based on a three-layer steady-state model and two-layer unsteady-state model, Guo et al. (2010) established a three-layer unsteady-state model of slurry flow in an annular space, which simplified the dynamic analysis process of slurry motion parameters.

In summary, the empirical model is based on experiments to determine key parameters such as the dimensionless particle diffusion coefficient and slurry motion constitutive relationship, and it establishes a semi-empirical equation describing the slurry motion or uses experimental data to perform a statistical regression on the velocity and concentration distributions of the slurry transportation. Therefore, the application range of the empirical model is limited by the data coverage of the experimental measurements. Thus, it can complete accurate calculations when the engineering parameters meet the data coverage and high measurement accuracy. The layer-based model is based on a unified theoretical basis, and the research has good continuity. It has gradually developed from a two-layer steady-state model to a three-layer unsteady-state model, which can accurately predict the solid hydraulic transport characteristics under different working conditions. Among them, the steady-state model focuses on describing the distribution state of the slurry motion after full development of each layer of fluid, whereas the unsteady-state model focuses on the dynamic development process of each parameter. Therefore, the layer-based model can describe the transport characteristics of each layer, but in essence, each layer of fluid is artificially homogenized; that is, each layer of fluid in the same section contains a liquid phase and solid phase with uniform velocity. In that model, the mechanism of the gradual evolution of slurry velocity and concentration distributions caused by liquid–solid interaction is not described, and the concentration distribution of each layer is determined only based on the basic equation of convection diffusion, without considering the influence of particle size distribution. For that reason, its application is limited to transportation in a pipeline, and there is relatively less research on transportation in open channels, where the randomness and uncertainty of particle movement in the slurry will be more significant owing to the lack of pipe wall constraints. The layered model should consider the influence of multiple factors and be more inclusive and uniform.

In transportation engineering, the slurry contains a variety of particle size gradations, and the transport characteristics are significantly affected by the velocity and concentration distributions of particles of different sizes. It is important to explore the changes in the parameters of slurry motion and physical properties in different positions during hydraulic transportation to further understand the micro field of the slurry motion and property characteristics (such as pipeline wear-erosion intensity, energy loss, and particle motion morphology). In this study, considering the randomness and uncertainty of solid transportation, a spatio-temporal evolution model for the hydraulic transport characteristics of particulate solids was established. This model is suitable for hydraulic transport in pressure pipelines and open channels, and it can be used to analyze the influence of changes in the motion and property parameters of the liquid–solid phase on the characteristics of the temporal-spatial evolution of slurry velocity and concentration distributions. The rationality of the model was verified through laboratory experiments. Through an interaction analysis of the slurry components, this work explores the influence of solid transport on the slurry motion and property parameters, fills the gap in the evolution mechanism of the distributions of slurry velocity and concentration in existing models, and overcomes the limitation that layer-based models can only be used in pressure pipelines. This has important guiding significance for the engineering design of particulate solid hydraulic transport.

DISTURBANCE EFFECT OF PARTICLE TRANSPORT ON THE TRANSITION LAYER FLOW FIELD

In hydraulic transport, particles on the sedimentary bed flow under the action of the liquid phase when the flow velocity is sufficiently high, and they eventually settle in the sedimentary bed under gravity. Such liquid–solid interactions lead to continuous activation, sedimentation, and re-activation of the particle swarm so that a transition layer is formed above the sedimentary bed (Syamlal and O'Brien, 1987), which has an intense exchange of mass and momentum between the liquid and solid phases. In the upper part of the transition layer, the velocity approaches that of the incoming flow and the concentration approaches zero, whereas in the lower part, the velocity approaches zero and the concentration approaches that of the sedimentary bed. Under a constant inflow velocity, the variations in the distribution of velocity and concentration in the transition layer are due to the invasion of solid particles, and they together lead to a variation in fluid mass flow in the transition layer. Therefore, the variation in the thickness of the sedimentary bed is related to the inhomogeneity of the mass flow distribution of the fluid in the transition layer.

When the shear force in the transition layer is sufficient to overcome the resistance of particles in the sedimentary bed, the particles invade the transition layer and begin to migrate. At the same time, the fluid clusters surrounding the particles in the transition layer will also receive a reaction force from the solids, which has a tendency to hinder the fluid movement. The reaction force can only be balanced by the shear force and therefore, as the solid particles in the transition layer continue to invade, the internal flow shear force gradually splits into two parts (Anderson and Haff, 1991):

$$\tau = \tau_l + \tau_s \tag{1}$$

where τ is the flow shear force of the transition layer, τ_s is the solid–phase shear force, which is used to overcome the reaction force from the material particles, and τ_l is the liquid phase shear force, which is derived from the velocity gradient of the transition layer fluid and is used to overcome the resistance to movement of particles in the sedimentary bed. **Equation 1** shows that particle intrusion causes a continuous change in τ_s and τ_l. With continuous intrusion, the solid concentration in the transition layer increases holistically, resulting in an increase in the reaction force acting on the internal fluid, and then τ_s increases accordingly. Therefore, under the condition of constant τ, τ_l decreases accordingly, indicating that with an increase in solid concentration in the transition layer, the power to activate particles on the bed surface decreases, and the collision frequency between the moving and stationary particles increases. The momentum exchange caused by collision has a significant influence on the motion state of the moving particles themselves, but it is not sufficient to overcome the motion resistance of the stationary particles on the bed surface (Owen, 1964). It can be concluded that the intrusion of particles in the transition layer increases the solid concentration and reduces the velocity gradient of the slurry, and the activation efficiency of the stationary particles decreases accordingly. Such a negative feedback mechanism causes the concentration and velocity fields in the transition layer to converge to a steady state. Therefore, the evolution of the slurry motion and property parameters in the transition layer is related to the particle motion state, and the characteristics of the spatio-temporal evolution of particles can be obtained based on the analysis of the particle transport characteristics.

The motion of particles in the transition layer conforms to the parabolic trajectory (Syamlal and O'Brien, 1987), that is, the particles decelerate first and then accelerate under the action of viscous resistance and gravity in the vertical direction after activation. Eventually, particles sink to the sedimentary bed and collide with the stationary particles at the corresponding position, and then embed in the sedimentary bed or rebound and enter the transition layer again to start a new transportation. In this section, the particle transport is divided into collision motion between moving and static particles and parabolic motion in the transition layer. By analyzing the stress state of a single particle and the trend of distribution of the particle swarm momentum in the two stages, the evolution laws of the slurry motion and property parameters in the transition layer are finally obtained.

Collision Model

The model assumes that particles in the sedimentary bed and transition layer are completely elastic spheres, so the energy loss caused by the impact and collision between particles due to plastic deformation can be ignored, the particle transport is limited in a two-dimensional plane composed of gravity direction and flow direction, and the influence of random disturbance is not considered.

Based on the assumptions above, as shown in **Figure 1**, the collision motion can be simplified as particle A in the transition layer colliding with the stationary particle B on the sedimentary bed at the collision angle α (the angle between the particle movement direction and flow direction), and the contact angle between A and B is β (the angle between the particle center line and the flow direction). Mt_0 is the momentum when particle A collides with B. It can be decomposed into Mt_{0h} and Mt_{0v} along the flow and gravity directions, where Mt_{0v} is the momentum accumulation of particle A along the gravity direction before collision. Without considering the influence of parabolic motion in the transition layer on the change of particle momentum, if the transportation of particle A maintains continuity, the momentum of A in the gravity direction after collision should be greater than Mt_{0v}. Further, Mt_0 can be decomposed into Mt_L and Mt_1 along the line of the particle center line and its vertical direction, where Mt_L is the momentum component that will be transferred to particle B after collision, and Mt_1 is the initial momentum of particle A after collision. Therefore, when the component Mt_{1v} of Mt_1 along the gravity direction is greater than Mt_{0v}, the continuity of particle transport can be maintained. Although the two decompositions above have the same dynamic significance, they express the momentum distribution state before and after particle collision with different emphases. Based on the above analysis, it can be concluded that the essence of particle collision lies in the momentum exchange and redistribution between particles. The key to maintaining the continuity of particle motion lies in the relative sizes of Mt_{1v} and Mt_{0v}. Based on the geometric relationships between the components,

$$\frac{\Delta Mt_{1v}}{Mt_{0h}} = \frac{Mt_{1v} - Mt_{0v}}{Mt_{0h}} = \sin(\beta - \alpha)\frac{\cos\beta}{\cos\alpha} - \tan\alpha \tag{2}$$

According to **Eq. 2**, under a given collision angle α, the relative sizes of Mt_{0v} and Mt_{1v} are only related to the contact angle β, but the value of β is constrained by the arrangement of particles on the sedimentary bed. When there is no gap between particles on the bed surface, the minimum contact angle $\beta_{\min}$ is obtained when the particles are tangent to the adjacent particles C along the direction of transport velocity. The maximum contact angle $\beta_{\max}$ is obtained when the particle is tangent to the static particle B along the velocity direction. According to the geometric relationship between the particles, it can be concluded that

$$\beta_{\max} = 90^\circ + \alpha \tag{3}$$

$$\beta_{\min} = \arcsin(1 - \sin\alpha) + \alpha \tag{4}$$

When there is a gap between particles, $\beta_{\min}$ decreases with an increase in the gap distance. Under the condition that the moving and static particles are spheres of the same size and the collision angle α is given, the probability of the contact angle β between the moving particles and the static particles on the bed will vary with the size of the impact area. When $\beta = \alpha$, the impact area of the moving particles is the largest, and it corresponds to the large circle of the static particles. According to the geometric relationship, the collision area and β, α satisfy the following relationship:

$$C = 2\pi R\cos(\beta - \alpha) \tag{5}$$

where C is the collision area, and R is the radius of the particle circle. Correspondingly, under the condition of a given collision angle α, the larger the value of β is, the lower the probability of its occurrence.

It can be observed from **Figure 1** that when the moving particle A collides with the stationary particle B on the bed

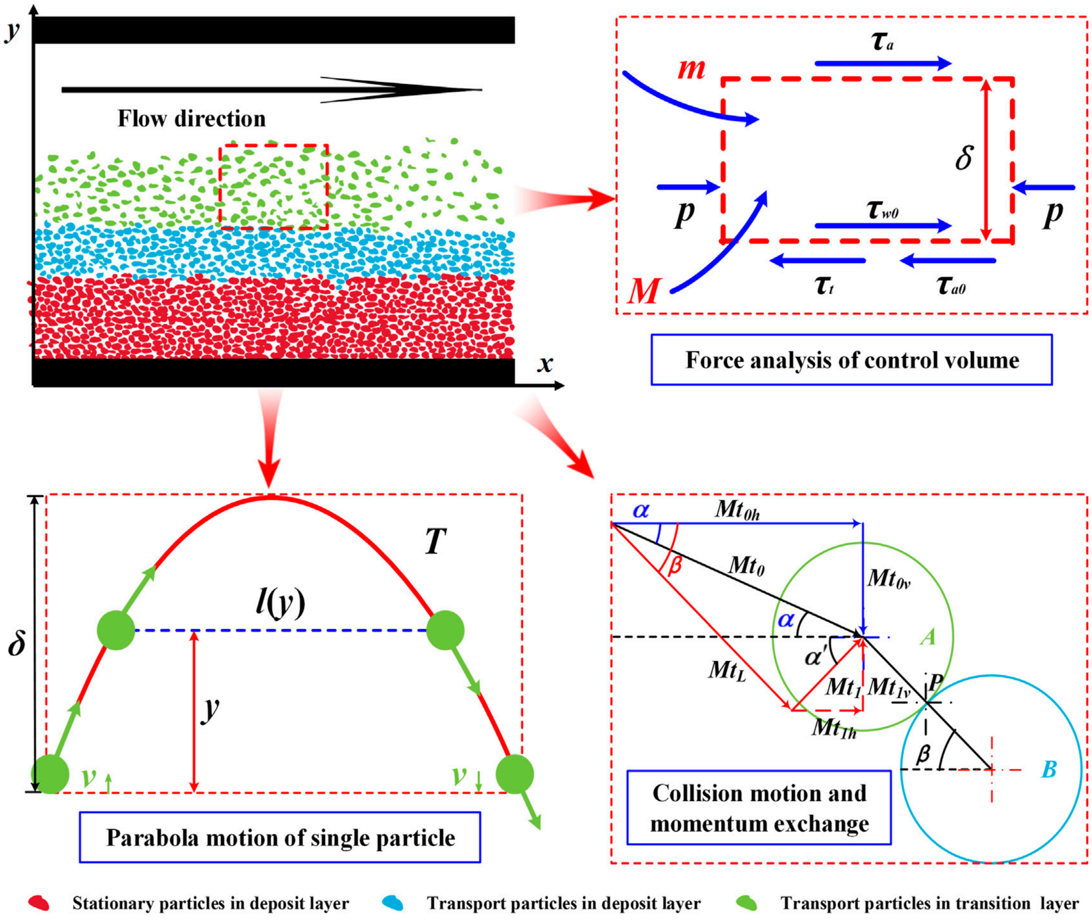

FIGURE 1 | Momentum distribution of transported particles and static particles on the sedimentary bed.

surface, momentum exchange Mt_L is generated along the direction of the line connecting the A and B centers. The size of the residual momentum Mt_1 determines whether the particles can move sustainably, and its direction determines the direction of transport speed. According to the geometric relations, the direction α' of Mt_1 satisfies

$$\alpha' = \beta - 90^\circ \tag{6}$$

Eq. 6 shows that α' depends on contact angle β. When β is less than 90°, the component Mt_{1v} of Mt_1 is opposite to gravity, and particles can jump again after collision when Mt_{1v} is sufficient to overcome Mt_{0v}. When β is greater than 90°, Mt_{1v} is in the same direction as gravity, which means that the transported particle A will continue to collide with the stationary particle D after contacting the stationary particle B. As the initial momentum Mt_0 causes momentum loss Mt_L along the direction of the central line of A and B, the initial momentum of the secondary collision is Mt_1. According to the geometric relationship, the collision and contact angles corresponding to the second collision can be obtained as follows:

$$\alpha' = \beta - 90^\circ \tag{7}$$

$$\beta' = \arcsin\left(1 - \sin\alpha'\right) + \alpha' \tag{8}$$

where α' and β' are the collision and contact angles of the second collision, respectively; whether the particles can jump again depends on the relative size of Mt_{2V} and Mt_{3V}. According to **Eq. 2**, the following can be concluded:

$$\frac{\Delta Mt_{1v}}{Mt_{0h}} = \frac{\sin(\beta - \alpha)}{\cos\alpha}\left[\sin\left(\beta' - \alpha'\right)\cos\beta' - \sin\alpha'\right] \tag{9}$$

Momentum Gain of Transported Particles During Collision

According to **Eqs 2, 9** ($\beta > 90^\circ$), when the collision angle α varies from ~0° to 25°, the momentum gain of particles with different contact angles β can be calculated as shown in **Figure 2**. Under the condition of a given collision angle α, the momentum gain of the transported particles increases initially and then decreases as the contact angle β increases, partly because the given α determines the value of Mt_{0v}, and the trends of the momentum gain of transported particles only depend on Mt_{1v}, which is the vector difference between Mt_1 and Mt_{1h}. With an increase in β, both Mt_1 and Mt_{1h} increase. It can be concluded from the calculations shown in **Figure 2** that when $\beta < 50^\circ$, with the increase in

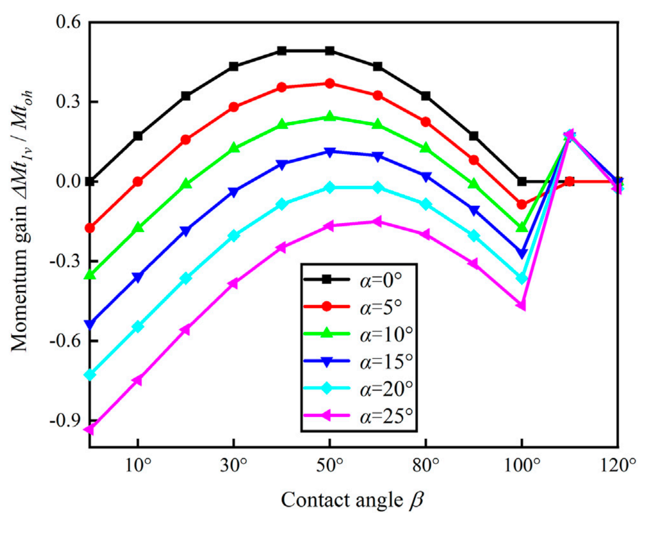

FIGURE 2 | Distribution of momentum gain of transported particles with different contact angles.

β, the increase in amplitude of Mt_1 is greater than that of Mt_{1h}, and thus the momentum gain of particles increases with the increase in contact angle β; when $\beta > 50^\circ$, with the increase in β, the increase in amplitude of Mt_1 is less than that of Mt_{1h}. Therefore, the momentum gain of the particles decreases with an increase in the contact angle β. When the contact angle β is approximately 50°, the momentum gain of the transported particles reaches a maximum. Further, under the given contact angle β, the momentum gain of the transported particles decreases with an increase in the collision angle α, and the momentum gain is negative when $\alpha > 20^\circ$. This occurs because the increase in α leads to an increase in Mt_{0v} and a decrease in Mt_{1v} under the given condition of β, and finally to a decreased momentum gain of the transported particles.

According to **Figure 2**, the momentum gain of single particles with different contact angles β can be obtained when the collision angle is α to determine the initial momentum and corresponding collision angle at the next jump. However, the initial momentum and contact angle of the transported particles contained in the particle swarm vary, which means that the initial momentum and the corresponding collision angle of particles at the next jump are in accordance with a certain probability distribution for the particle swarm. From **Eq. 5**, when the impact angle α is given, $|\beta-\alpha|$ determines the size of the collision area. Therefore, with an increase in contact angle β, the probability of its occurrence decreases. Based on the weighted average method, the momentum gain expectation of the particle swarm corresponding to different impact angles α can be obtained as follows:

$$\left(\frac{\overline{\Delta Mt_{1v}}}{Mt_{0h}}\right)_\alpha = \frac{\sum\limits_{\beta=0^\circ}^{120^\circ}\left[\frac{\Delta Mt_{1v}}{Mt_{0h}}\cos(\beta-\alpha)\right]}{\sum\limits_{\beta=0^\circ}^{120^\circ}\cos(\beta-\alpha)} \tag{10}$$

The calculation results are shown in **Figure 3**. The average momentum gain of the particles decreases with an increase in the collision angle α, which is consistent with the trend of the single-particle momentum gain in **Figure 2**. In addition, it can be concluded that the momentum change in the particle collision process tends to converge to a fixed value. For example, when particles collide with particles on a sedimentary bed with an impact angle of 0°, as shown at point A in **Figure 3**, the momentum gain generated during the collision process can be obtained through the gain curve (marked by the black line). Finally, the momentum obtained can reach the position of point B, where the momentum will remain until it collides with the particles on the bed. The collision angle corresponding to the next collision can be obtained by the momentum ratio curve (marked by the red line) to lead particles to reach point C if the momentum loss due to fluid resistance is not taken into account in the transport process. By analogy, the collision motion is actually the convergence process of the particle momentum. When the momentum of particles along the direction of gravity, Mt_{0v}, is large, the impact angle is large, and the corresponding negative momentum gain leads to a decreasing trend. When Mt_{0v} is small, the collision angle is small, and the corresponding positive momentum gain leads to an increasing trend. It can be concluded from **Figure 3** that the variation in the average momentum gain between positive and negative α makes the particle transport not only persistent but also tends to converge to the zero position of the ordinate of the average momentum gain curve, and this trend is independent of the initial momentum of the particles.

Asymptotic Behavior of the Momentum Probability Distribution of Particle Swarm Before and After Collision

Figure 2 shows the trend of the momentum gain of a single particle under different collision angles α and corresponding contact angles β. Combined with **Figure 3**, it can be observed that the particle momentum tends to converge to a fixed value under the condition that the momentum loss caused by fluid resistance is not considered, and this trend is independent of the

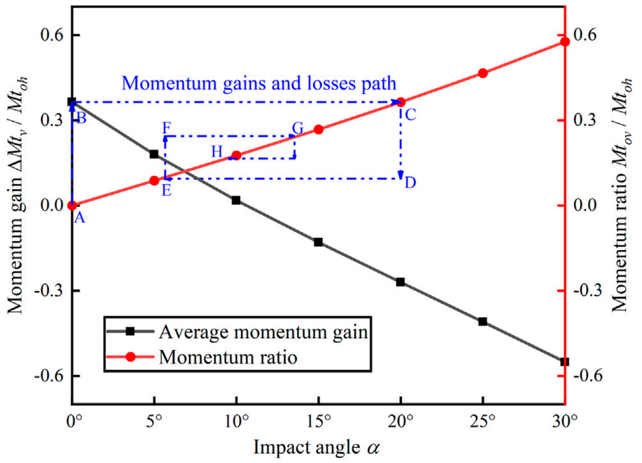

FIGURE 3 | Curves of average momentum gain and loss of particle collision motion with α

initial momentum of the particles. However, different particles contained in the particle swarm correspond to different initial momentums, that is, the initial momentum should follow a certain probability distribution. Referring to the trend of momentum of a single particle during the collision motion, the momentum distribution of the particle swarm should also converge with the transport process. In this section, the asymptotic behavior of the momentum distribution of the particle swarm in a collision motion is discussed.

From the average momentum gain curve in **Figure 3**, when the particle momentum before collision is large, it tends to decrease owing to the negative momentum gain during the collision motion. Otherwise, it tends to increase, which ensures that when the sample space of the particle swarm momentum is given, the particle momentum does not jump out of the sample space because the particle momentum is excessively large or excessively small. Then, the sample space of the particle swarm momentum can be assumed as follows:

$$\mathbf{\Omega} = \left[\left(\frac{Mt_{0v}}{Mt_{0h}}\right)_1, \left(\frac{Mt_{0v}}{Mt_{0h}}\right)_2, \ldots, \left(\frac{Mt_{0v}}{Mt_{0h}}\right)_n\right] \tag{11}$$

The momentum probability distribution corresponding to the particle swarm is

$$\boldsymbol{X}_k = \left[(x_k)_1, (x_k)_2, \cdots, (x_k)_n\right], \sum_{i=1}^{n} (x_k)_i = 1 \tag{12}$$

where k is the number of collisions, the probability distribution $\mathbf{X_k}$ represents the instantaneous state that the particle swarm reaches after k times of collision from the initial state, and $(x_k)_i$ is the proportion of particles with momentum $(Mt_{0v}/Mt_{0h})_i, i \in [1, n]$ in the whole particle swarm.

During the collision motion of the particle swarm, owing to the difference in momentum and contact angle β between particles, the corresponding momentum gain is also different. For example, any particle with momentum $(Mt_{0v}/Mt_{0h})_i$ before collision may convert to $(Mt_{0v}/Mt_{0h})_j$ after collision, where the value of j traverses 1–n when j takes different values corresponding to different probabilities, which is defined as the transition probability p_{ij} of the particle momentum from $(Mt_{0v}/Mt_{0h})_i$ to $(Mt_{0v}/Mt_{0h})_j$ through collision. From the arbitrariness of i and the ergodicity of j, it can be concluded that the collision motion of the particle swarm is essentially a conversion process of particles with different initial momentums in the sample space Ω, which is determined by the transfer probability matrix **P**:

$$\mathbf{P} = \begin{pmatrix} p_{11} & p_{12} & \cdots & p_{1n} \\ p_{21} & p_{22} & \cdots & p_{2n} \\ \vdots & \vdots & \ddots & \vdots \\ p_{n1} & p_{n2} & \cdots & p_{nn} \end{pmatrix} \tag{13}$$

The momentum of the particles still traverses the entire sample space after collision, but the corresponding probability distribution is transferred to $\mathbf{X_{k+1}}$, where the element $(x_{k+1})_j$ can be obtained using the full probability formula:

$$\mathbf{X_{k+1}} = \mathbf{X_k P} \tag{14}$$

The proportion of particles with momentum $(Mt_{0v}/Mt_{0h})_j$ in the particle swarm after collision $(x_{k+1})_j$ should be the sum traversed through the sample space of the product of the particle swarm momentum probability distribution $(x_k)_i$ and p_{ij} before collision. **Eq. 14** shows that the transition between adjacent states $\mathbf{X_k}$ and $\mathbf{X_{k+1}}$ corresponding to the momentum probability distribution before and after a particle swarm collision is completely determined by the transfer probability matrix **P**. It can be inferred from **Eq. 14**

$$\mathbf{X_k} = \mathbf{X_0 P^k} \tag{15}$$

Equation 15 shows that the state of the particle swarm after any collision depends only on the initial state $\mathbf{X_0}$ and the transfer probability matrix **P**. Therefore, whether the momentum distribution of the particle swarm converges with the transport process depends on the asymptotic quality of $\mathbf{P^k}$ when the collision number k approaches infinity.

According to **Eq. 13**, the i-th row element of the transfer probability matrix **P** represents the probability of the given particle momentum $(Mt_{0v}/Mt_{0h})_i$ transferred to $(Mt_{0v}/Mt_{0h})_j, j \in [1, n]$ after the collision. Because the value of j traverses the sample space, the elements in matrix **P** satisfy the following equation:

$$\begin{cases} \sum\limits_{j=1}^{n} p_{ij} = 1 \\ \forall p_{ij} \in [0, 1] \end{cases} \tag{16}$$

For any $m \in N^*, m > 1$, assuming That $\widetilde{\mathbf{P}} = \mathbf{P^m}$ Satisfies the above properties, then

$$\sum_{j=1}^{n} \left(p^{m+1}\right)_{ij} = \sum_{a=1}^{n}\sum_{b=1}^{n} \widetilde{P}_{ia} P_{ab} = \left(\sum_{a=1}^{n} \widetilde{P}_{ia}\right)\left(\sum_{b=1}^{n} P_{ab}\right) = 1 \tag{17}$$

Therefore, for any $m \in N^*$, $\widetilde{\mathbf{P}}$ is also the transfer probability matrix, which represents the momentum transfer probability of the particle swarm from state $\mathbf{X_0}$ to $\mathbf{X_m}$ after m collisions. Suppose that λ is any eigenvalue of the transfer probability matrix **P** and $\mathbf{V_\lambda}$ is its corresponding eigenvector, then $\widetilde{\mathbf{P}}$ satisfies

$$\mathbf{P}^m \mathbf{V_\lambda} = \lambda^m \mathbf{V_\lambda} \tag{18}$$

Therefore, when m tends to infinity, if $|\lambda| > 1$, there must be elements in $\lambda^m \mathbf{V_\lambda}$ that tend to infinity, whereas $\forall \left(p^m\right)_{ij} \in [0, 1]$ $\mathbf{P}^m \mathbf{V_\lambda}$ cannot tend to infinity. The two are contradictory, so any eigenvalue of **P** satisfies the following conditions:

$$|\lambda| \le 1 \tag{19}$$

For the n-dimensional matrix $\mathbf{P^T}$, the eigenvalues are assumed to be $\lambda_1, \lambda_2, \ldots, \lambda_n$, and the corresponding eigenvectors are $\mathbf{V}_{\lambda 1}$, $\mathbf{V}_{\lambda 2}$, . . . , $\mathbf{V}_{\lambda n}$, then

$$\begin{cases} \left(\mathbf{P}^T\right)^m \mathbf{V}_{\lambda 1}^T = \lambda_1^m \mathbf{V}_{\lambda 1}^T \\ \left(\mathbf{P}^T\right)^m \mathbf{V}_{\lambda 2}^T = \lambda_2^m \mathbf{V}_{\lambda 2}^T \\ \vdots \\ \left(\mathbf{P}^T\right)^m \mathbf{V}_{\lambda n}^T = \lambda_n^m \mathbf{V}_{\lambda n}^T \end{cases} \Leftrightarrow \begin{cases} \mathbf{V}_{\lambda 1} \mathbf{P}^m = \lambda_1^m \mathbf{V}_{\lambda 1} \\ \mathbf{V}_{\lambda 2} \mathbf{P}^m = \lambda_2^m \mathbf{V}_{\lambda 2} \\ \vdots \\ \mathbf{V}_{\lambda n} \mathbf{P}^m = \lambda_n^m \mathbf{V}_{\lambda n} \end{cases} \tag{20}$$

Therefore, according to the linear correlation or independence of such eigenvectors, the convergence conditions of the momentum distribution of the particle swarm are discussed in the following two cases:

① If the eigenvectors are linearly independent, then for any initial state $\mathbf{X_0}$, there are constants $c_1, c_2, \ldots c_n$, satisfying

$$\mathbf{X_0} = c_1\mathbf{V}_{\lambda1} + c_2\mathbf{V}_{\lambda2} + \cdots + c_n\mathbf{V}_{\lambda n} \tag{21}$$

Combined with **Eq. 20**, it can be obtained

$$\mathbf{X_0}\mathbf{P}^m = c_1\lambda_1^m\mathbf{V}_{\lambda1} + c_2\lambda_2^m\mathbf{V}_{\lambda2} + \cdots + c_n\lambda_n^m\mathbf{V}_{\lambda n} \tag{22}$$

From **Eq. 16**, the row sum of the **P** matrix is 1. Hence, $\lambda = 1$ must be one of its eigenvalues, assuming $\lambda_1 = 1$, and then

$$\lim_{m\to\infty}\mathbf{X_0}\mathbf{P}^m = \sum_{i=1}^{n} c_i\lambda_i^{m-1}\mathbf{V}_{\lambda i} \tag{23}$$

If and only if there is an eigenvalue $\lambda = -1$, the limit of the above equation does not exist, and the present period changes. When the eigenvalue of **P** does not contain $\lambda = -1$, then

$$\lim_{m\to\infty}\mathbf{X_0}\mathbf{P}^m = c_1\lambda_1\mathbf{V}_{\lambda1} \tag{24}$$

From **Eq. 12**, when m tends to infinity, the limit state of the particle swarm momentum probability distribution must satisfy the condition that the sum of each element is equal to 1, and thus c_1 in **Eq. 23** is also uniquely determined.

② If the eigenvectors are linearly related, then **P** must contain the eigenvalue $\lambda = 0$, and **P** is not full rank, assuming its rank is r; then,

$$\exists row \in [1,n], c_i \in \mathbf{R} \Rightarrow \forall j \in [1,n], \left(\mathbf{P}_{row}^T\right)_j = \sum_{i=1, i\neq row}^{n} c_i\left(\mathbf{P}_i^T\right)_j \tag{25}$$

where $\mathbf{P}_{row}^T$ is the row vector formed by the *ith* row element of $\mathbf{P}^T$, and $\left(\mathbf{P}_{row}^T\right)_j$ is the *jth* element of $\mathbf{P}_{row}^T$. Assuming that $\mathbf{V}_{\lambda 1}, \mathbf{V}_{\lambda 2}, \ldots \mathbf{V}_{\lambda r}$ are the largest linearly independent groups of eigenvectors, it can be obtained from **Eq. 20**

$$\forall i \in [1,r] \Rightarrow \sum_{j=1, j\neq row}^{n} \left(\mathbf{P}_{row}^T\right)_j (\mathbf{V}_{\lambda k})_j = \boldsymbol{\lambda}_k (\mathbf{V}_{\lambda k})_{row} \tag{26}$$

Substituting **Eq. 25** with **Eq. 26**, we Obtain

$$(\mathbf{V}_{\lambda k})_{row} = \sum_{i=1, i\neq row}^{n} c_i (\mathbf{V}_{\lambda k})_i \tag{27}$$

For any initial state $\mathbf{X_0}$ transferred to state $\mathbf{X_1}$ after collision, the following conditions are satisfied:

$$\mathbf{X}_\mathbf{1}^T = \mathbf{P}^T\mathbf{X}_\mathbf{0}^T = \left[\sum_{j=1, j\neq row}^{n} \left(\mathbf{P}_\mathbf{1}^T\right)_j \left(\mathbf{X}_\mathbf{0}^T\right)_j, \cdots, \sum_{j=1, j\neq row}^{n} \left(\mathbf{P}_{row}^T\right)_j \left(\mathbf{X}_\mathbf{0}^T\right)_j, \cdots, \sum_{j=1, j\neq row}^{n} \left(\mathbf{P}_\mathbf{n}^T\right)_j \left(\mathbf{X}_\mathbf{0}^T\right)_j\right]^T \tag{28}$$

Substituting **Eq. 25** with **Eq. 28**, we obtain

$$(x_1)_{row} = \sum_{i=1, i\neq row}^{n} c_i (x_1)_i \tag{29}$$

where

$$(x_1)_i = \sum_{j=1}^{n} \left(\mathbf{P}_i^T\right)_j \left(\mathbf{X}_\mathbf{0}^T\right)_j \tag{30}$$

Because the largest linearly independent group of eigenvectors contains only r elements, that is, it can only linearly represent any r-dimensional vector, let

$$\begin{aligned} \tilde{\mathbf{X}}_\mathbf{1}^T &= \left[(x_1)_1, (x_1)_2, \cdots, (x_1)_r\right]^T \\ \tilde{\mathbf{V}}_{\lambda k} &= \left[(\mathbf{V}_{\lambda k})_1, (\mathbf{V}_{\lambda k})_2, \cdots, (\mathbf{V}_{\lambda k})_r\right]^T, k \in [1,r] \end{aligned} \tag{31}$$

then there are constants $b_1, b_2, \ldots b_n$, such that

$$\tilde{\mathbf{X}}_\mathbf{1}^T = \sum_{i=1}^{r} b_i\tilde{\mathbf{V}}_{\lambda i} \tag{32}$$

combining **Eqs 27**, **29**, it can be obtained

$$\begin{aligned} \sum_{i=1}^{r} b_i\mathbf{V}_{\lambda i} &= \begin{bmatrix} \sum_{i=1}^{r} b_i(\mathbf{V}_{\lambda i})_1 \vdots \sum_{i=1}^{r} b_i(\mathbf{V}_{\lambda i})_r \sum_{i=1}^{r} b_i(\mathbf{V}_{\lambda i})_{row} \end{bmatrix} = \begin{bmatrix} \sum_{i=1}^{r} b_i(\mathbf{V}_{\lambda i})_1 \vdots \sum_{i=1}^{r} b_i(\mathbf{V}_{\lambda i})_r \sum_{j=1, j\neq row}^{n} c_j \sum_{i=1}^{r} b_i(\mathbf{V}_{\lambda i})_j \end{bmatrix} \\ &= \begin{bmatrix} \sum_{i=1}^{r} b_i(\mathbf{V}_{\lambda i})_1 \vdots \sum_{i=1}^{r} b_i(\mathbf{V}_{\lambda i})_r \sum_{j=1, j\neq row}^{n} c_j(x_1)_j \end{bmatrix} = \begin{bmatrix} (x_1)_1 \\ \vdots \\ (x_1)_r \\ (x_1)_{row} \end{bmatrix} = \mathbf{X}_\mathbf{1}^T \end{aligned} \tag{33}$$

Equation 33 shows that when any r-dimensional vector can be expressed linearly by the largest linearly independent group of eigenvectors, state $\mathrm{X}_\mathbf{1}$ can also be linearly described by the largest linearly independent group.

$$\lim_{m\to\infty}\mathbf{X_0}\mathbf{P}^m = \lim_{m\to\infty}\mathbf{X}_1\mathbf{P}^{m-1} = \sum_{i=1}^{r} b_i\lambda_i^{m-1}\mathbf{V}_{\lambda i} \tag{34}$$

From **Eq. 19**, the absolute value of any eigenvalue of **P** is not greater than 1, so if and only if there is an eigenvalue $\lambda = -1$, the limit of the above equation does not exist and the present period changes. When the eigenvalue does not contain -1, the above equation converges to

$$\lim_{m\to\infty}\mathbf{X_0}\mathbf{P}^m = \lim_{m\to\infty}\mathbf{X}_1\mathbf{P}^{m-1} = b_1\lambda_1\mathbf{V}_{\lambda1} \tag{35}$$

In summary, a sufficient condition for the momentum distribution of the particle swarm to converge with the progress of transport is that -1 is not an eigenvalue of the transfer probability matrix **P**.

Stationary Probability Distribution of Particle Swarm Momentum

Based on the above analysis, a sufficient condition is obtained that the momentum distribution of the particle swarm converges with the process of transport, but the stationary probability distribution of the particle swarm where it eventually converges to is unclear. **Equation 23** provides a method to solve the stationary probability distribution, which involves the power calculation of the transfer probability matrix. Once the sample space of the particle swarm momentum is large, the calculation becomes very complicated. Moreover, compared with the stationary probability distribution, which is a stable state, the particle swarm state obtained by each matrix operation of **Eq. 23** is in an instantaneous state, and the transfer of momentum distribution of the particle swarm has greater randomness and unpredictability at this time. This means not only that the method is cumbersome, but also that the intermediate calculation results have no significance for the final stationary probability distribution. Therefore, a more concise method is required to solve the stationary probability distribution of the particle swarm momentum.

If the momentum distribution of the particle swarm is convergent and the stationary probability distribution is $\mathbf{X_s}$ then, from **Eq. 23**, it can be concluded that

$$\lim_{m\to\infty} \mathbf{X_0}\mathbf{P}^m = \mathbf{X_0} \lim_{m\to\infty} \mathbf{P}^m = \mathbf{X}_s \tag{36}$$

From **Eq. 36**, the initial state $\mathbf{X_0}$ and the stationary probability distribution $\mathbf{X_s}$ are both definite quantities; therefore, the transfer probability matrix $\mathbf{P^m}$ also converges as the number of transitions increases. If it converges to **Q**, then **Q** should satisfy for any initial state $\mathbf{X_0}$ multiplied by it to obtain only the stationary probability distribution $\mathbf{X_s}$, so **Q** satisfies

$$\mathbf{Q} = \lim_{m\to\infty} \mathbf{P}^m = \begin{pmatrix} q_1 & q_2 & \cdots & q_n \\ q_1 & q_2 & \cdots & q_n \\ \vdots & \vdots & \ddots & \vdots \\ q_1 & q_2 & \cdots & q_n \end{pmatrix} \tag{37}$$

Equation 37 shows that the elements in each column of **Q** have the same value, and the stationary probability distribution **X** is obtained as follows:

$$\begin{aligned} \mathbf{X}_s = \mathbf{X}_0\mathbf{Q} &= \left(q_1 \sum_{i=1}^{n} (x_0)_i \quad q_2 \sum_{i=1}^{n} (x_0)_i \cdots q_n \sum_{i=1}^{n} (x_0)_i \right) \\ &= \left(q_1 \quad q_2 \quad \cdots \quad q_n \right) \end{aligned} \tag{38}$$

Therefore, only matrix **Q** is required, and the stationary probability distribution $\mathbf{X_s}$ can be uniquely determined. It can be obtained from **Eq. 38**

$$\mathbf{Q} = \left(\lim_{m\to\infty} \mathbf{P}^{m-1} \right) \cdot \mathbf{P} = \mathbf{Q} \cdot \mathbf{P} \Rightarrow \mathbf{X}_s = \mathbf{X}_s\mathbf{P} \tag{39}$$

The stationary probability distribution $\mathbf{X_s}$ can be obtained by solving **Eq. 39**.

① Existence of solutions to **Eq. 39**

It can Be obtained from **Eq. 16** that

$$\mathbf{P} \cdot \mathbf{1} = \mathbf{1} \Rightarrow (\mathbf{P} - \mathbf{I}) \cdot \mathbf{1} = \mathbf{0} \tag{40}$$

Therefore, the equation $(\mathbf{P} - \mathbf{I})\mathbf{X} = \mathbf{0}$ has a nonzero solution, which means that the coefficient matrix **(P - I)** is not full rank, and **Eq. 39** is equivalent to

$$(\mathbf{P}^T - \mathbf{I})\mathbf{X}_s^T = \mathbf{0} \tag{41}$$

As the coefficient matrix $(\mathbf{P^T}\text{-}\mathbf{I})$ is not full rank, it can be known that **Eq. 39** must have a non-zero solution.

② Probability meaning of the solution of **Eq. 39**

At each moment in the collision motion, the momentum distribution of the particle swarm is transferred to the given sample space. The proportion $(x_{k+1})_j$ of particles with momentum $(Mt_{0v}/Mt_{0h})_j$, $j \in [1, n]$ in state $\mathbf{X_{k+1}}$ at any moment is transferred from the collision of particles with different momentums in the particle swarm at the previous moment; then,

$$(x_{k+1})_j = \sum_{i}^{n} (x_k)_i p_{ij} \tag{42}$$

Equation 42 shows that the component $(x_{k+1})_j$ in state $\mathbf{X_{k+1}}$ represents the expectation that the momentum of the particle swarm at the last moment transfers to $(Mt_{0v}/Mt_{0h})_j$ after the collision. When the particle swarm reaches the stationary state $\mathbf{X_s}$, the momentum distribution no longer changes with the collision, indicating that the expectation of the momentum transfer of the particle swarm to $(Mt_{0v}/Mt_{0h})_j$ between adjacent moments is equal to the expectation of the transfer of momentum from $(Mt_{0v}/Mt_{0h})_j$ to other momentum. This means that the momentum of any given particle in the swarm transferred to other values through collisions will inevitably return to the initial value after several collisions to ensure the stationary state. Therefore, the elements in $\mathbf{X_s}$ are related to the number of transition steps. If Tm_{ij} is the number of transition steps required for the particle to reach $(Mt_{0v}/Mt_{0h})_j$ from momentum $(Mt_{0v}/Mt_{0h})_i$ for the first time, then

$$\begin{aligned} E(Tm_{ij}) &= E\left[E(Tm_{ij}|x_1)\right] = 1 \cdot P_{ij} + \sum_{k\neq j} \left[1 + E(Tm_{kj})\right] P_{ik} \\ &= 1 + \sum_{k\neq j} E(Tm_{kj}) P_{ik} \end{aligned} \tag{43}$$

where x_1 is the momentum reached by the particle after a collision. The particle may reach $(Mt_{0v}/Mt_{0h})_j$ after one collision, then $Tm_{ij} = 1$ is satisfied at this time, and the corresponding probability is p_{ij}. Conversely, if the particle does not reach $(Mt_{0v}/Mt_{0h})_j$ after one collision but reaches $(Mt_{0v}/Mt_{0h})_k$, then $Tm_{ij} = 1 + E(Tm_{kj})$ is satisfied under such conditions, and the corresponding probability is p_{ik}. Finally, the expectation of the transfer steps is obtained as

$$E(Tm_{ij}) + P_{ij}E(Tm_{jj}) = 1 + \sum_{k} P_{ik}E(Tm_{kj}) \tag{44}$$

Both sides of the equation are multiplied by $(x_s)_\mathrm{i}$ at the same time, and summed with i as the independent variable; then,

$$\begin{aligned} &\sum_{i} (x_s)_i E(Tm_{ij}) + E(Tm_{jj}) \sum_{i} (x_s)_i P_{ij} \\ &= \sum_{i} (x_s)_i + \sum_{k} E(Tm_{kj}) \cdot \left(\sum_{i} (x_s)_i P_{ik} \right) \end{aligned} \tag{45}$$

By combining **Eqs 42**, **12**, the following can be obtained:

$$(x_s)_j = \frac{1}{E\left(Tm_{jj}\right)} \tag{46}$$

Therefore, the probability meaning of the solution of **Eq. 39** is the reciprocal of the average number of collisions required for the particle momentum $(Mt_{0v}/Mt_{0h})_j$ to return to the initial value after collision and momentum transfer at a certain moment.

Parabola Model

After completing the collision motion between particles and momentum exchange, the parabolic motion in the transition layer begins. As shown in **Figure 1**, the parabolic motion of the particles is divided into two stages: upward and downward. In the upward stage, the particles decelerate along the gravity direction under the action of gravity G and fluid resistance F_{Dy}. When they reach the highest point P, the corresponding vertical velocity $v_\uparrow = 0$; in the downward stage, the directions of G and F_{Dy} are opposite, and the maximum vertical velocity is reached when the particles are about to collide with the static particles in the sedimentary bed. It can be observed that the parabolic motion also contains frequent stress interactions and momentum exchange between the liquid and solid. In this section, we analyze the stress state of the particles in the transition layer, the dynamic model of the particle parabolic motion, and the corresponding transfer probability matrix. On this basis, the trend and convergence of momentum in the parabolic motion of particle swarms are discussed.

As shown in **Figure 5**, during the upward stage of the particles, the changes in velocity satisfy

$$m\frac{dv_\uparrow}{dt} = -mg - \frac{1}{2}\rho_f A C_D v_\uparrow^2 \tag{47}$$

where ρ_f is the density of seawater, A is the particle cross-sectional area, v is the particle movement speed, and C_D is the drag coefficient with dimension 1, which is a function of the Reynolds number, Re, of the particle movement.

The momentum of the particle swarm gradually converges to a stable state as the collision progresses, and the corresponding Re should also converge under the given conditions of flow velocity and particle diameter. As shown in **Figure 4**, the Re probability distribution of the particle swarm at the steady state can be obtained according to **Figure 4**, and combined with the change curve of the drag coefficient C_D with Re (Syamlal and O'Brien, 1987). As shown in **Figure 4**, when Re is small, the transport medium is in laminar flow state. At this time, the particle settlement resistance is mainly viscous force, and C_D has a linear relationship with Re; With the increase of Re value, the movement of transport medium is gradually transformed into turbulence. At this time, the viscous force and turbulent resistance received by particle settlement can not be ignored, and C_D has a curve relationship with Re; When the value of Re increases to a certain extent, the transport medium is in the turbulent region. At this time, the viscous resistance of particle settlement can be ignored, and C_D remains constant with the change of Re. The fluctuation range of the value of the particle swarm C_D is negligible. Therefore, it can be considered that C_D remains constant during the parabolic motion, and its size can be measured by the terminal velocity of the particle settling:

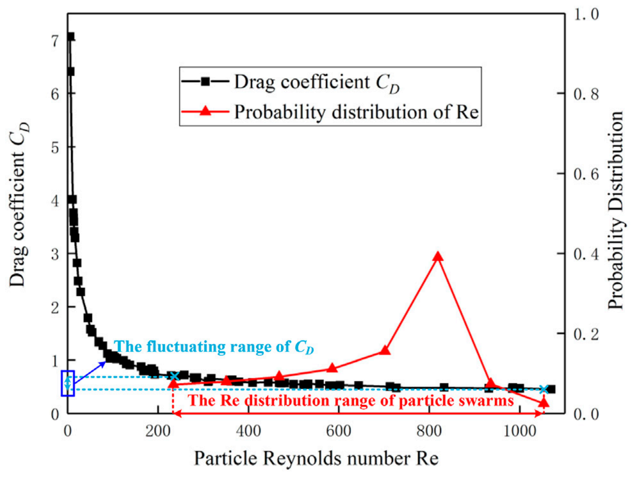

FIGURE 4 | Fluctuation range of C_D and probability distribution of Re during particle parabolic motion.

$$C_D = \frac{2mg}{\rho_f A v_t^2} \tag{48}$$

where v_t is the terminal velocity. Substituting **Eq. 48** into **Eq. 47**, we obtain

$$-\frac{1}{1+\left(v_\uparrow/v_t\right)^2} d\left(\frac{v_\uparrow}{v_t}\right) = d\left(\frac{t}{v_t/g}\right) \tag{49}$$

Integrating both sides of **Eq. 49**, and taking the particle motion state at the highest point P as the boundary condition, that is, $t = 0$ and $v_\uparrow = 0$ are satisfied, the motion equation of the particle upward stage can be obtained:

$$\frac{v_\uparrow}{v_t} = \tan\left(-\frac{t}{v_t/g}\right) \tag{50}$$

The motion equation of particles in the downward stage is as follows:

$$\frac{v_\downarrow}{v_t} = 1 - \frac{2}{1+\exp\left(\frac{2t}{v_t/g}\right)} \tag{51}$$

Equations 50, **51** indicate that when the particle motion velocity v and the corresponding time t are normalized by the end-settlement velocity v_t, the change in the dimensionless velocity v/v_t with dimensionless time $\frac{t}{v_t/g}$ is determined by the above equation. Taking the combined **Eq. 48**, v_t is only related to the particle size under a constant C_D. Therefore, the motion law of the particles is uniquely determined under the given distribution of particle size. **Figure 5** shows the variation of v/v_t with $\frac{t}{v_t/g}$, where the velocity of the particles rapidly drops to 0 during the ascending process, and then slowly rises to v_t during the descending process. When the particle moves at the initial velocity $v_0/v_t = 3$ (point A in **Figure 5**), the corresponding time $\frac{t_0}{v_t/g}$ can be obtained from **Eq. 50**, and the path lengths of the particles rising and falling are equal, indicating that the shadow area in the corresponding figure is

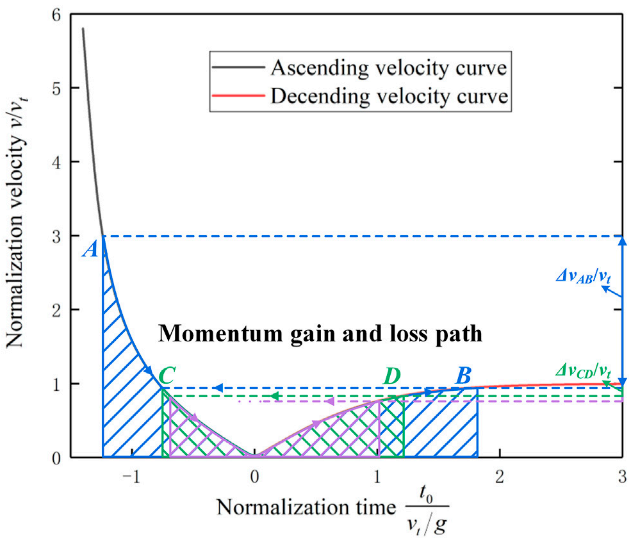

FIGURE 5 | Curve of parabolic motion speed with time and transfer path of particle momentum.

equal. Combining **Eqs 50**, **51**, the corresponding time when the particles fall to the bed (point B in **Figure 5**) can be obtained as follows:

$$\int_A^0 \frac{v_\uparrow}{v_t}\mathbf{d}\left(\frac{t}{v_t/g}\right) = \int_0^B \frac{v_\downarrow}{v_t}\mathbf{d}\left(\frac{t}{v_t/g}\right) \tag{52}$$

Equation 52 is substituted into **Eq. 51** to obtain the velocity v_1/v_t when the particles fall to the bed, and then the next parabolic motion starts with v_1/v_t as the initial velocity (point C in **Figure 5**) and cycles in turns. It can be concluded from the path of gain and loss of particle momentum shown in **Figure 5** that although the variation of particle momentum $\Delta v_{AB}/v_t$ and $\Delta v_{CD}/v_t$ decreases with the increase in motion time, the momentum gain during parabolic motion is negative. This means that without considering the momentum gain brought by the collision process, the particle momentum will gradually converge to zero, and the continuity of particle transport will no longer be satisfied.

Disturbance of Particles Transport on Transition Layer Flow Field

In this section, the particle swarm velocity distribution profile is obtained by analyzing the change law of the momentum of the particles during the transport process. Moreover, we considered the interaction between the fluid in the transition layer and the particles on the bed, and the mass of the particles flowing into the transition layer per unit time was obtained. Finally, on this basis, the disturbance law of particle transport in the flow field of the transition layer is discussed.

The transport of particles essentially alternates between the collision motion and the parabolic motion, that is, the particles begin the parabolic motion in the transition layer after the collision motion with the bed surface, and the change law of particle swarm momentum should satisfy

$$\mathbf{X}_1 = \mathbf{X}_0\mathbf{PR} \tag{53}$$

where **P** and **R** are the transfer probability matrix of the momentum change in the collision motion and the parabolic motion of the particle swarm, and the matrix **S** = **PR** obtained by the multiplication of the two is also the transfer probability matrix according to **Eq. 16**, which corresponds to the change in momentum of the particle swarm in the transport process.

When the particle moves to the highest point during the parabolic motion, the velocity along the gravity direction reaches the minimum value, which indicates that the particles stay at this position for the longest time. The velocity $v_\rightarrow$ of particles in the flow direction at this position can then be taken as the value of the velocity profile in the transport process of the particle swarm, which can be obtained by traversing the particle swarm momentum sample space, as shown in **Figure 6**. The particle swarm velocity increases with increasing elevation, but the increasing speed gradually slows down. This is because with an increase in $v_\rightarrow$ the fluid resistance of particles along the flow direction decreases gradually, that is, the velocity of particles remains constant until $v_\rightarrow$ increases to the flow velocity. When the transition layer fluid accelerates the particles, it will also be subject to the reaction of particles, which causes the original flow field to evolve with the transport process. According to the conservation of the fluid mass in the transition layer, the following can be obtained:

$$\tilde{v}(y) = \frac{1}{1+IPF}v_f(y) + \frac{IPF}{1+IPF}v_\rightarrow(y) \tag{54}$$

where $\tilde{v}(y)$ is the liquid–solid mixing velocity of the fluid at the corresponding y position in the transition layer, and IPF is the activation probability function of the static particles in the sedimentary bed, which is defined as the mass of the particles in the sedimentary bed that can be activated by the unit mass of the transition layer fluid velocity distribution v_f. This is related to the shear force of the transition layer fluid τ_a, τ_w, and the dimension is 1. In **Eq. 57**, both $v_f(y)$ and $v_\rightarrow(y)$ are known quantities; therefore, when the probability function IPF is obtained, the variation law of the transition layer flow field distribution can be obtained.

EVOLUTION OF PROPERTY AND MOTION CHARACTERISTICS OF SLURRY DURING HYDRAULIC TRANSPORTATION

The transportation of particles leads to the continuous evolution of the property and motion characteristics of the slurry, and the convergence of the momentum distribution with the transportation process indicates that the evolution of the velocity distribution, solid concentration distribution, mass flow

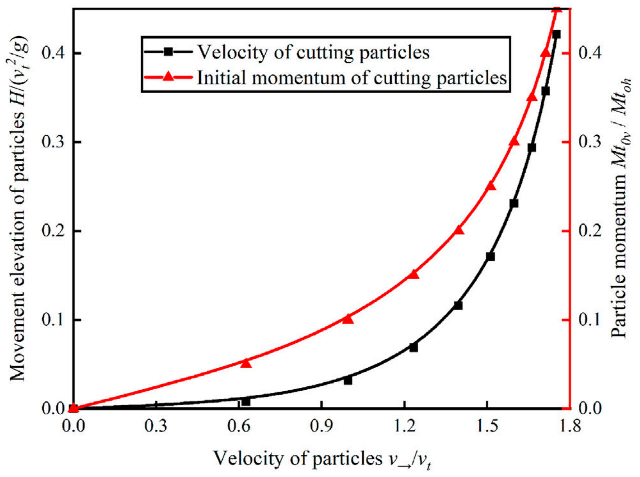

FIGURE 6 | Profile of particle swarm velocity distribution and diagram of momentum distribution.

distribution, and bed thickness of the transition layer should also be stable during hydraulic transport. In this section, according to the analysis of the mass and momentum exchange between the transition layer and the sedimentary bed in the transportation, the trend of velocity and solid concentration distributions in the transition layer is obtained, and on this basis, the characteristics of the evolution of the sedimentary bed geometry are explored.

Continuity Equation of Slurry in Transition Layer

Particles in the sedimentary bed begin to move under the action of the transition layer fluid, and the mass of the activated particles is related to the mass flow rate of the transition layer fluid. The activation probability function can be expressed as follows (Syamlal and O'Brien, 1987):

$$M = \int_0^\delta \rho v T dy \cdot IPF \tag{55}$$

where T is the movement period of particles, M is the mass of particles invading the transition layer during T, and IPF is the activation probability function of the particle, which can be expressed as (Sauermann et al., 2001)

$$IPF = n\left(\frac{\tau_{l0}}{\tau_t}\right) - 1 \tag{56}$$

where τ_{l0} is the liquid-phase shear force at the junction of the sedimentary bed and the transition layer. τ_t is the critical starting stress of material particles, and its calculation method can be referred to (Ahmed, 2001). When $\tau_{l0} > \tau_t$, then n > 1, and when $\tau_{l0} < \tau_t$, then n = 1. **Equation 56** shows that when and only when $\tau_{l0} > \tau_t$, particles will be activated in the sedimentary bed, and the activation efficiency of these particles depends on the trend of n. Based on the Taylor expansion and **Eq. 55**, the following equation can be obtained:

$$M = \int_0^\delta \rho v T dy \cdot \gamma\left(\frac{\tau_{l0}}{\tau_t} - 1\right) \tag{57}$$

where $\gamma = \left.\frac{\partial n}{\partial(\tau_{l0}/\tau_t)}\right|_{\tau_{l0}/\tau_t=1}$, and it can be considered as the contribution of factors other than the liquid shear stress to the activation of particles in the sedimentary bed, which characterizes the erosion intensity of the transition layer on the sedimentary bed and can be obtained through laboratory experiments or numerical simulation (Syamlal and O'Brien, 1987).

Taking the micro-element control volume in the transition layer as the research object, based on the law of conservation of mass, it can be concluded that

$$\frac{\partial}{\partial t}\left(\int_0^\delta \rho dy\right) + \frac{\partial}{\partial x}\left(\int_0^\delta \rho v dy\right) = \int_0^\delta \frac{\rho v}{l} dy \cdot \gamma\left(\frac{\tau_{l0}}{\tau_t} - 1\right) \tag{58}$$

where ρ is the fluid density of the transition layer, v is the fluid velocity, l is the average transport distance of the particles, and δ is the thickness of the transition layer. According to the stress state of the micro-element control volume, the expression of τ_{l0} can be obtained using the momentum theorem as follows:

$$\tau_{l0} = \tau_0 - \int_0^\delta \frac{\rho_s v}{l(y)} \Delta v(y) dy \tag{59}$$

The equation is based on the assumption that the flow velocity is uniform and time-invariant, where $\Delta v(y)$ is the difference between the horizontal component of the downward velocity and upward velocity during particle transport at position y, $l(y)$ is the horizontal distance of particles at position y from upward to downward, and τ_0 is the flow shear force of the fluid at the interface between the transition layer and the sedimentary bed. Based on the assumption that the slurry satisfies Newton's shear law, the following conclusions can be drawn:

$$\tau_0 = \mu \left.\frac{dv}{dy}\right|_{y=0} \tag{60}$$

where μ is the viscosity of the slurry in the transition layer, which is affected by the concentration of solid particles (Einstein, 1906):

$$\mu = \left(1 + 2.5C_v|_{y=0}\right)\mu_0 \tag{61}$$

where μ_0 is the viscosity of the slurry without solid particles, and C_v is the volume concentration of the solid phase in the transition layer. **Equation 58** shows that the change in fluid mass in the micro-element control body depends on the mass flow gradient in the flow direction and the invasion rate of particles in the sedimentary bed, and its trend is related to the distribution of the velocity field and solid concentration in the transition layer during transportation. Therefore, the characteristics of the evolution of the slurry properties and motion parameters depend on these two important parameters.

Characteristics of the Evolution of Flow Field and Solid Concentration Distributions in the Transition Layer

Based on the boundary conditions above, the velocity distribution in the transition layer can be assumed to be a polynomial distribution with five unknowns:

$$v(x,y,0) = U\left[2\left(\frac{y}{\delta}\right) - 2\left(\frac{y}{\delta}\right)^3 + \left(\frac{y}{\delta}\right)^4\right] \tag{62}$$

The concentration distribution of the solid phase can be expressed as follows:

$$C_v(x,y,0) = 0 \tag{63}$$

The flow field and solid concentration distributions in the transition layer gradually evolve with the transportation process. Based on the principle of mass conservation, the evolution of the solid concentration can be expressed as follows:

$$C_v(x,y,t+\Delta t) = C_v(x,y,t+\Delta t) + \frac{\int_0^\delta \rho(x,t)v(x,y,t)dy \cdot IPF \cdot MR(y)}{\int_0^\delta \rho_p v(x,y,t)dy} \tag{64}$$

The evolution of the flow field distribution is expressed as follows:

$$v(x,y,t+\Delta t) = \sqrt{\frac{\int_0^\delta \rho(x,t)v(x,y,t)dy \cdot IPF \cdot MR(y) \cdot v_{\rightarrow}(y) + \rho(x,t)v(x,y,t) \cdot v(x,y,t)}{\int_0^\delta \rho(x,t)v(x,y,t)dy \cdot IPF \cdot MR(y) + \rho(x,t)v(x,y,t)}} \tag{65}$$

where $MR(y)$ is the mass proportion of particles at the y position in the transition layer to the total mass of activated particles in Δt, as shown in **Figure 14**. In conclusion, on the basis of solving **Eqs. 64**, **65** to obtain the slurry movement law in the transition layer, the variation law of fluid mass flow can be analyzed using the continuous **Eq. 58**.

Model Solving Process

The solution of the mass conservation equation of the transition layer fluid is directly related to the characteristics of the evolution of the property parameters and motion parameters of the slurry; therefore, the solution of **Eq. 58** must be accompanied by the real-time solution of the flow field and solid concentration distributions of the transition layer. **Equation 58** contains three unknowns: slurry density ρ, velocity v, and liquid phase shear force τ_{l0}, and **Eq. 59** describes the decisive factors of τ_{l0}:

$$TVP\frac{\partial Q}{\partial t} + \frac{\partial Q}{\partial x} = \frac{Q}{l_s} \cdot \left(1 - \frac{Q}{Q_s}\right) \tag{66}$$

where Q_s is the saturated mass flow rate:

$$Q_s = \frac{(\tau - \tau_t)l}{\langle \Delta v \rangle} \tag{67}$$

TVP, $\langle \Delta v \rangle$, and l_s are process parameters:

$$TVP = \frac{\int_0^\delta \rho v dy}{\int_0^\delta \rho dy}, \langle \Delta v \rangle = \frac{\int_0^\delta \rho_p v \cdot \Delta v(y) dy}{\int_0^\delta \rho v dy}, l_s = \frac{l\tau_t}{\gamma(\tau - \tau_t)} \tag{68}$$

Equation 66 shows that the trend of the fluid mass flow rate in the transition layer is consistent with the trend of the solid-phase shear stress τ_s. The inflow of particles in the transition layer increases the mass flow rate, and the momentum exchange between the liquid and solid phases is more intense. However, it also leads to a decrease in the mass source term on the right side of **Eq. 66** and a decrease in the liquid phase shear force τ_l, thus weakening the growth rate of the mass flow rate and the solid phase shear force τ_s. Q_S corresponds to the flow shear force τ, which describes the carrying capacity of solid particles of the transition layer from the perspective of mass exchange and momentum exchange, respectively, and the evolution of Q and τ_s describes the negative feedback mechanism of the mass change in the transition layer from the qualitative and quantitative perspectives, respectively.

Definite Conditions for Solution of Slurry Motion Parameters in the Transition Layer

① Slurry mass flow.

At the initial time of transportation, there are no particles in the transition layer; therefore, analogous to the velocity distribution of the boundary layer (White and Corfield, 2006), the initial conditions of mass flow in the transition layer are satisfied:

$$Q(0,x) = 4.088\sqrt{\rho_l v_f \mu_0 x} \tag{69}$$

The change in the mass flow rate of the transition layer fluid at the inlet is equal to the mass of the particles flowing in time step Δt:

$$Q(t+\Delta t,0) = Q(t,0) + \int_0^\delta Q(t,0) \cdot IPF \cdot \Delta t \cdot MR(y) \cdot v_{\rightarrow}(y)dy \tag{70}$$

② Momentum distribution of particles.

The stress of the static particles in the sedimentary bed at the initial time satisfies the following requirements:

$$m_p\frac{dv_{\uparrow}}{dt} = \frac{1}{2}C_L A\rho_l U^2 - G \tag{71}$$

$$m_p\frac{dv_{\rightarrow}}{dt} = \frac{1}{2}C_D A\rho_l U^2 \tag{72}$$

where G is the floating weight of the particles, m_p is the weight of the particles, A is the cross-sectional area of the particles, C_L is the lifting force coefficient, and C_D is the drag force coefficient. The simultaneous **Eqs 71**, **72** show that the momentum of the particle swarm at the initial time satisfies the following equation:

$$\left.\left(\frac{Mt_{0v}}{Mt_{0h}}\right)_k\right|_{t=0} = \frac{C_L}{C_D} - \frac{4d_p g(\rho_p - \rho_l)}{3C_D\rho_l U^2} \tag{73}$$

Equation 73 shows that the momentum distribution of the particle swarm at the activating moment depends on the particle size distribution:

$$\mathbf{X}_0 = \begin{pmatrix} x_0\left(d_p\right)_1 & \cdots & x_0\left(d_p\right)_k & \cdots & x_0\left(d_p\right)_n \end{pmatrix} \tag{74}$$

The momentum evolution of the particle swarm in the transportation is consistent with the following:

$$\mathbf{X}_t = \mathbf{X}_0\mathbf{S}^t \tag{75}$$

Definite Conditions of Slurry Physical Parameters

After injection, the particles move along the flow direction for a certain distance and then deposit to the bottom of the pipeline or open channel. The transport distances of particles with different particle sizes along the flow direction are different, and thus they deposit at different positions. It is assumed that the particle size distribution of the material can be ranked from large to small as $\begin{pmatrix} (d_p)_1 & \cdots & (d_p)_k & \cdots & (d_p)_n \end{pmatrix}$, and then the morphology distribution of the sedimentary bed can be expressed as (Syamlal and O'Brien, 1987)

$$\Delta_i = x_{i+1} - x_i \tag{76}$$

$$w_i = \sqrt{\frac{6V_i}{\Delta_i \tan\theta}} \tag{77}$$

$$h_i = \sqrt{\frac{3V_i \tan\theta}{8\Delta_i}} \tag{78}$$

where Δ_i is the thickness of the sedimentary unit, x_i and x_{i+1} are the horizontal transport distances of particles with adjacent particle sizes, w_i is the width of the sedimentary unit, h_i is the height of the sedimentary unit, V_i is the proportion of the volume of material particles with particle size $(dp)_\mathrm{i}$ to the total volume of material, and θ is the accumulation angle, which is determined by laboratory experiments.

LABORATORY EXPERIMENT OF HYDRAULIC TRANSPORT

Laboratory experiments on slurry motion and changes in physical parameters during hydraulic transport were carried out. Based on the similarity criterion, a consistent relationship between the experimental parameters and engineering conditions was ensured, and the evolution law of the transition layer motion parameters and the change law of the sedimentary bed physical parameters were explored. Combined with the experimental measurement results and model calculation results, the rationality of this model was verified.

Experimental Device

As shown in **Figure 7**, in this experiment, a centrifugal pump injected water into the plexiglass open channel through an injection pipeline to form a strong water flow. The particles flowed homogeneously through the sand–water mixing tank at the injection point, and the flow speed and direction stability were controlled through the rectifier plate and guide grid group to simulate the stable flow situation in the process of trough transportation accurately. An acoustic Doppler velocimeter was set up in the open channel to monitor the variation in velocity at different positions during transportation in real time. The acoustic doppler velocimeter measures the three-dimensional velocity of X, Y and Z. Y is perpendicular to the X direction, and X and Y are in the same plane, Z is vertical upward. The three directions comply with the right-hand rule. The four "legs" of the flow meter are data acquisition points in four different directions (x, y, z) at the measurement position to measure the flow velocity and direction at the corresponding position, in which the red rectangle represents the x-axis. The evolution of the sedimentary bed was observed by a high-speed camera in real time.

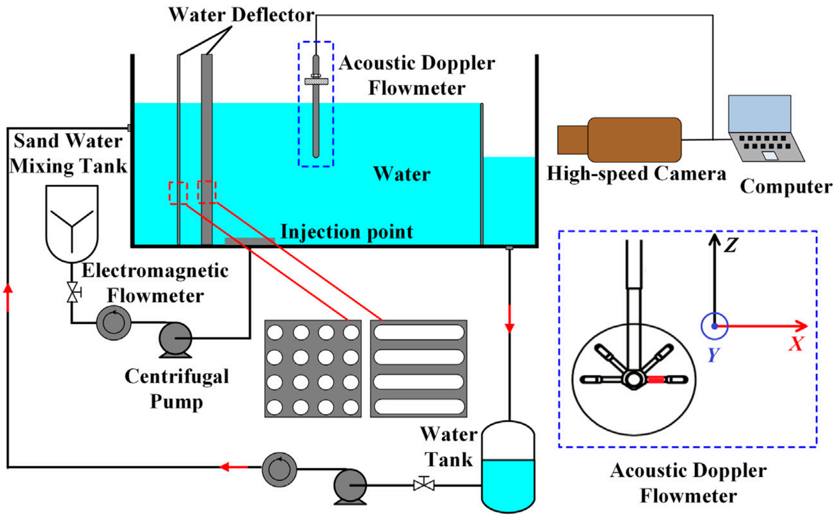

FIGURE 7 | Diagram of hydraulic transport simulation device.

TABLE 1 | Parameters of hydraulic transport simulation experiment.

Simulation variables	Simulation parameters	Experimental parameters
Width of open channel (m)	50	0.5
Flow velocity (m/s)	0.3	0.03
Flow direction	Single direction	Single direction
Average particle size (mm)	5	0.05
Particle density (g/cm^3)	2.7	2.7
Solid concentration of injected slurry (%)	12	12
Injection rate (m/s)	0.119	0.012
Time (s)	1,200	1,200

Experimental Parameters

The scale of real hydraulic transportation is large, so it is impossible to restore the experimental simulation of transportation process 1:1 in the laboratory. Therefore, the hydraulic transport simulation experiment must be carried out through the appropriate similarity criterion. As mentioned above, in the process of hydraulic transport, whether in the macro evolution of the geometry of the sedimentary bed and the flow field in the transition layer, or in the micro collision and parabola movement of the particle swarm, the gravity is always the key factor affecting its motion form. Therefore, the Froude number similarity criterion is selected here. According to the Froude similarity criterion,

$$Fr = \frac{v_m^2}{g_m l_m} = \frac{v_t^2}{g_t l_t} \tag{79}$$

Where v_m and v_t represent the transport medium velocity under laboratory simulation conditions and real hydraulic conveying conditions respectively, m/s, l_m and l_t represent the scale size under laboratory experiment and real conditions respectively, m, g_m and g_t represent the gravitational acceleration under laboratory experiment and real conditions respectively. The parameters of the hydraulic transport simulation experiment were designed as **Table 1**.

Description of Experimental Phenomena

Observe the process from particle return to stopping upward return. At 1 min, there is basically no rock debris return. At 2 min, the particle concentration increases, and then returns stably. A sharp fan-shaped sedimentary bed is formed at the bottom of the flume along the ocean current direction. The deposition positions of particles with different particle sizes are different, and the geometric shape of the deposition unit formed by material particles with corresponding particle sizes is in accordance with **Equation 76** (77).

Driven by the water flow, the material particles on the surface of the sedimentary bed begin to move and invade the transition layer against the resistance and resistance torque. The amount of invasion is controlled by **Eq. 57**. The moving particles climb over the upper surface of the paved sand layer after parabolic motion (50) (51) and collision motion (15). The sedimentary bed begins to evolve slowly as a whole, and the evolution law conforms to **Eq. 58**.

After 10 min of particle upward return process, all transported particles have entered the water tank. Keep the water velocity constant, observe the migration and deposition process of particles, and record the results every 5 min. In order to clearly observe the range of particle migration and deposition, the top view of the experimental process is shown in **Figure 8**.

When the particles stop returning, the sediment is in the shape of a sharp fan. Under the action of water flow, the tip of the sedimentary bed slowly disappears, the sand layer is a small sand dune along the width of the flume, and the sedimentary bed is accumulated in a horseshoe shape as a whole.

Comparative Analysis of Experimental Results and Model Calculation

Taking the simulation and experimental parameters listed in **Table 1**, the model calculation and experimental results are compared, as shown in **Figure 9**, where the color bar represents the height of the deposition bed. It can be observed that both of them show that the sedimentary bed presents, in general, a horseshoe-shaped accumulation, which indicates that the change in the morphological distribution of the sedimentary bed is affected by the transport of particles at the leading edge and the accumulation of particles at the tail, and the morphology evolution is that the particles in the front position are transported to the middle and rear positions of the sedimentary bed under the action of the liquid phase. It can be concluded that the intense parabolic and collision motions of the particles in the transition layer are accompanied by the synchronous evolution of the morphological distribution of the sedimentary bed, which ensures the continuity of particle transportation.

Table 2 presents the comparison between the experimental and model calculation data, and it can be observed that the maximum relative error is no more than 4%, which proves the rationality of the model. The velocity distribution of the transition layer is shown in **Figure 10**, where the continuous curve is the model calculation result of the velocity distribution in the transition layer, and the discrete points are the finite velocity points in the transition layer measured by acoustic Doppler velocimeter. It can be observed that the invasion of particles changes the original flow field distribution in the transition layer, and the change range of the velocity profile is different at different positions, but the influence area is mainly concentrated between positions A and B, which indicates that the particle transport is concentrated in this position. The continuous curve in **Figure 10** represents the calculated data of the model, and the discrete points represent the measured data. It can be observed that the two have good consistency.

ANALYSIS OF EVOLUTION OF SLURRY PROPERTY AND MOTION PARAMETERS IN HYDRAULIC TRANSPORTATION

The upper limit of the velocity distribution in the transition layer is determined by the incoming velocity u, and the change in velocity distribution directly affects the distribution of flow shear force τ in the transition layer. Thus, the incoming velocity u represents the power of particle activation to a certain extent. According to **Eq. 56**, the particles invade the transition layer from the sedimentary bed

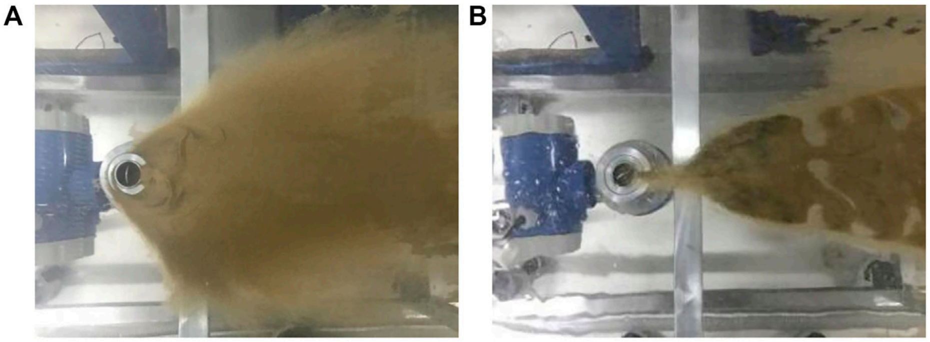

at 5min

at 10min

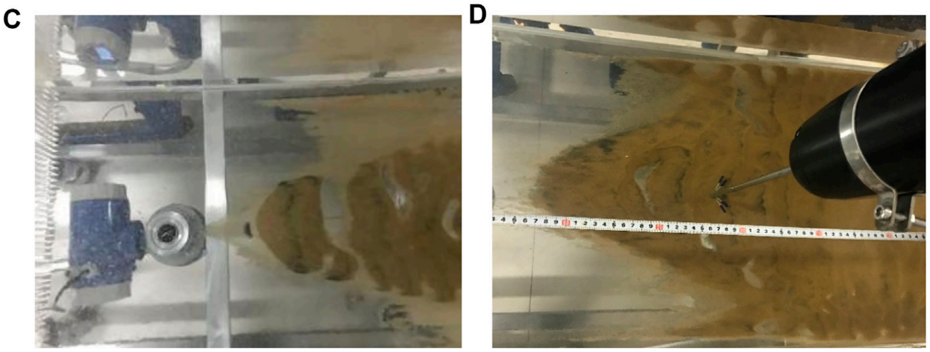

at 15min

at 20min

FIGURE 8 | Top view of the experimental process.

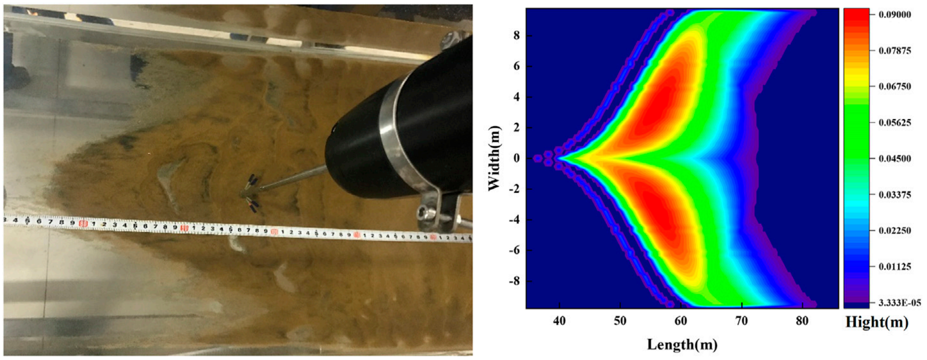

FIGURE 9 | Comparison of experimental and model calculation results of sedimentary bed morphology distribution.

TABLE 2 | Comparison of experimental data and model calculation data of sedimentary bed morphology distribution.

Morphological parameters of sedimentary bed	Length range/m	Width range/m	Coverage/m^2
Experimental data	34–88	0–20	726.8
Model calculation data	34.5–85.9	0–19.6	700.7
Relative error of this model	2.4%	2.0%	3.6%

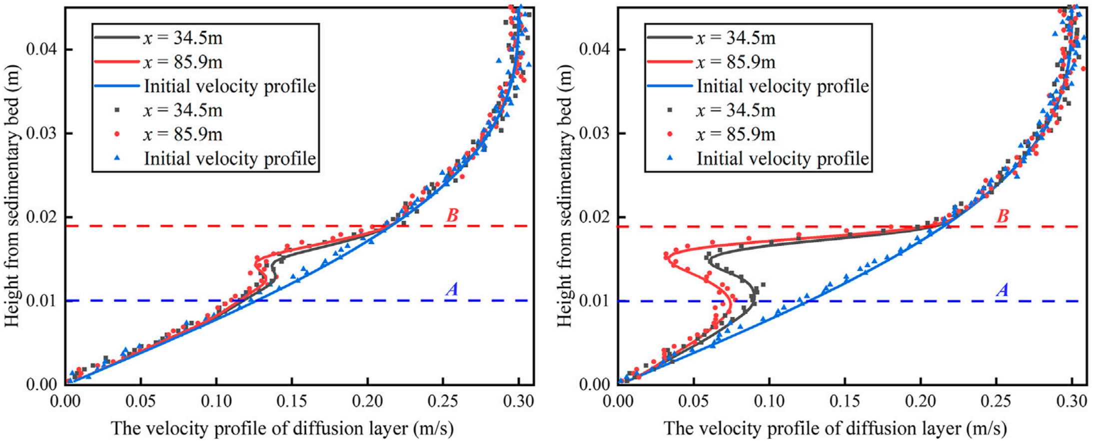

FIGURE 10 | Comparison of experimental and model calculation data of slurry velocity distribution.

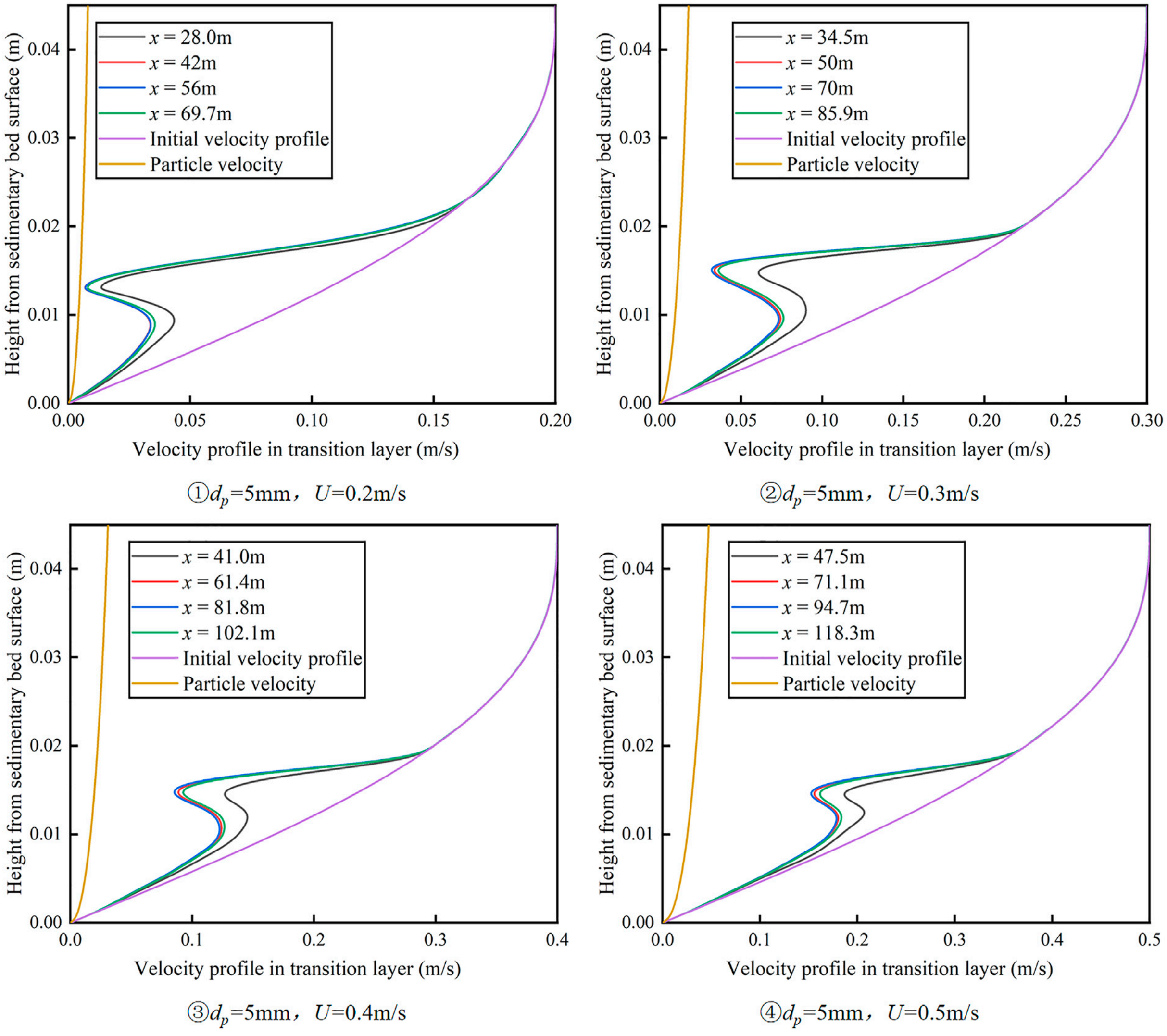

FIGURE 11 | Variation of velocity distribution in the transition layer with flow velocity.

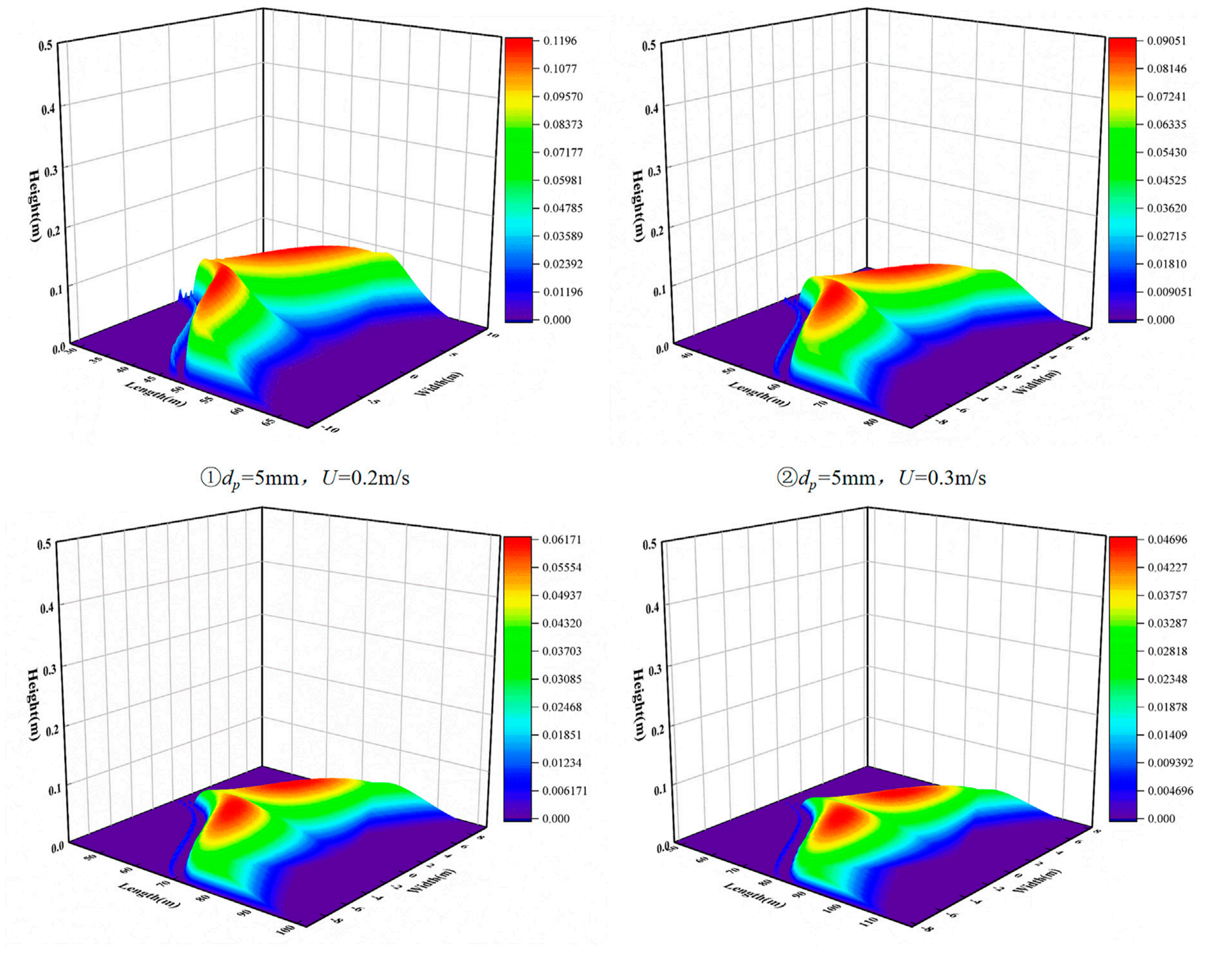

①d_p=5mm，U=0.2m/s

②d_p=5mm，U=0.3m/s

③d_p=5mm，U=0.4m/s

④d_p=5mm，U=0.5m/s

FIGURE 12 | Variation of sedimentary bed morphology distribution with flow velocity.

when $\tau_{l0} > \tau_t$, and τ_t depends on the particle property parameters. In conclusion, the relationship between the flow motion parameters and the particle property parameters is the key factor affecting the particle motion state, which directly leads to a change in the particle invasion strength, determines the non-uniformity of fluid mass flow in the transition layer, and affects the evolution of the distribution of the sedimentary bed. In this section, based on the model, the characteristics of the evolution of slurry property and motion parameters in hydraulic transportation under different incoming flow velocities U and the distribution of particle size d_p are simulated and calculated.

Characteristics of the Evolution of Slurry Property and Motion Parameters

Evolution of Flow Field and Solid Concentration in the Transition Layer

Pure water was used as the transport medium, flow velocity u = 0.3 m/s, particle density ρ = 2,751 kg/m3, and the particle size distribution satisfies the normal distribution $d_p \sim \mathrm{N}\,(5, 0.5)$, the total transportation volume is TTV = 75 m (Ihle et al., 2014). As can be observed, there is a difference in velocity distribution between the particle swarm and liquid phase during transportation, which tends to reduce the fluid velocity in the transition layer as a whole. The weakening range is related to the solid concentration at different positions on the sedimentary bed surface. The minimum value of the slurry velocity is obtained at position A in the figure, which corresponds to the maximum value of the solid concentration at this position. The solid content in the transition layer increases continuously during transportation, but the concentration distribution maintains the same change trend with time. This indicates that the transport of intrusive particles can reach the stationary state in a short time, and the velocity distribution has the same change response. The influence of particle motion on the flow field in the transition layer is limited to position B, which indicates that the range of particle motion is limited to the B position under the given flow motion parameters and solid property parameters.

Evolution of Mass Flux in the Transition Layer

According to the mass conservation **Eq. 66**, the variation in the mass flow rate in the transition layer depends on the transportation $\partial Q/\partial x$ along the flow direction and the

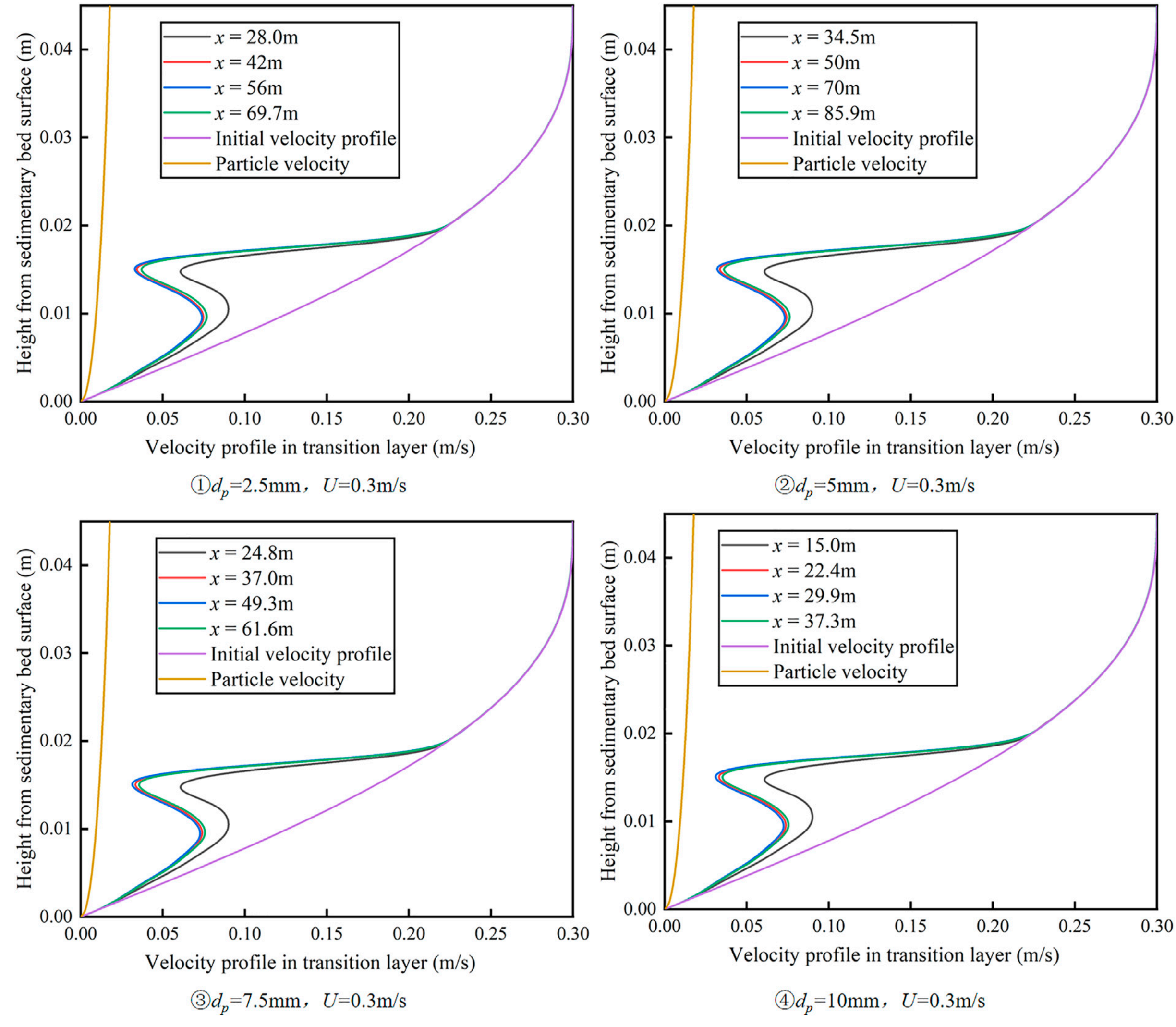

FIGURE 13 | Variation of velocity distribution in the transition layer with particle size distribution.

invasion of particles in the sedimentary bed, which are affected by the flow field distribution in the transition layer. At the same time, the invasion of solid particles leads to the movement of particles in the sedimentary bed. Hence, the evolution of mass flux in the transition layer is a complex process affected by multiple factors. It can be observed that the areas with severe mass flow changes are concentrated at the front edge of the sedimentary bed, whose extent is the most dramatic in the interval of 0–300 s. This is because the transition layer does not contain particles at the initial moment. According to **Eq. 69**, position A has the largest mass flow gradient, and therefore the mass flow increase rate is the highest during the initial time interval and reaches the peak value at t = 300 s. However, at the same time, it can be found that the particle intrusion reduces the overall velocity distribution at this location, and the activation efficiency of particles decreases accordingly. Therefore, at t = 300 s, the highest point of the mass flow rate gradually shifts to other locations. Position B at the front edge of the sedimentary bed was a pure liquid phase after the injection was completed; therefore, the increase rate in solid phase concentration was the slowest. Therefore, this position gradually becomes the highest point of mass flow increase rate and reaches saturation at t = 800 s, which indicates that the amount of activated particles per unit time at this location is equal to the outflow along the flow direction, until the thickness of the sedimentary bed at this location approaches zero.

Influence of Flow Velocity on Slurry Property and Motion Parameters

Figure 11 shows the evolution of the velocity distribution in the transition layer under different flow velocities. It can be observed that with the increase in flow velocity, the influence of particle invasion on the original velocity field gradually decreases, which indicates that the flow velocity

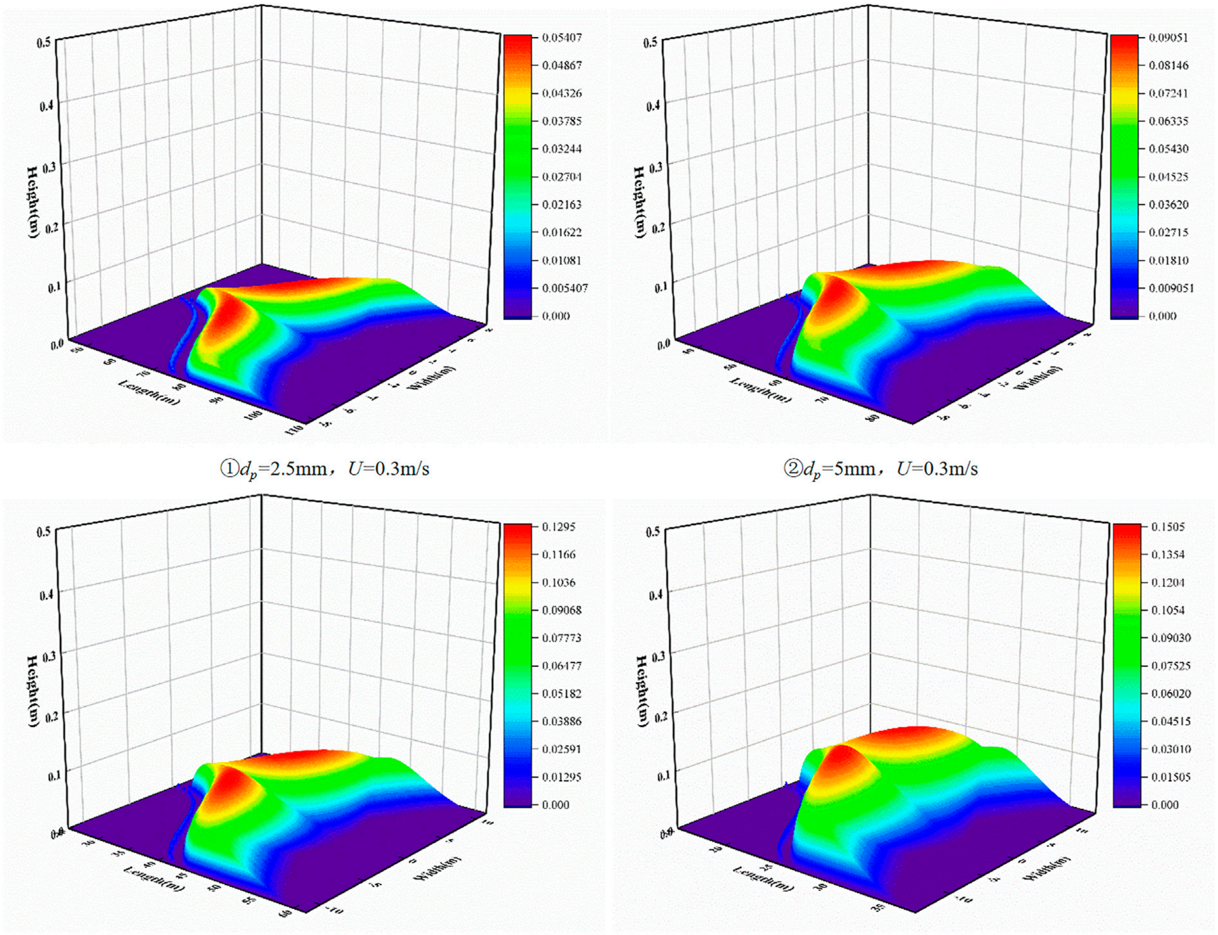

①d_p=2.5mm，U=0.3m/s ②d_p=5mm，U=0.3m/s

③d_p=7.5mm，U=0.3m/s ④d_p=10mm，U=0.3m/s

FIGURE 14 | Variation of sedimentary bed morphology distribution with particle size distribution.

can reflect the hydraulic energy of the transport medium to a certain extent. With the increase in flow velocity, the activation ability of the transition layer with respect to the particles in the sedimentary bed increases, and the thickness of the sedimentary bed decreases as a whole, which is consistent with the trend of the distribution of the sedimentary bed in **Figure 12**.

Influence of Particle Size Distribution on Property and Motion Parameters of Slurry

Figure 13 shows the evolution of the bed morphology distribution for different particle size distributions. As can be observed, the bed thickness increases with an increase in the average particle diameter. However, according to **Figure 14**, the velocity distribution of the transition layer does not respond to the change in particle size, which indicates that the morphological change of the sedimentary bed is simply caused by the change in the initial deposition position caused by the change in particle size distribution, and the change in particle size distribution has little effect on the transport of the transport medium.

CONCLUSION

1) Based on the analysis of the stress state of a single particle and the momentum distribution of the particle swarm, and considering the randomness and uncertainty of particle motion during transportation, a layered model of slurry hydraulic transportation suitable for transportation in pressure pipelines and open channels is established. Compared with the laboratory experiment data, the maximum error of the model calculation is less than 5%, which proves the rationality of the model calculation.
2) The movement of particles during transportation can be divided into two stages: parabolic motion and collision motion, and the momentum distribution of particles in the two stages converges to a stationary state with transportation.

3) The transition layer disturbs the stress state of the particles on the surface of the sedimentary bed, which leads to secondary transportation of particles. The particles intruding into the transition layer disturb the flow field in the transition layer, which causes the distribution of the deposit bed, and the flow field in the transition layer evolves gradually with transportation. The convergence of the particle swarm momentum ensures a stationary state in the evolution process.
4) The property and motion characteristics of the slurry during transportation were simulated and calculated using the proposed model. With an increase in the incoming flow velocity, the shape distribution of the sedimentary bed decreased as a whole, and the extent of disturbance of the flow field in the transition layer decreased as a whole, whereas with an increase in the particle size, the shape distribution of the sedimentary bed showed an overall expansion trend, and the extent of disturbance of the flow field in the transition layer remained basically unchanged.

DATA AVAILABILITY STATEMENT

The original contributions presented in the study are included in the article/supplementary material, further inquiries can be directed to the corresponding author.

AUTHOR CONTRIBUTIONS

ZZ provided the overall idea, SP designed the laboratory experiment, WL was responsible for data analysis, ST did image processing, and ZW and BS provided research funds.

FUNDING

The Special Project for Innovation for “Seventh Generation Ultra-Deepwater Drilling Platform ((2016) No. 24)” Supported by Ministry of Industry and Information Technology, and the Construction Project of Taishan Scholars have no grant numbers.

REFERENCES

Ahmed, R. (2001). *Mathematical Modeling and Experimental Investigation of Solids and Cuttings Transport*. Trondheim: Norwegian University of Science and Technology.

Anderson, R. S., and Haff, P. K. (1991). “Wind Modification and Bed Response during Saltation of Sand in Air,” in *Aeolian Grain Transport* (Vienna: Springer), 1, 21–51. doi:10.1007/978-3-7091-6706-9_2

Capecelatro, J., and Desjardins, O. (2013). Eulerian-Lagrangian Modeling of Turbulent Liquid-Solid Slurries in Horizontal Pipes. *Int. J. multiphase flow* 55, 64–79. doi:10.1016/j.ijmultiphaseflow.2013.04.006

Cho, H., Shah, S. N., and Osisanya, S. O. (2002). A Three-Segment Hydraulic Model for Cuttings Transport in Coiled Tubing Horizontal and Deviated Drilling. *J. Can. Pet. Tech.* 41 (06). doi:10.2118/02-06-03

Cuisinier, O., Auriol, J.-C., Le Borgne, T., and Deneele, D. (2011). Microstructure and Hydraulic Conductivity of a Compacted Lime-Treated Soil. *Eng. Geology.* 123 (3), 187–193. doi:10.1016/j.enggeo.2011.07.010

Doron, P., and Barnea, D. (1993). A Three-Layer Model for Solid-Liquid Flow in Horizontal Pipes. *Int. J. Multiphase Flow* 19 (6), 1029–1043. doi:10.1016/0301-9322(93)90076-7

Einstein, A. (1906). Eine neue Bestimmung der Moleküldimensionen. *Ann. Phys.* 324 (2), 289–306. doi:10.1002/andp.19063240204

Gillies, R. G., Shook, C. A., and Xu, J. (2004). Modelling Heterogeneous Slurry Flows at High Velocities. *Can. J. Chem. Eng.* 82 (5), 1060–1065.

Guo, X. L., Wang, Z. M., and Long, Z. H. (2010). Study on Three-Layer Unsteady Model of Cuttings Transport for Extended-Reach Well. *J. Pet. Sci. Eng.* 73 (1-2), 171–180. doi:10.1016/j.petrol.2010.05.020

Hunt, J. N. (1954). The Turbulent Transport of Suspended Sediment in Open Channels. *Proc. R. Soc. Lond. A.* 224 (1158), 322–335. doi:10.1098/rspa.1954.0161

Ihle, C. F., Tamburrino, A., and Montserrat, S. (2014). Identifying the Relative Importance of Energy and Water Costs in Hydraulic Transport Systems through a Combined Physics- and Cost-Based Indicator. *J. Clean. Prod.* 84, 589–596. doi:10.1016/j.jclepro.2013.11.070

Karabelas, A. J. (1977). Vertical Distribution of Dilute Suspensions in Turbulent Pipe Flow. *Aiche J.* 23 (4), 426–434. doi:10.1002/aic.690230404

Kaushal, D. R., Seshadri, V., and Singh, S. N. (2002). Prediction of Concentration and Particle Size Distribution in the Flow of Multi-Sized Particulate Slurry through Rectangular Duct. *Appl. Math. Model.* 26 (10), 941–952. doi:10.1016/s0307-904x(02)00054-9

Kaushal, D. R., and Tomita, Y. (2003). Comparative Study of Pressure Drop in Multisized Particulate Slurry Flow through Pipe and Rectangular Duct. *Int. J. Multiphase Flow* 29 (9), 1473–1487. doi:10.1016/s0301-9322(03)00125-3

Kaushal, D. R., and Tomita, Y. (2002). Solids Concentration Profiles and Pressure Drop in Pipeline Flow of Multisized Particulate Slurries. *Int. J. multiphase flow* 28 (10), 1697–1717. doi:10.1016/s0301-9322(02)00047-2

Kempe, T., Vowinckel, B., and Fröhlich, J. (2014). On the Relevance of Collision Modeling for Interface-Resolving Simulations of Sediment Transport in Open Channel Flow. *Int. J. multiphase flow* 58, 214–235. doi:10.1016/j.ijmultiphaseflow.2013.09.008

Levy, A., and Mason, D. J. (2000). Two-layer Model for Non-suspension Gas-Solids Flow in Pipes. *Powder Technol.* 112 (3), 256–262. doi:10.1016/s0032-5910(00)00300-4

Matousek, V. (2002). Pressure Drops and Flow Patterns in Sand-Mixture Pipes. *Exp. Therm. Fluid Sci.* 26 (6-7), 693–702. doi:10.1016/s0894-1777(02)00176-0

Muddle, D. M., and Briggs, K. M. (2019). Macropore Structure and Permeability of clay Fill Samples from a Historic clay Fill Earthwork. *Transportation Geotechnics* 19, 96–109. doi:10.1016/j.trgeo.2019.02.003

Nguyen, D., and Rahman, S. S. (1996). “A Three-Layer Hydraulic Program for Effective Cuttings Transport and Hole Cleaning in Highly Deviated and Horizontal wells,” in *SPE/IADC Asia Pacific Drilling Technology* (Kuala Lumpur, Malaysia: Society of Petroleum Engineers). doi:10.2118/36383-ms

Orell, A. (2007). The Effect of Gas Injection on the Hydraulic Transport of Slurries in Horizontal Pipes. *Chem. Eng. Sci.* 62 (23), 6659–6676. doi:10.1016/j.ces.2007.07.067

Owen, P. R. (1964). Saltation of Uniform Grains in Air. *J. Fluid Mech.* 20 (2), 225–242. doi:10.1017/s0022112064001173

Pati, S., Mehta, S. K., and Borah, A. (2017). Numerical Investigation of Thermo-Hydraulic Transport Characteristics in Wavy Channels: Comparison between raccoon and Serpentine Channels. *Int. Commun. Heat Mass Transfer* 88, 171–176. doi:10.1016/j.icheatmasstransfer.2017.09.001

Patterson, L. A., and Maloney, K. O. (2016). Transport of Hydraulic Fracturing Waste from Pennsylvania wells: A County-Level Analysis of Road Use and Associated Road Repair Costs. *J. Environ. Manag.* 181, 353–362. doi:10.1016/j.jenvman.2016.06.048

Pope, S. B. (2001). *Turbulent Flows*. Cambridge University Press.

Pullum, L., Boger, D. V., and Sofra, F. (2018). Hydraulic mineral Waste Transport and Storage. *Annu. Rev. Fluid Mech.* 50, 157–185. doi:10.1146/annurev-fluid-122316-045027

Ravelet, F., Bakir, F., Khelladi, S., and Rey, R. (2013). Experimental Study of Hydraulic Transport of Large Particles in Horizontal Pipes. *Exp. Therm. Fluid Sci.* 45 (2), 187–197. doi:10.1016/j.expthermflusci.2012.11.003

Roco, M. C., and Balakrishnam, N. (1985). Multi-Dimensional Flow Analysis of Solid-Liquid Mixtures. *J. Rheology* 29 (4), 431–456. doi:10.1122/1.549819

Sauermann, G., Kroy, K., and Herrmann, H. J. (2001). Continuum Saltation Model for Sand Dunes. *Phys. Rev. E Stat. Nonlin Soft Matter Phys.* 64 (3), 031305. doi:10.1103/PhysRevE.64.031305

Stanić, F., Jaćimović, N., Ranđelović, A., and Despotović, J. (2017). Laboratory Investigation of Hydraulic Characteristics of Fly Ash as a Fill Material from the Aspects of Pollutant Transport. *Water Sci. Technol.* 76 (4), 976–982. doi:10.2166/wst.2017.243

Syamlal, M., and O'Brien, T. J. (1987). *The Derivation of a Drag Coefficient Formula from Velocity-Voidage Correlations*. NETL, Morgantown, WV: Technical Note, US Department of energy, Office of Fossil Energy.

White, F. M., and Corfield, I. (2006). *Viscous Fluid Flow*. New York: McGraw-Hill.

Wilson, K. C. (1987). Analysis of Bed-Load Motion at High Shear Stress. *J. Hydraulic Eng.* 113 (1), 97–103. doi:10.1061/(asce)0733-9429(1987)113:1(97)

Xie, Y., Jiang, J., Tufa, K. Y., and Yick, S. (2015). Wear Resistance of Materials Used for Slurry Transport. *Wear* 332-333, 1104–1110. doi:10.1016/j.wear.2015.01.005

You, L., and Liu, H. (2002). A Two-phase Flow and Transport Model for the Cathode of PEM Fuel Cells. *Int. J. Heat mass transfer* 45 (11), 2277–2287. doi:10.1016/s0017-9310(01)00322-2

Yu, M.-h., Wei, H.-y., and Wu, S.-b. (2015). Experimental Study on the Bank Erosion and Interaction with Near-Bank Bed Evolution Due to Fluvial Hydraulic Force. *Int. J. Sediment Res.* 30 (1), 81–89. doi:10.1016/s1001-6279(15)60009-9

Zhang, C. X., Liu, W., Wang, L. L., Wang, C., Yang, S. Y., and You, X. Y. (2013). Simulation of Pollutant Transportation in Yinluan Open Channel under the Effects of Wind. *Amm* 419, 842–847. doi:10.4028/www.scientific.net/amm.419.842

Conflict of Interest: The authors declare that the research was conducted in the absence of any commercial or financial relationships that could be construed as a potential conflict of interest.

frontiers
in Earth Science

ORIGINAL RESEARCH
published: 25 November 2021
doi: 10.3389/feart.2021.792232

Migration and Distribution Characteristics of Proppant at the Corner of Horizontal Fracture Network in Coal Seam

Qingying Cheng[1], Haoze Li[2], Bingxiang Huang[2], Xinglong Zhao[2], Zheng Sun[2], Xuejie Jiao[2] and Heng Li[2]*

[1]Jiangsu Key Laboratory of Fire Safety in Urban Underground Space, China University of Mining and Technology, Xuzhou, China,
[2]State Key Laboratory of Coal Resources and Safe Mining, China University of Mining and Technology, Xuzhou, China

A complex fracture network is composed of many similar structures. The migration law of proppant at each structure is the core and basic content of the migration law of proppant in complex fracture network, and there is little research. In this study, the EulerianEulerian method (TEM) is used to analyze the migration and distribution characteristics of solid–liquid two phases at the fracture corner according to different corner types of the fracture network. The results show that the migration characteristics of proppant in the corner area can be divided into the corner anomaly area, buffer area, and stability area; the influence of the turning angle on proppant migration is mainly concentrated at the corner and in the range of 4 times the fracture width after turning. The probability of sand plugging at the corner of the "Y → T" fracture is lower than that of "L → I", higher than that of the "X → +" wing branch fracture, and lower than that of the main fracture. At the corner of the fracture network, after the solid flow turns, the proppant will form a high sand area on the side of the impact fracture surface, then rebound back to the fracture, form a sand-free area on the other side, and form a high-velocity core in the refraction interval. At the corner of the "L → I" fracture, there are one high sand area, one non-sand area, two low-velocity areas, and one high-velocity area; there are three low-velocity areas, two sand-free areas, and one high sand area at the corner of the "Y → T" fracture; at the corner of the "X → +" fracture, there is a high sand area and no sand-free area, and the flow velocity of the main fracture is much greater than that of the wing branch fracture.

Keywords: coal seam, fracture network, corner, proppant migration, distribution characteristics

Edited by:
Zhiyuan Wang,
China University of Petroleum (Huadong), China

Reviewed by:
Pei Li,
China Coal Research Institute (China), China
Ling Chen,
Texas A and M University, United States

****Correspondence:***
Haoze Li
lihaoze@cumt.edu.cn

Specialty section:
This article was submitted to Economic Geology, a section of the journal Frontiers in Earth Science

Received: *10 October 2021*
Accepted: *04 November 2021*
Published: *25 November 2021*

Citation:
Cheng Q, Li H, Huang B, Zhao X, Sun Z, Jiao X and Li H (2021) Migration and Distribution Characteristics of Proppant at the Corner of Horizontal Fracture Network in Coal Seam. Front. Earth Sci. 9:792232. doi: 10.3389/feart.2021.792232

INTRODUCTION

Coalbed methane is mainly composed of methane. Each unit of combustion produces less carbon dioxide than coal and oil. It does not produce ash and release toxic and harmful gases. It is a clean energy (Bustin and Clarkson, 1998; Song and Elsworth, 2018; Wang and Elsworth, 2018). The development of coalbed methane can reduce the content of coalbed methane and internal gas pressure; greatly reduce the probability of gas outburst, gas explosion, coal and gas outburst accidents; and effectively ensure the safe and efficient production of coal mines. Meanwhile, methane and carbon dioxide are the two main gases causing the greenhouse effect (Zachos et al., 2001; Parmesan and Yohe, 2003; Zachos et al., 2008), in which the impact of methane on the greenhouse effect is 20 times that of carbon dioxide (Mooney et al., 1987; Gorham, 1991), and the instability of methane in the air is much higher than that of carbon dioxide, which may produce greater side effects (Mooney et al., 1987). Moreover, in the process of coal seam mining, due to the low concentration of gas drainage, some mines directly discharge low-concentration gas into the air, aggravating the "greenhouse effect." Therefore, the development and utilization of coalbed methane has a certain positive significance to alleviate the "greenhouse effect." These advantages show that CBM has good development prospects and is expected to become an important part of the future energy structure.

In order to improve the exploitation efficiency of coalbed methane, hydraulic fracturing (Huang et al., 2011; Lv et al., 2012), CO_2 phase change fracturing (Colmenares and Zoback, 2007; Xu et al., 2017), nitrogen fracturing (Cai et al., 2015; Qin et al., 2017), and other methods are often used to transform the coal seam, activate the internal bedding and cleat of the coal seam, and form a complex fracture network system penetrating each other. The key of fracturing technology is to form fractures with high conductivity (Li et al., 2021). However, under the action of closure stress, the coal seam fracture is easy to close. Therefore, in order to ensure that the fracture is open after the pumping stops and backflow, and increase the duration of effective fracture opening, proppant needs to be added to the fracture to support the fracture to maintain the fracture conductivity (Li et al., 2020). The migration and distribution of proppant is one of the core technologies to maintain fracture opening (Yan et al., 2016; Guo et al., 2017; Zheng et al., 2017; Wang et al., 2018).

In the project site, due to the formation of fracture network system after fracturing, the migration law of proppant is complex, and effective real-time observation means have not been developed. In order to observe the migration and distribution characteristics of proppant in fractures, the laboratory test and numerical simulation are often used. The laboratory test can observe the distribution characteristics of proppant in the fracture network after the test by tomography (3D XRM) (Liu and Sharma, 2005; Huang B. X. et al., 2019; Yatin et al., 2020) or establish a simple fracture network system through the transparent glass to observe the proppant migration process in the fracture (Bandara et al., 2020). However, the aforementioned two methods have some shortcomings. The former can only observe or simulate the final distribution characteristics of proppant in real fractures, while the latter has a simple fracture network, the fracture shape is non-actual fracture shape, the fracture surface is smooth or uniform roughness, and the reservoir filtration is not considered.

Numerical methods have been widely used because of their advantages of evolvable flow details that are difficult to obtain from experiments and revealing the internal flow mechanism of solid–liquid two phases (Blais et al., 2017; Peng et al., 2019). During proppant migration, there are multiple phases such as solid phase, liquid phase, and even gas, and there are multiple fields such as pore fracture field, stress field, seepage field, and temperature field. Numerical simulation often simplifies the actual situation. At present, the commonly used numerical simulation methods for proppant migration are divided into E-L (Eulerian–Lagrangian) method (Akhshik et al., 2015; Wang et al., 2019) and E-E (Eulerian–Eulerian) method (Xiong et al., 2021). The E-L method regards fluid as the continuous phase and solid particles as a discrete phase for modeling and calculation. Common model calculation methods mainly include discrete particle method (DPM) (Zhang et al., 2017) and the computational fluid dynamics discrete element method (CFD-DEM) (Patankar et al., 2000; Chen et al., 2012; Hu et al., 2021); The E-E method regards fluid and solid particles as continuous phases penetrating each other for simulation. The common model calculation method is a two-fluid model (TEM). Compared with the E-L method, the E-E method requires less calculation and has relatively low requirements for computer configuration. It allows the effective modeling of large-scale systems with a large number of particles, which is conducive to the application to the actual engineering scale. Therefore, the E-E method is widely used in the research field of proppant migration and distribution.

At present, the numerical research on the law of proppant migration and distribution mainly focuses on the flow law in non-permeable simple fractures, and the research on the law of proppant migration in complex fracture network is less. A complex fracture network is composed of many similar structures. The migration law of proppant at each structure is the core and basic content of the migration law of proppant in complex fracture network, and there is little research. The basic law of proppant migration and distribution at the corner of the fracture network has the positive significance for proppant selection and fluid attribute setting and provides theoretical guidance for safe and efficient exploitation of coalbed methane. Therefore, it is necessary to clarify the migration law of proppant at different fracture corners, so as to deeply analyze the migration and distribution characteristics of proppant in the fracture network. This study mainly focuses on the migration and distribution of proppant at the corner of the horizontal fracture network and uses the E-E method (TEM) to analyze the migration and distribution characteristics of proppant at the corner of the horizontal fracture network in the coal seam.

FRACTURING FRACTURE MORPHOLOGY OF COAL SEAM

According to a large number of coal fracturing tests, it shows that the main fracture and wing branch fracture are formed by fracturing in the coal seam. The expansion and extension of the main fracture and wing branch fracture are integrated with the bedding and cleat system in the coal seam to form a complex fracture network structure. According to the local characteristics of the fracture network structure, the fracture network structure can be divided into multiple simple structures, and its morphology is mainly divided into "L → l" (Zhao et al., 2019), "Y → T" (Chen et al., 2019; Cheng et al., 2020), and "X → +" (Ai et al., 2018; Tan et al., 2011, 2019). The fracturing fracture network morphology often presents three types of combined states (**Figure 1**).

FIGURE 1 | Fracture network.

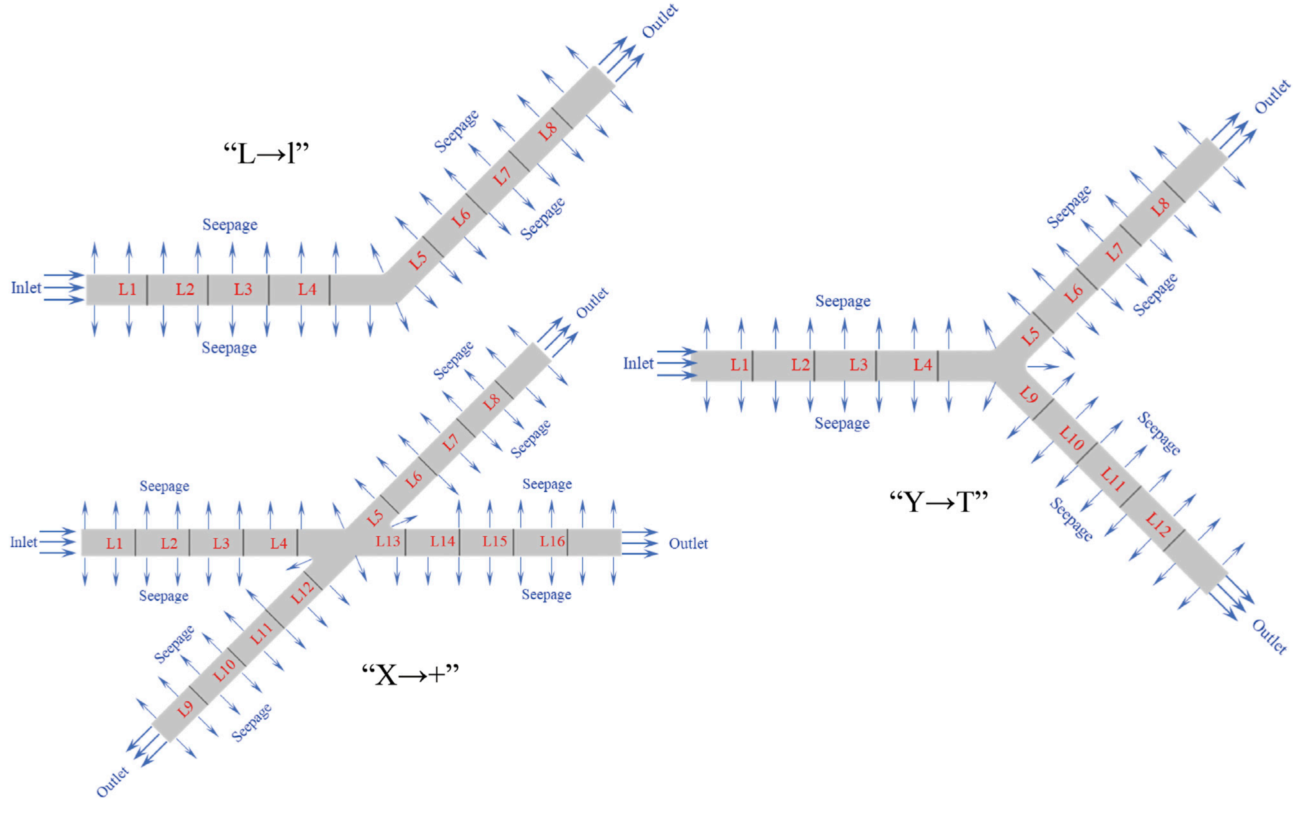

FIGURE 2 | Geometric models of “L → L,” “Y → T,” and “X → +” when the angle is 45°.

TABLE 1 | Model parameter setting.

Symbol	Physical meaning	Value	Unit
ρ_y	Liquid density	1,000	kg/m^3
ρ_g	Solid density	2,650	kg/m^3
μ_y	Liquid-phase dynamic viscosity	0.001	Pa·s
u_y	Inlet liquid velocity (Hu et al., 2018)	0.1	m/s
u_g	Inlet solid velocity (Hu et al., 2018)	0.1	m/s
p_0	Outlet pressure	0.1	MPa
ϕ_g	Proppant volume fraction	0.15	—
d_g	Proppant particle size (Chang et al., 2018; Wu and Sharma, 2019; Chun et al., 2020)	600 (20/40 mesh)	um
κ	Permeability of porous media (Huang et al., 2019b)	0.52	mD
T	Temperature	293	K
H	Fracture width (Suri et al., 2019)	0.002	m

MATHEMATICAL MODEL OF PROPPANT MIGRATION IN FRACTURE

Geometric Model

Based on the contents of **section 2**, the fracture corner can be divided into three types: "L → l," "Y → T," and "X → +." In order to facilitate the research, the angle of "L → l" type corner is divided into 0°, 30°, 45°, 60°, 90°, and 135°, and a total of eight measuring lines L1 ~ L8 are set in the model for analysis; the angle of the "Y → T" type corner is divided into 30°, 45°, 60°, 90°, and 135°, and a total of twelve measuring lines L1 ~ L12 are set in the model for analysis; the angle of "X → +" type corner is divided into 30°, 45°, 60°, and 90°, and a total of sixteen measuring lines L1 ~ L16 are set in the model for analysis. The geometric models of "L → L," "Y → T," and "X → +" when the angle is 45° are shown in **Figure 2**.

Basic Assumptions

The E-E method is used to study the proppant migration and distribution characteristics in the water pressure fracture of the coal seam. The collision between solid particles is considered in the simulation process. In order to study this goal, the following assumptions are made for the model: 1) the proppant particle size in the fracture is uniform; 2) the mass transfer between the fracture surface and the solid fluid is ignored; 3) the influence of bubbles on proppant migration is not considered; 4) the material transfer between two-phase flow is zero; and 5) the skeleton is a rigid body without deformation.

Governing Equations

Mass Balance

Assuming that there is no mass transfer between two phases, the mass conservation equation can be expressed as follows (Zhang et al., 2020):

$$\frac{\partial \phi_g}{\partial t} + \nabla \cdot \left(\phi_g u_g\right) = 0, \tag{1}$$

$$\nabla \cdot \left(\phi_g u_g + u_y\left(1 - \phi_g\right)\right) = 0, \tag{2}$$

$$\phi_y = 1 - \phi_g, \tag{3}$$

where ϕ_y is the volume fraction of the liquid phase, dimensionless; ϕ_g is the volume fraction of solid phase, dimensionless; u_y is the velocity tensor of the liquid phase, m/s; and u_g is the velocity tensor of the solid phase, m/s.

Momentum Balance

The momentum equation of liquid phase and dispersed phase is (Van Wachem et al., 2001) as follows:

$$\rho_y\phi_y\left[\frac{\partial\left(u_y\right)}{\partial t} + u_y\nabla\cdot\left(u_y\right)\right] = -\phi_y\nabla p + \nabla\cdot\left(\phi_y\tau_y\right) + \phi_y\rho_y g + F_{my} + \phi_y F_y, \tag{4}$$

$$\rho_g\phi_g\left[\frac{\partial\left(u_g\right)}{\partial t} + u_g\nabla\cdot\left(u_g\right)\right] = -\phi_g\nabla p + \nabla\cdot\left(\phi_g\tau_g\right) - \nabla p_s + \phi_g\rho_g g + F_{mg} + \phi_g F_g, \tag{5}$$

$$\tau_y = \mu_y\left(\nabla u_y + \left(\nabla u_y\right)^T - \frac{2}{3}\left(\nabla\cdot u_y\right)I\right), \tag{6}$$

$$\tau_g = \mu_g\left(\nabla u_g + \left(\nabla u_g\right)^T - \frac{2}{3}\left(\nabla\cdot u_g\right)I\right), \tag{7}$$

where p is the mixing pressure, assuming that the two-phase pressures are equal, Pa; ρ_g is the solid density, kg/m^3; ρ_y is the density of liquid phase, kg/m^3; τ_g is the viscous stress tensor of solid phase, Pa; τ_y is the viscous stress tensor of liquid phase, Pa; p_s is the solid pressure, Pa; g is the gravitational acceleration tensor, m/s^2; F_m is the momentum transfer phase between phases, F_{my} is the force tensor of other relative liquid phases, F_{mg} is the force tensor of other relative solid phases, N/m^3; F is any other volume force tensor, N/m^3; μ_y is the dynamic viscosity of the liquid, Pa·s; μ_g is the dynamic viscosity of the solid, Pa·s; and I is the unit tensor.

Dispersed Phase Viscosity

The dynamic viscosity of the two-phase mixture is not easy to obtain. Based on experience and analysis, the researchers obtained that the viscosity of the mixture is a function of the dispersion volume fraction, which can be expressed as follows (Enwald et al., 1996):

$$\mu_{\mathrm{h}} = \mu_{\mathrm{y}}\left(1 - \frac{\phi_g}{\phi_{\mathrm{gmax}}}\right)^{-2.5\phi_{\mathrm{gmax}}\left(1-\frac{0.6\mu_{\mathrm{y}}}{\mu_{\mathrm{g}}+\mu_{\mathrm{y}}}\right)}, \tag{8}$$

where ϕ_{gmax} is the maximum filling limit. The default value of solid particles is 0.62, and the default value of droplets/bubbles is 1.

Phase to Phase Momentum Transfer

Considering the particles, droplets, or bubbles in the fluid flow, it is affected by multiple forces, such as resistance, added mass force, and lift. The most important force is resistance, especially in fluids containing highly concentrated dispersed solids. Therefore, the resistance in the momentum equation is expressed as follows (Ergun, 1952; Wen and Yu, 1966):

$$F_{\mathrm{dy}} = -F_{\mathrm{dg}} = \beta \mathrm{u}_{\mathrm{slip}}, \tag{9}$$

$$\mathrm{u}_{\mathrm{slip}} = \mathrm{u}_{\mathrm{g}} - \mathrm{u}_{\mathrm{y}}, \tag{10}$$

$$\beta = \begin{cases} C_{\mathrm{d}}\dfrac{3\phi_{\mathrm{y}}\phi_{\mathrm{g}}\rho_{\mathrm{c}}}{4d_g}\left|\mathrm{u}_{\mathrm{slip}}\right|\phi_{\mathrm{y}}^{-2.65} & , \quad \phi_c > 0.8 \\ 150\dfrac{\mu_{\mathrm{y}}\phi_{\mathrm{g}}^2}{\phi_{\mathrm{y}}d_{\mathrm{g}}^2} + 1.75\dfrac{\phi_{\mathrm{g}}\rho_{\mathrm{y}}}{4d_g}\left|\mathrm{u}_{\mathrm{slip}}\right| & , \quad \phi_c < 0.8 \end{cases}, \tag{11}$$

where β is the drag coefficient; U_{slip} is the slip velocity between phases, m/s; d_{g} is the diameter of solid particles, m; and C_{d} is the drag coefficient of a single solid particle. C_{d} is a function of Reynolds number (Re), which is calculated by using the Schiller–Naumann relationship (Gidaspow, 1994):

$$\mathrm{Re} = \frac{\phi_y d_{\mathrm{d}}\rho_{\mathrm{y}}\left|\mathrm{u}_{\mathrm{slip}}\right|}{\mu_{\mathrm{y}}} \tag{12}$$

$$C_{\mathrm{d}} = \begin{cases} \dfrac{24}{\mathrm{Re}}\left(1 + 0.15\mathrm{Re}^{0.687}\right) & \mathrm{Re} < 1000 \\ 0.44 & \mathrm{Re} > 1000 \end{cases}. \tag{13}$$

Solid Pressure

Solid pressure simulates particle interaction due to collision and friction between particles. The solid pressure model adopts the basic assumption of gradient diffusion (Enwald et al., 1996):

$$\nabla p_{\mathrm{s}} = -10^{-10.5\phi_{\mathrm{y}}+9.0}\nabla\phi_{\mathrm{y}}. \tag{14}$$

Darcy's Law

Considering the filtration of liquid phase on the fracture surface and not the filtration of solid phase, Darcy's law is adopted to obtain the filtration rate of liquid phase as follows (Fan et al., 2019):

$$\mathrm{u} = -\frac{\kappa}{\mu_{\mathrm{y}}}\nabla p, \tag{15}$$

where u is the Darcy velocity tensor, m/s; κ is the permeability of the porous medium, m^2.

Initial Parameters and Solution Settings

The physical parameters required in the numerical simulation of sand-carrying fluid migration in fractures are shown in **Table 1**. The parameters in **Table 1** are assigned to the control equation, and then iterative calculation is carried out. The calculation process lasts for 600 ms.

RESULTS AND ANALYSIS

This section will analyze the migration law and distribution characteristics of solid–liquid two phases at the fracture corner from three aspects: proppant volume fraction distribution characteristics, proppant velocity distribution characteristics, and liquid-phase velocity distribution characteristics at the fracture corner.

Proppant Migration Characteristics at the Corner of "L → l" Fracture

The distribution characteristics of proppant volume fraction of proppant migration at the corner of "L → l" fracture are summarized in **Figure 3**. As shown in **Figure 3A**, when the rotation angle is 0°, the proppant gradually migrates to the fracture depth. In the front section of proppant migration, the middle volume fraction is high, and the volume fraction on both sides is low and is symmetrically distributed along the centerline. When the rotation angle is 30°, the proppant will hit the right fracture surface when it reaches the rotation angle, resulting in the decrease in proppant migration speed. With the passage of time, a high–volume fraction proppant distribution area will be formed at the corner. At 400 ms, the high–volume fraction area tends to be stable, and the proppant will refract and migrate forward after hitting the right fracture surface. At 400 ms, the high–volume fraction region tends to be stable, the proppant refracts and moves forward after hitting the right fracture surface, and a proppant void is formed in the left fracture surface region between incident and refraction, and the volume fraction of proppant in this void is close to 0. With the passage of time, the migration of proppant gradually changed into the form of high/middle volume fraction and symmetrical low volume fraction along the midline (400 ms). When the angle is 45°, the proppant strikes the lower surface of the fracture, part of the proppant flows back to the inlet direction, forming a larger high–volume fraction region at the corner of the lower surface of the fracture, and the width of the high–volume fraction region of the proppant moving forward increases. When the rotation angle is 60°, the backflow of proppant is more significant, and the area of high–volume fraction proppant at the rotation angle increases, but the width of high–volume fraction proppant moving forward decreases, and the proppant empty area increases compared with 45°. When the rotation angle is 90°, a triangular-like high–volume fraction region is formed at the rotation angle, the width of the high–volume fraction region of proppant moving forward is further reduced, and the range of proppant void is further increased. When the rotation angle is 135°, the proppant

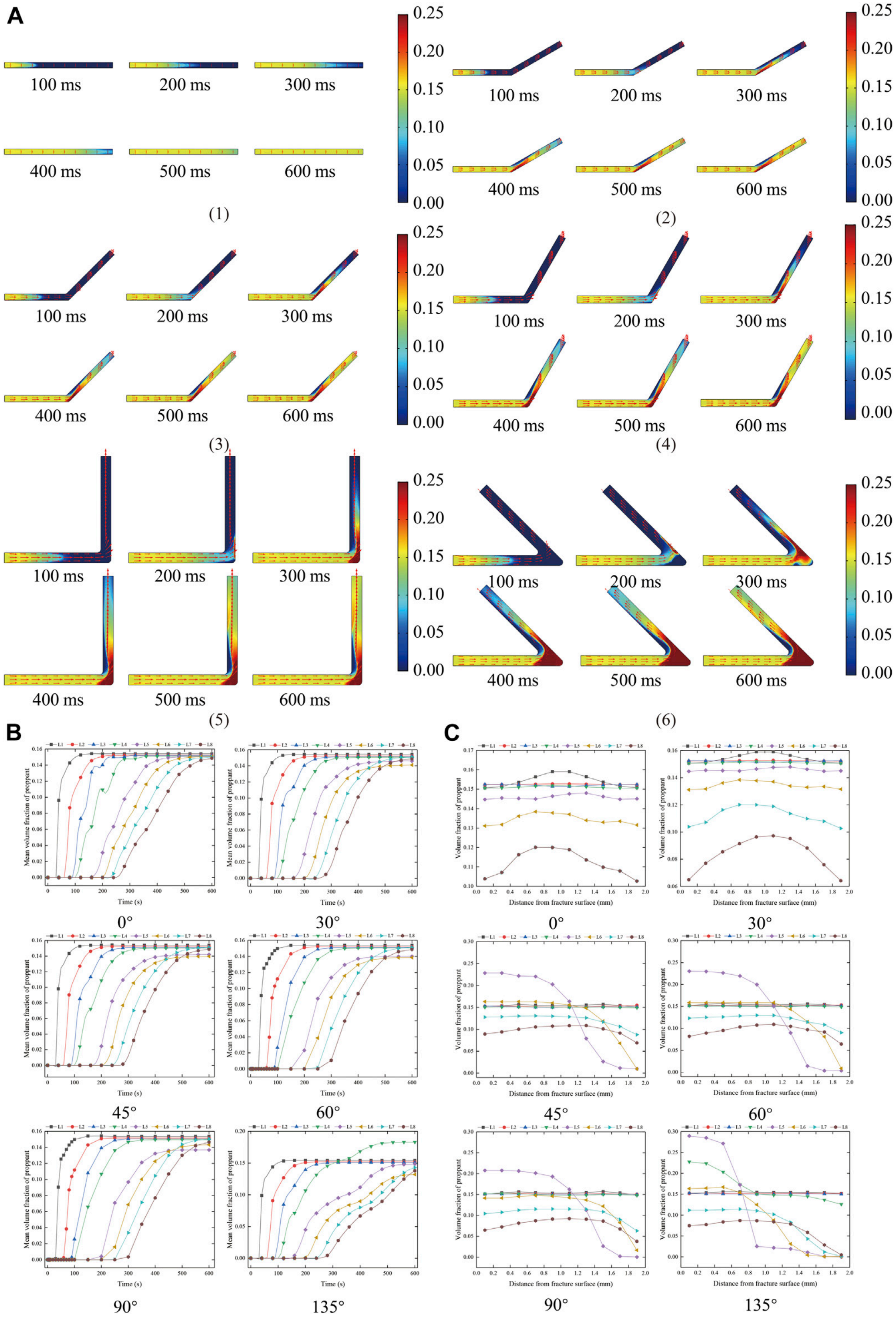

FIGURE 3 | Distribution characteristics of proppant volume fraction at the corner of "L → I." **(A)** Distribution characteristics of proppant volume fraction at the corner of "L → I" fracture. (1) 0°, (2)30°, (3) 45°, (4) 60°, (5) 90°, (6) 135°. **(B)** The distribution of mean proppant volume fraction of each measuring line at different times at the corner of "L → I." **(C)** Distribution of proppant volume fraction of each measuring line at the corner of "L → I" at 400 ms.

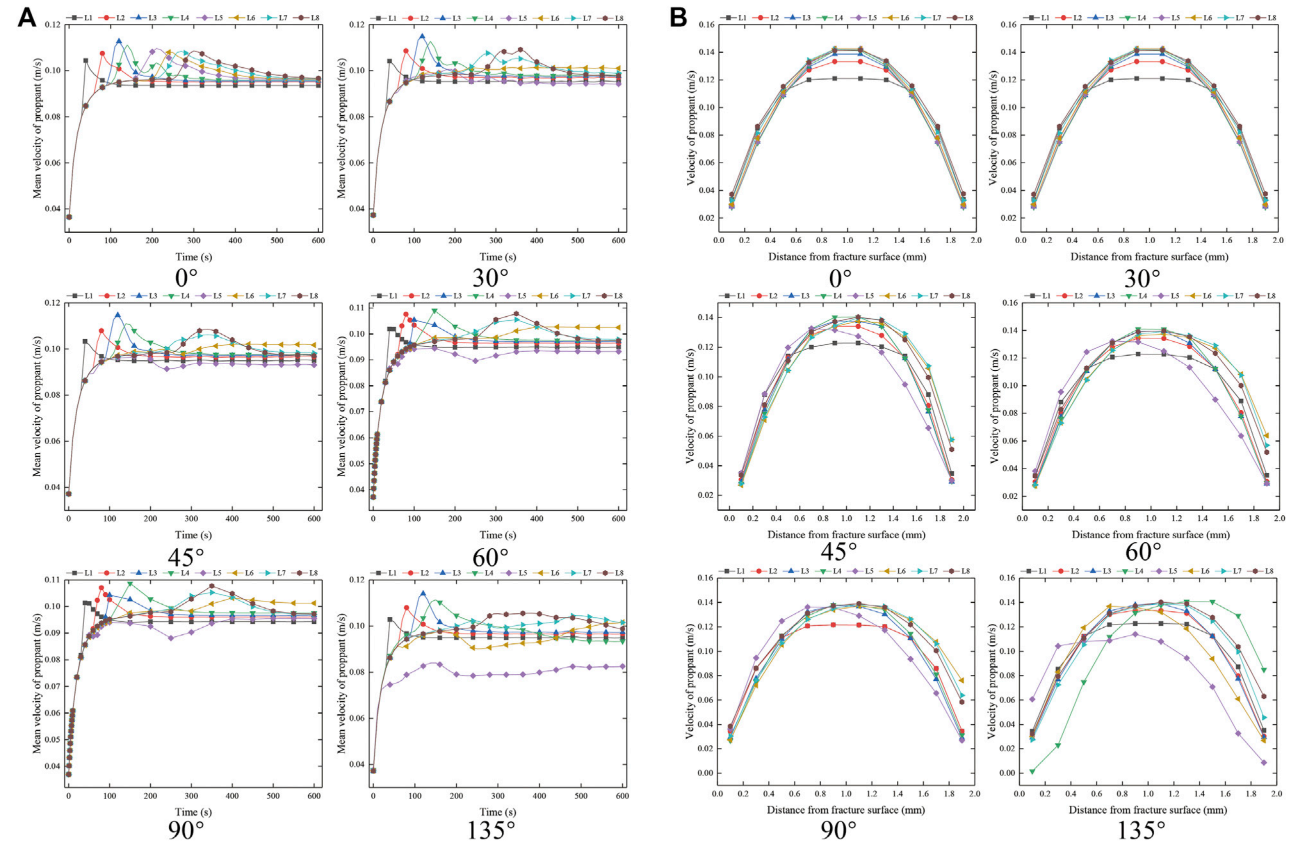

FIGURE 4 | Proppant velocity distribution characteristics at the corner of "L → l." **(A)** Distribution of mean proppant velocity of each measuring line at different times at the corner of "L → l." **(B)** Proppant velocity distribution of each measuring line at the corner of "L → l" at 400 ms.

migration produces new changes. First, the proppant migrates to the fracture and migrates directly perpendicular to the fracture surface, forming a high-volume integral sand area at the fracture surface. Then the proppant flows back along the wall and converges with the proppant migrating forward to form a high–volume fraction proppant with the same fracture width. As the proppant dose moving forward decreases, the time required for proppant migration to change to the original form increases (500 ms). At the same time, the flow area of the liquid phase at the corner is compressed. The high–volume fraction proppant at the 135° corner is very easy to cause fracture plugging.

The mean proppant volume fraction of each measuring line at different times of the "L → l" fracture corner is summarized in **Figure 3B**. As shown in **Figure 3B**, in the proppant volume fraction stabilization stage, with the increase in the corner angle, the average proppant volume fraction not reaching the corner is close to the initial proppant volume fraction. When the angle of rotation is not greater than 90°, the mean value of the proppant volume fraction after turning for a certain distance (L7 and L8) is close to the initial proppant volume fraction, while the mean value of proppant volume fraction at the fracture corner and the area just passing through the fracture corner changes greatly. When the rotation angle is not greater than 60°, the mean proppant volume fraction of L5 and L6 gradually decreases by about 6%, and the mean proppant volume fraction of L5 is greater than L6; when the angle is 90°, the mean volume fraction of L6 is greater than L5; when the rotation angle is 135°, the average proppant volume fraction of L4 increases by about 20%, the average proppant volume fraction of L5 is close to the initial volume fraction, and the average proppant volume fraction of L6 decreases by about 10%. This is due to the backflow of proppant in the corner area, which increases the volume fraction at the corner inlet, and the backflow reduces the total amount of proppant moving forward.

The distribution of proppant volume fraction of each measuring line at 400 ms for "L → l" fracture is summarized in **Figure 3C**. As shown in **Figure 3C**, when the proppant moves through the corner, the proppant volume fraction near the right fracture surface increases, and the proppant volume fraction on the left fracture surface decreases. With the increase in migration distance, the proppant volume fraction near the right fracture surface gradually decreases, the proppant volume fraction near the left fracture surface gradually increases, and the proppant volume fraction of L5 and L6 survey lines is close to 0, indicating that this area is in the proppant empty area.

The distribution characteristics of proppant velocity at the corner of "L → l" are summarized in **Figure 4**. As shown in

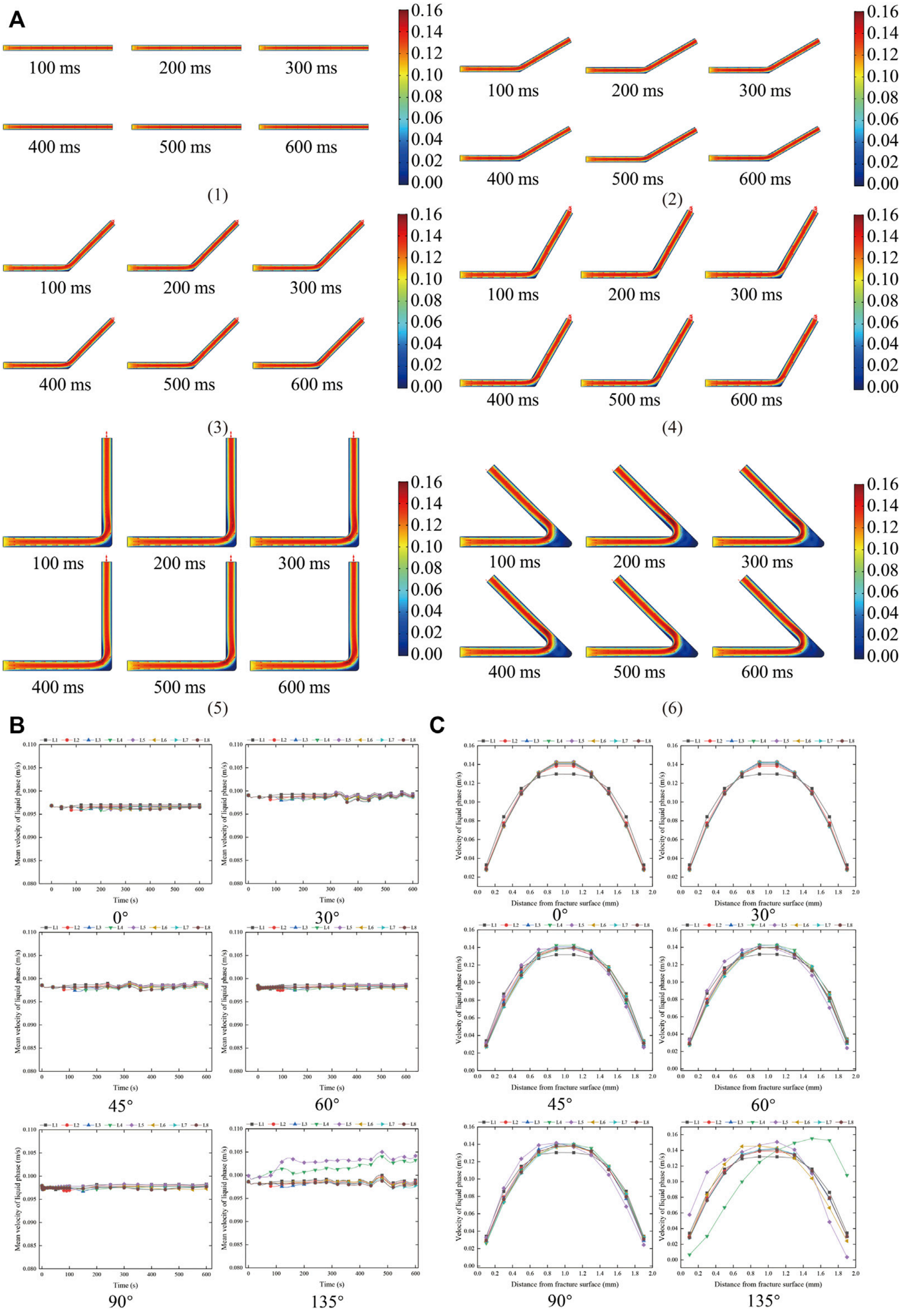

FIGURE 5 | Distribution characteristics of liquid-phase velocity at the corner of "L → l." **(A)** The characteristics of liquid-phase velocity distribution at the corner of "L → l." (1) 0°, (2)30°, (3) 45°, (4) 60°, (5) 90°, (6) 135°. **(B)** Distribution of mean liquid-phase velocity of each survey line at different times at the corner of "L → l." **(C)** Liquid-phase velocity distribution of each measuring line at the corner of "L → l" at 400 ms.

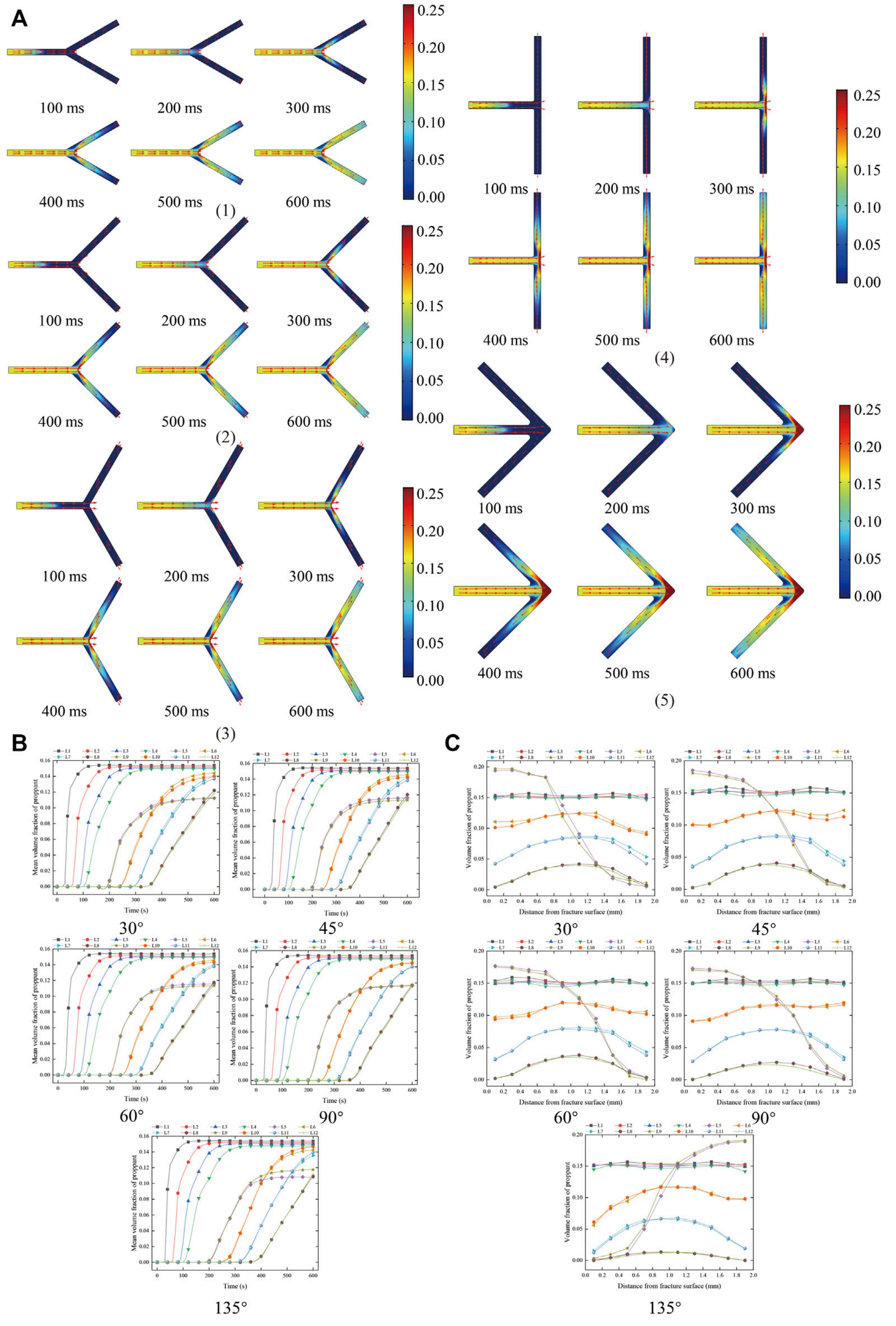

FIGURE 6 | Distribution characteristics of proppant volume fraction at the corner of "Y → T." **(A)** Distribution characteristics of proppant volume fraction at the corner of "Y → T" fracture. (1) 30°, (2) 45°, (3) 60°, (4) 90°, (5) 135°. **(B)** The distribution of mean proppant volume fraction of each measuring line at different times at the corner of "Y → T." **(C)** Distribution of proppant volume fraction of each measuring line at the corner of "Y → T" at 400 ms.

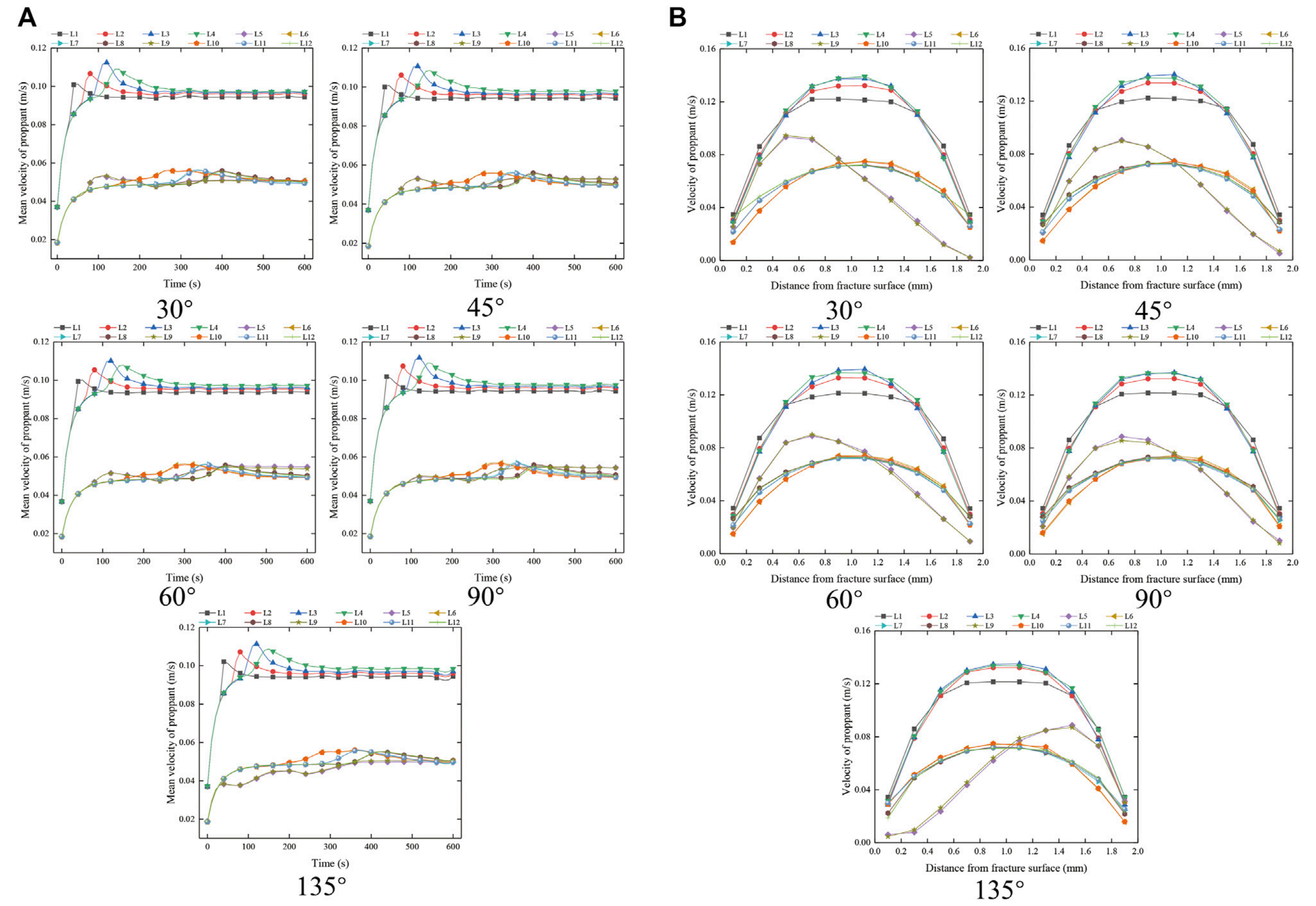

FIGURE 7 | Proppant velocity distribution characteristics at the corner of "Y → T." **(A)** Distribution of mean proppant velocity of each measuring line at different times at the corner of "Y → T." **(B)** Proppant velocity distribution of each measuring line at the corner of "Y → T" at 400 ms.

Figure 4A, with the passage of time, the average proppant migration velocity of L1 ~ L4 survey lines shows rapid increase → slow decrease → tend to be stable. The farther away from the entrance, the longer the proppant migration velocity reaches the peak; the average proppant migration velocity of L5 and L6 survey lines is gradually increase → gradually decrease → slowly increase → tend to be stable. In the stable stage, the proppant migration velocity of L6 survey line is greater than that of the inlet section, and that of L5 survey line is less than that of the inlet section; the average proppant migration velocity of L7 and L8 survey lines is as follows: rapid increase → slow increase → rapid increase → slow decrease → tend to be stable. The peak time of L7 and L8 survey lines is slightly later than the trough time of L5 and L6 survey lines. With the increase in the angle of rotation angle, the trough points of the average proppant migration velocity of L5 and L6 measuring lines gradually decrease. It can be seen from **Figure 4B** that the velocity distribution of proppant in the fracture is "slow at both ends and fast in the middle." At 400 ms, when the angle is not greater than 90°, the peak point of proppant migration velocity shifts to the right fracture surface with the increase in the angle. When the angle is greater than 90°, the peak value of proppant migration velocity before turning shifts to the left fracture surface, the peak value of proppant migration velocity after steering shifts to the right fracture surface, and the migration area increases.

The distribution characteristics of liquid-phase velocity at the corner of "L → l" fracture are summarized in **Figure 5**. As shown in **Figure 5A**, when the liquid phase migrates to the corner, the migration space is compressed, a high-speed fluid is formed in the central area, and a low-speed area appears on both sides. With the increase in the rotation angle, the low-speed region of the liquid phase gradually increases, and the low-speed region of the right fracture region is greater than that of the left fracture region. According to **Figure 5B** and **Figure 5C**, when the rotation angle is not greater than 90°, the liquid-phase mean velocity remains stable and the manifold is stable. The velocity shifts to the right fracture surface in a short area after passing the rotation angle and then remains stable again; when the turning angle is greater than 135°, the mean velocity of the liquid phase increases gradually at the turning angle, the velocity peak before turning is close to the left fracture surface, and the velocity peak after turning is also

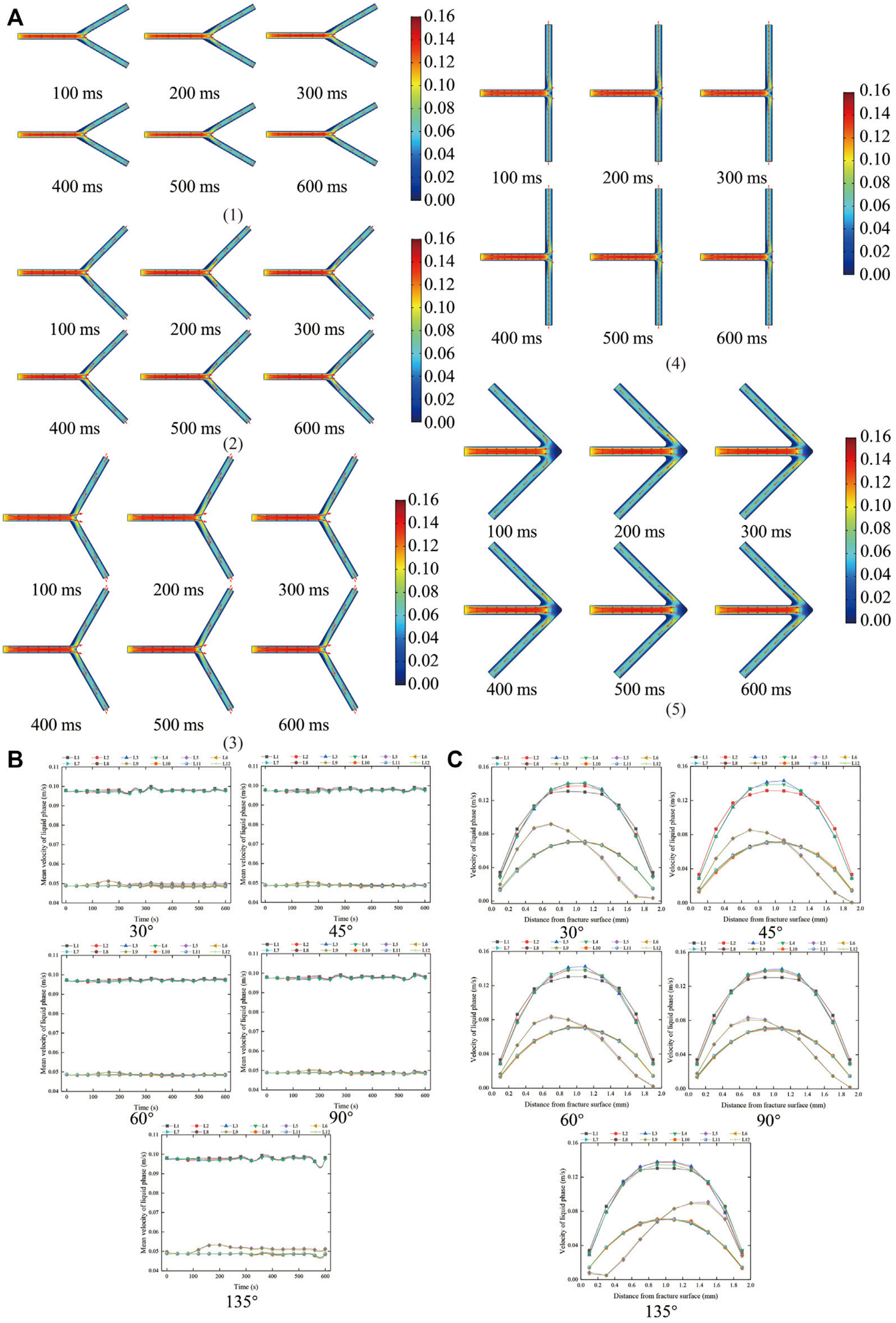

FIGURE 8 | Distribution characteristics of liquid-phase velocity at the corner of "Y → T." **(A)** The characteristics of liquid-phase velocity distribution at the corner of "Y → T." (1) 30°, (2) 45°, (3) 60°, (4) 90°, (5) 135°. **(B)** Distribution of mean liquid-phase velocity of each survey line at different times at the corner of "Y → T." **(C)** Liquid-phase velocity distribution of each measuring line at the corner of "Y → T" at 400 ms.

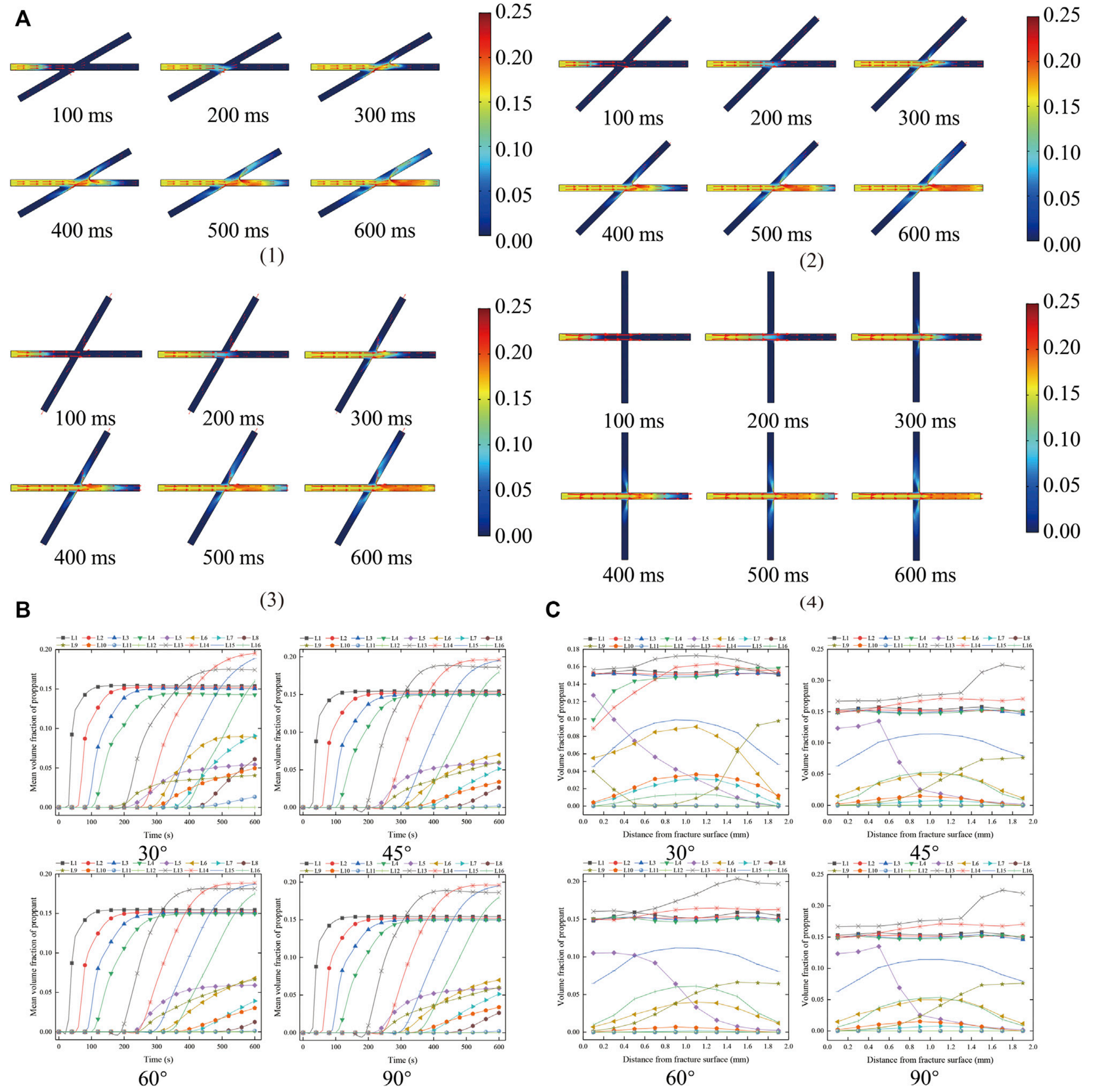

FIGURE 9 | Distribution characteristics of proppant volume fraction at the corner of "X → +." **(A)** Distribution characteristics of proppant volume fraction at the corner of "X → +" fracture. (1) 30°, (2) 45°, (3) 60°, (4) 90°. **(B)** The distribution of mean proppant volume fraction of each measuring line at different times at the corner of "X → +." **(C)** Distribution of proppant volume fraction of each measuring line at the corner of "X → +" at 400 ms.

offset to the left fracture surface. This shows that the turning area near the right fracture surface is mainly the proppant distribution area, and the liquid-phase volume velocity is close to 0. The increase in the proppant area will increase the probability of fracture plugging.

To sum up, at the corner of "L → l," the proppant empty area will be formed on the left fracture surface, and the proppant area with high volume fraction will be formed on the right fracture surface. The migration speed of the continuous phase in the two areas is low, and the velocity in the center of the continuous phase between the two areas is fast. With the increase in the angle of the corner, the volume fraction of proppant on the right side of the fracture corner gradually increases, the proppant return flow gradually increases, the high–volume fraction proppant area at

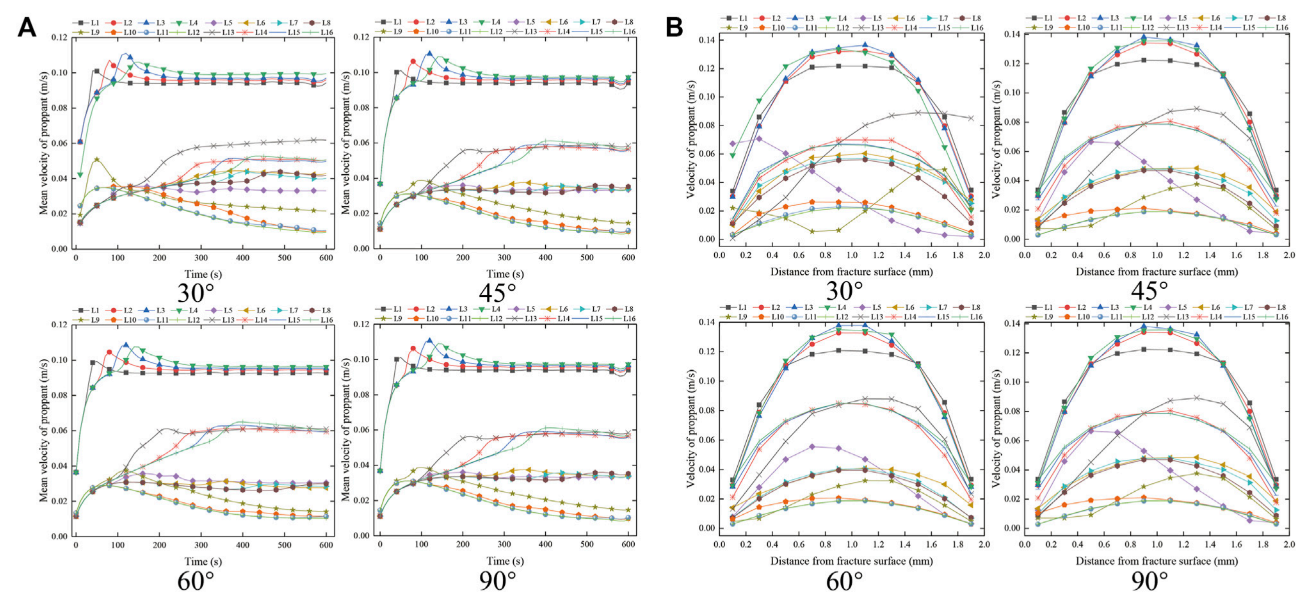

FIGURE 10 | Proppant velocity distribution characteristics at the corner of "X → +." **(A)** Distribution of mean proppant velocity of each measuring line at different times at the corner of "X → +." **(B)** Proppant velocity distribution of each measuring line at the corner of "X → +" at 400 ms.

the corner gradually increases, and the width of the high–volume fraction proppant area moving forward reaches the maximum when the corner is 45°. When the angle is greater than 90°, the width of the area with high volume fraction at the angle is similar to the fracture width, which is easy to cause fracture blockage. A sand-free area with volume fraction close to "0" is formed on the left side of the fracture. The area width and area gradually increase with the increase in the angle. With the passage of time, the proppant migration velocity before steering is as follows, rapid increase → slow decrease → tend to be stable; corner, gradually increase → gradually decrease → slowly increase → tend to be stable; after steering, rapidly increase → slowly increase → rapidly increase → slowly decrease → tend to be stable.

Proppant Migration Characteristics at the Corner of "Y → T" Fracture

The distribution characteristics of proppant volume fraction at the corner of "Y → T" fracture are summarized in **Figure 6**. As shown in **Figure 6**, since the fracture is in the "Y → T" shape, at the fracture corner, the two-phase fluid will impact the corner position, and the proppant volume fraction at the corner increases. With the increase in the corner angle, the high–volume fraction area of proppant at the corner increases. When the proppant enters the turned fracture, it first migrates forward along the right fracture, and then gradually fills the whole fracture width. Two sand-free areas are formed in the corner area. With the increase in the corner angle, the sand-free area gradually increases. Because the shape is symmetrical up and down, the volume fraction of proppant flowing to the two wing branch fractures is equal. After turning, after a certain distance (L6 and L9 in **Figure 6B,C**), the dispersed phase manifold gradually becomes regionally stable, forming a fluid approximately symmetrical along the midline. When the angle is greater than 90°, the high–volume fraction area of proppant at the corner is obviously smaller than the "L → l" fracture, which is not easy to cause fracture blockage. It is easy to know from **Figure 6B,C** that with the passage of time, the farther away from the inlet, the slower the average increase rate of proppant volume fraction and the longer the time required to stabilize. After turning, the proppant volume fraction near the right fracture surface is high, gradually decreases along the direction perpendicular to the fracture surface, and the proppant volume fraction on the left fracture surface is close to 0.

The distribution characteristics of proppant velocity at the corner of "Y → T" fracture are summarized in **Figure 7**. As shown in **Figure 7**, the proppant migration velocity in the wing branch fracture is lower than that in the main fracture, and the proppant migration velocity of each wing branch fracture accounts for about 1/2 of the main fracture. The distribution characteristics of proppant migration velocity in the main fracture are similar to those of the "L → l" fracture. The migration law in the wing branch fracture is rapid increase → slow increase → tend to be stable. After turning, the peak position of proppant migration velocity tends to the right fracture, which is more obvious than the "L → l" fracture.

The distribution characteristics of liquid-phase velocity at the corner of "Y → T" fracture are summarized in **Figure 8**. As shown in **Figure 8**, when the steering angle is not greater than 90°, the liquid-phase manifold basically remains unchanged with the passage of time, and the flow velocity in the wing branch fracture is 1/2 of the main fracture. After turning, the tendency of the peak value of liquid migration velocity to the

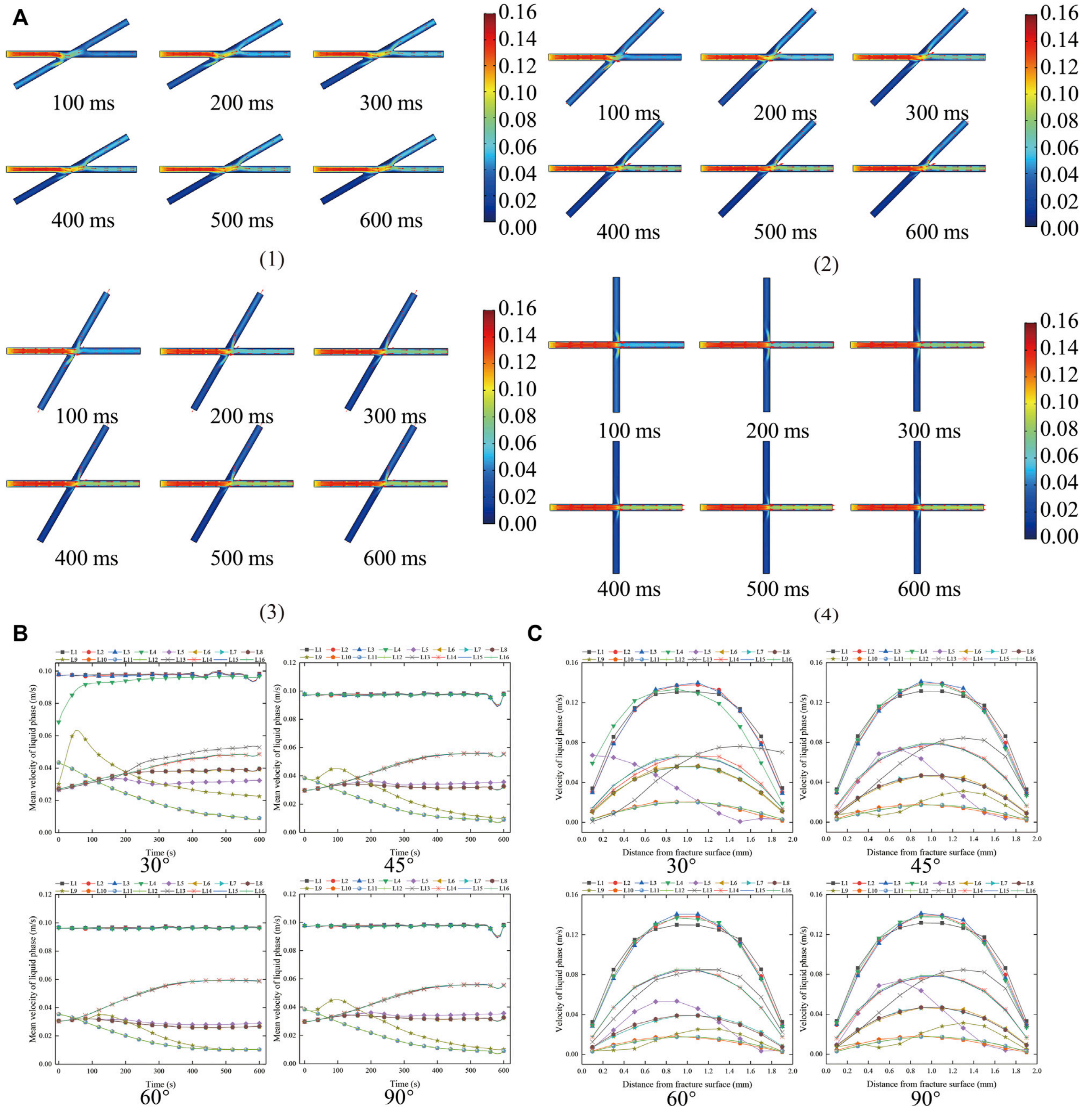

FIGURE 11 | Distribution characteristics of liquid-phase velocity at the corner of "X → +." **(A)** The characteristics of liquid-phase velocity distribution at the corner of "X → +." (1) 30°, (2) 45°, (3) 60°, (4) 90°. **(B)** Distribution of mean liquid-phase velocity of each measuring line at different times at the corner of "X → +." **(C)** Liquid-phase velocity distribution of each measuring line at the corner of "X → +" at 400 ms.

right fracture is more obvious than that of "L → l" fracture, and the peak velocity is about 1.2 times that of the other survey lines of the wing branch fracture. With the increase in the fracture angle, the fluid forms two small low-velocity regions on the left side of the wing branch fracture and a large low-velocity region on the right side of the fracture. When the steering angle is greater than 90°, the velocity of the liquid phase just entering the secondary fracture is slightly higher after steering.

To sum up, the migration law of proppant in the "Y → T" fracture is that the migration velocity of proppant and continuous phase in the wing branch fracture is reduced by 1/2 of the main fracture, and three low-velocity regions, two sand-free regions,

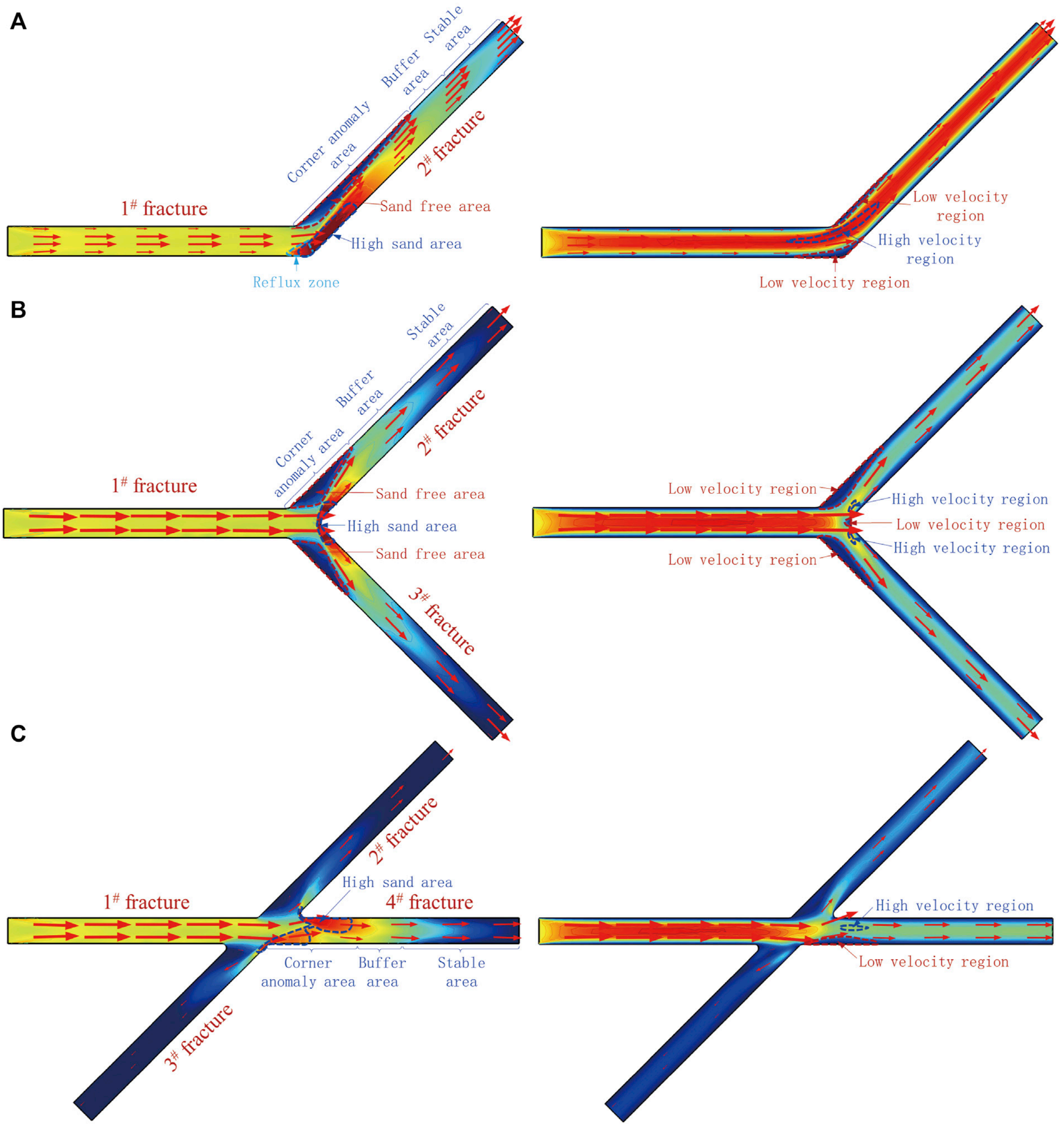

FIGURE 12 | Proppant migration and distribution characteristics at fracture corner. **(A)** "L → l" **(B)** "Y → T" **(C)** "X → +."

and a large high-volume-fraction region are formed at the corner. Due to the increase in secondary fractures, sand plugging will be less than "L → l."

Proppant Migration Characteristics at the Corner of "X → +" Fracture

The distribution characteristics of proppant volume fraction at the corner of "X → +" fracture are summarized in **Figure 9**. As shown in **Figure 9**, when proppant migrates from the main fracture (1# fracture) to the corner of "X → +" fracture, it will first deflect to the secondary fracture (3# fracture) at an obtuse angle with the migration direction and then migrate to the main fracture (4# fracture). When passing through the intersection, the proppant dose entering the main fracture (4# fracture) > the proppant dose at an acute angle with the proppant migration direction (2# fracture) > the proppant dose at an obtuse angle with the migration direction (3# fracture). With the increase in the angle, the difference between the proppant integral number of 2# fracture and 3# fracture becomes smaller and smaller. When just passing through the intersection, the volume fraction of proppant in 4# fracture increases to form a high concentration support and area. With the passage of time, the volume fraction of proppant in 4# fracture is greater than that in 1# fracture. This is because the volume fraction of proppant in 4# fracture flows to 2#, 3# fracture is greater than that of proppant, resulting in an increase of 20% in the volume fraction of proppant in 4# fracture, which is easier to block the fracture. The form of proppant entering the secondary fracture is similar to that of "L → l" fracture. The total amount of proppant in the fracture is 4# fracture >1# fracture >2# fracture >3# fracture. The time required for proppant volume fraction to reach the stable stage is 3# fracture >2# fracture >4# fracture >1# fracture.

The distribution characteristics of proppant velocity at the corner of " X → +" fracture are summarized in **Figure 10**. As shown in **Figure 10**, the proppant migration velocity is as follows: 1# fracture >4# fracture >3# fracture >2# fracture. With the increase in the fracture angle, the proppant migration velocity in each secondary fracture decreases discretely, and the proppant migration velocity in the same secondary fracture is almost the same. With the passage of time, the 1# proppant migration velocity in the fracture shows rapid increase → slow decrease → tend to be stable; The proppant migration velocity in 2# fracture shows that it increases rapidly → increases slowly → tends to be stable; the proppant migration velocity in 3# fracture shows as follows: slow decrease → tend to be stable; the proppant migration velocity in 4# fracture shows that it increases rapidly → tends to be stable. In the stable stage, the migration velocity of 2# fracture proppant is about 38% of that of 1# fracture; the migration velocity of proppant in 3# fracture is about 10% of that in 1# fracture; the migration velocity of proppant in 4# fracture is about 58% of that in 1# fracture.

The distribution characteristics of liquid-phase velocity at the corner of " X → +" fracture are summarized in **Figure 11**. As shown in **Figure 11**, the liquid-phase velocity is 1# fracture >4# fracture >3# fracture >2# fracture. With the increase of fracture angle, the dispersion of liquid-phase migration velocity in each secondary fracture decreases, and the liquid-phase migration velocity in the same secondary fracture is almost the same. With the passage of time, the 1# liquid velocity in the fracture tends to be stable; the velocity of liquid phase in 2# fracture increases slowly at first and then tends to be stable; the velocity of liquid phase in 3# fracture decreases gradually and then tends to be stable; the velocity of liquid-phase migration in 4# fracture increases gradually and then tends to be stable. In the stable stage, the liquid velocity of 2# fracture is about 25% of that of 1# fracture; the liquid-phase velocity of 3# fracture is about 10% of that of 1# fracture; the liquid velocity of 4# fracture is about 58% of that of 1# fracture.

In conclusion, no sand-free zone is formed in the "X → +" fracture, and the volume fraction of 4# fracture proppant is increased by 20%; the total amount of proppant in the fracture is given as follows: 4# fracture >1# fracture >2# fracture >3# fracture; the time required for proppant volume fraction to reach the stable stage is 3# fracture >2# fracture >4# fracture >1# fracture; the two-phase migration velocities are 1# fracture >4# fracture >3# fracture >2# fracture.

Characteristics and Basic Laws of Proppant Migration at Fracture Corner

According to 4.1–4.3, the migration characteristics of proppant and liquid phase at the corners of "L → l", "Y → T," and "X → +" fractures are mainly manifested in the areas of high-volume-fraction of proppant, empty area, high and low speed of liquid phase, etc. The details of each type of 45° (400 ms) are summarized in **Figure 12**. As shown in **Figure 12**, there is a high-volume-fraction proppant area at the fracture corner, and there is a sand-free area in "L → l" and "Y → T" types. The probability of blockage at the corner of "Y → T" fracture is lower than that of "L → l"; compared with the "X → +" type 2# and 3# fractures, the probability of blockage is higher, while the probability of blockage is lower than that of 4# fracture. The migration characteristics of proppant in the corner area can be divided into three areas: corner anomaly area, buffer area, and stability area. The influence of rotation angle on proppant migration is mainly concentrated at the rotation angle and in the range of 4 times the fracture width after steering. When the proppant migration exceeds 4 times the fracture width, the influence of rotation angle on proppant migration law can be ignored.

The characteristics and basic laws of proppant migration of fracture corners provide theoretical guidance for the migration and distribution of proppant for coalbed methane exploitation and have guiding significance for high-efficiency coalbed methane production.

CONCLUSION

In this study, the E-E method (TEM) is used to analyze the migration and distribution characteristics of solid–liquid two phases at the fracture corner in detail through the three aspects of proppant volume fraction distribution, proppant velocity distribution, and liquid-phase velocity distribution at the fracture corner. The main conclusions are as follows:

1) The migration characteristics of proppant in the corner area can be divided into corner anomaly area, buffer area, and stability area; the influence of the turning angle on proppant migration is mainly concentrated at the corner and in the range of 4 times the fracture width after turning. When the proppant migration exceeds 4 times the fracture width, the influence of corner on the proppant migration law can be ignored.

2) The probability of sand plugging at the corner of "Y → T" fracture is lower than that of "L → l," higher than that of "X → +" wing branch fracture, and lower than that of the main fracture.

3) At the corner of the fracture network, after the solid flow turns, the proppant will form a high sand area on the side of the impact fracture surface, then rebound back to the fracture, form a sand-free area on the other side, and form a high-velocity core in the refraction interval.

4) At the corner of the "L → l" fracture, there are one high sand area, one non-sand area, two low-velocity areas, and one

high-velocity area; there are three low-velocity areas, two sand-free areas, and one high sand area at the corner of "Y → T" fracture; at the corner of "X → +" fracture, there is a high sand area and no sand-free area, and the flow velocity of the main fracture is much greater than that of the wing branch fracture.

DATA AVAILABILITY STATEMENT

The original contributions presented in the study are included in the article/Supplementary Materials, further inquiries can be directed to the corresponding author.

AUTHOR CONTRIBUTIONS

QC contributed to funding acquisition and supervision; HL helped with simulation, data analysis, and manuscript drafting; BH designed methodology; XZ assisted with supervision; ZS carried out simulation; XJ performed data analysis; and HeL performed simulation.

ACKNOWLEDGMENTS

The research is supported by the Fundamental Research Funds for the Central Universities (2019XKQYMS25).

REFERENCES

Ai, C., Li, X.-X., Zhang, J., Jia, D., and Tan, W.-J. (2018). Experimental Investigation of Propagation Mechanisms and Fracture Morphology for Coalbed Methane Reservoirs. *Pet. Sci.* 15 (4), 815–829. doi:10.1007/s12182-018-0252-z

Akhshik, S., Behzad, M., and Rajabi, M. (2015). CFD-DEM Approach to Investigate the Effect of Drill Pipe Rotation on Cuttings Transport Behavior. *J. Pet. Sci. Eng.* 127, 229–244. doi:10.1016/j.petrol.2015.01.017

Bandara, K. M. A. S., Ranjith, P. G., and Rathnaweera, T. D. (2020). Laboratory-scale Study on Proppant Behaviour in Unconventional Oil and Gas Reservoir Formations. *J. Nat. Gas Sci. Eng.* 78, 103329. doi:10.1016/j.jngse.2020.103329

Blais, B., Bertrand, O., Fradette, L., and Bertrand, F. (2017). CFD-DEM Simulations of Early Turbulent Solid-Liquid Mixing: Prediction of Suspension Curve and Just-Suspended Speed. *Chem. Eng. Res. Des.* 123, 388–406. doi:10.1016/j.cherd.2017.05.021

Bustin, R. M., and Clarkson, C. R. (1998). Geological Controls on Coalbed Methane Reservoir Capacity and Gas Content. *Int. J. Coal Geol.* 38 (1), 3–26. doi:10.1016/s0166-5162(98)00030-5

Cai, C., Li, G., Huang, Z., Tian, S., Shen, Z., and Fu, X. (2015). Experiment of Coal Damage Due to Super-cooling with Liquid Nitrogen. *J. Nat. Gas Sci. Eng.* 22, 42–48. doi:10.1016/j.jngse.2014.11.016

Chang, O., Kinzel, M., Dilmore, R., and Wang, J. Y. (2018). Physics of Proppant Transport through Hydraulic Fracture Network. *J. Energ Resour-asme.* 140, 329123. doi:10.1115/1.4038850

Chen, J., Li, X., and Cao, H. (2019). Experimental Investigation of Coal-like Materials for Hydraulic Fracturing Based on Fluid-Solid Interaction. *J. Nat. Gas Sci. Eng.* 69, 102928. doi:10.1016/j.jngse.2019.102928

Chen, X., Zhong, W., Sun, B., Jin, B., and Zhou, X. (20122012). Study on Gas/solid Flow in an Obstructed Pulmonary Airway with Transient Flow Based on CFD-DPM Approach. *Powder Tech.* 217, 252–260. doi:10.1016/j.powtec.2011.10.034

Cheng, Q., Huang, B. X., Huang, B., Zhao, X., Chen, S. L., Li, H. Z., et al. (2020). Numerical Investigation on the Mechanism of Rock Directional Fracturing Method Controlled by Hydraulic Fracturing in Dense Linear Multiholes. *Shock and Vibration* 2020 (21), 1–10. doi:10.1155/2020/6624047

Chun, T., Li, Y., and Wu, K. (2020). Comprehensive Experimental Study of Proppant Transport in an Inclined Fracture. *J. Pet. Sci. Eng.* 184, 106523. doi:10.1016/j.petrol.2019.106523

Colmenares, L. B., and Zoback, M. D. (2007). Hydraulic Fracturing and Wellbore Completion of Coalbed Methane wells in the Powder River Basin, Wyoming: Implications for Water and Gas Production. *Bulletin* 91 (1), 51–67. doi:10.1306/07180605154

Enwald, H., Peirano, E., and Almstedt, A.-E. (1996). Eulerian Two-phase Flow Theory Applied to Fluidization. *Int. J. Multiphase Flow* 22, 21–66. doi:10.1016/s0301-9322(96)90004-x

Ergun, S. (1952). Fluid Flow through Packed Columns. *Chem. Eng. Prog.* 48, 89–94.

Fan, M., McClure, J., Han, Y. H., Ripepi, N., Westman, E., Gu, M., et al. (2019). Using an experiment/simulation-integrated Approach to Investigate Fracture-Conductivity Evolution and Non-darcy Flow in a Proppant-Supported Hydraulic Fracture. *SPE J.* 24 (4), 1912–1928. doi:10.2118/195588-pa

Gidaspow, D. (1994). *Multiphase Flow and Fluidization*. San Diego: Academic Press.

Gorham, E. (1991). Northern Peatlands: Role in the Carbon Cycle and Probable Responses to Climatic Warming. *Ecol. Appl.* 1 (2), 182–195. doi:10.2307/1941811

Guo, J., Wang, J., Liu, Y., Chen, Z., and Zhu, H. (2017). Analytical Analysis of Fracture Conductivity for Sparse Distribution of Proppant Packs. *J. Geophys. Eng.* 14, 599–610. doi:10.1088/1742-2140/aa6215

Hu, X., Wu, K., Song, X., Yu, W., Tang, J., Li, G., et al. (2018). A New Model for Simulating Particle Transport in a Low-Viscosity Fluid for Fluid-Driven Fracturing. *Aiche J.* 64 (9), 3542–3552. doi:10.1002/aic.16183

Hu, X., Yang, Z., and Chen, Y. (2021). Fluid-driven Particle Transport Patterns in a Confined Geometry, Effect of Flow Velocity and Particle Concentration. *J. Nat. Gas Sci. Eng.* 92. doi:10.1016/j.jngse.2021.103998

Huang, B., Liu, C., Fu, J., and Guan, H. (2011). Hydraulic Fracturing after Water Pressure Control Blasting for Increased Fracturing. *Int. J. Rock Mech. Mining Sci.* 48 (6), 976–983. doi:10.1016/j.ijrmms.2011.06.004

Huang, B. X., Li, H. Z., Cheng, Q. Y., and Zhao, X. L. (2019a). Compaction and Embedment Characteristics of Proppant in Hydraulic Fractures of Coal Seams. *Nat. Gas Industry* 39, 48–54. doi:10.3787/j.issn.1000-0976.2019.04.006

Huang, H., Babadagli, T., Li, H. A., Develi, K., and Wei, G. (2019b). Effect of Injection Parameters on Proppant Transport in Rough Vertical Fractures: An Experimental Analysis on Visual Models. *J. Pet. Sci. Eng.* 180, 380–395. doi:10.1016/j.petrol.2019.05.009

Li, H., Huang, B., Cheng, Q., Zhao, X., Chen, B., and Zhao, L. (2021). Mechanism of Single Proppant Pressure Embedded in Coal Seam Fracture. *Energy Fuels* 35 (9), 7756–7767. doi:10.1021/acs.energyfuels.0c04360

Li, H., Huang, B., Cheng, Q., and Zhao, X. (2020). Optimization of Proppant Parameters for CBM Extraction Using Hydrofracturing by Orthogonal Experimental Process. *J. Geophys. Eng.* 17 (3), 493–505. doi:10.1093/jge/gxaa009

Liu, Y., and Sharma, M. M. (2005). *SPE Annual Technical Conference and Exhibition*. Dallas, Texas, 9–12. October. SPE-96208-MS. doi:10.2118/96208-msEffect of Fracture Width and Fluid Rheology on Proppant Settling and Retardation, an Experimental Study

Lv, Y., Tang, D., Xu, H., and Luo, H. (2012). Production Characteristics and the Key Factors in High-Rank Coalbed Methane fields: A Case Study on the Fanzhuang Block, Southern Qinshui Basin, China. *Int. J. Coal Geology.* 96-97, 93–108. doi:10.1016/j.coal.2012.03.009

Mooney, H. A., Vitousek, P. M., and Matson, P. A. (1987). Exchange of Materials between Terrestrial Ecosystems and the Atmosphere. *Science* 238 (4829), 926–932. doi:10.1126/science.238.4829.926

Parmesan, C., and Yohe, G. (2003). A Globally Coherent Fingerprint of Climate Change Impacts across Natural Systems. *Nature* 421 (6918), 37–42. doi:10.1038/nature01286

Patankar, N. A., Singh, P., Joseph, D. D., Glowinski, R., and Pan, T.-W. (2000). A New Formulation of the Distributed lagrange Multiplier/fictitious Domain Method for Particulate Flows. *Int. J. Multiphase Flow* 26 (9), 1509–1524. doi:10.1016/s0301-9322(99)00100-7

Peng, Z., Galvin, K., and Doroodchi, E. (2019). Influence of Inclined Plates on Flow Characteristics of a Liquid-Solid Fluidised Bed: A CFD-DEM Study. *Powder Tech.* 343, 170–184. doi:10.1016/j.powtec.2018.11.047

Qin, L., Zhai, C., Liu, S., Xu, J., Yu, G., and Sun, Y. (2017). Changes in the Petrophysical Properties of Coal Subjected to Liquid Nitrogen Freeze-Thaw - A Nuclear Magnetic Resonance Investigation. *Fuel* 194, 102–114. doi:10.1016/j.fuel.2017.01.005

Song, C., and Elsworth, D. (2018). Strengthening Mylonitized Soft-Coal Reservoirs by Microbial Mineralization. *Int. J. Coal Geology.* 200, 166–172. doi:10.1016/j.coal.2018.11.006

Suri, Y., Islam, S. Z., and Hossain, M. (2019). A New CFD Approach for Proppant Transport in Unconventional Hydraulic Fractures. *J. Nat. Gas Sci. Eng.* 70, 102951. doi:10.1016/j.jngse.2019.102951

Tan, P., Jin, Y., Hou, B., Yuan, L., and Xiong, Z. (2011). Experimental Investigation of Hydraulic Fracturing for Multi-type Unconventional Gas Co-exploitation in Ordos Basin. *Arab J. Sci. Eng.* 44 (12), 10503–10511. doi:10.1007/s13369-019-03974-9

Tan, P., Jin, Y., Yuan, L., Xiong, Z.-Y., Hou, B., Chen, M., et al. (2019). Understanding Hydraulic Fracture Propagation Behavior in Tight sandstone-coal Interbedded Formations: an Experimental Investigation. *Pet. Sci.* 16 (1), 148–160. doi:10.1007/s12182-018-0297-z

van Wachem, B. G. M., Schouten, J. C., van den Bleek, C. M., Krishna, R., and Sinclair, J. L. (2001). Comparative Analysis of CFD Models of Dense Gas-Solid Systems. *Aiche J.* 47 (5), 1035–1051. doi:10.1002/aic.690470510

Wang, J., and Elsworth, D. (2018). Role of Proppant Distribution on the Evolution of Hydraulic Fracture Conductivity. *J. Pet. Sci. Eng.* 166, 249–262. doi:10.1016/j.petrol.2018.03.040

Wang, X., Yao, J., Gong, L., Sun, H., Yang, Y., Zhang, L., et al. (2019). Numerical Simulations of Proppant Deposition and Transport Characteristics in Hydraulic Fractures and Fracture Networks. *J. Pet. Sci. Eng.* 183, 106401. doi:10.1016/j.petrol.2019.106401

Wang, Z., Pan, J., Hou, Q., Niu, Q. H., Niu, Q., Tian, J., et al. (2018). Changes in the Anisotropic Permeability of Low-Rank Coal under Varying Effective Stress in Fukang Mining Area, China. *Fuel* 234, 1481–1497. doi:10.1016/j.fuel.2018.08.013

Wen, C. Y., and Yu, Y. H. (1966). Mechanics of Fluidization. *Chem. Eng. Prog. Symp. Ser.* 62, 100–110. doi:10.1016/S0032-0633(98)00014-2

Wu, C. H., and Sharma, M. M. (2019). Modeling Proppant Transport through Perforations in a Horizontal Wellbore. *SPE J.* 4 (24), 1777–1789. doi:10.2118/179117-pa

Xiong, W., Shen, K., Ba, Q., Liu, Y., and Zhou, H. (2021). A Liquid-Solid Model to Optimize the Application of Friction Reducers for Hydraulic Fracturing/cutting in the Underground Coal Mine. *Energy Sci Eng* 9 (9), 1568–1582. doi:10.1002/ese3.930

Xu, J., Zhai, C., Liu, S., Qin, L., and Wu, S. (2017). Pore Variation of Three Different Metamorphic Coals by Multiple Freezing-Thawing Cycles of Liquid CO2 Injection for Coalbed Methane Recovery. *Fuel* 208, 41–51. doi:10.1016/j.fuel.2017.07.006

Yan, X., Huang, Z., Yao, J., Song, W., Li, Y., and Gong, L. (2016). Theoretical Analysis of Fracture Conductivity Created by the Channel Fracturing Technique. *J. Nat. Gas Sci. Eng.* 31, 320–330. doi:10.1016/j.jngse.2016.03.038

Yatin, S., Sheikh, Z. L., and Mamdud, H. (2020). Effect of Fracture Roughness on the Hydrodynamics of Proppant Transport in Hydraulic Fractures. *J. Nat. Gas Sci. Eng.* 80, 103401.

Zachos, J. C., Dickens, G. R., and Zeebe, R. E. (2008). An Early Cenozoic Perspective on Greenhouse Warming and Carbon-Cycle Dynamics. *Nature* 451 (7176), 279–283. doi:10.1038/nature06588

Zachos, J., Pagani, M., Sloan, L., Thomas, E., and Billups, K. (2001). Trends, Rhythms, and Aberrations in Global Climate 65 Ma to Present. *Science* 292 (5517), 686–693. doi:10.1126/science.1059412

Zhang, G., Li, M., and Gutierrez, M. (2017). Numerical Simulation of Proppant Distribution in Hydraulic Fractures in Horizontal wells. *J. Nat. Gas Sci. Eng.* 48, 157–168. doi:10.1016/j.jngse.2016.10.043

Zhang, Q., Zhu, W., Liu, W., Yue, M., and Song, H. (2020). Numerical Simulation of Fractured Vertical Well in Low-Permeable Oil Reservoir with Proppant Distribution in Hydraulic Fracture. *J. Pet. Sci. Eng.* 195, 107587. doi:10.1016/j.petrol.2020.107587

Zhao, H., Wang, X., and Liu, Z. (2019). Experimental Investigation of Hydraulic Sand Fracturing on Fracture Propagation under the Influence of Coal Macrolithotypes in Hancheng Block, China. *J. Pet. Sci. Eng.* 175, 60–71. doi:10.1016/j.petrol.2018.12.031

Zheng, X., Chen, M., Hou, B., Ye, Z., Wang, W., Yin, C., et al. (2017). Effect of Proppant Distribution Pattern on Fracture Conductivity and Permeability in Channel Fracturing. *J. Pet. Sci. Eng.* 149, 98–106. doi:10.1016/j.petrol.2016.10.023

Conflict of Interest: The authors declare that the research was conducted in the absence of any commercial or financial relationships that could be construed as a potential conflict of interest.

frontiers
in Earth Science

ORIGINAL RESEARCH
published: 30 November 2021
doi: 10.3389/feart.2021.786996

Characterization of Physical Field and Flow Assurance Risk Analysis of Subsea Cage-Sleeve Throttling Valve

*Donglei Jiang[1], Wenbo Meng[1], Yi Huang[1], Yi Yu[1], Youwei Zhou[2], Zhichen Jiang[2] and Yonghai Gao[2]**

[1]Engineering and Technology Operating Center, Zhanjiang Branch of CNOOC Ltd, Zhanjiang, China, [2]School of Petroleum Engineering, China University of Petroleum(East China), Qingdao, China

The subsea production system is presently widely adopted in deepwater oil and gas development. The throttling valve is the key piece of equipment of the subsea production system, controlling the safety of oil and gas production. There are many valves with serious throttling effect in the subsea X-tree, so the hydrate formation risk is relatively high. In this work, a 3D cage-sleeve throttling valve model was established by the numerical simulation method. The temperature and pressure field of the subsea throttling valve was accurately characterized under different prefilling pressure, throttling valve opening degree, and fluid production. During the well startup period, the temperature of the subsea pipeline is low. If the pressure difference between the two ends of the pipeline is large, the throttling effect is obvious, and low temperature will lead to hydrate formation and affect the choice of throttling valve material. Based on the analysis of simulation results, this study recommends that the prefilling pressure of the subsea pipe is 7–8 MPa, which can effectively reduce the influence of the throttling effect so that the downstream temperature can be kept above 0°C. At the same time, in regular production, a suitable choke size is opened to match the production, preventing the serious throttling effect from a small choke size. According to the API temperature rating table, the negative impact of local low temperature caused by the throttling effect on the temperature resistance of the pipe was considered, and the appropriate subsea X-tree manifold material was selected to ensure production safety. The hydrate phase equilibrium curve is used to estimate the hydrate formation risk under thermodynamic conditions. Hydrate inhibitors are injected to ensure downstream flow safety.

Keywords: cage-sleeve throttling valve, subsea prefilling pressure, opening degree, hydrate prevention, flow assurance

Edited by:
Weiqi Fu,
China University of Mining and Technology, China

Reviewed by:
Haiwen Zhu,
University of Tulsa, United States
Mingzheng Yang,
Louisiana State University, United States

***Correspondence:**
Yonghai Gao
upcgaoyh@126.com

Specialty section:
This article was submitted to Economic Geology, a section of the journal Frontiers in Earth Science

Received: *30 September 2021*
Accepted: *01 November 2021*
Published: *30 November 2021*

Citation:
Jiang D, Meng W, Huang Y, Yu Y, Zhou Y, Jiang Z and Gao Y (2021) Characterization of Physical Field and Flow Assurance Risk Analysis of Subsea Cage-Sleeve Throttling Valve. Front. Earth Sci. 9:786996. doi: 10.3389/feart.2021.786996

INTRODUCTION

In 1947, American engineers first proposed the concept of a “subsea wellhead” (Li and An, 2020), which laid the foundation for the development of a subsea production system. At present, subsea production systems are widely used in deep-water oil and gas fields, such as offshore Brazil and the south China sea (Hong et al., 2018). With further research and a full understanding of production conditions, the technologies and equipment of subsea production systems will play a dominant role in the future of deepwater oil and gas development.

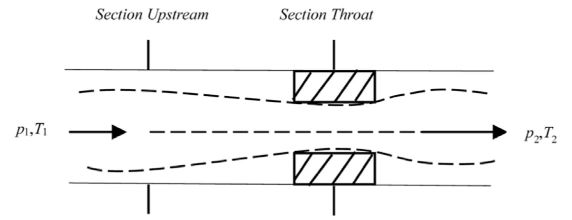

FIGURE 1 | Throttling schematic diagram of the internal flow channel of a single throttling hole.

The subsea X-tree is the key equipment in the subsea production system to control oil and gas production safety. The stable opening and closing of the valve in the X-tree play a role in oil and gas production. Valve flow capacity is mainly evaluated by C_v value, and different internal structure has different C_v value (Grace and Frawley, 2011). Only by knowing the valve internal structure can an engineer accurately judge the flow capacity of the valve. From the onshore experience, valves are vulnerable to fluid erosion, so a lot of researches have focused on the problem of sand erosion and throttling valves (Gharaibah and Zhang, 2015). However, in valves, chokes, and jumper bent pipelines on the wing of the subsea X-tree (Zhao et al., 2014), the oil and gas flow turbulence is intensified, with serious throttling effect, so the temperature and pressure drop is obvious. At the same time, the low temperature at the seabed further aggravates the risk of hydrate formation. On site, hydrate inhibitors are often injected to ensure stable production. Furthermore, the subsea chokes confront the fluid erosion and the low temperature of throttling effect, which has certain requirements for the temperature resistance of the pipe material. Based on the requirements of offshore flow assurance, researchers need to study the temperature and pressure field under different production conditions (Sotoodeh, 2019).

Compared with onshore oil and gas development, offshore operations are more difficult and have high cost and technical requirements. Subsea production equipment cannot be replaced as easily as onshore. The numerical simulation method is adopted to provide a relevant basis for the reliability of the equipment. Cameron, FMC, and others possess the majority of the subsea X-tree, subsea throttling valves, and related equipment market share (Rassenfoss, 2011). The internal structure of subsea equipment is very complicated, so there are few studies on 3D simulation of real objects at present. When simulating the physical field of subsea throttling valves, scholars usually use a 2D variable diameter model instead of a 3D cage-sleeve model to describe the throttling effect at the throttling valve. In order to accurately characterize the physical field at the cage-sleeve throttling valve, a 3D cage-sleeve throttling valve model is established in this study.

This study characterizes the temperature and pressure distribution of the subsea chokes, the main throttling part of the subsea X-tree. We assess downstream temperature and hydrate formation risk for different gas production and valve opening degree. In the well startup period, if the pressure difference between the throttling valve ends is too large, the throttling effect is very obvious (Ju et al., 2021). Throttle valve opening degree and production should be a good match. At last, the prefilling pressure of downstream sea pipe is analyzed and the reasonable pressure design value is recommended. To avoid hydrate formation, hydrate inhibitors are often injected to ensure safe production.

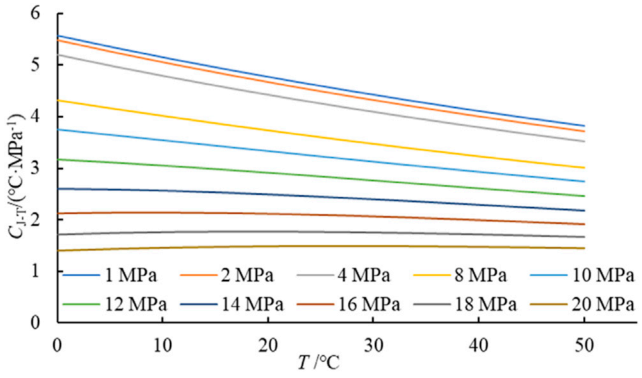

FIGURE 2 | Reference values of J-T coefficients under different temperature and pressure.

JOULE-THOMSON EFFECT OF SUBSEA THROTTLING VALVE

The subsea throttling valve plays the role of controlling and regulating the flow in the subsea production system. When the gas flows through the throttling valve, the flow area decreases, and turbulence increases (Zhang et al., 2010). The dominant control function is the small hole in the throttling valve cage. The internal flow channel of a single throttling hole is shown in **Figure 1**.

The Joule-Thomson effect, also known as the throttling effect, occurs when gas passes through the orifice, which is the main cause of the low temperature of the throttling valve. After the natural gas passes through the throttling valve, the pressure drops, and the expansion of the gas needs to absorb heat, leading to the temperature drop in downstream of the choke. The lower the downstream pressure, the more obvious the temperature drop. Generally speaking, when natural gas reaches the throttle valve, both the temperature and pressure will drop under the Joule-Thomson cooling effect. The ratio of the change of temperature and pressure in isoenthalpy is usually expressed as the Joule-Thomson coefficient, or throttling expansion coefficient (Shoghl et al., 2020):

$$C_{\mathrm{J-T}} = \left(\frac{\mathrm{d}T}{\mathrm{d}p}\right)_H \tag{1}$$

According to **Eq. 1**, the throttling temperature drop caused by pressure drop can be calculated by **Eq. 2** after transpose integration:

$$\Delta T = T_2 - T_1 = \int_{p_1}^{p_2} \mu \mathrm{d}p = \mu \Delta p \tag{2}$$

Different gases have different values of Joule-Thomson coefficient under different temperatures and pressures. This

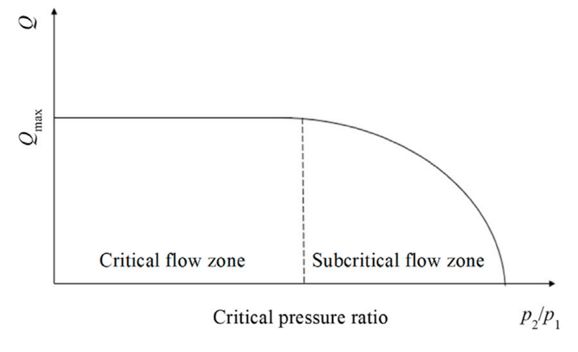

FIGURE 3 | Relation graph of natural gas pressure ratio and production.

study simulates the Joule-Thomson coefficient under different temperatures and pressures for pure methane gas, and the specific values are shown in **Figure 2**. It can be seen that the higher the gas temperature and pressure is, the lower the $C_{\text{J-T}}$ value is, indicating that the gas throttling effect is weak under high temperature and high pressure. The $C_{\text{J-T}}$ value is about 1.5°C/MPa at 20 MPa and about 2.7–3.7°C/MPa at 10 MPa. If the gas pressure drops from 20 to 10 MPa, according to **Eq. 2**, the temperature drop range affected by the throttling effect is 15.0–37.0°C.

In real production, a reasonable development plan needs to be adopted. In the throttling process of natural gas, there are two flow states: critical flow and subcritical flow. Under the critical flow state, the pressure fluctuation generated at the downstream cannot affect the upstream pressure through the throttling valve (Zheng et al., 2020). However, the pressure difference between the two ends of the throttling valve is large, so the negative impact of the large throttling effect should be considered comprehensively.

Critical pressure ratio is commonly used to divide critical flow state and subcritical flow. The critical pressure ratio is defined as:

$$\beta = \frac{\text{Downstream pressure}}{\text{Upstream pressure}} = \frac{p_2}{p_1} = \left(\frac{2}{\kappa+1}\right)^{\frac{\kappa}{\kappa-1}} \tag{3}$$

Where, κ is the adiabatic index of natural gas, dimensionless; The κ value is a function of temperature and pressure and is closely related to gas properties. When the downstream pressure to upstream pressure ratio is less than the critical pressure ratio, production through the valve will not change. Production and pressure ratio are illustrated in **Figure 3**.

Generally, scholars believe that when the pressure after throttling is about half of the pressure before throttling, the critical flow state can be reached. In the critical flow state, there is a maximum critical flow $q_{\max}$. **Eq. 4** is the calculation formula of gas critical flow production in a single hole:

$$q_{\max} = \frac{0.408 p_1 d^2}{\sqrt{\gamma_g T_1 Z_1}} \sqrt{\left(\frac{\kappa}{\kappa-1}\right)\left[\left(\frac{2}{\kappa+1}\right)^{\frac{2}{\kappa-1}} - \left(\frac{2}{\kappa+1}\right)^{\frac{\kappa+1}{\kappa-1}}\right]} \tag{4}$$

Where, $q_{\max}$ is the volume flow of gas in standard condition, $10^4\ \text{m}^3\ \text{d}^{-1}$; p_1 is the upstream pressure, MPa; p_2 is downstream pressure, MPa; d is the diameter of the choke hole, mm; and γ_g is the relative density of the gas. T_1 is the throttling valve inlet temperature, K; Z_1 is the gas compression factor at the inlet of the throttling valve; κ is the adiabatic index of the gas, $\kappa = c_p/c_v$.

When natural gas is in a subcritical flow state, the formula of gas flow in a single hole is as follows:

$$q_{\max} = \frac{0.408 p_1 d^2}{\sqrt{\gamma_g T_1 Z_1}} \sqrt{\left(\frac{\kappa}{\kappa-1}\right)\left[\left(\frac{p_2}{p_1}\right)^{\frac{2}{\kappa}} - \left(\frac{p_2}{p_1}\right)^{\frac{\kappa+1}{\kappa}}\right]} \tag{5}$$

According to the above two formulas, when the economic production range is determined, a reasonable size of single-hole choke can be estimated. Considering the number of holes and their distribution, an appropriate throttling valve can be preliminarily selected. When the flow is in the subcritical flow state, the flow rate varies with the pressure difference between the two ends of the throttling valve. Therefore, it is more necessary to adjust the throttling valve size to match different production procedures.

GEOMETRIC MODEL AND MESHING

The cage-sleeve throttling valve is a commonly used choke type in the subsea production system. Compared with needle valves and orifice valves, the cage-sleeve throttling valve has a symmetrical distribution of throttling holes. When the gas passes through a throttling hole, it is a mutual hedge to consume energy. This structure improves the gas flow field distribution in the throttling valve so that the production is more stable.

This study designs a 3D cage-sleeve throttling valve model using Solidworks, and its structure is shown in **Figure 4**. The core parts of the cage-sleeve throttling valve are the cage sleeve and the plunger. Its working principle is to control the movement of the internal plunger through the stem, then the plunger covers the cage-sleeve holes to adjust the flow area (Malavasi and Messa, 2014), directly affecting the flow ability of the throttling valve, and finally achieving the purpose of throttling. The pipe inner diameter in the inlet and outlet of this model is 4 ″1/2 (114 mm). Each row of the throttling holes is arranged in parallel along the axis of the cage-sleeve and has an angle of 60° along the circumference. The number of holes in each row is 5, so the total number of throttling holes is 30. Large holes meet the requirements of high production and small holes can flow low production.

The throttling holes on the cage sleeve are not continuous, and the size of the holes is not the same. This study uses the method of the specific area defining the opening degree, which is the ratio of the open hole area to the total area of the cage-sleeve hole (Feng et al., 2017). The opening degree is calculated as shown in :

$$\eta = \frac{A_{\text{open}}}{A_{\text{total}}} \times 100\% \tag{6}$$

According to **Eq. 4** and **5** for single-hole calculation and simulation results, the flow rate of the throttling valve in this study has exceeded $200\times10^4\ \text{sm}^3/\text{d}$, which already meets the production requirements, when the 9, 6, and 3 mm throttling holes are all opened. On this basis, five groups of production opening degrees were determined. Since the gas flow capacity of different sized holes is not consistent, the number of holes determining the opening degree does not increase uniformly.

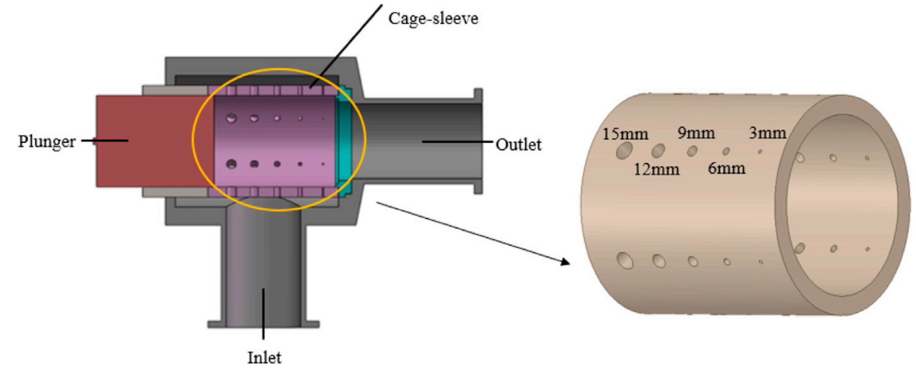

FIGURE 4 | Diagram of the cage-sleeve throttling valve structure.

TABLE 1 | The number of opened throttling holes with their different opening degrees.

Opening degree/%	The number of 3 mm holes	The number of 6 mm holes	The number of 9 mm holes
7.14	6	0	0
21.43	6	3	0
35.71	6	6	0
67.86	6	6	3
89.29	6	6	5

In order to set an appropriate opening degree gradient, the final number of opened throttling holes is determined, as shown in **Table 1**:

According to each different opening degree, we establish different geometric models, and then grid the model, specifically in the vicinity of the throttling holes for local grid refinement. This study used tetrahedrons mesh which was suitable for unstructured models. The element size is 5–10 mm, and the face size of the hole is 0.5–1.0 mm. The number of mesh is from 1 million to 3 million, and mesh meets the requirement of skewness, minimum orthogonal quality, and maximum aspect ratio, which ensure the accuracy and efficiency of computations in simulation software. The fluid of numerical computation is pure methane, following the SRK equation of real gas state equation, and the Realizable K-ε turbulence model and energy equation were adopted. The throttling inlet pressure is 20 MPa, and the inlet temperature is set at 330 K. As for the temperature of the wall, 280 K is set in our study, which is the temperature at the seabed. The second-order upwind scheme is used for discrete schemes, and the steady-state model is used for computation (Li et al., 2018).

DETAILED CHARACTERIZATION OF PHYSICAL FIELD OF SUBSEA THROTTLING VALVE AFFECTED BY DIFFERENT FACTORS

By using numerical simulation software ANASY Fluent, the temperature, pressure, and velocity fields of high-pressure gas flowing through the orifice of the subsea throttling valve can be accurately characterized. According to the different backpressure of subsea pipeline and the opening degree of subsea throttling valve, the influence of the Joule-Thomson effect on the safety of gas flow under different factors is analyzed, then the local high-risk area of subsea throttling valve is found out. Finally, the safe and feasible operation suggestions of subsea throttling valve are put forward.

Appropriate Downstream Pipe Prefilling Pressure

As gas reaches the subsea wellhead, the pressure in the wellbore slightly decreases, so the subsea wellhead pressure is usually high during the early production stage. Subsea production piping to the central processing platform is usually prefilled with nitrogen to reduce the pressure difference between the upstream and downstream of the subsea throttling valves, reducing the temperature plunge caused by the throttling effect.

Prefilling pressure is a factor that needs to be considered in the field, and appropriate prefilling pressure is selected to meet the requirements of efficient and safe production. Unilaterally reducing the throttling pressure difference at both ends of the choke will consume a large amount of nitrogen, which will have certain requirements on the capacity of the prefilling pump and increase the cost. However, low prefilling pressure leads to low temperatures and hydrate formation risk after throttling. In order to determine the appropriate prefilling pressure, this paper simulates the subsea cage-sleeve throttling valve with a downstream prefilling pressure of 3–14 MPa and obtains the corresponding physical field parameters.

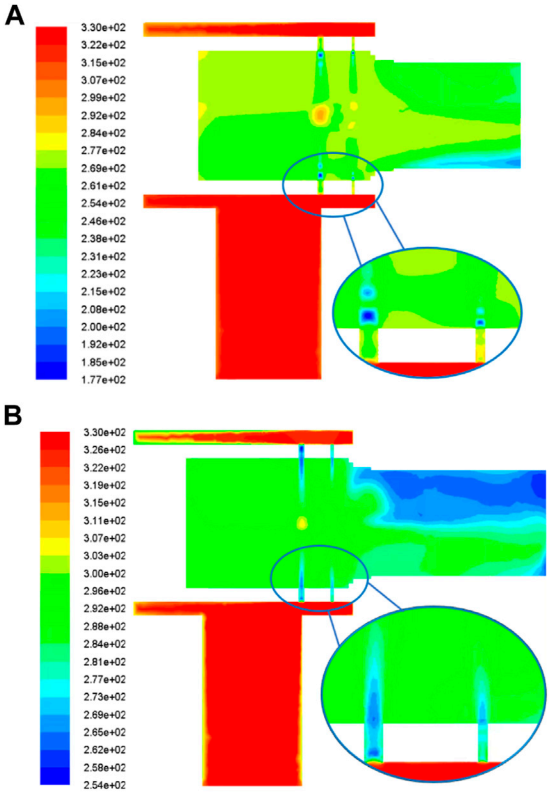

FIGURE 5 | Vertical profiles of choke temperature under prefilling pressure of 4 MPa **(A)** and 8 MPa **(B)**.

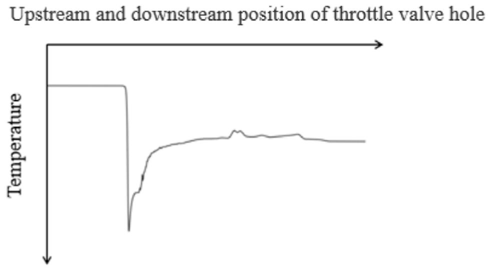

FIGURE 6 | Temperature trend curve of the throttling valve hole.

Firstly, the throttling valve is analyzed as a whole. It can be concluded from **Figure 5** that the temperature of the gas will decrease to varying degrees after passing through the subsea cage-sleeve throttling valve. When the prefilling pressure is 4 MPa, the downstream temperature has been as low as −20°C, and the local low temperature at the outlet of the valve hole on the cage is as low as −90°C. When the downstream prefilling pressure is 8 MPa, the downstream temperature is slightly above 0°C, but there was still low temperature locally at the holes.

As for the local temperature change of the throttling holes, the overall trend is shown in **Figure 6**, which will first drop sharply at the valve hole and then rise up downstream. The same goes for pressure (Yu et al., 2017).

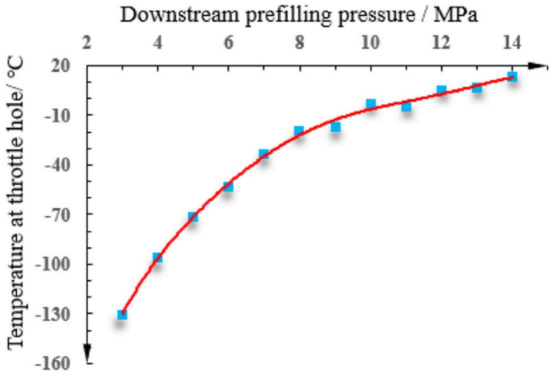

FIGURE 7 | Temperature curve of throttling at different prefilling pressures.

The lowest temperature of the holes under different prefilling pressures is shown in **Figure 7**. The lowest temperature at the throttling holes can be as low as −100°C. For subsea X-trees, jumper bent pipelines and subsea gas transmission pipelines, the steel of low temperature resistant is required to be used once the temperature falls below −40°C, which will increase operating costs (Wang et al., 2013). Therefore, in the selection of prefilling pressure, the downstream needs to be filled at least 7 MPa to meet the requirements.

At the same time, the speed in the cage hole is the largest in the whole throttling valve. One advantage of the cage-sleeve throttling valve is that the holes are distributed relative to each other along the cage, which dissipates the kinetic energy of the gas and reduces the vibration of the throttling valve. As can be seen from **Figure 8**, a violent vortex will be formed at the left plunger of the throttling valve, and a gas jet section will be formed along the outlet section at the right.

Under different prefilling pressure, the maximum speed in the cage holes is shown in **Figure 9**. At the lower prefilling pressure, the gas velocity is over the local speed of sound. In the critical flow state, the large gas flow rate will cause serious cage-sleeve erosion, so choosing a throttling valve material needs to consider the maximum capability of erosion resistance (Nøkleberg and Søntvedt, 1998). If the gas carries sand, it will cause more serious abrasion damage (Zhu et al., 2021).

Throttling Valve Opening Degree to Match Production

As a component connecting the subsea wellhead and downstream gas pipeline, the main function of the subsea throttling valve is to match the appropriate production under different valve opening degrees. By simulating five groups of throttling valves with different opening degrees, the physical field parameters with corresponding opening degrees are obtained.

For production, the greater the valve opening degree, the greater the volume of gas through the same upstream and downstream pressure conditions. As shown in **Figure 10**, as the pressure difference between upstream and downstream

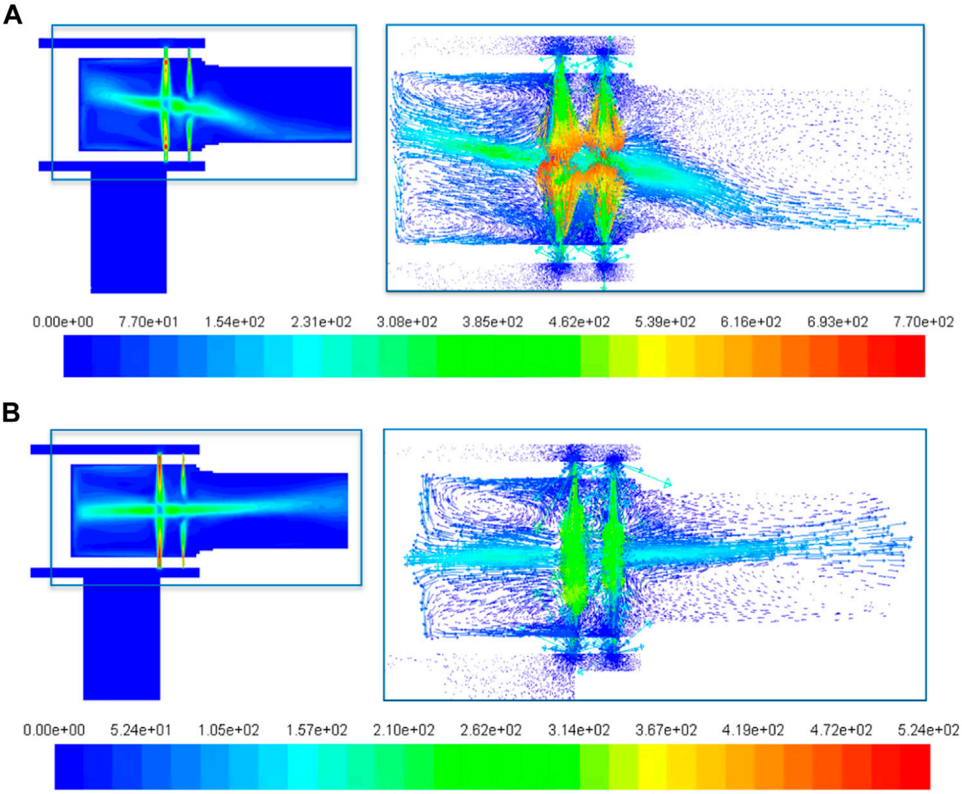

FIGURE 8 | The vertical profile and vector diagram of throttling valve velocity under the prefilling pressure of 3 MPa **(A)** and 7 MPa **(B)**.

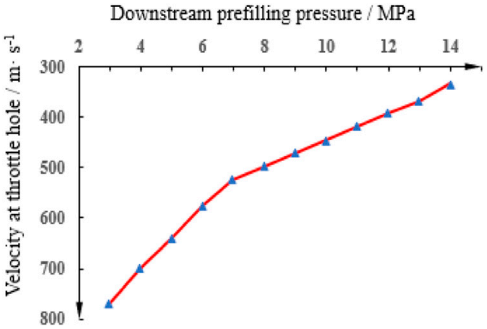

FIGURE 9 | Peak velocity curve at valve hole under different prefilling pressures.

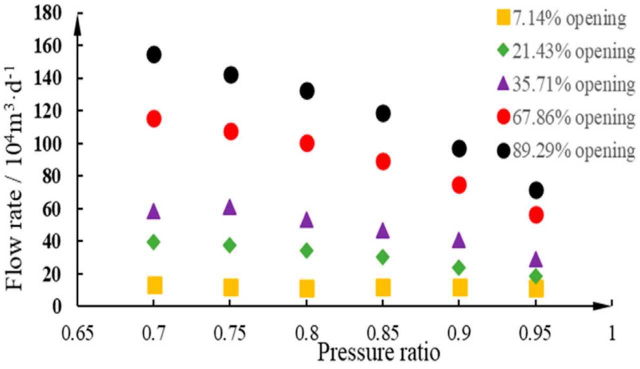

FIGURE 10 | Diagram of flow rate and upstream and downstream pressure ratio through the throttling valve in different opening degrees.

increases, the pressure ratio between downstream and upstream gradually decreases from one, and the gas production gradually increases. When the critical pressure difference is reached, the gas production will no longer increase, and the gas will be in a critical flow state. Especially when the smaller opening degree, the control ability, and the flow capability of the valve are relatively weak. Once the gas production rapidly rises, it will be easy to reach the critical flow state. When the pressure difference continues to increase, the flow rate of gas does not change.

There are two approaches to regulating production. One is to keep the pressure difference unchanged, then only change the valve opening degree; The other is to keep the opening degree constant and change downstream pressure. In the field, the easier parameter to confirm is the upstream and downstream pressure difference, so we usually choose to adjust the opening degree of the valve to adjust the gas production. In offshore gas development, we expect a high production. There are corresponding risks if the throttling valve opening degree is

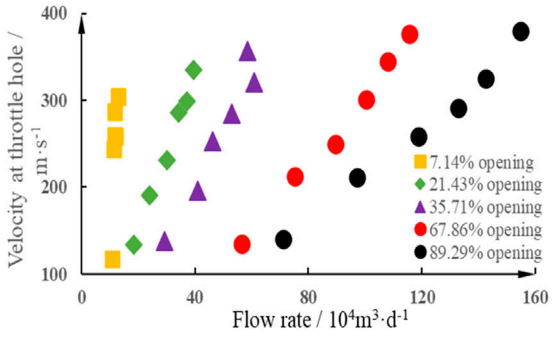

FIGURE 11 | Diagram of flow rate and throttling holes speed through the throttling valve in different opening degrees.

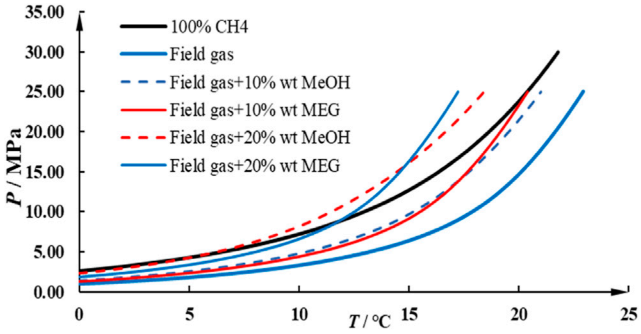

FIGURE 13 | Phase equilibrium curves of hydrate formation in different conditions.

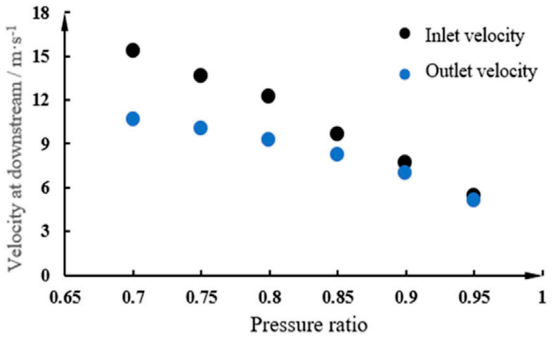

FIGURE 12 | Comparison diagram of inlet and outlet velocity under different pressure ratios at an opening degree of 89.29%.

not adjusted properly. For example, under a certain flow rate, if the throttling valve is selected with a small opening degree, the downhole pressure needs to be reduced more to ensure the stability of production, and the throttling effect will be intensified. Therefore, the valve opening degree needs to match the flow capacity of the gas. At the same time, the impact of low temperature caused by the throttling effect should be reduced.

The velocity distribution at the throttling holes in the cage is related to the production. It can be seen from **Figure 11** that the maximum velocity of gas passing through the holes is limited by the production at a small opening degree. As the opening degree increases, the velocity at the throttling holes decreases at the same flow rate. Under the condition of a large opening degree, the large and small holes in the cage are opened at the same time, and the maximum speed at the holes will increase gradually. This is consistent with the cognition that the larger the opening degree, the stronger the gas flow capacity (Zhang and Zhao, 2021).

After the gas flows through the throttling valve holes, the downhole velocity gradually tends to be stable as the pipe diameter increases. However, the downstream pressure is lower than the upstream pressure, so the velocity of gas downstream is increased compared with the upstream velocity, so the shear stress of gas on the downstream pipe wall increases accordingly (Li et al., 2021). **Figure 12** shows the inlet and outlet velocity of the throttling valve under different pressure ratios at the opening degree of 89.29%. It shows that the downstream velocity is slightly higher than the upstream flow rate when the upstream and downstream pipe diameters are the same. In the design of the downstream pipeline, it is necessary to consider the stability of film formation in the pipeline after corrosion inhibitor injection. If the corrosion inhibitor film is more stable, the downstream gas velocity can be greater. Therefore, the gas velocity after throttling should be considered when analyzing the maximum design gas velocity of the subsea pipeline. In the case of fixed corrosion inhibitor film stability, the downstream velocity can not exceed the safety design value by reducing the throttling pressure difference or increasing the downstream pipe diameter.

Risk Analysis at Subsea Throttling Valve

Through the temperature field simulation of the throttling valve, it is found that when the backpressure in the pipeline is 7 MPa, the downstream temperature is around 0°C. If no corresponding solutions are taken, the risk of hydrate formation will be extremely high under a low-temperature and high-pressure condition (Fu et al., 2020). At present, the common solution of hydrate prevention is to change the thermodynamic formation conditions of hydrate and inject a large amount of methanol and ethylene glycol before the producing wing valve (Wang et al., 2018).

The temperature of hydrate formation can be increased by injecting different weights of hydrate inhibitor. **Figure 13** is the phase equilibrium curve of hydrate formation obtained through simulation under different thermodynamic conditions. As can be seen from the figure, the different hydrate inhibitors with the same mass fraction have slightly different inhibition effects. Under the condition of high temperature and pressure, the injection effect of ethylene glycol is better than that of methanol. Therefore, it is recommended to inject ethylene glycol before going through the subsea throttling valve, then methanol after going through the cooling and depressurization of the throttling valve.

TABLE 2 | API temperature rating table.

Temperature rating	Min°C	Max°C	Min°F	Max°F
K	−60	82	−75	180
L	−45	82	−50	180
P	−29	82	−20	180
R	Room temperature		Room temperature	
S	−18	66	0	150
T	−18	82	0	180
U	−18	121	0	250
V	2	121	35	250
X	−18	180	0	350
Y	−18	345	0	650

In the stable stage of production, the temperature upstream of the subsea throttling valve can reach 70°C and the pressure is up to 30 MPa. Even if the temperature and pressure drop rapidly after the gas passes through the throttling valve, the risk of hydrate formation is low. However, in the shut-in stage, due to the lack of an upstream gas heat source and the influence of the low temperature of the seabed, once the well starts up, the risk of hydrate formation will be very high under the superposition of the throttling effect at the subsea throttling valve. It is necessary to accurately characterize the temperature and pressure field at the subsea throttling valve and put forward the corresponding hydrate inhibitor injection scheme (Guan et al., 2014).

Low temperature will not only have the risk of hydrate formation but also affect the strength of the manifold. Subsea pipeline has requirements on temperature resistance range, and API has made relevant standards on temperature rating of materials related to subsea X-tree, as shown in **Table 2** (Jiang et al., 2018). It shows that pipelines with different temperature levels meet different production conditions. For high temperature and high-pressure gas wells, once there is a serious throttling effect, the gas temperature changes sharply, and the material of pipelines and valves have to adapt to large temperature changes. Therefore, in the early design and valve selection, it is necessary to accurately consider the throttling valve temperature change.

CONCLUSION AND RECOMMENDATION

The structure of subsea X-trees is complex, and there are many valves. The size of the flow channel at the holes of the subsea throttling valve changes significantly, and the throttling effect is significant, so the temperature and pressure drop is large. It is necessary to take the fine characterization of physical field and risk analysis of subsea cage-sleeve throttling valve, so the following conclusions are drawn:

1) Determining the appropriate prefilling pressure in the downstream pipeline is conducive to the safe production of the subsea throttling valve. Based on the characteristics of the cage-sleeve throttling valve and the Joule-Thomson effect, it is recommended to prefill the downstream of the throttling valve at a pressure of about 7 MPa for the simulated deepwater well case. This can not only reduce the throttling effect, avoid extreme low temperature, and reduce the risk of hydrate formation, but also reduce the risk of valve hole erosion.
2) Select the throttling valve opening degree to match the production. The throttling valve controls the fluid flow and ensures regular production. Before the selection and design of the throttling valve, it is necessary to understand the flow characteristics of the throttling valve and match the appropriate opening degree considering the downstream pressure and expected production.
3) The temperature field and velocity field at the subsea throttling valve can be accurately described by the simulation of the 3D model, which is helpful to analyze the risk of hydrate formation under different conditions, select appropriate throttling valve materials and ensure the smooth subsea production.

These physical fields are based on the cage-sleeve throttling valve model that we built, and the physical field varies slightly from model to model. Meanwhile, this study is based on the steady-state model, and future researchers can study the transient model to more accurately describe the physical field dynamic process of the subsea throttling valve.

DATA AVAILABILITY STATEMENT

The raw data supporting the conclusion of this article will be made available by the author, without undue reservation.

AUTHOR CONTRIBUTIONS

DJ, WM, YH, and YY contributed to the conception and design of the study. ZJ organized the database. YZ performed the statistical analysis. YG wrote the first draft of the manuscript. YZ and ZJ wrote sections of the manuscript. All authors contributed to manuscript revision, read, and approved the submitted version.

ACKNOWLEDGMENTS

The authors gratefully acknowledge the financial support provided by the Science and Technology Major Program of CNOOC Ltd. (No. CNOOC-KJ135ZDXM38ZJ05ZJ) and the National Natural Science Foundation of China (No. 51876222).

REFERENCES

Feng, S., Zhang, J., Wang, P., Jin, Z., and Li, Y. (2017). Study on Valve Core Size and Opening Degree of Sleeve Choke Used in Gas Production. *Oil Field Equipment* 46 (1), 48–53. doi:10.3969/j.issn.1001-3482.2017.01.012

Fu, W., Wang, Z., Zhang, J., Cao, Y., and Sun, B. (2020). Investigation of Rheological Properties of Methane Hydrate Slurry with Carboxmethylcellulose. *J. Pet. Sci. Eng.* 184, 106504. doi:10.1016/j.petrol.2019.106504

Gharaibah, E., and Zhang, Y. "Flow Assurance Aspects and Optimization of Subsea Choke Valve - Sand Management and Erosion," in Proceedings of the OTC Brasil, Rio de Janeiro, Brazil, October 2015. doi:10.4043/26250-MS

Grace, A., and Frawley, P. (2011). Experimental Parametric Equation for the Prediction of Valve Coefficient (Cv) for Choke Valve Trims. *Int. J. Press. Vessels Piping* 88 (2), 109–118. doi:10.1016/j.ijpvp.2010.11.002

Guan, L., Ren, J., Sun, B., and Gao, Y. (2014). An Optimization of Hydrate Inhibitor and its Injection Method for the Testing of Deep Water Gas Wells. *China Offshore Oil and Gas* 26 (2), 55–60.

Hong, C., Estefen, S. F., Wang, Y., and Lourenço, M. I. (2018). An Integrated Optimization Model for the Layout Design of a Subsea Production System. *Appl. Ocean Res.* 77, 1–13. doi:10.1016/j.apor.2018.05.009

Jiang, D., Li, Z., Qin, H., Wang, E., Xu, F., and Wang, Y. (2018). Type Selection and Function Design of Subsea Christmas Tree in Lingshui 17-2 Gas Field. *China Pet. Machinery* 46 (7), 31–38. doi:10.16082/j.cnki.issn.1001-4578.2018.07.007

Ju, P., Li, D., Jing, Y., Wang, W., and Zhang, H. (2021). Low Temperature Analysis during Initial Start-Up of Deepwater Christmas Tree. *J. Salt Sci. Chem. Industry* 50 (05), 50–52. doi:10.16570/j.cnki.issn1673-6850.2021.05.015

Li, Q., Sun, Q., Cheng, B., Liu, G., Yao, H., Wang, J., et al. (2021). Key Technologies for Engineering Design of Deepwater Subsea Production System in LS17-2 Gas Field. *China Offshore Oil and Gas* 33 (3), 180–188. doi:10.11935/j.issn.1673-1506.2021.03.021

Li, Z., and An, W. (2020). Progress and Outlook of Equipment Engineering Technologies for Subsea Oil and Gas Production System in China. *China Offshore Oil and Gas* 32 (02), 134–141. doi:10.11935/j.issn.1673-1506.2020.02.016

Li, Z., Luo, X., Chen, J., Ma, Q., and Kong, X. (2018). Numerical Simulation and Hydrate Formation Analysis of Sleeve Choke. *J. Chengde Pet. Coll.* 20 (3), 43–46+73. CNKI:SUN:CDSY.0.2018-03-013.

Malavasi, S., and Messa, G. V. "CFD Modelling of a Choke Valve under Critical Working Conditions," in Proceedings of the ASME 2014 Pressure Vessels and Piping Conference, Anaheim, California, July 2014. doi:10.1115/pvp2014-28629

Nøkleberg, L., and Søntvedt, T. (1998). Erosion of Oil & Gas Industry Choke Valves Using Computational Fluid Dynamics and Experiment. *Int. J. Heat Fluid Flow* 19 (6), 636–643. doi:10.1016/S0142-727X(98)10039-5

Rassenfoss, S. (2011). Growing Offshore Water Production Pushes Search for Subsea Solutions. *J. Pet. Tech.* 63 (8), 36–40. doi:10.2118/0811-0036-JPT

Shoghl, S. N., Naderifar, A., Farhadi, F., and Pazuki, G. (2020). Prediction of Joule-Thomson Coefficient and Inversion Curve for Natural Gas and its Components Using CFD Modeling. *J. Nat. Gas Sci. Eng.* 83, 103570. doi:10.1016/j.jngse.2020.103570

Sotoodeh, K. (2019). A Review on Subsea Process and Valve Technology. *Mar. Syst. Ocean Technol.* 14 (4), 210–219. doi:10.1007/s40868-019-00061-4

Wang, J., Zhou, X., Chen, H., and Chen, J. (2013). Simulation and Analysis on Cold Temperature Propagation in Downstream of Subsea Production Choke under Momentary Flowing during Gas Well Startup: Case Study of Panyu Deep Water Gas Field. *China Offshore Oil and Gas* 25 (6), 105–108. CNKI:SUN:ZHSD.0.2013-06-020.

Wang, Z., Zhao, Y., Zhang, J., Pan, S., Yu, J., and Sun, B. (2018). Flow Assurance during Deepwater Gas Well Testing: Hydrate Blockage Prediction and Prevention. *J. Pet. Sci. Eng.* 163, 211–216. doi:10.1016/j.petrol.2017.12.093

Yu, P., Liu, Z., Wu, X., Kong, R., Wang, W., Li, T., et al. (2017). Optimization Design and Application of Subsea Surface Chokes. *Oil Field Equipment* 46 (4), 61–65. doi:10.3969/j.issn.1001-3482.2017.04.015

Zhang, B., and Zhao, J. (2021). Research on the Influence of Throttle Valve Cage Sleeve Structure on Throttling Effect. *Appl. Eng.* 5 (1), 16–21. doi:10.11648/j.ae.20210501.13

Zhang, J., Wu, Z., Huang, L., Lu, P., Wang, J., and Li, Y. (2010). Method Study on Anomalous Pressure Gas Wellhead Choke Valve Turndown Ratio Control. *Oil Drilling Prod. Tech.* 32 (S1), 115–117. doi:10.3969/j.issn.1000-7393.2010.z1.031

Zhao, X., Wang, D., Liu, W., Ren, G., and Jin, L. (2014). Flow Numerical Simulation for Production Channel in Subsea X 'mas Tree Based on CFD. *China Pet. Machinery* 42 (11), 105–108. doi:10.3969/j.issn.1001-4578.2014.11.025

Zheng, J., Yan, X., and Dou, Y. (2020). Research on Failure Characteristics of Natural Gas Downhole Throttle. *J. Fail. Anal. Preven.* 20 (4), 1155–1161. doi:10.1007/s11668-020-00919-5

Zhu, H., Zhu, J., Lin, Z., Zhao, Q., Rutter, R., and Zhang, H.-Q. (2021). Performance Degradation and Wearing of Electrical Submersible Pump (ESP) with Gas-Liquid-Solid Flow: Experiments and Mechanistic Modeling. *J. Pet. Sci. Eng.* 200, 108399. doi:10.1016/j.petrol.2021.108399

Conflict of Interest: Author DJ, WM, YH, and YY were employed by the company CNOOC.

The remaining authors declare that the research was conducted in the absence of any commercial or financial relationships that could be construed as a potential conflict of interest.

frontiers
in Earth Science

ORIGINAL RESEARCH
published: 01 February 2022
doi: 10.3389/feart.2021.816873

Study on Hydrate Risk in the Water Drainage Pipeline for Offshore Natural Gas Hydrate Pilot Production

Yu Guimin[1]*, *Jin Hao*[2] *and Kong Qingwen*[3]

[1]*Drilling and Completion Office, China National Offshore Oil Corporation (CNOOC), Beijing, China,* [2]*CNOOC Shenzheng Company, China National Offshore Oil Corporation (CNOOC), Shenzheng, China,* [3]*School of Petroleum Engineering, China University of Petroleum (East China), Qingdao, China*

Hydrate plug in the drainage line is a serious flow assurance problem for the pilot production of offshore natural gas hydrates. Current research focuses on hydrate deposition in the annular flow and the oil-dominated system. The multiphase flow system in the drainage line is a water-dominated system which is normally a bubbly flow. In this work, a new model is developed to study the temperature and pressure field in the drainage line considering that the flow pattern is bubbly flow. Combining with the methane hydrate phase equilibrium curve, the hydrate formation region in the drainage line can be established. The hydrate formation region is enlarged with the ESP pressure increasing and the water production rate decreasing, since the ESP can supply extra pressures in the drainage line and the heat transfer phenomenon is enhanced between the drainage line and environment under the low water production rate condition. The model pointed out that the risk of hydrate formation rises up as the hydrate concentration increases beyond 6%. This study can lay a theoretical foundation for the efficient prevention of gas hydrates in the drainage line during offshore natural gas hydrate pilot or long-term production.

Keywords: methane hydrate, drainage line, hydrate formation, bubbly flow, risk

OPEN ACCESS

Edited by:
Weiqi Fu,
China University of Mining and Technology, China

Reviewed by:
Yang Zhao,
Missouri University of Science and Technology, United States
Jianjun Zhu,
China University of Petroleum, Beijing, China

***Correspondence:**
Yu Guimin
yugm@cnooc.com.cn

Specialty section:
This article was submitted to Economic Geology, a section of the journal Frontiers in Earth Science

Received: *17 November 2021*
Accepted: *06 December 2021*
Published: *01 February 2022*

Citation:
Guimin Y, Hao J and Qingwen K (2022) Study on Hydrate Risk in the Water Drainage Pipeline for Offshore Natural Gas Hydrate Pilot Production. Front. Earth Sci. 9:816873. doi: 10.3389/feart.2021.816873

INTRODUCTION

Natural gas hydrate is a kind of new energy resource which compensates the lacks of onshore crude oil and natural gas. Natural gas hydrate are crystalline inclusion compounds where methane molecules are enclosed by water clathrates under low temperature and high pressure condition (Fu et al., 2019a). Normally, natural gas hydrate reservoirs are found in deep water, plateau, or high latitude areas. For example, in South China Sea, natural gas hydrates are located in the region where water depth is about 1000 m and local temperature is close to 4°C (Fu et al., 2020a; Sun et al., 2020).

China has conducted two successful pilot productions of natural gas hydrate in the Shenhu area of South China Sea. The production rates of natural gas hydrates for two pilot production have reached 5000 m^3/d and 2.87×10^4 m^3/d respectively (Xu et al., 2017). Since decomposition of natural gas hydrates results in large water production rate in the well, the down hole separation technology is utilized in the natural gas hydrate well. The submersible electrical pump is used to upload the water through the drainage pipeline. The natural gas is produced though the gas line. According to the published data, the actual separation efficiency of the gas-liquid separator in Japan's first hydrate trial production was around 80–90% (Liu et al., 2021). Since the down hole separation cannot complete separate gas and liquid, some parts of gas may be entrained into the drainage line, as shown **Figure 1**

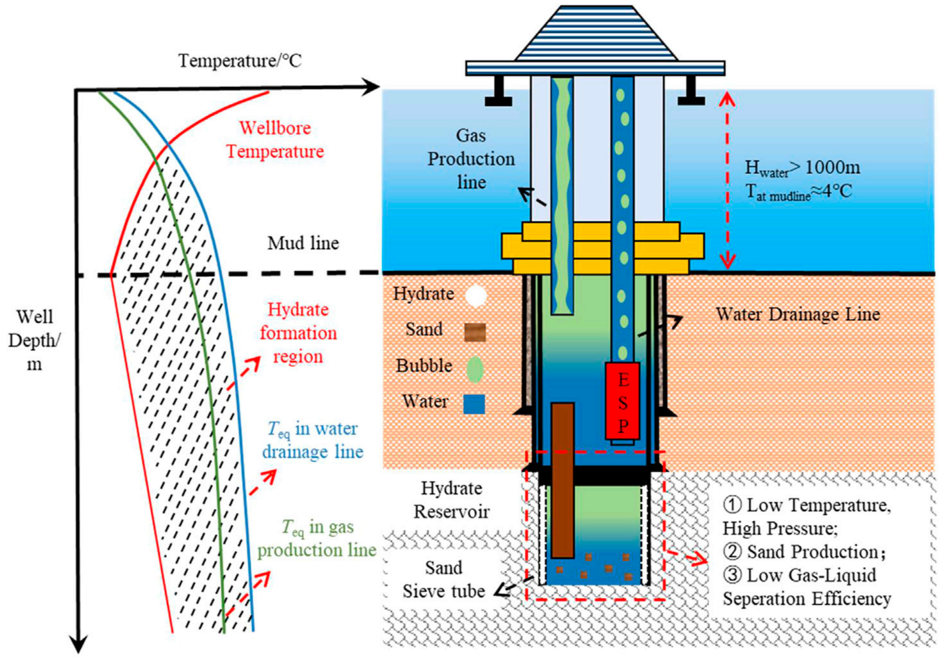

FIGURE 1 | Hydrate formation region in the water drainage line and the gas production line for the pilot production of natural gas hydrates.

(Ye et al., 2020). Considering the low temperature and high pressure near the mud line, gas hydrates may be formed in the drainage line which induce the risk of hydrate blockage. The hydrate formation area in the drainage pipeline is larger than that in the gas production pipeline. This is because the liquid is a continuous phase in the drainage pipeline, and the mechanical energy of the liquid is higher than that of the gas, leading to higher pressure in the drainage pipeline. Therefore, the hydrate flow assurance in the water drainage pipeline becomes an important research area for the development of natural gas hydrates (Ye et al., 2020).

Current research on the hydrate flow assurance focuses on the hydrate problems in the water-oil-gas mixed transportation pipeline and the testing stage of gas wells (Zerpa et al., 2013; Chen et al., 2019). In the water-oil-gas mixed transportation pipeline, predecessors tended to study the rheology of water-in-oil emulsion and the mechanism of hydrate particle agglomeration (Lv et al., 2013; Shi et al., 2018; Peng et al., 2012), conducted the experiments to reveal the rheology of the hydrate slurries formed from diesel oil/condensate oil and water dispersed systems. The hydrate concentrations reach 30 vol% and the rheology of hydrate slurry obeys the power law model which exhibits shear-thinning behaviors. Based on Peng et al.'s study, Yan et al. (2014) further experimentally studied the rheology of hydrate slurries in water-in-oil emulsion with anti-agglomerant. In Yan et al.'s work, the water cut is up to 30 vol% and anti-agglomerant dosage is 3.0 wt%. The rheology of water-in-oil emulsion also plays a shear-thinning behavior. Considering the high energy density of hydrate slurry, Clain et al. (2012) experimentally investigated rheology of hydrate slurries in TBPB-water mixtures which is proven as a pseudoplastic fluid. Fu et al. (2018), Fu et al. (2019a), Fu et al. (2019b), and Fu et al. (2019c) presented a novel work on the methane hydrate formation in bubbly flow and revealed the influences of bubble behaviors on the hydrate formation, including bubble breakup, coalescence, and deformation. The presented model has been incorporated in the commercial software which used to predict the hydrate risk in the deep-water wellbore. Wang et al. (2010), Fu et al. (2020a), Fu et al. (2020b), Fu et al. (2020c), and Fu et al. (2020d) primarily studied the rheology of hydrate slurry in bubbly flow which is an important work in the hydrate flow assurance in the pilot production of natural gas hydrates and the drilling and production of deep-water oil and gas. Based on their experimental analysis, the dual behaviors of hydrate slurries are exhibited firstly where it behaves as the shear-thinning at the low shear rate condition and the shear-thickening behavior at the high shear rate condition. The hydrate blockage in the hydrate slurry in the water-continuous system is considered to be induced by the aggregation of hydrate particles. The rheology of hydrate slurry normally is considered as shear-thinning and a few cases exhibit as shear-thickening, where it depends on the interactions between hydrate particles.

As the natural gas production from deep water environment becomes popular, the hydrate flow assurance in the gas-dominated system rises up (Hegde et al., 2015; Li et al., 2015). In the testing stage of gas well, predecessors studied the hydrate formation and depositions in the annular flow. Di Lorenzo et al. (2014a)and Di Lorenzo et al. (2014b) firstly conducted experiments to study the characteristics of methane hydrate formation and deposition in the annular flow. In their works, the hydrate formation is evaluated from the liquid film of annular flow and the hydrate deposits inside the liquid film along the pipe wall. Wang et al. (2016) and Wang et al. (2017) enriched the hydrate formation and deposition model in the annular flow. Based on the characteristic of annular flow, they further consider the influence of water entrainment and liquid droplet deposition on the hydrate formation and deposition. Their model pointed out that 24–31% of hydrate particle formed from liquid droplets will deposit on the pipe wall, and an effective deposition ratio is proposed to describe the actual hydrate particle deposited on the pipe wall. The developed model is much closer to the industrial condition and has been widely accepted by field engineers. Based on Wang et al.'s model, Zhang et al. (2013) developed a real-time estimation model for hydrate deposition in the deep-water gas well testing. The model is enabled to calculate the distributions of pressure drop influenced by the hydrate deposition which considers the dynamic effect of hydrate behavior on fluid flow and surface roughness. Overall, in annular flow, the hydrate risk is normally induced by the hydrate deposition along the pipe wall and the pressure drop is the dominant factor to display the hydrate risk in the tubing. The variations of pressure drops are induced by the shrinkage of pipe inner diameter.

In this work, the flow pattern in the drainage line is bubbly hydrate slurry which is a water-continuous system. The hydrate formation in the liquid mainly alters the rheology of the fluid which finally changes the pressure drop. This work aims to develop a pressure drop prediction model for the drainage line in natural gas hydrate well by considering the influence of hydrate formation on the rheology of bubbly flow. The developed model provides a method to predict the risk of hydrate blockage in the drainage line.

MODEL DEVELOPMENT

The accurate calculation of the temperature and pressure along the drainage line is an important foundation for predicting the hydrate formation region and developing hydrate management strategy for the drainage line. Prior to building the temperature and pressure prediction model, the gas-liquid flow behavior and the mass transfer mechanism between the drainage line and the sea water should be well understood.

In offshore natural gas production, the formation fluid decomposed from natural gas reservoirs are the mixed fluid of gas and liquid. The downhole production system is designed to artificially lift the gas and liquid through the gas line and the drainage line separately. Thinking that lower pressure drops are caused by the gas flow, the natural gas hydrate reservoir can provide efficient energy to lift gas to the platform. But the submersible electrical pump (ESP) installed at the drainage line is necessary to compensate the pressure drop, since higher pressure drops are caused by the liquid flowing. The ESP has a higher demand on the void fraction in the drainage line. If the void fraction is larger than 10%, the ESP would experience serious surge and the efficiency of liquid lifting is lowered seriously. However, the bubbly flow is unavoidable in the drainage line since the downhole separator cannot separate gas and liquid completely.

Moreover, the biggest difference between the conventional deep wellbore for oil and gas and the wellbore for natural gas hydrate is that the most parts of wellbore in the natural gas hydrate reservoir are located in the environment of the low temperature and the high pressure. The gas and liquid flowing in the wellbore can form gas hydrates easily which increases the risks of hydrate blockage. Generally, the heating or the chemical inhibitor injection in the bottom hole becomes an unavoidable measure to prevent hydrate blockage in the wellbore. If the hydrate formation happened in the drainage line, the pressure drops in the drainage line may increase theoretically and the load of the ESP be increased at the same time. Thus, the production efficiency of natural gas hydrates is also degraded.

Continuity Equation

Considering that the downhole separation technology cannot completely separate water and gas, some gas will be entrained in the drainage line. Thus, the drainage line has a gas-liquid two-phase flow, where the inflow of gas and liquid is from the natural gas hydrate reservoirs and the suction of the ESP. Because most of the gas will flow in the gas line, the flow pattern may be bubbly flow. The mass of gas and liquid are conserved and the mass conservation equations are given as **Eq. 1** and **Eq. 2** (Doron and Barnea, 1996; Doron et al., 1997; Zhang et al., 2021).

$$\frac{\partial}{\partial t}\left(AE_g\rho_g\right) + \frac{\partial}{\partial z}\left(AE_g\rho_g v_g\right) = Q_g \tag{1}$$

$$\frac{\partial}{\partial t}\left(AE_l\rho_l\right) + \frac{\partial}{\partial z}\left(AE_l\rho_l v_l\right) = Q_l \tag{2}$$

where A is the cross-section area of drainage pipe, m^2, E_g is the volumetric fraction of gas phase, dimensionless, E_l is the volumetric fraction of liquid phase, dimensionless, ρ_l is liquid density, kg/m^3, ρ_g is gas density, kg/m^3, v_g is gas velocity, m/s, v_l is liquid velocity, m/s, t is production time of natural gas hydrate, s, z is the location of drainage line, m, Q_g is gas flow rate, m^3/s, and Q_l is liquid flow rate, m^3/s.

Momentum Conservation Equation

The gas and liquid in the drainage line is mainly subject to gravity, pressure difference force, and friction. Considering that the void fraction in the drainage line is less than 5%, the gas expansion induced by the temperature increasing is ignored. Based on the momentum conservation theory, the momentum conservation equation in the drainage line considers the variations of gas volumetric fractions and liquid volumetric fractions induced by gas expansion, which is given as **Eq. 3** (Kokpmar and Gogus, 2001; Eskin and Scarlett, 2005; Sun et al., 2011; Zhang et al., 2021).

$$\frac{\partial}{\partial t}\left(AE_g\rho_g v_g + AE_l\rho_l v_l\right) + \frac{\partial}{\partial z}\left(AE_g\rho_g v_g^2 + AE_l\rho_l v_l^2\right) + \frac{\partial(Ap)}{\partial z} + Af_r\frac{\rho_m v_m^2}{2d} + A\rho_m g\cos\theta = 0 \tag{3}$$

where ρ_m is the mixed density of gas and liquid, kg/m^3, v_m is the mixed velocity of gas and liquid, m/s, θ is the inclined angle of the drainage line, °, P is pressure, Pa, d is the diameter of drainage line, m, and subscript g and l are gas and liquid phase. The mixed density is calculated based on the density and the volumetric fraction of gas and liquid, as **Eq. 4**.

$$\rho_m = \rho_g E_g + \rho_l E_l \tag{4}$$

Temperature Calculation Equation

The temperature field in the drainage line plays an important role in determinations of the hydrate formation region and calculations of the pressure field. The heat exchange occurs during the flow of the mixed gas-liquid fluid in the drainage line which is induced by the temperature difference between the drainage line and the sea water. Ignoring the effect of hydrate formation on the temperature, the temperature field in the drainage line can be evaluated by **Eq. 5** (Hasan and Kabir, 2012).

$$\frac{\partial}{\partial t}\left[A\rho_m\left(C_{pm}T + v_m^2/2\right)\right] + \frac{\partial}{\partial s}\left[A\rho_m v_m\left(H + v_m^2/2\right)\right] = -A\rho_m v_m g\sin\theta + Q \tag{5}$$

where C_{pm} is the specific heat at the constant pressure of the mixed fluid, J/(kg·°C), T is the mixed fluid temperature, °C, H is the enthalpy of mixed fluid, J/kg, Q is the heat exchange rate between the and environment, J/(m·s), ρ_{m} is the density of mixed fluid, kg/m^3, and v_{m} is the velocity of mixed fluid, m/s.

Considering that the drainage line is above the mud line, the heat exchange rates between drainage line and sea water are calculated by **Eq. 6** (Zhang et al., 2021).

$$Q_1 = \frac{2r_{\mathrm{to}}U_{\mathrm{to}}}{vr_{\mathrm{ti}}^2}\cdot\left(T_{\mathrm{sea}} - T_{\mathrm{f}}\right) H \le H_{\mathrm{sea}} \tag{6}$$

where T_{sea} is the temperature of sea water, °C, and T_{f} is the temperature of drainage line, °C.

The total heat transfer coefficient (U_{to}) is a critical parameter participating in the calculation of temperature field and affecting the heat transfer rate. Considering the thickness of the drainage line, U_{to} can be calculated by **Eq. 7** (Zhang et al., 2021).

$$U_{to}^{-1} = \frac{r_{to}}{r_{ti}h_c} + \frac{r_{to}\ln\left(r_{to}/r_{ti}\right)}{k_p} \tag{7}$$

where r_{to} is the outer radius of the drainage line, m, r_{ti} is the inner radius of the drainage line, m, h_{c} is the thermal conductivity of the fluid, W·m^{-1}·K^{-1}, and k_{p} is the conductivity of the drainage line,

$$\mathrm{W}\cdot\mathrm{m}^{-1}\cdot\mathrm{K}^{-1}$$

Hydrate Slurry Rheology Model

The rheology of the mixed fluid participates in the calculation of pressure drop in the drainage line. Considering that the flow pattern in the drainage line is bubbly flow, the hydrate formation induces the bubbly flow transiting to the hydrate slurry bubbly flow which is a gas-liquid-hydrate mixed flow. Since the void fraction is less than 5%, the influence of bubbles on the rheology of hydrate slurry is ignored. Sun et al. (2020) has experimentally revealed the rheology of hydrate slurry bubbly flow where it performs as a non-Newtonian fluid. The non-Newtonian fluid index and the consistency faction can be calculated by **Eq. 8** and **Eq. 9** (Sun et al., 2020).

$$n = 2.51\alpha_{hydr} + 1.92 \tag{8}$$

$$K = 3\times 10^{-7}\alpha_{hydr}^{-2.07} \tag{9}$$

where n is the non-Newtonian fluid index, K is the consistency factor, and α_{hydr} is the hydrate concentration in the hydrate slurry, %.

The shear rate of the hydrate slurry presents the influence of flow velocity on the apparent viscosity of the hydrate slurry. The hydrate slurry in the drainage line is considered as a shear-thickening fluid, since the flow rate is higher than the critical flow rate. Thus, the apparent viscosity increases with the hydrate concentration and the shear rate increasing. The shear rate and the apparent viscosity are be calculated by **Eq. 10** and **Eq. 11** (Sun et al., 2020).

$$\gamma = \frac{8v_{HS}}{D}\frac{3n+1}{4n} \tag{10}$$

$$\mu_{app} = 3\times 10^{-7}\alpha_{hydr}^{-2.07}\gamma^{2.51\alpha_{hydr}+0.92} \tag{11}$$

Where γ is the shear rate, s^{-1}, and μ_{app} is the apparent viscosity of the hydrate slurry, mPas.

Hydrate Phase Equilibrium Model

The hydrate formation region is the cross-section area between the hydrate equilibrium curve and the temperature-pressure curve along the drainage line. In the field condition, the gas decomposed from the natural gas reservoir is pure methane. The produced water has a few salinities owing to the sea water and the formation water. However, the salinities can increase the hydrate equilibrium condition which enhances the difficulty for crystallization of gas hydrates and is beneficial for the hydrate prevention. Considering a safety factor for the hydrate prevention, the liquid phase is treated as a pure water in the drainage line (Zhang et al., 2021).

$$P_e = 10^6\exp\left(\sum_{n=0}^{5} a_n\left(T + \Delta T_d\right)^n\right) \tag{12}$$

where Pe is the hydrate phase equilibrium pressure, MPa, $a_0 = -1.94138504464560\times 10^5$, $a_1 = 3.31018213397926\times10^3$, $a_2 = -2.25540264493806\times 10$, $a_3 = 7.67559117787059\times 10^{-2}$, $a_4 = -1.30465829788791\times 10^{-4}$, $a_5 = 8.86065316687571\times 10^{-8}$.

SOLUTION METHOD

The pressure, temperature, pressure drop, and ESP power are calculated by the algorithm which reveals the influences of hydrate formation on the multiphase flow behaviors in the drainage line. The hydrate formation region and the hydrate risk in the drainage line are evaluated by the developed model. The algorithm of the developed model is achieved by the visual basic language. The detailed solution steps are presented in **Figure 2** and described as follows:

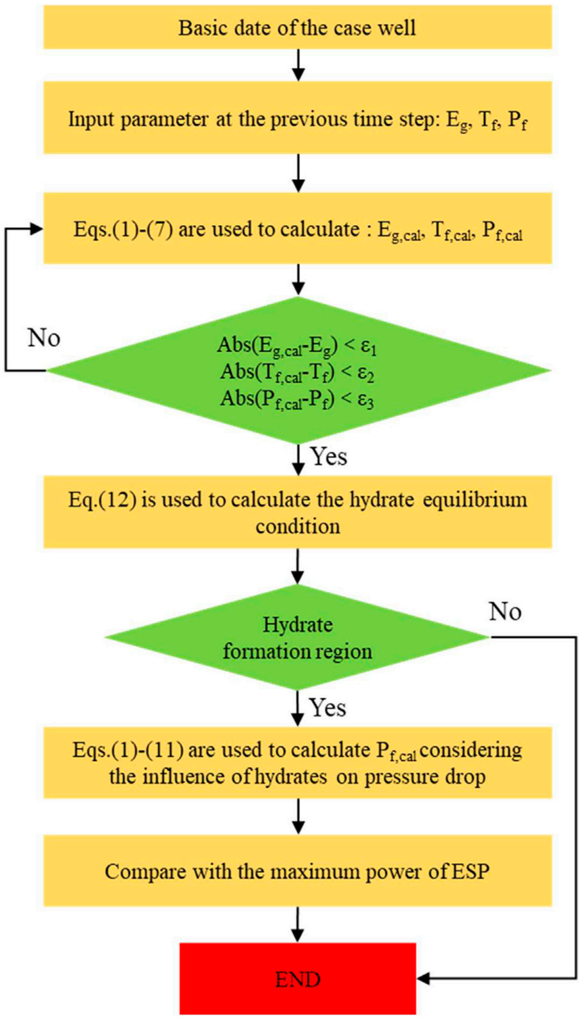

FIGURE 2 | Algorithm for predicting the risk of hydrate in the drainage line during the pilot production of offshore natural gas hydrate.

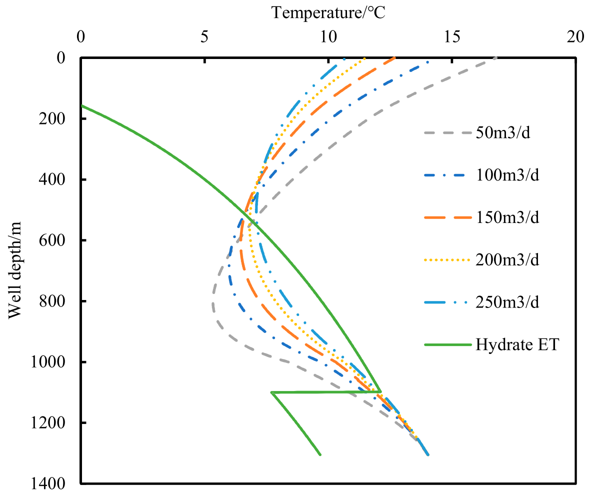

FIGURE 3 | Hydrate formation region in the drainage line under varied water production rates.

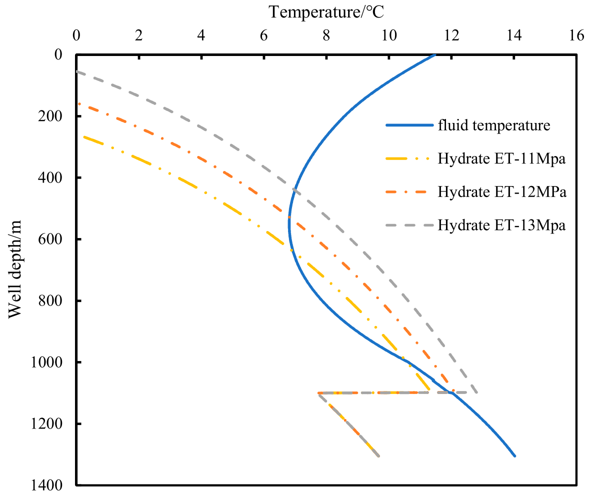

FIGURE 4 | Hydrate formation region in the drainage line under varied pump pressures.

1) Obtaining basic information from the pilot production well, including gas-liquid flow rate, well head pressure and temperature, gas-liquid volumetric fraction, etc., the drainage line is divided into a few of control volumes. The dividing standard of control volume is 0.1 m. Gas-liquid flow rates are assumed to be constant.
2) In each control volume, void faction, temperature, and pressure are calculated by **Eqs 1–11**. The flow velocities of gas, liquid, and hydrate are obtained sequentially by the Runge-Kutta method prior to the calculation error within the allowable range.
3) Based on temperature and pressure in the drainage line, the methane hydrate equilibrium temperature and pressure are calculated by using **Eq. 12**. Comparing the temperature of the drainage line (T_f) and the gas hydrate equilibrium temperature (T_{ef}), if $T_f > T_{eq}$, no hydrate formation happens in the drainage line and stops the calculation. If $T_f < T_{eq}$, gas hydrate would form in the drainage line and the consequent steps should be taken.
4) After the hydrate formation region is confirmed, the pressure drops in the hydrate formation region should consider the influence of hydrate formation which uses **Eqs 8–11**. The new bottom hole pressure and pressure drop (ΔP_d) in the drainage line can be calculated based on the rheology of hydrate slurry. The comparisons between the pressure drop in the drainage line (ΔP_d) and the ESP power (ΔP_p) are conducted. If $\Delta P_d < \Delta P_p$, the ESP can work effectively. If $\Delta P_d > \Delta P_p$, the ESP is over-loaded and cannot lift the liquid to the platform effectively. A hydrate management should be taken in the drainage line and stop the calculation.

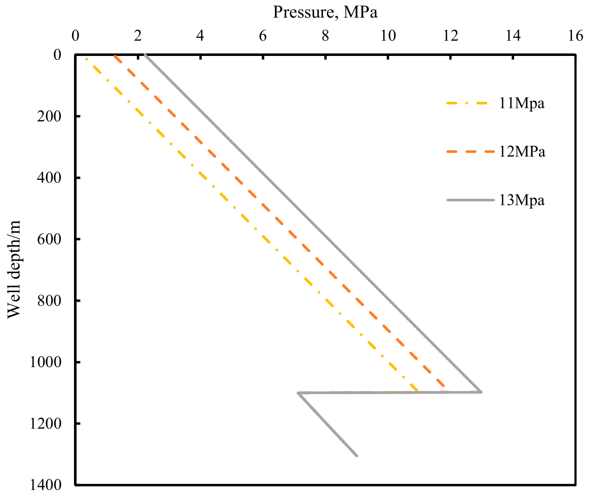

FIGURE 5 | The drainage line pressure distributions along the drainage line.

CASE STUDY

The risk of hydrate formation in the drainage line is analyzed based on the pilot production well during the second pilot production of natural gas hydrates in the Nankai Trough of Japan. In the pilot environment profile, the depth of sea water is 995 m, the mud line temperature is closed to 3.5°C, the geothermal gradient is 3°C/100 m, reservoir pressure is about 13 MPa (1,309.4 m), reservoir temperature is about 13.7°C, thickness of hydrate reservoir is about 60 m. In the wellbore profile, the first casing size is 13–3/8″, the second casing size is 8–1/2″, and the riser size is 9–5/8″. In the production profile, the average gas production is 8,330 Sm^3/d and the average water production is 343.6 m^3/d.

After comparing the temperature field and the methane hydrate equilibrium temperatures along the drainage line, the drainage line faces the risk of hydrate formation. **Figures 3** and **4** exhibit the hydrate formation regions under the different water production rates and the ESP pressure. **Figure 3** indicates that the fluid temperatures decrease gradually in the drainage line from the platform at the first and then increase gradually, where the dash curves are temperatures of fluid under varied water production rates and the solid green curve is the methane hydrate equilibrium temperature. As the water decomposed from the hydrate reservoir flows from the bottom hole to the platform, the temperatures of fluid decease gradually due to the geothermal temperature decreasing at the beginning. After the water passes though the wellhead, the fluid temperatures in the drainage line increase gradually since the temperatures of sea water increase with the water depth decrease. Moreover, an interesting observation is found that the environment temperatures have larger influences on the water temperature in the drainage line at low water production rate condition. For instance, at the water production rates of 50 m^3/d, the water temperatures in the drainage line increase from 4.38 to 16.78°C as the water flows from the wellhead to the platform. The reason is speculated that, when the water flows under the lower rates, the environment and the drainage line will have an adequate heat transfer process between each other. The environment temperatures including the sea water temperature and the geothermal temperature have strong impacts on the water in the drainage line. Thus, at the low water flow rate condition, the temperatures of water at the platform will be close to the environment condition which is 16.78°C.

Moreover, starting from the bottom hole, the methane hydrate equilibrium curve decreases gradually. After sudden increasing at the well depth of 1108 m, the hydrate equilibrium curve starts to decrease gradually. The main reason inducing the hydrate equilibrium curve decreasing is that the wellbore pressure decreases gradually from the bottom hole to the platform. Since the ESP is installed at the well depth of 1108 m which can supply an extra pressure in the wellbore, the sudden increase of wellbore pressure leads to the sudden increase of the hydrate equilibrium curve. Although the installation of the ESP can effectively lift the water to the platform and improve the production efficiency of natural gas hydrates, the ESP also increases the pressure of the drainage line which increases the risk of hydrate formation.

Figure 4 exhibits the influences of the ESP pressures on the hydrate formation region. The dashed line is the methane hydrate equilibrium curves under the ESP pressures of 11, 12, and 13 MPa. The solid blue line is the fluid temperature in the drainage line. As shown in **Figure 4**, the increases of the ESP pressures will enlarge the hydrate formation region in the drainage line. Under the ESP pressure of 11 MPa, the hydrate formation region is located in the well depth from 1104 to 646 m which the total length is 458 m. Under the ESP pressure of 13 MPa, the total length of hydrate formation region is 652 m which is from 1098 to 446 m. The hydrate formation region is increased about 194 m. Since the increases of the ESP pressure can increase the flow pressure of water in the drainage line, the high flow pressures favor hydrate formation in the drainage line.

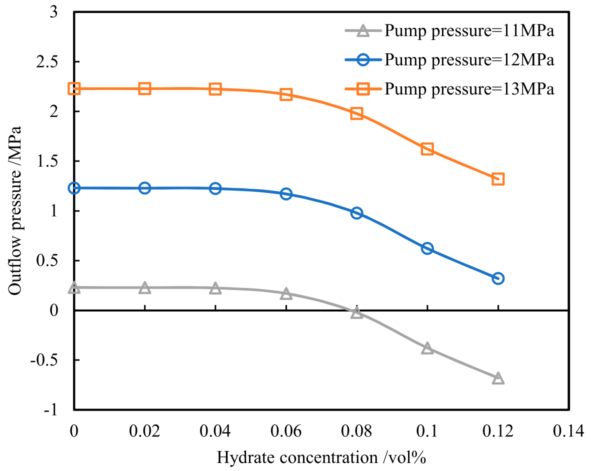

FIGURE 6 | The outflow pressures at the platform along hydrate concentrations under varied pump pressure conditions.

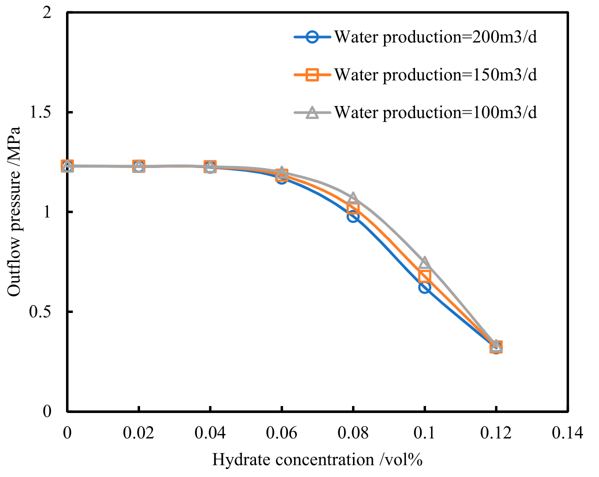

FIGURE 7 | The outflow pressures along hydrate concentrations under varied water production rates.

Figure 5 shows that the influence of ESP pressure on the water flow pressure in the drainage line. The water flowing pressure are same in the section of wellbore from the bottom hole to the location that ESP is installed. After the water flows passing though the ESP pump, the pressure in the drainage line is suddenly increased. Since the ESP pump provides the extra energy to the water inside the drainage line and enables the water flow faster which increases the efficiency of liquid uploading, the water flowing pressures increase due to the extra energy correspondingly. Based on **Figure 4**, although the increase of ESP pressure can increase water flowing pressure inside the drainage line and enhance the efficiency of liquid uploading, the hydrate formation region and the risk of hydrate in the drainage line also enlarges at the same time.

Figure 6 shows the pressures at the platform along the hydrate concentration increasing under the varied ESP pressure conditions. As shown in **Figure 6**, the increasing pump pressures increases the outflow pressure of water in the drainage line at the platform. It demonstrates that the increase pump pressures can increase the efficiency of liquid uploading and the natural gas hydrate production. Focusing on the case of pump pressure at 11 MPa, when the hydrate concentrations increase beyond 8% inside the drainage line, the outflow pressures become negative. The increases of hydrate concentrations increase the apparent viscosity of the mixed fluid and the wall resistances between fluid and pipe wall also increase correspondingly. Thus, the pressure drops of the fluid flowing in the drainage line increase and the flow velocities of the mixed fluid decrease at the same time. The native outflow pressures mean that the ESP cannot upload the water to the platform. The production problem induced by the hydrate formation is risen up and the hydrate management measures should be taken to deal with the problem. In the analysis of **Figure 4**, it is mentioned that the increase of ESP pressure will increase the hydrate formation area and thus increase the risk of hydrate formation in the drainage pipeline. However, the increase of hydrate formation area does not necessarily mean that the risk of flow barrier formation will increase. Outflow pressure more directly reflects the risk of flow barrier. Increasing the ESP pressure within a certain range can effectively lift fluid in the line that has increased viscosity due to hydrate formation. Therefore, in the pressure range of 11–13 Mpa discussed in this paper, the higher the ESP pressure, the lower the risk of flow barrier formation in the drainage line.

Figure 7 presents that the influences of water production rates and hydrate concentrations on the outflow pressure of the drainage line at the platform. As seen in **Figure 7**, the increases of water production rates result in outflow pressure decreasing at the platform. The reason is that the higher water production rates have higher flow velocities of water in the drainage line and higher friction losses between water flow and pipeline. Considering the pressure losses induced by the wall resistance contain the 99% of the total pressure losses in bubbly flow, the higher friction losses stand for the higher pressure drops and lower outflow pressure at the platform. Moreover, when the hydrate concentration is beyond 6%, the outflow pressures are decreasing dramatically for all water production rate conditions. When the hydrate concentration in pipeline is low, the non-Newtonian fluid properties of hydrate grout are not obvious, and the fluid properties of hydrate grout mainly depend on the properties of continuous phase fluid, which can be considered as Newtonian fluid. The shear stress has a linear relationship with flow velocity, the rheological index is 1, and the viscosity can approximate to that of the continuous phase fluid in the tube (Sun et al., 2020). When the hydrate concentration exceeds 6%, the hydrate grout begins to show the characteristics of non-Newtonian fluid, the viscosity increases suddenly, the pressure drop increases, and the outlet pressure of drainage pipeline decreases. It speculates that the risks of hydrates becomes serious where the hydrate formation, deposition, and agglomerate happened in the drainage line. The hydrate management measures are suggested to be used in the drainage line when the hydrate concentration is found beyond 6%. The measures include hydrate inhibitor injection, heating, lower water production rate, etc.

CONCLUSION

In this work, a model is developed to forecast the hydrate formation region and the risk of hydrate in the drainage line for the offshore natural gas hydrate pilot production. The model calculates the temperature-pressure field in the drainage line and the methane hydrate phase equilibrium curve by incorporating the influence of hydrate on the rheology of mixed fluid. An algorithm is developed correspondingly by the visual basic language. The model shows that the hydrate formation region is enlarged as the ESP pressure increases and the water production rate decreases. The ESP pressures increasing can increase the water flowing pressure in the drainage line which favors hydrate formation. The water production rates decreasing can enable better heat transfer between the drainage line and environment. The fluid temperature in the drainage line will decrease faster as the environmental temperature decreasing at the lower water production rate condition. Moreover, when the hydrate concentration is beyond 6%, the outflow pressure at the platform will drop sharply, the risk of hydrate formation appears, and the hydrate management measure is necessary. In the future, the model should be studied further by considering the hydrate deposition and agglomerate in the drainage line and the influence of hydrate inhibitors on the hydrate formation in the drainage line should be revealed as well.

DATA AVAILABILITY STATEMENT

The original contributions presented in the study are included in the article/**Supplementary Material**, further inquiries can be directed to the corresponding author.

AUTHOR CONTRIBUTIONS

YG: Conceptualization, Methodology, Supervision, Writing-Original Draft, Writing—Review and Editing JH: Data Curation, Resources, Investigation, Formal analysis, Writing-Review and Editing KQ: Investigation, Methodology, Formal analysis, Writing—Review and Editing.

SUPPLEMENTARY MATERIAL

The Supplementary Material for this article can be found online at: https://www.frontiersin.org/articles/10.3389/feart.2021.816873/full#supplementary-material

REFERENCES

Chen, Y., Gong, J., Shi, B., Yao, H., Liu, Y., Fu, S., et al. (2019). Investigation in Methane Hydrate Reformation in Water-Dominated Bubbly Flow. *Fuel* 263, 116691. doi:10.1016/j.fuel.2019.116691

Clain, P., Delahaye, A., Fournaison, L., Mayoufi, N., Dalmazzone, D., and Fürst, W. (2012). Rheological Properties of Tetra-N-Butylphosphonium Bromide Hydrate Slurry Flow. *Chem. Eng. J.* 193-194, 112–122. doi:10.1016/j.cej.2012.04.027

Di Lorenzo, M., Aman, Z. M., Kozielski, K., Norris, B. W. E., Johns, M. L., and May, E. F. (2014a). Underinhibited Hydrate Formation and Transport Investigated Using a Single-Pass Gas-Dominant Flowloop. *Energy Fuels* 28, 7274–7284. doi:10.1021/ef501609m

Di Lorenzo, M., Aman, Z. M., Sanchez Soto, G., Johns, M., Kozielski, K. A., and May, E. F. (2014b). Hydrate Formation in Gas-Dominant Systems Using a Single-Pass Flowloop. *Energy Fuels* 28, 3043–3052. doi:10.1021/ef500361r

Doron, P., and Barnea, D. (1996). Flow Pattern Maps for Solid-Liquid Flow in Pipes. *Int. J. Multiphase Flow* 22 (2), 273–283. doi:10.1016/0301-9322(95)00071-2

Doron, P., Simkhis, M., and Barnea, D. (1997). Flow of Solid-Liquid Mixtures in Inclined Pipes. *Int. J. Multiphase Flow* 23 (2), 313–323. doi:10.1016/s0301-9322(97)80946-9

Eskin, D., and Scarlett, B. (2005). Model of the Solids Deposition in Hydrotransport: An Energy Approach. *Ind. Eng. Chem. Res.* 44 (5), 1284–1290. doi:10.1021/ie049453t

Fu, W., Wang, Z., Sun, B., and Chen, L. (2018). A Mass Transfer Model for Hydrate Formation in Bubbly Flow Considering Bubble-Bubble Interactions and Bubble-Hydrate Particle Interactions. *Int. J. Heat Mass Transfer* 127, 611–621. doi:10.1016/j.ijheatmasstransfer.2018.06.015

Fu, W., Wang, Z., Duan, W., Zhang, Z., Zhang, J., and Sun, B. (2019a). Characterizing Methane Hydrate Formation in the Non-Newtonian Fluid Flowing System. *Fuel* 253, 474–487. doi:10.1016/j.fuel.2019.05.052

Fu, W., Wang, Z., Sun, B., Ji, C., and Zhang, J. (2019b). Multiple Controlling Factors for Methane Hydrate Formation in Water-Continuous System. *Int. J. Heat Mass Transfer* 131, 757–771. doi:10.1016/j.ijheatmasstransfer.2018.10.025

Fu, W., Wang, Z., Yue, X., Zhang, J., and Sun, B. (2019c). Experimental Study of Methane Hydrate Formation in Water-Continuous Flow Loop. *Energy Fuels* 33, 2176–2185. doi:10.1021/acs.energyfuels.9b00132

Fu, W., Wang, Z., Zhang, J., Cao, Y., and Sun, B. (2020a). Investigation of Rheological Properties of Methane Hydrate Slurry with Carboxmethylcellulose. *J. Pet. Sci. Eng.* 184, 106504. doi:10.1016/j.petrol.2019.106504

Fu, W., Wang, Z., Zhang, J., and Sun, B. (2020b). Methane Hydrate Formation in a Water-Continuous Vertical Flow Loop with Xanthan Gum. *Fuel* 265, 116963. doi:10.1016/j.fuel.2019.116963

Fu, W., Wang, Z., Chen, L., and Sun, B. (2020c). Experimental Investigation of Methane Hydrate Formation in the Carboxmethylcellulose (CMC) Aqueous Solution. *SPE J.* 25, 1042–1056. doi:10.2118/199367-PA

Fu, W., Wang, Z., Sun, B., Xu, J., Chen, L., and Wang, X. (2020d). Rheological Properties of Methane Hydrate Slurry in the Presence of Xanthan Gum. *SPE J.* 25, 2341–2352. doi:10.2118/199903-PA

Hasan, A. R., and Kabir, C. S. (2012). Wellbore Heat-Transfer Modeling and Applications. *J. Pet. Sci. Eng.* 86-87, 127–136. doi:10.1016/j.petrol.2012.03.021

Hegde, G. A., Sum, A. K., and Danielson, T. J. (2015). *Multiphase Flow Modeling for Gas Hydrates in Flow Assurance*. Paper presented at the Offshore Technology Conference, Houston, TX, May 2015.

Kokpmar, M. A., and Gogus, M. (2001). Critical Flow Velocity in Slurry Transporting Horizontal Pipelines. *J. Hydraul. Eng.* 127 (9), 763–771. doi:10.1061/(ASCE)0733-9429(2001)127:9(763)

Li, L., Xu, H.-l., and Yang, F.-q. (2015). Three-phase Flow of Submarine Gas Hydrate Pipe Transport. *J. Cent. South. Univ.* 22, 3650–3656. doi:10.1007/s11771-015-2906-y

Liu, Z., Sun, B., Wang, Z., Lou, W., and Zhang, J. (2021). Modeling of Multiphase Flow in marine Gas Hydrate Production System and its Application to Control the Production Pressure Difference. *J. Nat. Gas Sci. Eng.* 85, 103687. doi:10.1016/j.jngse.2020.103687

Lv, X., Shi, B., Wang, Y., and Gong, J. (2013). Study on Gas Hydrate Formation and Hydrate Slurry Flow in A Multiphase Transportation System. *Energy Fuels* 27, 7294–7302. doi:10.1021/ef401648r

Peng, B.-Z., Chen, J., Sun, C.-Y., Dandekar, A., Guo, S.-H., Liu, B., et al. (2012). Flow Characteristics and Morphology of Hydrate Slurry Formed from (Natural Gas+diesel Oil/condensate Oil+water) System Containing Anti-agglomerant. *Chem. Eng. Sci.* 84, 333–344. doi:10.1016/j.ces.2012.08.030

Shi, B., Ding, L., Liu, Y., Yang, J., Song, S., Wu, H., et al. (2018). Hydrate Slurry Flow Property in W/O Emulsion Systems. *RSC Adv.* 8, 11436–11445. doi:10.1039/c7ra13495a

Sun, B., Wang, Z., Gong, P., and Song, R. (2011). Application of a Seven-Component Multiphase Flow Model to Deepwater Well Control. *Acta Petrol. Sin.* 32 (06), 1042–1049. doi:10.7623/syxb201106018

Sun, B., Fu, W., Wang, Z., Xu, J., Chen, L., Wang, J., et al. (2020). Characterizing the Rheology of Methane Hydrate Slurry in a Horizontal Water-Continuous System. *SPE J.* 25, 1026–1041. doi:10.2118/195586-PA

Wang, W., Fan, S., Liang, D., and Li, Y. (2010). A Model for Estimating Flow Assurance of Hydrate Slurry in Pipelines. *J. Nat. Gas Chem.* 19, 380–384. doi:10.1016/s1003-9953(09)60094-3

Wang, Z. Y., Zhao, Y., Sun, B. J., Chen, L. T., Zhang, J. B., and Wang, X. Y. (2016). Modeling of Hydrate Blockage in Gas-Dominated Systems. *Energy Fuels* 30 (6), 4653–4666. doi:10.1021/acs.energyfuels.6b00521

Wang, Z., Zhang, J., Sun, B., Chen, L., Zhao, Y., and Fu, W. (2017). A New Hydrate Deposition Prediction Model for Gas-Dominated Systems with Free Water. *Chem. Eng. Sci.* 163, 145–154. doi:10.1016/j.ces.2017.01.030

Xu, H., Luo, X., Peng, D., and Chen, A. (2017). First Successful Trail Collection of Natural Gas Hydrate in China. *Geol. China* 44 (3), 620–621. doi:10.12029/gc20170323

Yan, K.-L., Sun, C.-Y., Chen, J., Chen, L.-T., Shen, D.-J., Liu, B., et al. (2014). Flow Characteristics and Rheological Properties of Natural Gas Hydrate Slurry in the Presence of Anti-agglomerant in a Flow Loop Apparatus. *Chem. Eng. Sci.* 106, 99–108. doi:10.1016/j.ces.2013.11.015

Ye, J., Qin, X., Xie, W., Lu, H., Ma, B., Qiu, H., et al. (2020). Main Progress of the Second Gas Hydrate Trial Production in the South China Sea. *Geol. China* 47 (3), 557–568. doi:10.12029/gc20200301

Zerpa, L. E., Rao, I., Aman, Z. M., Danielson, T. J., Koh, C. A., Sloan, E. D., et al. (2013). Multiphase Flow Modeling of Gas Hydrates with a Simple Hydrodynamic Slug Flow Model. *Chem. Eng. Sci.* 99, 298–304. doi:10.1016/j.ces.2013.06.016

Zhang, B., Wu, Q., Gao, X., Liu, C., and Ye, Y. (2013). Memory Effect on Hydrate Formation and Influential Factors of its Sustainability in New Hydrate-Based Coal Mine Methane Separation Method. *Int. J. Environ. Pollut.* 53 (3/4), 201–212. doi:10.1504/ijep.2013.059913

Zhang, J., Sun, Q., Wang, Z., Wang, J., Sun, X., Liu, Z., et al. (2021). Prediction of Hydrate Formation and Plugging in the Trial Production Pipes of Offshore Natural Gas Hydrates. *J. Clean. Prod.* 316, 128262. doi:10.1016/j.jclepro.2021.128262

Conflict of Interest: Authors YG and JH are employed by the company China National Offshore Oil Corporation CNOOC.

The remaining author declares that the research was conducted in the absence of any commercial or financial relationships that could be construed as a potential conflict of interest.

frontiers | Frontiers in Earth Science

TYPE Original Research
PUBLISHED 27 September 2022
DOI 10.3389/feart.2022.853809

OPEN ACCESS

EDITED BY
Huazhou Li,
University of Alberta, Canada

REVIEWED BY
Facheng Gong,
University of Alberta, Canada
Xin Chen,
University of Alberta, Canada

*CORRESPONDENCE
Na Wei,
1434785340@qq.com
Lin Jiang,
linjiang_2020@163.com
Shuanshi Fan,
1809654231@qq.com

SPECIALTY SECTION
This article was submitted to Economic Geology,
a section of the journal
Frontiers in Earth Science

RECEIVED 13 January 2022
ACCEPTED 25 August 2022
PUBLISHED 27 September 2022

CITATION
Wei N, Jiang L, Fan S, Liu A, Li H, Zhang S, Zhang C and Xue J (2022), Experimental investigation of maldistribution characteristics of gas-liquid two-phase flow in a horizontal pipeline.
Front. Earth Sci. 10:853809.
doi: 10.3389/feart.2022.853809

Experimental investigation of maldistribution characteristics of gas-liquid two-phase flow in a horizontal pipeline

Na Wei[1,2,3]*, Lin Jiang[1,2,3]*, Shuanshi Fan[1]*, Anqi Liu[4], Haitao Li[1,2,3], Shenghui Zhang[1,2,3], Chao Zhang[1,2,3] and Jin Xue[1]

[1]State Key Laboratory of Oil and Gas Reservoir Geology and Exploitation, Southwest Petroleum University, Chengdu, China, [2]State Key Laboratory of Natural Gas Hydrate, Beijing, China, [3]Marine Natural Gas Hydrate Research Institute, Southwest Petroleum University, Chengdu, China, [4]Geological Explorations and Development Institute, Chuanqing Drilling Engineering Company, Limited, Chengdu, China

In the flow distribution of oil and gas gathering and transportation system, the flow pattern, inertia force, gravity, and other factors will lead to uneven flow distribution of each outlet pipe, which will seriously affect the economy and safety of the gathering and transportation system. Therefore, it is of great significance to analyze the characteristics of gas–liquid two-phase flow in horizontal pipelines. For this reason, an experimental device for maldistribution control of gas–liquid two-phase flow is developed in this article. In order to solve the problem of flow maldistribution in gas–liquid two-phase flow pipe, the test experiments of maldistribution control under the conditions of three flow patterns (stratified flow, slug flow, and annular flow) are carried out. Through experiments, we revealed the control law of flow pattern to liquid maldistribution and gas maldistribution with or without flute pipes and formed the maldistribution control scheme of gas–liquid two-phase flow in the horizontal pipeline. It is found that it is more beneficial to the control of average liquid maldistribution degree under the condition of slug flow pattern in horizontal manifold without flute pipe, and it is more beneficial to the control of average gas maldistribution degree under the condition of annular flow pattern without flute pipe. Without the function of the flute pipe and in the annular flow pattern, it is beneficial to the control of average maldistribution degree of gas–liquid two-phase flow. The findings of this research can be used as a reference for the field maldistribution control of oil and gas gathering and transportation systems.

KEYWORDS

maldistribution, horizontal pipeline, Gas-liquid two-phase flow, flow pattern, experimental investigation

Introduction

In the oil and gas gathering and transportation system, when the flow is distributed in the manifold system, the flow pattern, inertia force, gravity, and other factors will lead to the uneven flow distribution of each outlet pipe (Kaichiro and Ishi, 1984; McQuillan and Whalley, 1985), which will affect the economy and safety of the gathering and transportation system. At present, there are few literature reports on the maldistribution problem of process systems in oil and gas fields. At the beginning, it is pointed out that in the system of a nuclear power plant, joint box, and heat exchanger, when the single-phase flow is distributed (Lahey, 1986; Yang and Azzopardi, 2007), the boundary layer separation occurs after the flow passes through the diffusion section due to the different angle of the left and right outlet of the double-hole flow (Azzopardi, 1999). As a result, maldistribution of the flow is easy to occur.

Kim et al. (1995) analyzed the effect of parallel pipe shape and Reynolds number on the flow distribution of parallel branch pipes at low Reynolds number, and found that the flow distribution in the parallel pipe set depends largely on the pipe shape and Reynolds number, and compared the effect of different shapes of pipes on the flow distribution of branch pipes. Duan and Liang-cai (2016) proposed a new method of splitter splitting to improve the flow maldistribution in parallel pipe sets. The effects of branch spacing, collector diameter, branch diameter, and inlet flow rate on the flow maldistribution in the parallel group were investigated. Miao (1999) established a physical model for the flow of single-phase fluids in distribution and convergence tubes with variable-pitch openings and obtained analytical solutions for the flow characteristics in the distribution and convergence tubes. The flow rate and flow deviation equations between small orifices, as well as the distribution of the pitch function and its discrete solution for uniform distribution and uniform pooling of flow, are derived. Li (2010) studied the gas–liquid two-phase flow distribution characteristics of a single-inlet radially introduced, four-branch pipe vertically led upward distribution coupled box using experimental studies and numerical simulations. Improved geometry of the coupled box with the addition of a flute pipe was proposed. By comparison, the flute pipe structure can greatly improve distribution uniformity. Zhu et al. (2013) studied the effect of inlet dryness on the flow distribution of the combined box and found that the flow maldistribution of the combined box without the introduction of a flute pipe was most serious when the inlet dryness was low, and the flow deviation of individual branch pipes gradually diminished as the inlet dryness increased. Li (2017) analyzed the influence law of structural factors, working condition factors, and phase changes on the flow distribution in the heat exchanger network for two typical parallel piping methods, Z-type and U-type, and obtained the relationship equation between fluid inhomogeneity and impedance ratio in the parallel heat exchanger system under two conditions of Z-type piping and U-type piping. Marchitto et al. (2012) experimentally investigated the main mechanisms driving the flow field distribution in a two-phase horizontal collector in order to design an improved collector to optimize the flow field distribution in a compact heat exchanger. Chen et al. (2019) analyzed that uneven distribution, turbulence, and inertial forces are the main causes of partial flow in single-phase flow manifold systems; compared with single-phase flow manifolds, the causes of partial flow in gas–liquid two-phase flow manifolds also include flow patterns, differences in inertia between gas and liquid phases, and the ability of gases to carry liquids. Marchitto et al. (2012) investigated the effect of flow direction in a straight parallel channel collector on the two-phase flow distribution, examining the effect of operating conditions, collector shape, and inlet nozzle in the range of 0.2–1.2 and 1.5–16.5 m/s for liquid and gas apparent velocities, respectively. It was confirmed that the flow distribution of liquid and gas in the collector could be greatly improved by a reasonable selection of the location, diameter, and number of flow openings between the feed distributor and the parallel channel system connected to the collector. Zhou et al. (2017) studied the single-phase flow distribution of a central compact parallel heat exchanger through a cylindrical head with a circular cross-section and a circular tube using CFD numerical simulation. The influence of key geometric parameters such as collector diameter and number of tubes on the flow field distribution was investigated, considering the influence of geometric parameters on the flow field distribution. Hao et al. (2016) analyzed the effects of heat flow density ratio, total flow rate, and system pressure on the flow distribution in parallel tubes. The results showed that the flow distribution became significantly worse with the increase of heat flow density and concentration ratio; the flow distribution was improved with the decrease of system pressure. Lee and Lee (2004) simulated the distribution of two-phase annular flow at the head-channel connection of the corresponding component of a compact heat exchanger. It has been found that: when the intrusion depth is zero, the amount of liquid separated through the rear channel is low. However, this trend reverses with deeper intrusion depths. The deeper intrusion prevents the liquid from flowing into the channels installed at the front of the collector. Wang and Newby (2018) used the sewage settling tank of the oil transfer and drainage station to analyze the causes of the flow maldistribution type with the help of Fluent and Gambit software to simulate the media motion pattern, establish a 2D pipeline model, and analyze the fluid motion pattern in the pipeline.

A flute pipe is a small pipe in flute shape, which has several small holes distributed on it. It is originally widely used in the development of spacecraft and the heat exchanger part of the generator unit. Later, petroleum engineers gradually find it possible to adapt it to the gathering and transportation of oil and gas. Yan (2019) used the variable diameter flute pipe shunt technology to design a high-efficient heat exchanger suitable for two-tube heat recovery, which solves the disadvantage of uneven heat transfer of the two-tube heat recovery. To investigate the influence of piccolo tube parameters on temperature distribution on a concave surface, Zhang et al. (2017) performed a numerical simulation considering the external and internal flows. The effects of jet-hole diameter, jet-to-jet spacing, circumferential orifice location, jet-hole arrangement, and flute pipe position on the concave surface temperature distribution were analyzed. Wang (2012) advanced a full-scale calculation method of piccolo heat and flow distribution based on the design principle of flute pipe, and demonstrated a flute pipe instance to reflect the change of the heat and flow of the flute pipe in the flow direction.

Previous scholars mostly focused on the phenomenon of flow maldistribution in the process of heat transfer but were seldom involved in the maldistribution phenomenon of gas–liquid two-phase flow in the process of oil and gas transportation. In addition, their research methods mostly fall in numerical simulation, which will be more or less deviated from the engineering practice. Therefore, in this article, we have developed an experimental device for maldistribution control of gas–liquid two-phase flow in a horizontal pipeline, aiming at the problem of uneven flow distribution of gas–liquid two-phase flow in the horizontal pipeline. The test experiments of maldistribution control under the conditions of three flow patterns (stratified flow, slug flow, and annular flow) are carried out, and the control law of flow pattern to liquid and gas flow maldistribution with or without flute pipe is revealed. The maldistribution control scheme of gas–liquid two-phase flow in a horizontal pipeline is formed.

Experimental investigation of maldistribution of gas-liquid two-phase flow in a horizontal pipeline

Purpose of the experiment

The flow distribution prototype of the horizontal manifold is applied to carry out test experiments of flow maldistribution under the conditions of stratified flow, slug flow, and annular flow and different gas–liquid ratios and the data of inlet velocity, inlet pressure, and inlet gas–liquid flow rate, outlet velocity, outlet pressure, and outlet gas–liquid flow rate are tested and the critical phenomenon of horizontal stratified flow, slug flow, and annular flow is determined, respectively. Based on the analysis of the flow pattern, gas–liquid ratio, converted gas-phase speed, converted liquid-phase speed, pressure, and other process operating parameters on the flow maldistribution in the gas–liquid two-phase flow manifold, the control scheme of flow maldistribution in gas–liquid two-phase flow manifold is formed, and the control effect of the three flow maldistribution control prototypes is evaluated and improvement suggestions are proposed.

Experimental setup

1) Experimental apparatus

The main experimental apparatus are as follows: horizontal inlet pipe, horizontal outlet pipe, flow distribution prototype (as shown in Figure 1A, and the flute pipe inside is as shown in Figure 1B), electronic scale, pressure sensor, anemometer, computer, air compressor, liquid collector, pump, and HD camera.

Experimental setup of flow maldistribution test is as shown in Figure 2. The transparent plexiglass pipe with a diameter of 50 mm and wall thickness of 5 mm is the main pipe and is connected with the tee. The red joint one is the connecting joint, the flute pipe is installed in the manifold, the diameter of the flute pipe is 20 mm, the total length is divided into 5 segments, the length of each section is 560 mm, and each section is connected by thread, with a total connection length of 2.8 m. A pressure sensor is installed on the conduit pipe from the 20 cm on both sides of the tee and at the outlet of the two leading-out pipes.

2) Experimental materials

Air, water, and pigment.

Experimental steps

1) Equipment inspection before the experiment. Whether there are leaks in the gas and liquid pipelines, whether the data acquisition system is running normally, and whether the gas booster pump and the pump operation and flow rate adjustment are available should be checked.
2) When the air compressor and water pump are turned on, after the gas flow and liquid flow are stable, the liquid flow is kept unchanged, and the gas flow is adjusted through the gas throttle valve. After the gas flow is stable, the gas flowmeter flow on the gas pipeline and the liquid flowmeter on the liquid pipeline should be read, and the inlet pressure in the corresponding inlet pipe and the experimental time of each group should be read and recorded.
3) The high-definition camera and the pressure sensor on the computer should be turned on, and the gas–liquid two-phase flow pattern changes and pressure data of the horizontal lead-in tube and horizontal outlet pipes 1 and 2 during the whole experiment should be recorded. At the same time, the timing begins by the timekeeper, and the operator begins to measure the liquid mass of the horizontal exit tube 1 and the horizontal outlet pipe 2 at the same time, while the rest of the personnel begin to measure the gas-phase wind speed at the two ends of the horizontal outlet pipe 1 and outlet pipe 2 with the wind anemometer. The experiment should be repeated twice again.

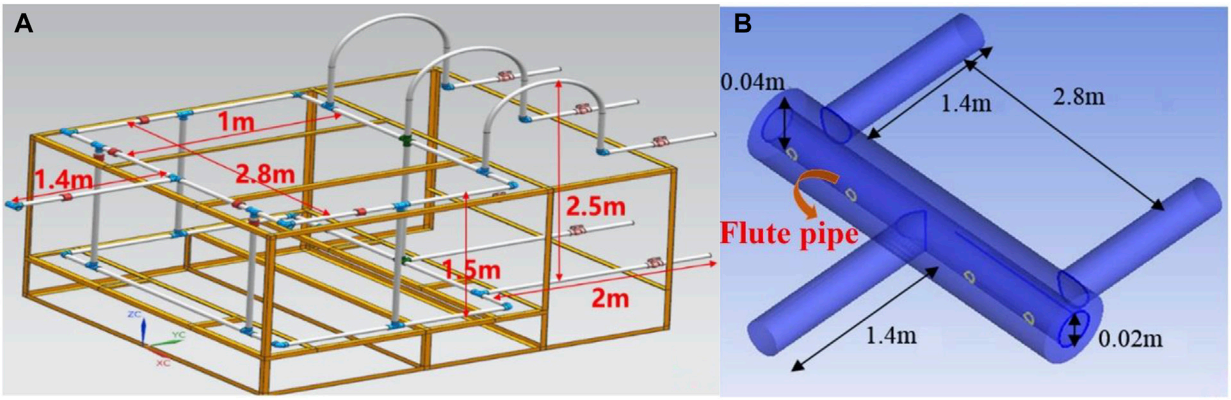

FIGURE 1
Flow distribution prototype for flow maldistribution test. **(A)** Schematic diagram of flow distribution prototype **(B)** Schematic diagram of flute pipe.

FIGURE 2
Experimental setup of flow maldistribution test.

TABLE 1 Experimental parameters of flow maldistribution in the horizontal manifold.

Density	Viscosity	Pressure (MPa)	Temperature (°C)
1000 kg/m^3	2.98×10^{-3} Pa·s	0.1	20

4) After the experimental test is completed, the wind speed at both ends of the outlet is recorded and the liquid weight of the two outlets is measured.
5) The liquid flow rate must be kept unchanged, the gas flow rate should be changed and the experiment should be carried out again until the upper and lower criticality of the stratified flow is determined and the experimental workload is completed at the end of the experiment.
6) The liquid flow rate should be changed, the gas flow rate through the gas throttle valve should be adjusted, and the above experimental steps should be repeated until all the tests are completed.

All the detailed experimental parameters are listed in Table 1.

Experimental phenomena

Flow rate of gas and liquid in the inlet under different flow pattern conditions is as shown in Table 2. The experimental phenomenon of flow maldistribution in stratified flow in a horizontal manifold is as shown in Figure 3. The stratification of the gas–liquid interface in the inlet pipe is obvious, and the interface ripple is serious, but the ripple is smaller and denser. The liquid and gas in outlet pipe 1 fully mix and move forward, and the liquid moves forward in a small wave shape, which is relatively regular. The gas–liquid migration phenomenon in

TABLE 2 Flow rate of gas and liquid in the inlet under different flow pattern conditions.

Flow pattern	Flow rate of gas in the inlet (L/s)	Flow rate of liquid in the inlet (L/s)	Gas–liquid ratio
Stratified flow	2.09	0.10	20.90
	5.48	0.10	54.80
	7.86	0.10	78.60
	2.70	0.17	15.88
	6.01	0.17	35.35
	8.78	0.17	51.65
Slug flow	2.37	0.35	6.77
	5.71	0.35	16.31
	7.86	0.35	22.46
	5.32	0.65	6.65
	7.40	0.65	11.38
	10.21	0.65	15.71
Annular flow	12.34	0.16	77.13
	15.62	0.16	97.6.3
	18.20	0.16	113.75
	18.18	0.35	51.94
	23.31	0.35	66.60
	26.64	0.35	76.11

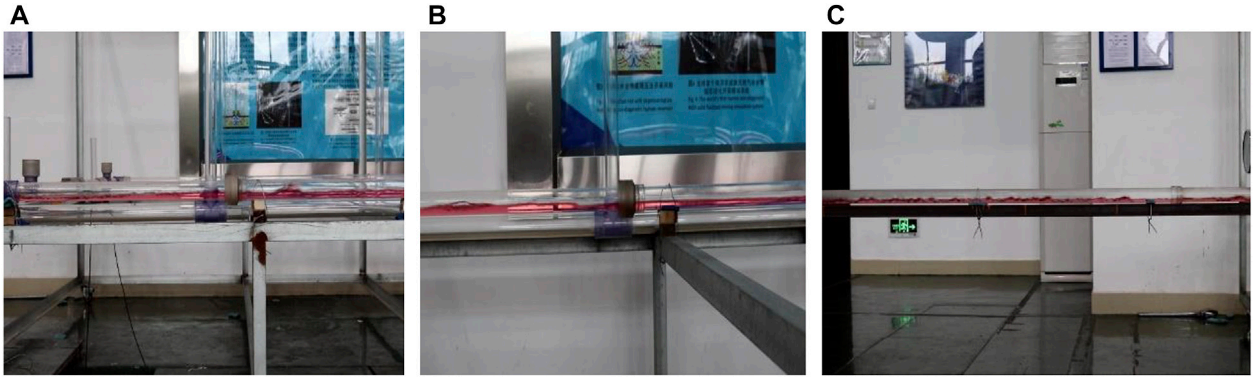

FIGURE 3
Experimental phenomenon of flow maldistribution in stratified flow in horizontal manifold [**(A)** outlet pipe 1, **(B)** outlet pipe 2, and **(C)** inlet pipe].

outlet pipe 2 is similar to that in outlet pipe 1. The liquid and gas in outlet pipe 2 are fully mixed and moved forward, the liquid level fluctuation is relatively smooth, and the ripple is not serious. The liquid flow rate of outlet pipe 1 is slightly larger than that of outlet pipe 2, and the gas flow rate of exit tube 1 is larger than that of outlet pipe 2, resulting in a phenomenon of flow maldistribution.

Test analysis of maldistribution of gas-liquid two-phase flow in a horizontal pipeline

The calculation procedures of maldistribution degree for gas and water are shown as follows:

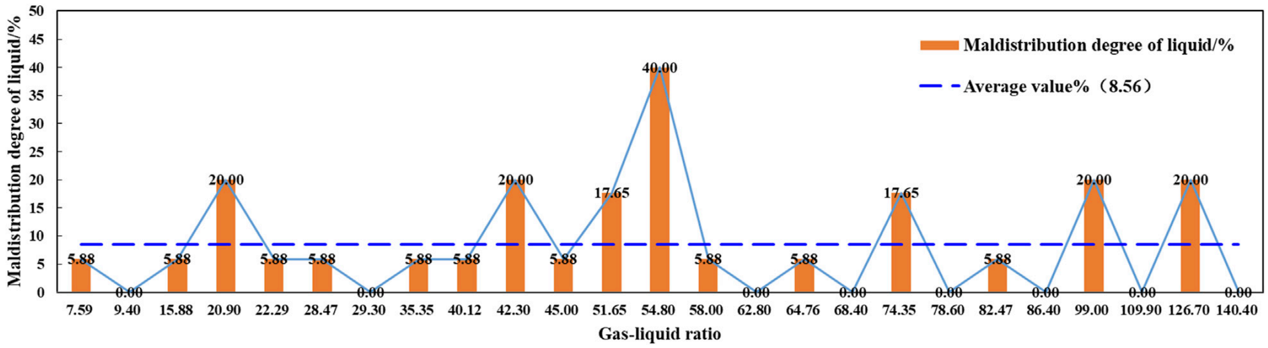

FIGURE 4
Histogram of gas–liquid ratio and maldistribution degree of liquid in stratified flow in horizontal manifold without flute pipes (liquid injection volume 0.10L/s+0.17L/s).

$$\Delta S_{gas} = \frac{\left|Q_{out,gas} - \frac{Q_{in,gas}}{2}\right|}{\frac{Q_{in,gas}}{2}} \times 100\% \qquad (1)$$

$$\Delta S_{liquid} = \frac{\left|Q_{out,liquid} - \frac{Q_{in,liquid}}{2}\right|}{\frac{Q_{in,liquid}}{2}} \times 100\%, \qquad (2)$$

where ΔS_{gas} is the maldistribution degree for gas, ΔS_{liquid} is the maldistribution degree for liquid, $Q_{out,gas}$ is the flow rate of gas in the outlet, $Q_{out,liquid}$ is the flow rate of liquid in the outlet, $Q_{in,gas}$ is the flow rate of gas in the inlet, and $Q_{in,\,liquid}$ is the flow rate of liquid in the inlet.

The flow pattern can be determined by many methods, and they all have their own merits and demerits. In this work, the flow pattern is determined by the gas–liquid ratio and the flow phenomenon of gas–liquid in the pipe, combined with the flow rate of gas and liquid meanwhile. The flow rate of gas and liquid in the inlet under different flow pattern conditions is shown as follows.

Maldistribution test of stratified flow in horizontal manifold without flute pipe

Through the analysis of histogram of gas–liquid ratio and maldistribution degree of liquid in stratified flow in horizontal manifold without flute pipe (as shown in Figure 4), it can be found that the overall trend of the maldistribution degree of liquid with the increase of gas–liquid ratio is as follows: first, the maldistribution degree of liquid is relatively stable, but some of them are large, and then there is a sharp zigzag change. The maldistribution degree of partial gas is 0, and when the gas–liquid ratio is 9.40, 29.30, 62.80, 68.40, 78.60, 86.40, 109.90, and 140.40, the maldistribution degree of liquid is the lowest to 0. When the gas–liquid ratio is 54.80, the peak value of maldistribution is 40%. When the gas–liquid ratio is 20.90, 42.30, 54.80, 74.35, 99.00, and 126.70, the value of maldistribution is 20%.

Through the analysis of histogram of gas–liquid ratio and maldistribution degree of gas in stratified flow in horizontal manifold without flute pipes (as shown in Figure 5), it is found that the overall trend of maldistribution degree of gas with the increase of gas–liquid ratio is as follows: first, the maldistribution degree of gas changes in a zigzag shape, and then the range of change becomes smaller. When the gas–liquid ratio is 9.40, the maldistribution degree of gas is the lowest, as low as 0, and when the gas–liquid ratio is 51.65, the maximum maldistribution degree of gas is 18.45%.

Maldistribution test of stratified flow in horizontal manifold with flute pipe

The analysis of the histogram of gas–liquid ratio and maldistribution degree of liquid in stratified flow in horizontal manifold with flute pipe (Figure 6) show that the maldistribution degree of liquid changes sharply with the increase of gas–liquid ratio. When the gas–liquid ratio is 10.10, 30.00, 39.70, 54.70, 65.10, 84.70, and 101.60, the maldistribution degree of liquid is as low as 0.005%, and when the gas–liquid ratio is 72.47 and 82.35, the deviation degree is the highest, which is 52.94%.

Through the analysis of histogram of gas–liquid ratio and maldistribution degree of gas in stratified flow in horizontal manifold with flute pipe (Figure 7), it is found that the overall trend of maldistribution degree of gas with the increase of gas–liquid ratio is as follows: the maldistribution degree of gas first increases with the increase of gas–liquid ratio, and then changes in a zigzag shape. When the gas–liquid ratio is 101.60, the maldistribution degree of gas is the smallest, as low as 0.79%, and when the gas–liquid ratio is 24.00, the maximum maldistribution degree of gas is 25.00%.

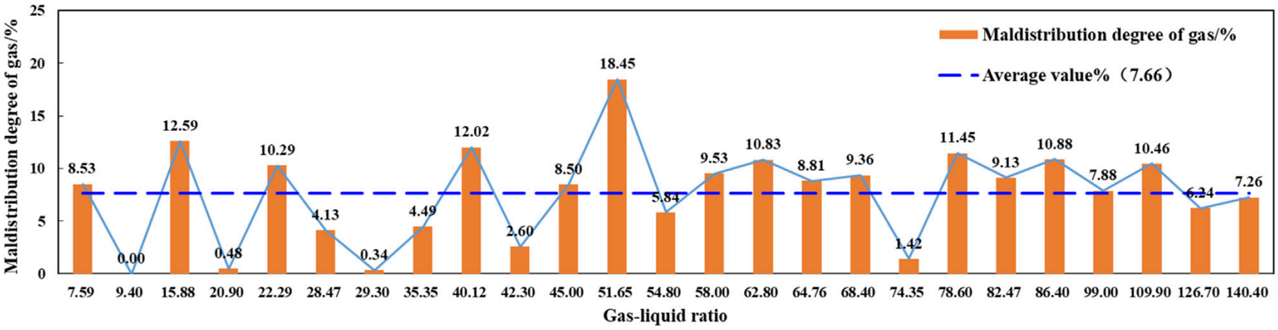

FIGURE 5
Histogram of gas–liquid ratio and maldistribution degree of gas in stratified flow in horizontal manifold without flute pipes (liquid injection volume 0.10L/s+0.17L/s).

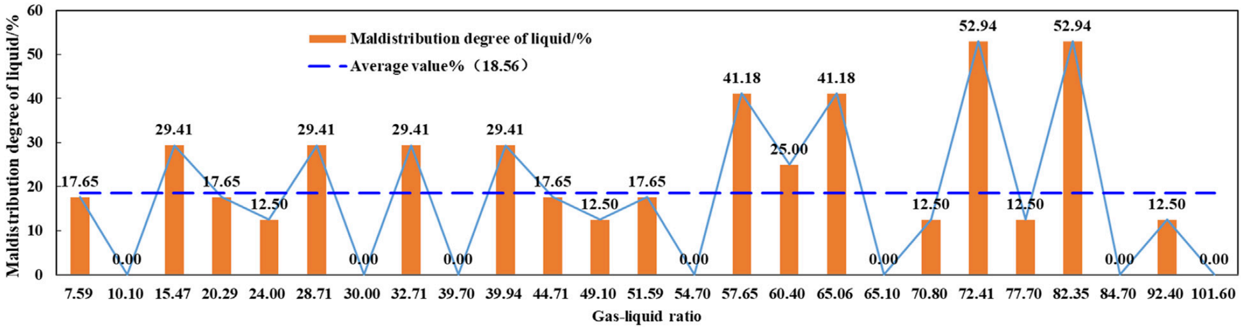

FIGURE 6
Histogram of gas–liquid ratio and maldistribution degree of liquid in stratified flow in horizontal manifold with flute pipes (liquid injection volume 0.10L/s+0.17L/s).

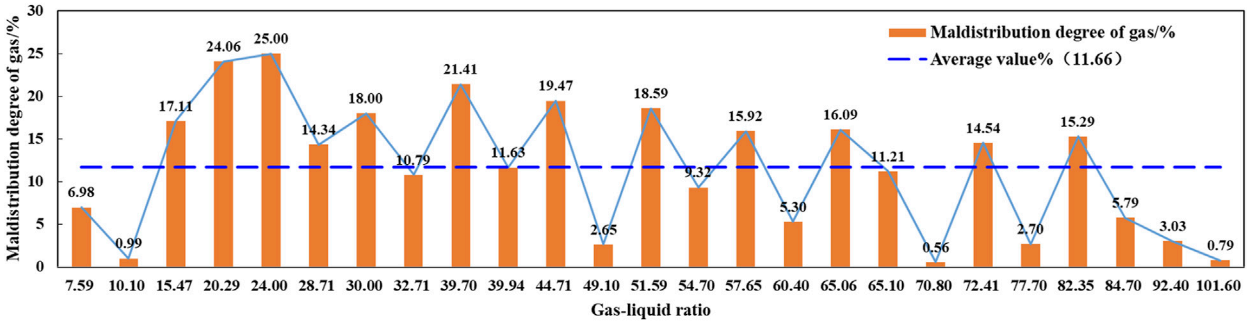

FIGURE 7
Histogram of gas–liquid ratio and maldistribution degree of gas in stratified flow in horizontal manifold with flute pipes (liquid injection volume 0.10L/s+0.17L/s).

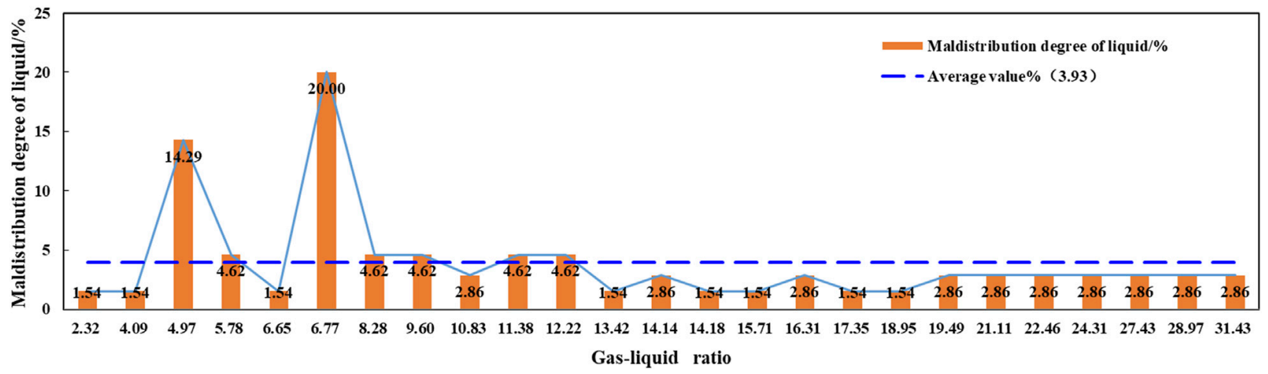

FIGURE 8
Histogram of gas–liquid ratio and maldistribution degree of liquid in slug flow in horizontal manifold without flute pipes (liquid injection volume 0.35L/s+0.65L/s).

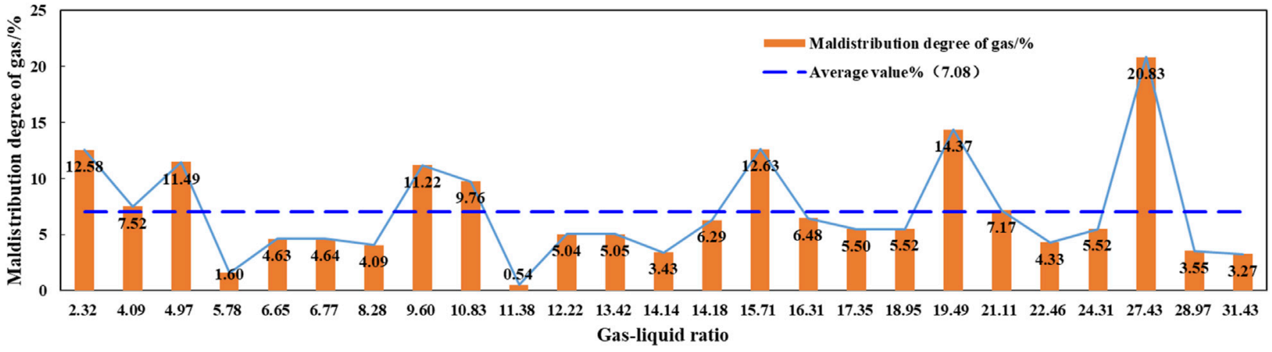

FIGURE 9
Histogram of gas–liquid ratio and maldistribution degree of gas in slug flow in horizontal manifold without flute pipes (liquid injection volume 0.35L/s+0.65L/s).

Maldistribution test of slug flow in horizontal manifold without flute pipe

Through the analysis of histogram of gas–liquid ratio and maldistribution degree of liquid in slug flow in horizontal manifold without flute pipe (Figure 8), it is found that the overall trend of liquid maldistribution degree with the increase of gas–liquid ratio is that it fluctuates slightly at first, and then decreases to a certain extent and then tends to be relatively stable. When the gas–liquid ratio is 6.77, the maldistribution degree of liquid is the largest, which is 20.00%. Through the analysis of the histogram of gas–liquid ratio and maldistribution degree of gas in slug flow in horizontal manifold without flute pipe (Figure 9), it is found that the overall trend of maldistribution degree of gas is relatively stable with the increase of gas–liquid ratio, but there is a larger maldistribution degree of gas when the gas–liquid ratio is 27.43, which is 20.83%.

Maldistribution test of slug flow in horizontal manifold with flute pipe

Through the analysis of histogram of gas–liquid ratio and maldistribution degree of liquid in slug flow in horizontal manifold with flute pipe (Figure 10), it is found that the overall trend of the maldistribution degree of liquid with the increase of the gas–liquid ratio is that the maldistribution degree of liquid increases gradually with the gas–liquid ratio, then decreases sharply, and then increases sharply, and finally tends to be relatively stable. When the gas–liquid ratio is 1.94, the maldistribution degree of

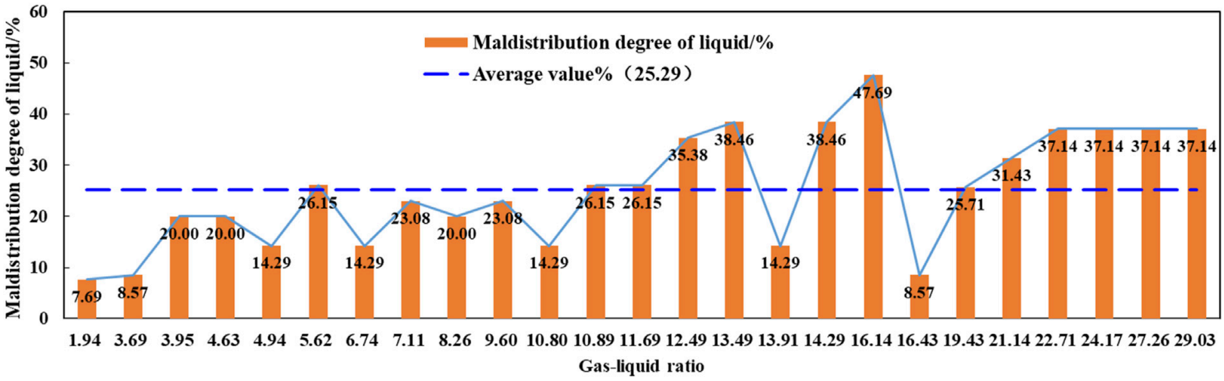

FIGURE 10
Histogram of gas–liquid ratio and maldistribution degree of liquid in slug flow in horizontal manifold with flute pipes (liquid injection volume 0.35L/s+0.65L/s).

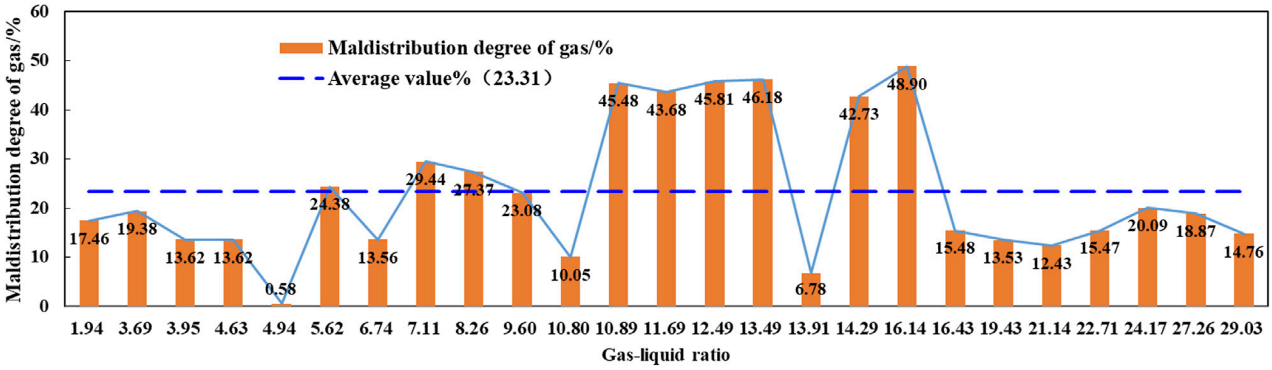

FIGURE 11
Histogram of gas–liquid ratio and maldistribution degree of gas in slug flow in horizontal manifold with flute pipes (liquid injection volume 0.35L/s+0.65L/s).

liquid is as low as 7.69%, and when the gas–liquid ratio is 16.14, the peak maldistribution degree of liquid is 47.69%.

Through the analysis of histogram of gas–liquid ratio and maldistribution degree of gas in slug flow in horizontal manifold with flute pipe (Figure 11), it is found that the overall trend of maldistribution degree of gas with the increase of gas–liquid ratio is that it changes in a zigzag shape at first, then the value is larger and more stable in the range of gas–liquid ratio of 10.89–13.49, and the maldistribution degree of gas is stable and small in the range of the gas–liquid ratio of 16.43–29.03. When the gas–liquid ratio is 4.94, the maldistribution degree of gas is the lowest, as low as 0.58%, and when the gas–liquid ratio is 46.67, the maximum maldistribution degree of gas is 48.90%.

Maldistribution test of annular flow in horizontal manifold without flute pipe

Through the analysis of histogram of gas–liquid ratio and maldistribution degree of liquid in annular flow in horizontal manifold without flute pipes (Figure 12), it is found that the overall trend of maldistribution degree of liquid fluctuates with the increase of gas–liquid ratio, but the fluctuation range is not very large, and then decreases to be stable when it increases to 25%. When the gas–liquid ratio is 70.06 and 103.38, the maldistribution degree of liquid is as low as 0, and when the gas–liquid ratio is 89.38, the peak value of the maldistribution degree is 25.00%. Through the analysis of histogram of gas–liquid ratio and maldistribution degree of gas in annular flow in horizontal manifold without flute pipes (Figure 13), we can see that the overall trend of maldistribution degree of gas is

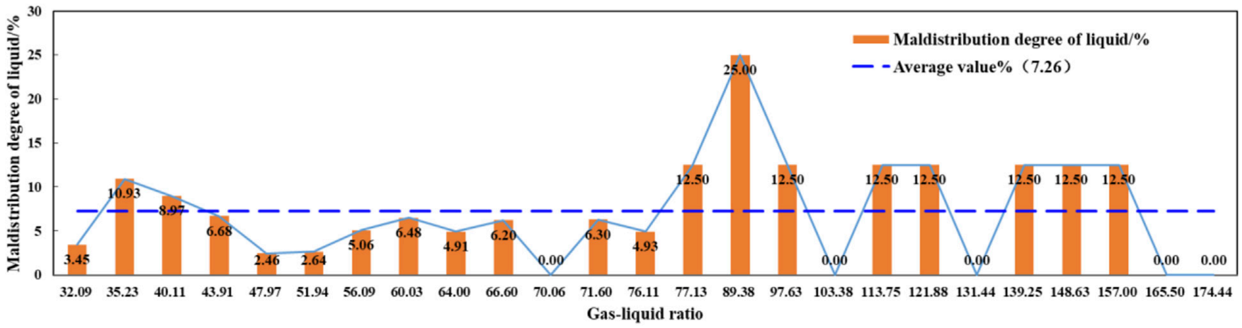

FIGURE 12
Histogram of gas–liquid ratio and maldistribution degree of liquid in annular flow in horizontal manifold without flute pipes (liquid injection volume 0.16L/s+0.35L/s).

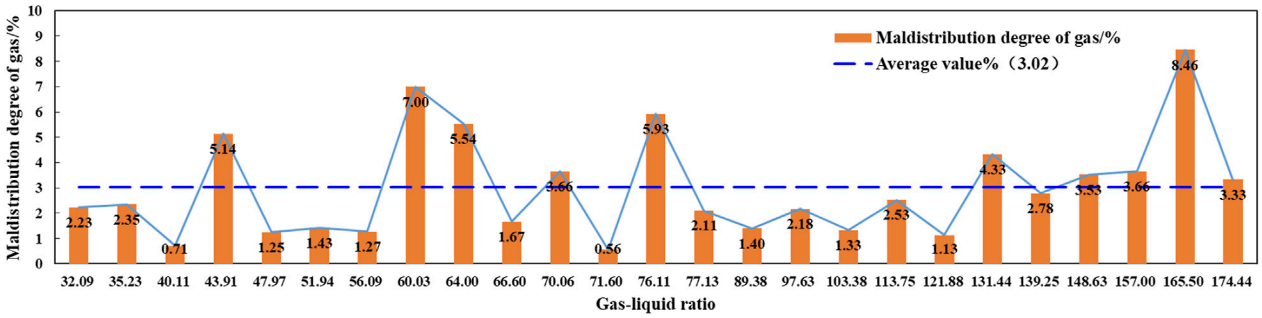

FIGURE 13
Histogram of gas–liquid ratio and maldistribution degree of gas in annular flow in horizontal manifold without flute pipes (liquid injection volume 0.16L/s+0.35L/s).

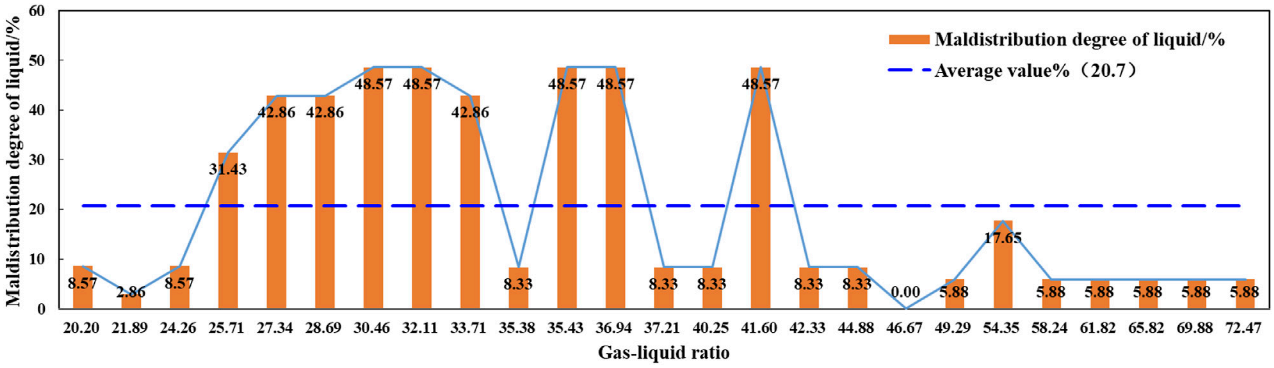

FIGURE 14
Histogram of gas–liquid ratio and maldistribution degree of liquid in annular flow in horizontal manifold with flute pipes (liquid injection volume 0.16L/s+0.35L/s).

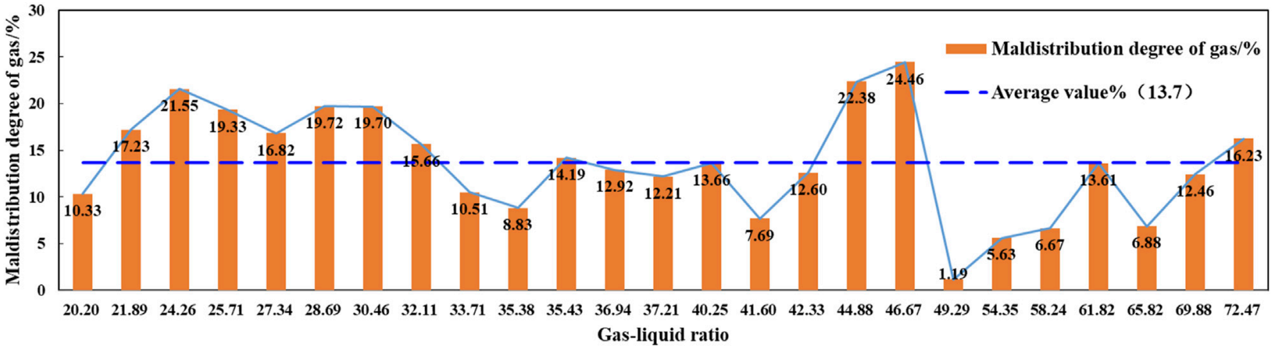

FIGURE 15
Histogram of gas–liquid ratio and maldistribution degree of gas in annular flow in horizontal manifold with flute pipes (liquid injection volume 0.16L/s+0.35L/s).

zigzag with the increase of gas–liquid ratio. When the gas–liquid ratio is 71.60, the maldistribution degree of gas is the lowest, as low as 0.56%. When the gas–liquid ratio is 165.50, the maximum maldistribution degree of gas is 8.46%.

The comparative analysis shows that the horizontal manifold without a flute pipe is beneficial to control the maldistribution of liquid when the gas–liquid ratio is in the range of 32.09–76.11, and the horizontal manifold without a flute pipe is beneficial to control the maldistribution of gas when the gas–liquid ratio is in the range of 32.09–174.44.

Maldistribution test of annular flow in horizontal manifold with flute pipe

Through the analysis of histogram of gas–liquid ratio and maldistribution degree of liquid in annular flow in horizontal manifold with flute pipe (Figure 14), it can be seen that with the increase of gas–liquid ratio, the overall trend of maldistribution degree of liquid decreases slightly at first, then increases sharply, then the zigzag shape changes sharply, and then tends to be relatively stable. When the gas–liquid ratio is 46.67, the maldistribution degree of liquid is as low as 0, and the peak maldistribution degree is 48.57%.

Through the analysis of the histogram of gas–liquid ratio and maldistribution degree of gas in annular flow in horizontal manifold with flute pipes (Figure 15), it is found that the overall trend of maldistribution degree of gas is zigzag with the increase of gas–liquid ratio. When the gas–liquid ratio is 49.29, the maldistribution degree of gas is the lowest, as low as 1.19%. When the gas–liquid ratio is 46.67, the maximum maldistribution degree of gas is 24.46%.

The comparative analysis shows that the addition of flute pipe into the horizontal manifold is beneficial to control the maldistribution degree of liquid when the gas–liquid ratio is in the range of 20.20–24.26 and 42.33–72.47, and the introduction of flute pipes is beneficial to control the maldistribution degree of gas when the gas–liquid ratio is in the range of 33.71–35.38, 41.60–42.33, and 49.29–69.88.

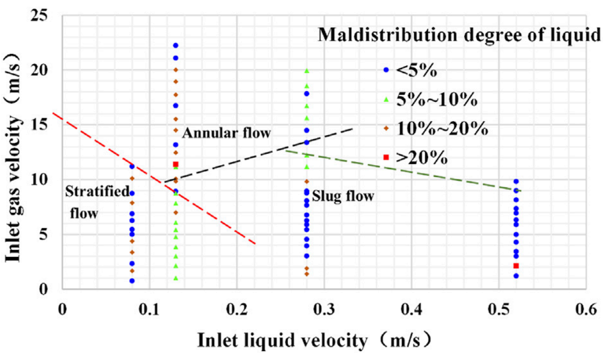

FIGURE 16
Scatter diagram of liquid maldistribution degree in different flow patterns in horizontal manifold without flute pipes.

Analysis of maldistribution control in different flow patterns

According to the analysis of the maldistribution degree of liquid and gas of stratified flow, slug flow, and annular flow when flute pipe is considered and not considered, we obtained the scatter diagram of liquid maldistribution degree in different flow patterns in horizontal manifold with and without flute pipe and histogram of flow pattern and average liquid maldistribution degree in the horizontal manifold.

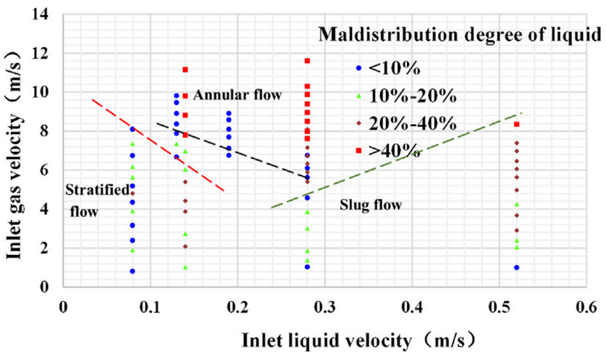

FIGURE 17
Scatter diagram of liquid maldistribution degree in different flow patterns in horizontal manifold with flute pipe.

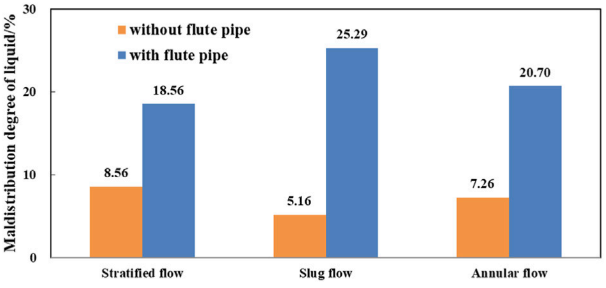

FIGURE 18
Histogram of flow pattern and average liquid maldistribution degree in the horizontal manifold.

Through the analysis of the scatter diagram of liquid maldistribution degree in different flow patterns in horizontal manifold with and without flute pipes (Figures 16, 17), and the histogram of flow pattern and average liquid maldistribution degree in horizontal manifold (Figure 18), it is found that under the condition that the flute pipe is not added in the horizontal manifold, the average maldistribution degree of liquid in stratified flow, slug flow, and annular flow are 8.56, 5.16, and 7.26%, respectively. The average maldistribution degree of liquid under the three flow patterns is small as a whole, and the average maldistribution degree of liquid under the stratified flow condition is greater than that under the slug flow and annular flow conditions. Average maldistribution degree of liquid under the slug flow condition is less than that under the stratified flow and annular flow conditions.

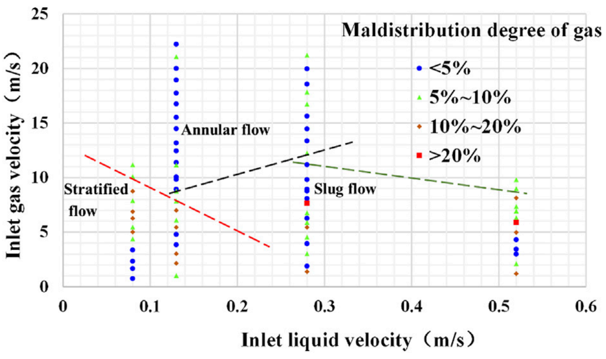

FIGURE 19
Scatter diagram of gas maldistribution degree in different flow patterns in horizontal manifold without flute pipe.

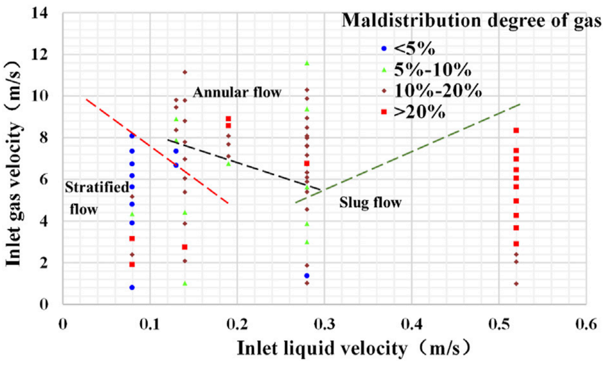

FIGURE 20
Scatter diagram of gas maldistribution degree in different flow patterns in horizontal manifold with flute pipe.

Under the condition of introducing a flute pipe into the horizontal manifold, the average maldistribution degree of liquid in stratified flow, slug flow, and annular flow are 18.56, 25.29, and 20.70%, respectively. However, the average maldistribution degree of liquid under the condition of stratified flow is less than that of slug flow and annular flow. The average maldistribution degree of liquid under the condition of slug flow is greater than that of stratified flow and annular flow. Compared with the horizontal manifold with and without the introduction of a flute pipe, the absence of a flute pipe is beneficial to control the average maldistribution degree of liquid. The introduction of a flute pipe will aggravate the maldistribution degree of liquid, especially under the condition of slug flow pattern. This is because after the gas–liquid fluid enters the flute pipe, the cross-section becomes smaller and the gas–liquid velocity increases relatively. The flow of the liquid becomes more unstable, so the flow maldistribution is more likely to occur at the two outlets. Under the condition of the slug flow pattern,

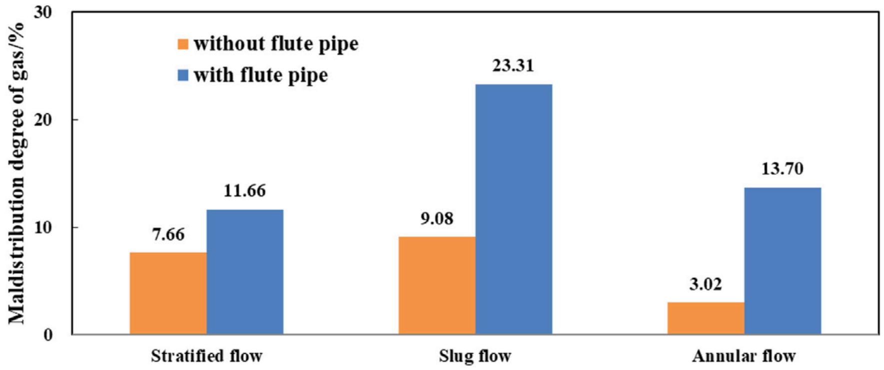

FIGURE 21
Histogram of flow pattern and average gas maldistribution degree in the horizontal manifold.

the gas–liquid interface is in direct contact with the upper part of the flute pipe due to violent fluctuations, which separates the gas phase located in the upper part of the pipe into an aeroelastic and forms the slug flow pattern.

Through the analysis of the scatter diagram of gas maldistribution degree in different flow patterns in horizontal manifold with and without flute pipes (Figures 19, 20), and the histogram of flow pattern and average gas maldistribution degree in horizontal manifold (Figure 21), it is found that under the condition that flute pipe is not added in the horizontal manifold, the average maldistribution degree of gas in stratified flow, slug flow, and annular flow is 7.66, 9.08, and 3.02%, respectively. The average maldistribution degree of gas under the three flow patterns is small as a whole, and the average maldistribution degree of gas in the slug flow condition is greater than that in the stratified flow and annular flow conditions. Under the condition of annular flow, the average maldistribution degree of gas is less than that of stratified flow and slug flow.

When the flute pipe is introduced into the horizontal manifold, the average maldistribution degree of gas in stratified flow, slug flow, and annular flow are 11.66, 23.31, and 13.70%, respectively. However, the average maldistribution degree of gas under the condition of stratified flow is less than that of slug flow and annular flow. The average maldistribution degree of gas under the condition of slug flow is greater than that of stratified flow and annular flow. The introduction of a flute pipe will aggravate the maldistribution degree of gas, especially under the condition of an annular flow pattern. This is because after the gas–liquid fluid enters the flute pipe, the cross-section becomes smaller and the gas–liquid velocity increases relatively. The flow of the gas becomes more unstable, so the flow maldistribution is more likely to occur at the two outlets. Under the condition of an annular flow pattern, the central part of the flute pipe is a gas core with droplets, and there is a liquid film on the pipe wall. Under the influence of gravity, the liquid film of the lower pipe wall is thicker than that of the upper tube wall.

Through comparative analysis of the horizontal manifold with and without the introduction of flute pipe, the absence of flute pipes is conducive to the control of the average maldistribution degree of gas. Under the condition of introducing a flute pipe, it is disadvantageous to the control of the average maldistribution degree of liquid and gas in the slug flow pattern.

Conclusion

1) The influence of flow pattern and the introduction of flute pipes on the maldistribution degree of liquid and gas under the condition of different gas–liquid ratios is revealed.
   ① When the flute pipe is not introduced into the horizontal pipe under the condition of stratified flow, it is beneficial to control liquid maldistribution when the gas–liquid ratio is in the range of 22.29–40.12 and 58.00–86.40, and it is beneficial to control gas maldistribution when the gas–liquid ratio is in the range of 7.59–45.00 and 54.80–140.40.
   ② When the flute pipe is introduced into the horizontal pipe under the condition of stratified flow, it is beneficial to control both liquid and gas maldistribution when the gas–liquid ratio is in the range of 84.70–101.60, 77.70, 70.80, 49.10, and 10.10.
   ③ When the flute pipe is not introduced into the horizontal pipe under the condition of slug flow, it is beneficial to control liquid maldistribution when the gas–liquid ratio is in the range of 5.78–6.65 and 8.28–31.4, and it is beneficial to control gas maldistribution when the gas–liquid ratio is in the range of 4.09–10.83, 12.22–18.95, 21.11–24.31, and 54.80–140.40.
   ④ When the flute pipe is introduced into the horizontal pipe under the condition of slug flow, it is beneficial to control

liquid maldistribution when the gas–liquid ratio is in the range of 1.94–3.69 and 16.43, and it is beneficial to control gas maldistribution when the gas–liquid ratio is in the range of 16.43–22.71, 4.94, and 13.91.

⑤ When the flute pipe is not introduced into the horizontal pipe under the condition of annular flow, it is beneficial to control liquid maldistribution when the gas–liquid ratio is in the range of 3.45–4.93, 165.50–174.44, 103.38, and 131.44, and it is beneficial to control gas maldistribution when the gas–liquid ratio is in the range of 2.23–174.44.

⑥ When the flute pipe is introduced into the horizontal pipe under the condition of annular flow, it is beneficial to control liquid maldistribution when the gas–liquid ratio is in the range of 46.67–49.29 and 58.24–72.47, and it is beneficial to control gas maldistribution when the gas–liquid ratio is in the range of 49.29–58.24 and 65.82.

2) A maldistribution control scheme of gas–liquid two-phase flow in the horizontal pipeline is proposed: it is more beneficial to the control of average liquid maldistribution in the horizontal manifold of slug flow pattern without the introduction of flute pipe; it is more beneficial to the control of average gas maldistribution in the horizontal manifold of annular flow pattern without the introduction of flute pipe; it is more beneficial to the control of both average liquid and gas maldistribution in the horizontal manifold of annular flow pattern without the introduction of flute pipe.

Data availability statement

The original contributions presented in the study are included in the article/Supplementary Material; further inquiries can be directed to the corresponding authors.

Author contributions

NW, LJ, and SF contributed to conception and design of the study. NW, LJ, and AL established the experiment model. HL, SZ, CZ, and JX performed the experiments, calculations and analysis. LJ wrote the first draft of the manuscript. NW, and SF wrote sections of the manuscript. All authors contributed to manuscript revision, read, and approved the submitted version.

Funding

The work described in this article is supported by the National Natural Science Foundation of China (U20B6005 and 51874252), the National Key Research and Development Program of China (2021YFC28000903), 111 Project (D21025), and the High-end Foreign Expert Introduction Program (G2021036005L).

Conflict of interest

AL was employed by the company Chuanqing Drilling Engineering Company.

The remaining authors declare that the research was conducted in the absence of any commercial or financial relationships that could be construed as a potential conflict of interest.

Publisher's note

References

Azzopardi, B. J. (1999). Phase separation at T-junction. *Multiph. Sci. Technol.* 11 (4), 1–143.

Chen, H., Li, Q., Yao, H., Li, Y., and Gong, J. (2019). Study on the flow maldistribution problem of the gathering and transportation manifold for gas-liquid two phase flow. *Oil-Gas Field Surf. Eng.* 38 (3), 1–6. doi:10.3969/j.issn.1006-6896.2019.03.001

Duan, F., and Liang-cai, C. (2016). Numerical simulation of flow distribution characteristics of manifold with mid-plate. *Pipeline Tech. Equip.* 4, 1–4. doi:10.3969/j.issn.1004-9614.2016.04.001

Hao, Y., Wang, Y., and Hu, T. (2016). The flow distribution in the parallel tubes of the cavity receiver under variable heat flux. *Appl. Therm. Eng.* 108 (1), 641–649. doi:10.1016/j.applthermaleng.2016.07.168

Kaichiro, M., and Ishi, M. (1984). Flow regime transition criteria for upward two-phase flow in vertical tubes. *Int. J. Heat. Mass Transf.* 27 (5), 723–737. doi:10.1016/0017-9310(84)90142-x

Kim, S., Choi, E., and Cho, Y. I. (1995). The effect of header shapes on the flow distribution in a manifold for electronic packaging applications. *Int. Commun. Heat Mass Transf.* 22 (3), 329–341. doi:10.1016/0735-1933(95)00024-s

Lahey, R. T. (1986). Current understanding of phase separation mechanisms in branching conduits. *Nucl. Eng. Des.* 95, 145–161. doi:10.1016/0029-5493(86)90043-9

Lee, J., and Lee, S. (2004). Distribution of two- phase annular flow at header -channel junctions. *Exp. Therm. Fluid Sci.* 28 (3), 217–222. doi:10.1016/s0894-1777(03)00042-6

Li, X. (2017). "Simulation of flow distribution characteristics of natural gas liquefaction heat exchanger networks," (China: Shandong University). Master thesis.

Li, Y. (2010). "Experimental and numerical simulation of gas-liquid two-phase flow in distribution header," (Beiging: North China Electric Power University). Doctoral thesis.

Marchitto, A., Fossa, M., and Guglielmini, G. (2012). The effect of the flow direction inside the header on two-phase flow distribution in parallel vertical channels. *Appl. Therm. Eng.* 36, 245–251. doi:10.1016/j.applthermaleng.2011.10.008

McQuillan, K. W., and Whalley, P. B. (1985). Flow patterns in vertical two-phase flow. *Int. J. Multiph. Flow* 11 (2), 161–175. doi:10.1016/0301-9322(85)90043-6

Miao, Z. (1999). Flow characteristics of single phase fluid in multiorifice distributing pipe and collecting pipe. *J. Shanghai Jiaot. Univ.* 33 (3), 297–300.

Wang, D. (2012). Research on piccolo heat and flow distribution of civil aircraft anti-ice system. *Civ. Aircr. Des. Res.* 11, 1–5. doi:10.19416/j.cnki.1674-9804.2012.s1.041

Wang, Q., and Newby, B. M. Z. (2018). Layer-by-layer polyelectrolytes coating of alginate microgels for sustained release of sodium benzoate and zosteric acid. *J. Drug Deliv. Sci. Technol.* 46(37), 46–54. doi:10.1016/j.jddst.2018.04.019

Yan, L. (2019). Study on the application of variable diameter flute tube shunt technology in multi-on-line heat recovery. *Electron. World* 15, 196–197.

Yang, L. M., and Azzopardi, B. J. (2007). Phase split of liquid-liquid two-phase flow at a horizontal T-junction. *Int. J. Multiph. Flow* 33 (2), 207–216. doi:10.1016/j.ijmultiphaseflow.2006.08.004

Zhang, J., Guan, T., and Shan, Y. (2017). Influence of piccolo tube parameters on temperature distribution on hot-air anti-icing concave surface. *J. Nanjing Univ. Aeronautics Astronautics* 49 (5), 669–675. doi:10.16356/j.1005-2615.2017.05.010

Zhou, J., Sun, Z., Ding, M., Bian, H., Zhang, N., and Meng, Z. (2017). CFD simulation for flow distribution in manifolds of central- type compact parallel flow heat exchangers. *Appl. Therm. Eng.* 126, 670–677. doi:10.1016/j.applthermaleng.2017.07.194

Zhu, B., Pang, L.-P., and Lv, Y.-X. (2013). Study on gas-liquid two phase flow distribution in headers with multiple parallel branch tubes. *J. North China Electr. Power Univ.* 40 (2), 95–100. doi:10.3969/j.issn.1007-2691.2013.02.017

Frontiers in Earth Science

Investigates the processes operating within the major spheres of our planet

Advances our understanding across the earth sciences, providing a theoretical background for better use of our planet's resources and equipping us to face major environmental challenges.

Discover the latest Research Topics

See more →

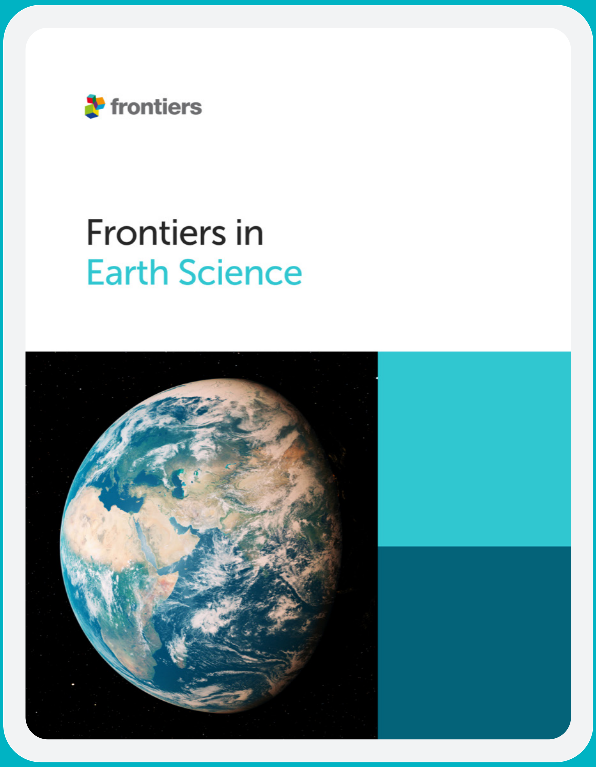

Frontiers

Avenue du Tribunal-Fédéral 34
1005 Lausanne, Switzerland
frontiersin.org

Contact us

+41 (0)21 510 17 00
frontiersin.org/about/contact